Imperial College London

Attosecond transient absorption spectroscopy in atomic species

Emma Rose Simpson

December 2016

Laser Consortium

Imperial College London

Department of Physics

QOLS Group

Thesis submitted in partial fulfillment of the requirements for the degree of Doctor of Philosophy of Imperial College London and the Diploma of Imperial College.

For my family,
who always believe in me.

Acknowledgements

I would like to thank my supervisor, Professor Jon Marangos, for his support and guidance throughout the PhD, and in the writing this thesis. I would also like to thank all of those who I have worked with during my time at Imperial College, in particular the ones who have contributed towards the work I present here. To those who have accompanied me during the many late nights, weekends and frustrated hours in the lab: thank you, I hope we can look back fondly on the experience. To my family who have supported me throughout - I would not be where I am today if it was not for you. To my partner Nils - thank you for always being there for me. In particular thank you for the many late night dinners, and for frequently reminding me of life outside and beyond the PhD. Finally, a big thank you to the excellent friends I have made throughout my studies, I hope our friendship will continue for many years to come.

Declaration

I hereby declare that the work presented in this thesis is my own unless otherwise acknowledged or made reference to in the text.

Emma Rose Simpson

The copyright of this thesis rests with the author and is made available under a Creative Commons Attribution Non-Commercial No Derivatives licence. Researchers are free to copy, distribute or transmit the thesis on the condition that they attribute it, that they do not use it for commercial purposes and that they do not alter, transform or build upon it. For any reuse or redistribution, researchers must make clear to others the licence terms of this work.

Abstract

When high intensity laser light is focused into a gaseous target, high energy photons can be produced through the strongly nonlinear effect of high order harmonic generation. For a 30 fs, 800 nm or 1400 nm wavelength laser pulse, the result is a train of attosecond pulses produced at odd harmonic frequencies of the driving laser field, spanning energy ranges into the 100s eV. These attosecond pulses can access timescales characteristic to the movement of electrons in atoms, and by exploiting their properties as an ultrafast probe, electron dynamics in evolving atomic systems can be observed.

This thesis presents the development of a pump-probe beamline capable of performing transient absorption spectroscopy experiments with resolution better than 150 as. Accompanying a full description of the experimental setup and methods, investigations are made into the attosecond transient absorption from strong field dressed helium and krypton atoms around their first ionisation edge, and 3d ionisation edge respectively. The result of the delay dependent transient absorption measurement is modulations to the recorded absorption amplitude for the harmonic orders around the respective ionisation thresholds. We investigated intensity regimes with an 800 nm laser field approaching the strong field ionisation threshold in helium.

Experimental results are presented considering first the response of strong field dressed helium using an 800 nm laser field, and second the response of strong field dressed helium and krypton using a 1400 nm laser field. The use of the longer 1400 nm wavelength allows access to higher energy probe harmonics, enabling laser dressed krypton core to continuum, and core to Rydberg state transitions to be studied. By comparing the effect to the delay dependent absorption modulation as additional parameters are varied, information can be gained about the behaviour of the electrons. The parameters studied as a function of delay include: the dressing field intensity, target backing pressure and dressing field relative linear polarisation, aligned both parallel and perpendicular with respect to the probing harmonic pulse train. Key results include a strong suppression of the modulation amplitude for the above ionisation threshold harmonic orders when the dressing field linear polarisation is changed from parallel to perpendicular in the helium target. This is reproduced at both 800 nm and 1400 nm driving wavelengths.

Contents

List of Figures **11**

List of Tables **17**

Abbreviations **18**

1 Introduction **21**

1.1 History of the Field . . . 22
1.2 Motivation of Beamline Design . . . 24
1.3 Introduction to the Thesis . . . 26
1.4 Author Contribution . . . 27
1.4.1 Author Presentations . . . 28

2 The Interaction of Light and Matter **30**

2.1 Effect of Light on Matter . . . 31
2.1.1 Introduction to Quantum Light-Matter Interaction . . . 32
2.2 Ionisation mechanisms . . . 34
2.2.1 Weak Field Regime . . . 34
2.2.1.1 Single-photon Ionisation . . . 35
2.2.1.2 Multi-photon Ionisation . . . 35
2.2.1.3 Above Threshold Ionisation . . . 37
2.2.2 Strong Field Regime . . . 38
2.2.2.1 Tunnel Ionisation . . . 38
2.2.2.2 Over the Barrier Ionisation . . . 40
2.2.3 Ponderomotive Energy . . . 41
2.2.4 Keldysh Parameter . . . 43
2.3 The Effect of Matter on Light . . . 44
2.3.1 Dispersion . . . 44
2.3.2 Effects of Nonlinear Interaction . . . 45

2.3.2.1 The Pockels Effect . . . 47
2.3.2.2 Third Order Nonlinearities - The Optical Kerr Effect . . . 48
2.4 High Order Harmonic Generation . . . 49
2.4.1 Semi-Classical Three Step Model . . . 49
2.4.1.1 Time-frequency Mapping . . . 54
2.4.1.2 Strong Field Approximation . . . 54
2.4.1.3 Wavepacket Spreading . . . 56
2.4.2 Macroscopic Effects . . . 57
2.4.2.1 Phase Matching . . . 57
2.5 Pump-Probe Experiments . . . 60
2.5.1 Attosecond Transient Absorption Spectroscopy . . . 61
2.5.2 Modulation Mechanisms . . . 62
2.5.2.1 Light Induced States . . . 63
2.5.2.2 "Which Way" Interference . . . 63
2.5.2.3 AC Stark Shift . . . 64
2.5.3 XUV initiated High harmonic Generation . . . 65

3 Ultrafast Light Sources: Generation and Characterisation 67
3.1 Laser Basics . . . 68
3.2 Femtosecond Light Sources . . . 70
3.2.1 Modelocking . . . 70
3.2.1.1 Modelocking Methods . . . 72
3.2.2 Chirped Pulse Amplification . . . 73
3.2.3 The KM Labs Red Dragon . . . 74
3.2.3.1 The Oscillator . . . 75
3.2.3.2 The First Stage Amplification . . . 76
3.2.3.3 The Second Stage Amplification . . . 77
3.2.4 Optical Parametric Processes . . . 78
3.2.4.1 The TOPAS . . . 78
3.2.4.2 TOPAS Stability . . . 80
3.3 Pulse Characterisation Techniques . . . 83
3.3.1 Frequency Resolved Optical Gating (FROG) . . . 83
3.3.2 Spectral Phase Interferometry for Direct Electric field Reconstruction (SPIDER) 85

4 Experimental Methods 87
4.1 The Beamline . . . 87
4.1.1 The Generation Chamber . . . 88

4.1.1.1 The Generation Beam . . . 88
4.1.1.2 The Dressing Field Beam . . . 91
4.1.2 The Toroidal Chamber . . . 92
4.1.3 The Interaction Chamber . . . 93
4.1.4 The Flat Field Spectrometer . . . 93
4.2 Spectral Filtering . . . 94
4.3 Stabilisation . . . 98
4.3.1 Laser Stability . . . 98
4.3.2 Generation Chamber Stability . . . 101
4.4 Phase Tagging Temporal Correction . . . 101
4.5 Offline Diagnostics . . . 102
4.5.1 Focus Measurements and Overlap . . . 104
4.5.2 Power Measurements . . . 105
4.5.3 Intensity Measurements . . . 105
4.6 Calibration of HHG Spectra . . . 106
4.7 800 nm Specific Methods . . . 109
4.7.1 Data Acquisition . . . 109
4.7.2 Data Processing . . . 111
4.7.2.1 Converting Transmission into Absorption Cross-Section . . . 116
4.7.2.2 Theoretical Methods . . . 117
4.8 Advances in the Beamline . . . 117
4.9 1400 nm Specific Methods . . . 119
4.9.1 Data Acquisition . . . 119
4.9.2 Data Processing . . . 121

5 Transient Absorption from 800 nm Laser Dressed Helium 123
5.1 Response to Varying the Pump-Probe Delay . . . 125
5.2 Relative Dressing Field Linear Polarisation Response . . . 130
5.3 Response to Varying the Dressing Field Peak Intensity . . . 136
5.4 Discussion . . . 140

6 Transient Absorption Using 1400 nm Dressing Field 150
6.1 Probing the Krypton 3d State Through Laser Dressed Transient Absorption . . . 151
6.1.1 Dressing Field Polarisation Dependence In Kr Target . . . 151
6.1.2 Dressing Field Peak Intensity Dependence In Kr Target . . . 155
6.1.3 Dependence on the Krypton Backing Pressure . . . 160
6.1.4 Delay Dependence In Kr Target . . . 166

6.1.5 Discussion . . . 170
6.2 Transient Absorption from Long Wavelength Laser Dressed Helium . . . 171
6.2.1 Dressing Field Polarisation Dependence . . . 171
6.2.2 Delay Dependence In He Target . . . 183
6.2.3 Discussion . . . 187

7 Perspectives and Future Work **189**
7.1 Spatial Filtering . . . 190
7.2 Upgrading to 1kHz Beamline . . . 193
7.3 Future Work . . . 194

Bibliography **195**

A Copyright Permissions **210**

List of Figures

1.1 Development and improvement of short pulse generation techniques over time. Reprinted by permission from Macmillan Publishers Ltd: Nature Physics [5], copyright 2007, modified from [26] © 2008 Canadian Science Publishing or its licensors. Reproduced with permission. 24

1.2 Chronology of the attainable peak pulse intensity along with the achievable electron energy for the given focused intensity ranges. Modified from [14], © IOP Publishing. Reproduced with permission. All rights reserved. 25

2.1 Perturbative regime ionisation mechanisms: single-photon ionisation, multi-photon ionisation and above threshold ionisation. 35

2.2 Schematic diagram of the large distortions that occur to the potential experienced by bound valence electrons in the presence of a strong dressing field. 39

2.3 Strong-field regime ionisation mechanisms: Tunnel ionisation and over-the-barrier ionisation. 40

2.4 Schematic diagram of carrier envelope phase. 46

2.5 Schematic diagram of the semi-classical 3-step model for high harmonic generation. 50

2.6 Calculated classical electron trajectories for high harmonic generation. 52

2.7 Cartoon picture of a typical high harmonic generation spectrum produced from a many cycle pulse. 53

2.8 High harmonic generation order vs. trajectory emission time. This plot has been reproduced from [90]. Reprinted with permission from AAAS. 55

2.9 Schematic diagram illustrating Gaussian beam propagation and Gouy phase across a focus. 59

2.10 Schematic diagram of the principles of attosecond transient absorption spectroscopy. 62

2.11 Schematic diagram of the mechanisms involved in producing modulation in the detected harmonic signal. 63

2.12 Schematic diagram of the technique of XUV initiated high harmonic generation. . . 66

3.1 Schematic diagram of a simplified four-level system illustrating the key components required for efficient lasing to occur. . . . 69
3.2 Absorption and emission spectra for Ti:Sapph laser [144]. Reprinted with permission courtesy of MIT Lincoln Laboratory, Lexington, Massachusetts. . . . 71
3.3 Illustration of the technique of modelocking. . . . 72
3.4 Schematic diagram of the technique of chirped pulse amplification (CPA). . . . 74
3.5 Schematic diagram of the Red Dragon laser set-up, and associated additional lasers. 75
3.6 Schematic drawing of the Oscillator set-up. . . . 76
3.7 Comparison of pump, probe and input powers as TOPAS delay 3 is adjusted. . . . 81
3.8 Comparison of the splitting ratio between the pump and probe powers as the TOPAS delay 3 is adjusted. . . . 82
3.9 Schematic diagram of a typical scanning FROG setup. . . . 84
3.10 Schematic diagram of the SPIDER used in the laboratory, based closely on the schematic provided with the APE SPIDER used in the lab [149]. . . . 85

4.1 Schematic of the beamline used to perform ATAS from laser dressed helium at 1400 nm. Modified with permission from SPIE [37]. . . . 89
4.2 Transmission spectrum of 150 nm aluminium filter from CXRO. . . . 96
4.3 Comparison of generated spectra with and without a 150 nm aluminium filter. . . . 97
4.4 Transmission spectrum of a 400 nm silicon, 200 nm zirconium composite filter from CXRO [151]. . . . 99
4.5 Comparison of generated spectra with and without a 400 nm silicon, 200 nm zirconium composite filter. . . . 100
4.6 The key steps associated with phase tagging the relative pump-probe delay for post acquisition temporal correction. . . . 103
4.7 Example focal spot image and focal spot scan to determine the peak intensity of the dressing field. . . . 107
4.8 Images showing the source harmonics and static absorption (field free transmission) raw harmonic spectra compared with the corresponding background subtracted versions. . . . 110
4.9 Typical box selection for the harmonics using the mean signal of the delay scan and standard deviation of the image stack as guidance. . . . 113
4.10 Determining the extra effective background due to scattered generation arm light in the presence of the target gas for high MCP voltages. . . . 115
4.11 Schematic of a typical scan procedure used to perform the 2-dimensional polarisation dependence transient absorption scans. . . . 121

5.1 Illustration of the electronic structure of helium. The singlet electronic shell energies were taken from the NIST catalogue [158]. 126

5.2 Transient absorption signal as a function of delay presented in both the time and frequency domains for a dressing field intensity 2.4×10^{14}W/cm^2. This Figure has been reproduced from reference [35]. © IOP Publishing. Reproduced with permission. All rights reserved. CC BY 3.0. 127

5.3 Transient absorption delay scan showing increase in transmission of harmonic 19 around the central temporal overlap position compared with the edges. 131

5.4 Delay dependent response of the absorption cross section as a function of parallel and perpendicular aligned pump-probe linear polarisation alignments. The dressing field peak intensity was calculated to be 1.3×10^{14}W/cm^2. This Figure has been modified from reference [35]. © IOP Publishing. Reproduced with permission. All rights reserved. CC BY 3.0. 133

5.5 Comparison between the singlet energy states of helium presented in the NIST catalogue [158] compared with those calculated for the results presented in this Chapter [35]. 134

5.6 Absorption cross section modulation amplitude in megabarns (Mb) for the $2\omega_1$ and $4\omega_1$ frequency components as a function of dressing field intensity. This Figure has been reproduced from reference [35]. © IOP Publishing. Reproduced with permission. All rights reserved. CC BY 3.0. 137

5.7 Negative absorption cross section obtained for a below ionisation threshold harmonic dressed with low peak intensity field (6.8×10^{12}W/cm^2). This Figure has been reproduced from reference [35]. © IOP Publishing. Reproduced with permission. All rights reserved. CC BY 3.0. 139

5.8 Example box selection for detected harmonics using perpendicularly aligned dressing and probing linear polarisations with dressing field intensity 1.3×10^{14} W/cm^2. The box selection is compared to the average signal in the delay scan and standard deviation of the recorded image stack. 143

5.9 Box selection to investigate sub-harmonic phase differences for data presented in Figure 5.8. 144

5.10 Relative phases for the different boxes selected over harmonic orders 13 to 19 as shown in Figure 5.9 for both parallel and perpendicular aligned linear dressing and probing field polarisations. 145

5.11 Box selection for the harmonic orders using the signal in the delay scan and standard deviation of the image stack as guidance. The data shown is from the dressing field intensity scan (recall Figure 5.6), corresponding to a dressing field intensity of 1.1×10^{14}W/cm^2. 146
5.12 Subharmonic box selection to investigate the different phase components within different regions of the harmonics presented in Figure 5.11. 147
5.13 Investigating the phase of different regions of harmonic 13 for different dressing field intensities. 148
5.14 Investigating the phase of different regions of harmonic 13 for different dressing field intensities relative to the phase for the box selecting the whole (averaged) harmonic signal. 148

6.1 Energy level diagram of the krypton atom. Values for the energy states were taken from references [162] and [163]. 152
6.2 Comparison of the transient absorption transmission signal and extracted Fourier components of laser dressed krypton for linear polarised dressing fields aligned both parallel, (θ=0°), and perpendicular, (θ=90°), with respect to the probing APT field polarisation. The peak dressing field intensity was calculated to be 4.5×10^{13}W/cm^2. 154
6.3 Mean harmonic spectrum obtained for the interleaved static absorption measurements recorded across the scan delay range shown in Figure 6.2, with the selected divergence range indicated along with the recorded generation and target backing pressures as a function of delay throughout the scan duration. 156
6.4 Transient absorption $2\omega_1$ frequency component amplitude response as a function of dressing field peak intensity. 158
6.5 Measured dressing field power, krypton target backing pressure, and peak intensity as a function of scan order for the different dressing field intensity delay scans used to construct Figure 6.4. 159
6.6 Transient absorption $2\omega_1$ frequency component amplitude response as a function of krypton target backing pressure. The dressing field peak intensity for the presented scans was calculated to be 4.0×10^{13}W/cm^2. 162
6.7 Mean field free transmission (static absorption reference) as a function of krypton backing pressure. 163
6.8 Measured dressing field power as a function of scan number and krypton backing pressure for the recorded delay scans at each backing pressure presented in Figure 6.6. 164
6.9 Average percentage absorption as a fraction of the total signal measured within the energy range 95.5 to 98.0 eV for each source harmonics reference as a function of krypton backing pressure. 165

6.10 Long duration transient absorption delay scan from laser dressed krypton. The dressing field peak intensity for the presented scan was calculated to be 6.5×10^{13}W/cm^2. 167

6.11 Mean harmonic spectrum recorded for the interleaved field free transmission (static absorption) reference measurements recorded across the scan delay range shown in Figure 6.10, with the selected divergence range indicated, along with the recorded generation and target backing pressures as a function of delay throughout the scan duration. 168

6.12 Log scale extracted Fourier amplitude components as a function of probing photon energy for the laser dressed krypton transient absorption delay scan presented in Figure 6.10. 169

6.13 Comparison of the transient absorption transmission signal of laser dressed helium for linear polarised dressing fields aligned both parallel, (θ=0°), and perpendicular, (θ=90°), with respect to the probing APT field polarisation. The dressing field peak intensity for the presented scans was calculated to be 6.2×10^{13}W/cm^2. 173

6.14 Mean harmonic spectrum recorded for the interleaved field free transmission (static absorption) reference measurements recorded across the scan delay range presented in Figure 6.13, with the selected divergence indicated along with the recorded generation and target backing pressures as a function of delay throughout the scan duration. . 175

6.15 Fourier amplitude as a function of probing photon energy extracted from the transient absorption delay scan using parallel aligned dressing and probe field linear polarisations. 176

6.16 Fourier amplitude as a function of probing photon energy extracted from the transient absorption delay scan using perpendicular aligned dressing and probe field linear polarisations. 177

6.17 Comparison of the recorded raw transient absorption transmission and processed transient absorption transmission for the parallel aligned dressing field linear polarisation. 179

6.18 Normalised spectra investigating the light induced states in the harmonic orders around 22.1 eV and 23.9 eV with parallel, θ=0°, and perpendicular, θ=90°, aligned relative dressing field linear polarisation. 182

6.19 Experimentally determined absorbance spectrum for an isolated attosecond pulse generated and dressed using 730 nm. This Figure has been reproduced from reference [20]. CC BY-NC-ND 3.0. 183

6.20 Raw and processed transient absorption delay measurement from laser dressed helium, with extracted log scale Fourier response at different delays throughout the scan duration. The dressing field peak intensity for the presented scan was calculated to be 4.0×10^{13}W/cm^2. 185
6.21 Fourier amplitude as a function of probing photon energy extracted from the one-dimensional laser dressed helium transient absorption delay scan, presented in Figure 6.20. 186
6.22 Mean harmonic spectrum recorded for the interleaved static absorption measurements recorded across the scan delay range shown in Figure 6.20. The selected divergence range is indicated, along with the recorded generation and target backing pressures as a function of delay throughout the scan duration. 187

7.1 Image of the TOPAS idler beam profile and focus with and without spatial filtering through the hollow core fiber. Image provided courtesy of Dr Dane Austin. 191
7.2 Image of the TOPAS idler harmonics generated using 314 mbar argon backing pressure in the generation target, and 350 mbar argon gradient fill in the hollow core fiber. . . 192

A.1 Permissions email from Journal for Figure 1.2, modified from reference [14]. 211
A.2 Permissions email from Author for Figure 1.2, modified from reference [14]. 212
A.3 Permissions email for Figure 3.2, reproduced from reference [144]. 213
A.4 Permissions email for Figure 4.1, modified from reference [37]. 214
A.5 Permissions email for Figures 5.2,5.4,5.6 and 5.7, reproduced and modified from reference [35]. 215
A.6 Permissions email for Figure 6.19, reproduced from reference [20]. 216

List of Tables

4.1 Generation beam optics selected for the different experiments. 88

6.1 Expected energy levels for light induced states with dressing field $\lambda = 1390\,\text{nm}$, corresponding to photon energy of $0.89\,\text{eV}$. This table is based closely on that presented by Reduzzi *et al.* in reference [114]. The field free energy levels are reproduced from reference [114], and confirmed using reference [158]. 180

Abbreviations

ADC	Algebraic diagrammatic construction
AOM	Acousto-optical modulator
APT	Attosecond pulse train
ASE	Amplified spontaneous emission
ATAS	Attosecond transient absorption spectroscopy
ATI	Above threshold ionisation
BG	Background
CEP	Carrier envelope phase
CPA	Chirped pulse amplification
CW	Continuous wave
DFG	Difference frequency generation
EM	Electromagnetic radiation
FEL	Free electron laser
FROG	Frequency resolved optical gating
FT	Fourier transform
FWHM	Full width at half maximum
GDD	Group delay dispersion
GVD	Group velocity dispersion
HCF	Hollow core fiber
HHG	High harmonic generation

IAP	Isolated attosecond pulse
Ip	Ionisation potential
IR	Infra-red
LCLS	Linac coherent light source
ML	Mode locked
MPI	Multi-photon ionisation
OPA	Optical parametric amplifier
OTBI	Over the barrier ionisation
PE	Potential energy
RMS	Root mean squared
SFA	Strong field approximation
SFG	Sum frequency generation
SPI	Single photon ionisation
SPIDER	Spectral phase interferometry for direct electric field reconstruction
SPM	Self phase modulation
SVEA	Slowly varying envelope approximation
TD	Time dependent
TDSE	Time-dependent Schödinger equation
TI	Tunnel ionisation
Ti:Sapph	Titanium doped sapphire crystal
Up	Ponderomotive energy
UVFS	Ultra-violet fused silica
XiHHG	Extreme ultra-violet initiated high harmonic generation
XUV	Extreme ultra-violet

Chapter 1

Introduction

The field of ultrafast science concerns itself with study on the fastest timescales. Over the past decades, the definitions have evolved as advances in laser technology have been made, and improvements to experimental techniques realised. Understanding the basic interactions that occur in an atom or molecule when it interacts with light has far-reaching applications, ranging from improved efficiencies for solar energy harvesting [1] to better understanding of biological radiation damage [2]. In fact all photo-chemistry is bound by the laws of light-matter interaction [3]. The binding of atoms to form molecules is determined by the electronic structure of the system, so understanding how the electrons move in atoms and molecules is critical.

In understanding the fundamentals of light-matter interaction we must observe changes that occur on a timescale similar to, or shorter than, the optical cycle period. For the femtosecond regime, information on molecular vibration and rotation can be resolved [3]. To access information on electron dynamics, however, timescales in the sub-femtosecond ($<$ fs) range must be explored [4]. Measuring such fast dynamics poses many problems and requires specialist techniques and equipment. Primarily, to resolve changes one must sample the system at intervals shorter than the characteristic timescale of the dynamic in order to map out the evolution of the system. The required minimum sampling rate will be determined by the Nyquist sampling theorem, probing the system at a frequency twice that of the highest expected dynamic. Developing the methods, techniques and technology required to enable measurement on these timescales has been the focus of the ultrafast community for the last 50 years [5].

Capturing information on the sub-fs timescale is challenging. Standard CCD cameras such as the Allied Vision Guppy cameras used in our beamline for laser profiling and imaging in the detector present typical frame rates corresponding to the 10s milliseconds timescale, limited by the readout time for the CCD chip. Other systems can increase the frame rate through reduction of the CCD array size which is being recorded. More advanced systems can exploit parallelisation of the readout

to access frame rates in the millions per second. Often this type of camera is limited to operate in burst mode however, recording only a limited number of images for each measurement. To eliminate the dependence on detector readout time for these ultrafast measurements, so called 'pump-probe' techniques have been developed, effectively freezing the interaction through the use of a precisely controlled delay [6]. In this way dynamics can be initiated in the target with an ultrashort pump, and information about the evolved state retrieved for a given delay time using an ultrashort probe. With precise control over the relative delay between the pump and probe pulses, this decouples the speed of the detection from the speed of the dynamic. Instead the required fast gating to resolve the ultrafast changes is applied through the pump and probe pulses [3].

Today the fastest artificial events we can create and characterise are ultrashort laser pulses, produced through highly nonlinear light-matter interactions [7]. The laser pulse durations achieved are far shorter than those that can be obtained using mechanical shutters (∼100 billion times faster) or electronic switching (∼1 million times faster).

The work presented in this thesis will give an overview of the general methods used to perform ultrafast experiments, and will describe in detail several of the different specific techniques used to extract information on the ultrafast timescale, namely: high harmonic generation (HHG), attosecond transient absorption spectroscopy (ATAS) and extreme ultra-violet initiated high harmonic generation (XiHHG).

1.1 History of the Field

The study of ultrafast phenomena has involved development in both the fields of laser physics and nonlinear optics. With the invention of the laser in 1960 by Maiman *et al.* [8], the field of nonlinear optics as we know it today was born. The availability of this new laser light source enabled unparalleled intensities, coherence and directionality to be achieved, opening the door to a wealth of new experimental possibilities, and providing opportunity for new insight and understanding about light-matter interaction.

In 1961 the first experiment demonstrating second order harmonic generation was undertaken by Franken *et al.* [9]. By focusing a 1 ms pulsed ruby laser into a crystalline quartz sample, the team succeeded in producing the second harmonic of the fundamental light. The recorded second order flux was very low, however in 1962 Maker *et al.* [10] managed to exploit the birefringence of the target crystal, improving the generation efficiency. By utilising the fast and slow axes of a birefringent crystal, control was demonstrated over the relative phase between the fundamental ruby light and the generated second order through the set angle of the crystal. By minimising phase slip between the fundamental and generated second order light in the crystal using the birefringent properties, the second order flux could be increased by maximising the number of contributing

emitters within the target length that interfere constructively. This macroscopic propagation effect is called phase matching and will be discussed in more detail in Chapter 2.

Over the following decades many important advances were made in the field of laser technology to improve the intensity, versatility and reduce the pulse duration of lasers, all important factors for the current day state-of-the-art ultrafast studies of electron dynamics in atoms and molecules. The developments of note for the work presented in this thesis include the demonstration of laser modelocking [11] producing a higher peak intensity, pulsed output to the laser, the discovery of titanium-doped sapphire (Ti:Sapph) crystal as a laser amplification medium [12], and the development of chirped pulse amplification (CPA) [13], enabling amplification of intense laser pulses through prior redistribution of energy in time. All of these developments are described in detail in Chapter 3.

The result of these advances on pulse duration and intensity can be seen in Figures 1.1 [5] and 1.2 [14] respectively. Rapid progress was made for both the pulse duration and focused intensity values directly following the invention of the laser. Once the damage threshold of the optics was reached and the focal spot sizes limited by the wavelength of the light, the achievable focused intensity plateaued. Advances in the reduction of the pulse duration continued until it too plateaued around the few-cycle limit achievable from a Ti:Sapph laser, around 6 fs [15]. With the invention of CPA in 1986 [13], rapid increase in the focused laser intensity was once again possible as larger amplification factors could be applied for the same final pulse pulse duration using this method. Advances towards sub-femtosecond pulses however was not possible until the development of new techniques that could access sufficient bandwidth at an appropriate central wavelength to support such short pulses, namely high harmonic generation (HHG) [16, 17].

High harmonic generation is a highly nonlinear technique for producing a large bandwidth of optical frequencies at wavelengths shorter than the input pulse. By focusing a high intensity laser into a target under vacuum, high energy, short pulsed light can be emitted. In 2001, Paul *et al.* [16] used the technique of HHG to experimentally generate and verify the sub-femtosecond nature of a train of attosecond pulses, and in the same year Hentschel *et al.* [17] measured the first iosolated attosecond pulse. These developments confirmed, for the first time, access to the sub-femtosecond regime, and opened the door to studies of electron dynamics requiring attosecond resolution [18–20]. More detail on the technique of HHG can be found in the High Order Harmonic Generation section in Chapter 2.

The quest for increasingly shorter probe pulses continues, and much research is still focused on developing better ways to produce high intensity, short duration pulses. To produce isolated attosecond pulses (IAPs), one must limit the duration of the input laser pulse used to create the HHG. In addition to amplitude gating of the generating pulse [17, 21] other methods include ionisation gating [22] and polarisation gating [23], to reduce the input to a single cycle, improving the probe

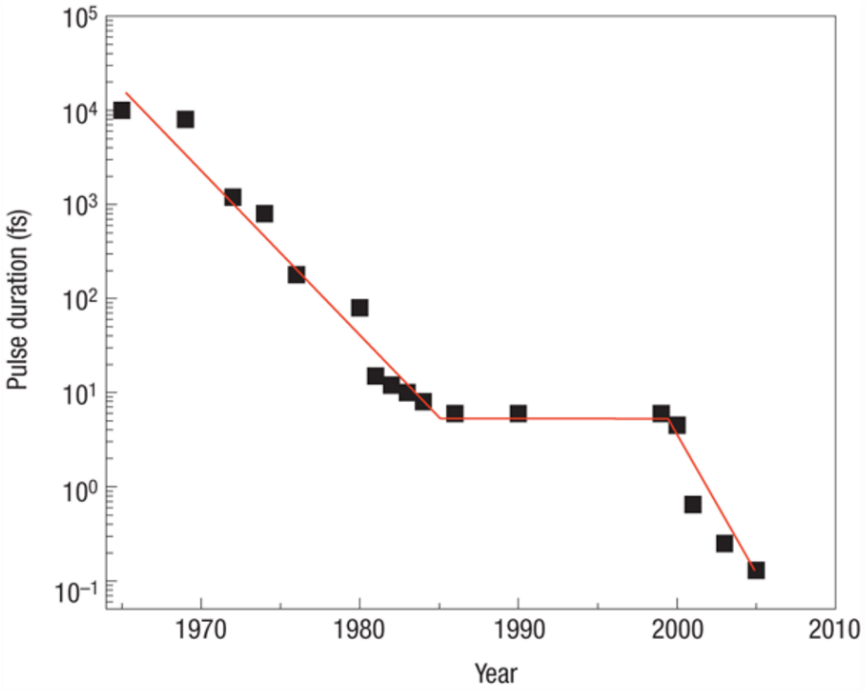


Figure 1.1: Development and improvement of short pulse generation techniques over time. Reprinted by permission from Macmillan Publishers Ltd: Nature Physics [5], copyright 2007, modified from [26] © 2008 Canadian Science Publishing or its licensors. Reproduced with permission.

resolution. Alternatively, methods to directly broaden the bandwidth of the driving laser pulse allowing further subsequent compression have also been explored. An example is hollow core fiber (HCF) pulse compression [24], where the third order nonlinear effect of self phase modulation (SPM) acts to broaden the frequency range comprising the pulse, enabling a shorter pulse duration to be realised following compression. SPM will be discussed in more detail in Chapter 2. Today, isolated attosecond pulses as short as 67 as have been produced and measured by Zhao *et al.* [7], allowing access to dynamics on the fastest timescales. A robust review of isolated attosecond pulse generation and application can be found in reference [25].

1.2 Motivation of Beamline Design

Significant time during the PhD was devoted to developing, building, characterising (and ultimately using) the pump-probe beamline in the Huxley 012 laboratory at Imperial College London. The design was motivated by the desire for maximum versatility, allowing for the possibility to perform a variety of different ultrafast experiments using targets in gaseous, solid and liquid phase. The large size of the first vacuum chamber (the generation chamber, see Figure 4.1) allows for different pump-probe configurations to be realised, and ensures sufficient space for control optics to be positioned. Additionally, space and connections are available in the generation chamber to include a second gas

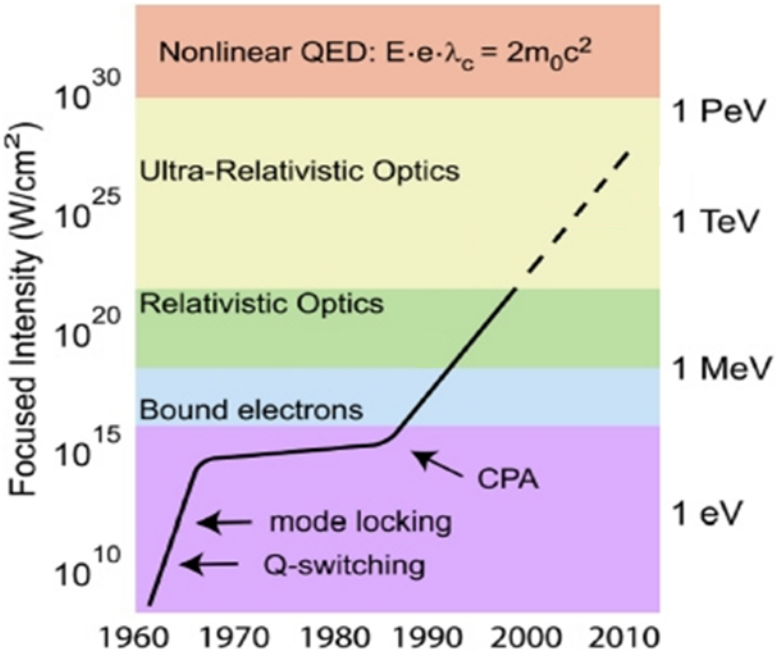


Figure 1.2: Chronology of the attainable peak pulse intensity along with the achievable electron energy for the given focused intensity ranges. Modified from [14], © IOP Publishing. Reproduced with permission. All rights reserved.

target to realise attosecond-pump attosecond-probe, vacuum ultra-violet (VUV) pump attosecond-probe, IR-pump attosecond-probe (or indeed any further combination of pump-probe) experiments to be performed. Currently we have only explored using the IR-pump-XUV-probe combination, and the work presented in this thesis used this arrangement. Furthermore, additional spare window ports in the main chamber could allow for a further laser pulse to be introduced, enabling, for example, pump-probe experiments using molecular alignment [27, 28], or two colour [29, 30] beams to be performed. The separate, non-collinear propagation of the pump and probe pulses in the main chamber allows for direct control over the individual pump-probe properties, for example the intensity, polarisation state as well as allowing for spectral filtering of any generated high harmonic light.

Designed to initially perform attosecond transient absorption experiments, the technique of transient absorption spectroscopy compliments and extends other existing methods to resolve ultrafast dynamical information, such as probing directly with high harmonic generation [31, 32], photoelectron spectroscopy [33], and Coulomb explosion [34]. More information on the technique of attosecond transient absorption spectroscopy (ATAS) can be found in Chapter 2.

1.3 Introduction to the Thesis

The work presented in this thesis expands upon the current knowledge of ultrafast electron dynamics in atoms following photo-excitation and ionisation through studies into the transient absorption response of strong field dressed helium and krypton atoms.

In Chapter 1 we have been introduced to the general area of nonlinear optics and the history of the field, highlighting some of the key improvements that have shaped the development of the field, and led to major progressions. In addition, a brief introduction as to the motivation behind the beamline development has also been explored. Chapter 2 expands the background by focusing on the interaction of light and matter, explaining the different relevant ionisation mechanisms along with the different regimes of nonlinear interaction. Important nonlinear effects are addressed including the technique of high order harmonic generation (HHG), attosecond transient absorption spectroscopy (ATAS) and extreme ultraviolet (XUV) initiated high harmonic generation (XiHHG). The theoretical assumptions used when considering strong field interaction are also discussed.

Chapter 3 introduces femtosecond light sources, and describes in detail the lasers used in the laboratory to obtain the results presented in this thesis. In addition, different relevant methods to characterise the generated femtosecond pulses are also described. The experimental methods are presented in Chapter 4, with a detailed description of the beamline setup. Experiment specific data acquisition and data processing methods are also given.

Chapter 5 presents the first results: delay dependent transient absorption from strong field dressed helium using an 800 nm driving laser and dressing field intensity approaching the strong field ionisation of the target. Different parameters are explored as a function of delay including the dressing field peak intensity, and dressing field relative linear polarisation aligned parallel or perpendicular with respect to the probing XUV pulse train. The main results in this Chapter were recently published, see reference [35], and results are discussed in the context of the current literature.

Chapter 6 presents additional results exploring attosecond transient absorption spectroscopy from strong field dressed helium and krypton targets using a 1400 nm driving laser field. Performing similar scans as for Chapter 5, exploring the dynamic response of the transient absorption signal for various control parameters, we can compare the results obtained for strong field dressed helium at both the 1400 nm and 800 nm laser field wavelengths. By recording scans covering the whole interaction envelope, we can simultaneously access the peak dressing field intensity, and lower dressing field intensity regions at the interaction edges. For the helium scans, visible light induced states (LIS) are observed for the lower intensity regions, and these are discussed in the context of the current literature. Finally, the delay dependent transient absorption from a core (3d) electronic level in krypton is explored as a function of target backing pressure, dressing field intensity and dressing field relative linear polarisation, aligned either parallel or perpendicular with respect to the probing

harmonic pulse train.

Chapter 7 concludes the thesis, discussing the limitations of the current setup, and explores possibilities for future work.

1.4 Author Contribution

For the completion of the work presented in this thesis, many individuals in addition to myself have contributed towards different parts of the overall design, construction, acquisition and analysis. I specifically have worked on many different aspects of the experimental setup, development and analysis, having been involved with the project since the initial beamline commissioning. I have played a key role in all of the data acquisition, analysis, and much of the beamline development, where instances of additional assistance are outlined below.

My main contributions to the presented work include the data acquisition and analysis of the 800 nm studies, taking a leading role in developing the analysis and results for publication. In addition I led much of the 1400 nm data acquisition, including implementation of many relevant beamline modifications to perform the experiments with this longer wavelength field. I have contributed significantly towards the 1400 nm data analysis, and have been a key part of the day-to-day alignment and operation of the beamline and associated lasers in the laboratory.

Specific external contributions to the presented work are acknowledged below:

The beamline design was conceived and developed primarily by Professor Jon Marangos, Dr Thomas Siegel, Dr Zsolt Diveki and Dr Simon Hutchinson prior to, and in the starting months of this PhD.

The construction and development of the initial beamline setup used to perform the 800 nm wavelength studies was performed primarily alongside Dr Thomas Siegel, Dr Zsolt Diveki and Dr Simon Hutchinson. Additional support was given by Alvaro Sanchez-Gonzalez and Lukas Miseikis. The 800 nm data acquisition was performed primarily by the same named group, using a data acquisition framework developed primarily by Dr Simon Hutchinson, and later on Alvaro Sanchez Gonzalez.

The preliminary analysis of the 800 nm work was performed by Dr Zsolt Diveki and Dr Simon Hutchinson, the latter of whom presented preliminary results in his PhD thesis titled: *Apparatus design and experimental studies of XUV initiated HHG* [36]. Further analysis into the 800 nm data was performed alongside Alvaro Sanchez-Gonzalez, including the preparation of the data for publication [35]. The main analysis framework was designed by Alvaro Sanchez Gonzalez, with input from myself through additions and modifications. The phase tagging design and implementation was performed primarily by Alvaro Sanchez-Gonzalez with support from Dr Zsolt Diveki. The theoretical

modelling of the 800 nm strong field dressed helium work was performed by Dr Marco Ruberti at Imperial College London, with input from Dr Luke Chipperfield and Dr Vitali Averbukh.

In swapping to the 1400 nm wavelength, additional changes were made to the beamline setup. With regards to the hardware, the new tube target for the generation chamber was designed by Dr Zsolt Diveki, and positioned and tested by myself and Dr Christian Strüber. The new tube target for the target interaction chamber was designed and implemented by Lukas Miseikis. The changes to the generation chamber beam paths were implemented primarily alongside Dr Christian Strüber based on ray tracing calculations performed by Alvaro Sanchez-Gonzalez. Christian Brahms, with input from Dr Christian Strüber and Dr Dane Austin, implemented the active stabilisation to the input beam along with logging software for the alignment and chamber pressures. A new data acquisition framework designed to enable more functionality was developed by Alvaro Sanchez-Gonzalez for the 1400 nm work. Additional user control functionality was implemented by Christian Brahms and Dr Christian Strüber to run scans using instruction sequences. The integrated data analysis framework was built by Dr Christian Strüber with much input from myself through many discussions. Additions and modifications to some of the analysis programs were made prior to use of this framework to produce the data plots for Chapter 6. Improvements to the Red Dragon laser were performed primarily by Dr Dane Austin (refined power feedback for the pump lasers and SPIDER feedback for the linear position of the compressor grating), and Dr Christian Strüber (installation of multiple alignment cameras within the Red Dragon amplification states).

The 1400 nm data was acquired primarily alongside Dr Christian Strüber, with support from Dr Peng Ye and Christian Brahms. The day to day setup, maintenance and running of the beam line was in general performed alongside Dr Christian Strüber. The laser and general lab maintenance was shared between group members for which I had an active and frequent role.

1.4.1 Author Presentations

As part of the PhD I have presented my work in the following ways:

- New Journal of Physics first author paper titled: *Polarisation response of delay dependent absorption modulation in strong field dressed helium atoms probed near threshold.* [35]
- Optics and Photonics 2015 conference proceedings first author paper titled: *A beamline for attosecond pump-probe experiments: towards tracking ultrafast electron dynamics in atoms and molecules.* [37]
- Atto2015 Conference, Saint-Sauveur, Québec, Canada. Oral presentation accepted, titled: *Vector Response of a Dressed Continuum Resolved by Transient Absorption.*
- Optics and Photonics Conference 2015, San Diego, USA. Oral presentation accepted, titled: *Vector Response of a Dressed Continuum Resolved by Transient Absorption.*

- Free Electron Lasers and Attosecond Light Sources: portals to ultrafast dynamics in AMO systems conference, UCL, UK. Poster presentation accepted, titled: *Probing Ultra-Fast Electron Dynamics through Laser-Dressed Attosecond Transient Absorption.*

- AIPT conference 2013, Aston University, UK. Poster presentation accepted, titled: *A New Beam-Line for XUV Initiated HHG and Attosecond Transient Absorption.*

Chapter 2

The Interaction of Light and Matter

The processes governing the interaction of light and matter are fundamental to our existence. Plants harness light from the Sun, transforming it through chemical reactions into energy to grow, in fact all photochemical reactions are bound by the laws of light-matter interaction. At the shortest measurable timescales electron rearrangement occurs, and it is on these timescales that the work in this thesis is focused.

Broadly we can categorise light-matter interaction into different regimes based on the intensity of the interacting field. For intensities $<10^{12}\,\mathrm{W/cm^2}$, interactions are well described by perturbations to the bound electronic potential [38], and the regime of interaction is known as the weak-field, or perturbative regime. With higher intensity fields, $\sim 10^{12}$ - $10^{15}\,\mathrm{W/cm^2}$, the resultant electric field strength becomes significant compared with the Coulomb binding between the valence electron and the nucleus [39], and it may no longer be valid to treat the incident field as a perturbation. At this point strong field effects start to occur and the interactions are said to be in the strong field regime. At even higher field intensities, $>10^{16}\,\mathrm{W/cm^2}$, we enter the relativistic regime where the contribution of the magnetic part of the incident EM wave can no longer be treated as negligible. The electrons in this regime travel at significant fractions of the speed of light and result from interaction field intensities far higher than those presented in this thesis [38].

The absolute division between a perturbative response and strong field effects is not well defined. Instead there is an overlap between the regimes where the description from both can be applied simultaneously [40]. For a given target atom or molecule, the regime of interaction will depend on both the intensity of the laser field as well as the ionisation potential, Ip, of the target, where the Ip defines how much energy is required to entirely remove a bound electron from the nucleus. For an atom or molecule with a lower Ip, the threshold between these two regimes will occur for a lower

intensity field.

To gain understanding of the field intensities required for strong field effects, we can consider the electric field strength between the electron and nucleus in a hydrogen atom. By dividing the Coulomb force between the proton and electron by the charge of electron, e, we can obtain a value for the electric field strength, E:

$$E = \frac{e}{4\pi\epsilon_0 a_0^2} = 5.14 \times 10^{11} \ \ \mathrm{Vm}^{-1}, \tag{2.1}$$

where ϵ_0 is the permittivity of free space, and a_0 is the Bohr radius. Using the equation relating the peak intensity of a laser field, I_{peak}, to the electric field amplitude, E_0:

$$I_{peak} = \frac{nc\epsilon_0}{2} E_0^2, \tag{2.2}$$

where n is the refractive index, c is the speed of light, the laser peak intensity required to match the intra-atomic electric field in a hydrogen atom is found to be 3.5x10^{16}W/cm^2.

The intensity required to match the electron-nucleus binding marks an extreme of the strong field response, and in reality strong field effects become important at much lower field intensities. Typically, strong field effects start to dominate for field intensities greater than $\sim 10^{13}$W/cm^2 [15,38,39]. At the other extreme, resonant single photon transitions can occur for even the weakest of dressing field intensities, described within the lowest order perturbation theory (LOPT) framework [41]. Both resonant and non-resonant, linear and nonlinear transitions can be described perturbatively, valid typically up to field intensities $\sim 10^{13}$ W/cm^2.

Investigating the interaction of light and matter requires consideration of how both the light affects the matter through, for example, excitations and ionisations, as well as how the matter affects the light through, for example, dispersion, propagation effects and nonlinearities. To start with we will consider how light affects matter.

2.1 Effect of Light on Matter

When light interacts with matter, the result is inherently quantum mechanical. Even with the lowest dressing field intensities, resonant single photon transitions can occur when a target absorbs a single quantum of light energy, a photon, to become excited or ionised. The quantum behaviour is even more apparent at the high intensity extreme where the effect of tunnel ionisation cannot be explained at all within a classical treatment. In the following section I will introduce the key equations and concepts required for a quantum understanding of the interaction of light with matter, along with an appreciation for the commonly used approximations.

The equations presented in this section, along with further details and associated derivations can

be found in part or in entirety in many good atomic physics textbooks, for example Woodgate [41] or Haken and Wolf [42], or in online course notes, for example [43] or [44].

2.1.1 Introduction to Quantum Light-Matter Interaction

In the language of quantum mechanics, the wave function, $\Psi(\mathbf{r},t)$, contains the entire information about a quantum system, and the modulus square of the wave function, $|\Psi(\mathbf{r},t)|^2$ defines the probability density. The wavefunction depends on both the position vector, $\mathbf{r}$, and the time, t. The general time dependent Schrödinger equation (TDSE) describes the evolution of a quantum system with time, and can be written as:

$$-i\hbar\frac{\partial}{\partial t}\Psi(\mathbf{r},t) = \hat{H}\Psi(\mathbf{r},t), \tag{2.3}$$

where $\hbar$ is the reduced Planck constant, and $\hat{H}$ is the Hamiltonian operator describing the total energy of the system.

When considering the application of an external field to an atom or molecule, the interaction Hamiltonian can be divided into two parts: a part corresponding to the unperturbed system, $\hat{H}_0$, and a part due to the influence of the interaction field, $\hat{H}_{int}$. To simplify the problem, a common semi-classical assumption is made where the field is treated classically, and the target treated quantum mechanically, enabling the effect of the matter on the light to be neglected. Instead, the interaction Hamiltonian just describes the effect of the light on the matter.

The linearity of the TDSE with the wavefunction means that any linear superposition of solutions to the TDSE will also be a solution. This principle of superposition means that when considering the interaction of quantum systems, for example where a resonant photon excites an electron from an initial state, Ψ_i, to a final state, Ψ_f, the wavefunction can be written as a linear superposition of the states:

$$\Psi(\mathbf{r},t) = c_i\Psi_i(\mathbf{r},t) + c_f\Psi_f(\mathbf{r},t), \tag{2.4}$$

where each of the wavefunctions has a corresponding amplitude coefficient, c_n, and each depends both on position, $\mathbf{r}$, and time, t.

The probability of the electron being in either state is governed by the light-matter interaction operator. The expectation value for finding the electron in the excited state is determined by the modulus square of the overlap integral between the initial state upon which the operator acts, and the final state of the interaction. To determine the light-matter interaction operator, two further approximations are commonly made to simplify the mathematics:

- For dressing field strengths much lower than that binding the electron to the nucleus, the term proportional to the square of the vector potential in the expansion of the laser dressed

Hamiltonian can be neglected.

- Provided the wavelength of the incident or outgoing light in the interaction is much greater than the atomic size, i.e. the interaction amplitude can be assumed constant across the atomic length, one can apply the dipole approximation. This approximation retains just the unity term in the multipole expansion of the plane wave representation of the vector potential, neglecting higher order terms.

With these approximations, the light-matter interaction operator is known as the dipole operator, $\hat{\mathbf{d}}$, and is given by:

$$\hat{\mathbf{d}} = q\mathbf{r}, \tag{2.5}$$

where q is the electronic charge. The well known dipole Hamiltonian, $\hat{H}_{int}$, for matter interacting with an external light field, $\mathbf{E}(t)$, can therefore be written as:

$$\hat{H}_{int} = -\hat{\mathbf{d}} \cdot \mathbf{E}(t). \tag{2.6}$$

When considering the interaction of light with matter, we are generally interested in understanding how likely it will be for particular transitions to occur. Assuming a linear polarisation along the $\hat{\mathbf{x}}$ direction, the matrix element of the transition dipole moment, d_{fi}, determines the strength of the transition from the initial state, i, to the final state, f, and is given by:

$$d_{fi} = \langle f|\hat{\mathbf{d}} \cdot \hat{\mathbf{x}}|i\rangle, \tag{2.7}$$

where the brackets denote the expectation value of the dipole moment transition.

For a simplified two-level system illuminated by coherent monochromatic light, the time dependent probability amplitude for finding the electron in the final state, f, having stared in the initial state, i, is given by [43]:

$$|c_f(t)|^2 = \frac{\Omega^2}{\Omega^2 + \delta^2} \sin^2\left(\frac{1}{2}\sqrt{\Omega^2 + \delta^2}t\right), \tag{2.8}$$

where c_f is the final state coefficient, δ is the detuning of the light from the resonance frequency, ω_0, given by $\delta = \omega - \omega_0$, and Ω is the Rabi frequency between the energy levels, defining the characteristic oscillation rate between the initial and final states for the two state system. The Rabi frequency is given by the following [43]:

$$\Omega = \frac{E_0\langle f|\hat{\mathbf{d}} \cdot \hat{\mathbf{x}}|i\rangle}{\hbar}, \tag{2.9}$$

where E_0 is the electric field amplitude.

For the resonance condition, $\delta = 0$, the probability amplitude $|c_f(t)|^2$ varies as $\sin^2$ between 0 and 1. For large detuning from resonance however, the probability amplitude for being in the upper state reduces, and the oscillation frequency increases.

For an incoherent analysis of the two level system, the rate of absorption from the initial state to the final state for a dipole interaction can be determined from the Einstein B_{12} coefficient, given by [43]:

$$B_{12} = \frac{\pi}{3\epsilon_0\hbar^2}|\langle f|\hat{\mathbf{d}}\cdot\hat{\mathbf{x}}|i\rangle|^2. \tag{2.10}$$

In the context of high harmonic generation, the ionised portion of the electron wave function is often described as a wave packet. This arises from the uncertainty relation between position, Δx, and momentum, Δp:

$$\Delta x \Delta p \geqslant \frac{\hbar}{2}. \tag{2.11}$$

If the momentum of an electron is well known, the position uncertainty will be large, hence the position of bound electrons being described probabilistically. Similarly, if the position of the ionised wavepacket is well known, the distribution of momenta will be large. An ionised electron is highly localised and so it must therefore contain a large spread of momenta. A linear superposition of all of the different possible momenta results in destructive interference outside all but a central region of constructive overlap, defining the duration of the electron wavepacket. This is important when considering the evolution of ionised electron wavepackets in the process of high harmonic generation, which will be discussed later in this Chapter.

2.2 Ionisation mechanisms

The removal of an electron from an atom or molecule results in a positively charged ion and a continuum electron free from the nuclear potential. This process may precede further direct ionisation of the resultant ion if the energy and intensity of the incident field permits. Alternatively further indirect ionisation may occur due to electron energy redistribution if the resultant ion was left in an excited state. This can result in the emission of a further electron in lieu of radiation to conserve energy, a process known as the Auger effect. These processes are examples of sequential ionisation, however it is also possible to directly remove multiple electrons at once instantaneously through non-sequential ionisation [45, 46]. Understanding what happens to the electronic structure of atoms and molecules following photo-ionisation is both important and challenging, and forms the focus of the work in this thesis. Achieving and understanding the first step: photo-ionisation is therefore vital. The following sections will describe the main ionisation mechanisms that are relevant to the work presented in this thesis.

2.2.1 Weak Field Regime

As discussed earlier in the Chapter, the weak field regime defines the range of intensities for which the result of the dressing field interacting with matter can be effectively treated as a perturbation

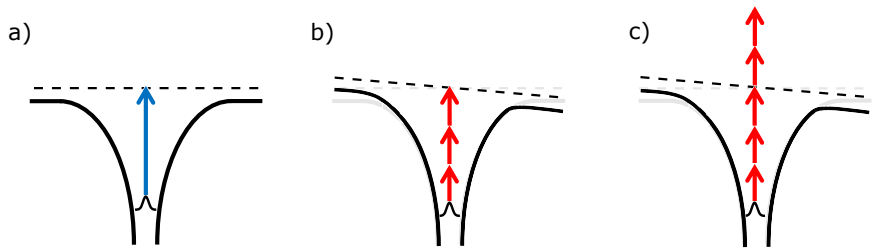


Figure 2.1: Perturbative regime ionisation mechanisms: a) single-photon ionisation, b) multi-photon ionisation and c) above threshold ionisation.

to the system. Typically this intensity range covers up to $\sim 10^{12}\mathrm{W/cm}^2$.

2.2.1.1 Single-photon Ionisation

First understood as the photoelectric effect by Albert Einstein in 1905 [47], single photon ionisation is a linear process where an electron is removed from the bound potential of an atom, molecule or ion through the absorption of a single quantum of light, a photon. In this way, the electron is born into the continuum with a kinetic energy $E_{kinetic}$ equal to the energy difference between the incident photon energy E_{photon} and the ionisation potential for the particular transition I_p. This can equal zero if the ionising photon is resonant with the transition.

$$E_{kinetic} = E_{photon} - I_p. \tag{2.12}$$

The ionisation rate Γ_{SPI} for a single photon process is linear with the number of photons N, depending also on the frequency dependent absorption cross section of the interaction $\sigma(\omega)$, and the number of absorbers in the interaction volume n given by equation 2.13.

$$\Gamma_{SPI} \propto Nn\sigma(\omega). \tag{2.13}$$

Alternatively the ionisation rate for a two level system can be calculated theoretically by considering equation 2.10, where the final state of the transition is a continuum state.

The process of SPI can be viewed schematically in Figure 2.1 a). Here a resonant transition is depicted where the incident photon has just sufficient energy to ionise the bound electron into the continuum.

2.2.1.2 Multi-photon Ionisation

First observed by Voronov *et al.* in 1965 [48], if the energy of the incident photons in the interacting field are insufficient to permit SPI, multi-photon ionisation (MPI) may occur provided the intensity of the incident light is sufficiently high. MPI requires the absorption of multiple photons to overcome

the ionisation threshold and promote an electron into the continuum. This is allowed by exciting the electron through a series of virtual states, each separated by the single photon energy, and with lifetimes defined by the time-energy uncertainty relation. So long as an additional photon is absorbed within the short-lived virtual state lifetime, the process can continue until a sufficient number of photons have been absorbed to overcome the ionisation energy of the electron. Consequently higher interaction intensities are required to enable this nonlinear process with efficiency compared with SPI.

Assuming N photons are required to ionise an electron from the target, the electron will be born into the continuum with an energy, E_{MPI}, equal to the energy difference between the sum of the N photons, NE_{photon}, and the ionisation threshold, Ip. This can be expressed mathematically as:

$$E_{MPI} = NE_{photon} - Ip. \tag{2.14}$$

The rate of MPI depends both on the frequency dependent generalised absorption cross section, σ_N, for the N^{th} order process, as well as the intensity, I, of the interacting field [38]. This is expressed mathematically as [39, 49]:

$$\Gamma_{MPI} \propto \sigma_N I^N. \tag{2.15}$$

Alternatively this can be written as a function of the theoretically calculable parameters [50]:

$$W = \hat{\sigma}^{(N)}(\omega, \rho)\left(\frac{cE^2}{8\pi\omega}\right)^N = \hat{\sigma}^{(N)}(\omega, \rho)\left(\frac{I}{\omega}\right)^N, \tag{2.16}$$

where W is the rate of MPI, E is the electric field amplitude, N is the integer number of photons required for MPI, I is the field intensity, ρ is the ellipticity of the radiation, ω is the frequency of the dressing field and $\hat{\sigma}^N(\omega, \rho)$ is the generalised multiphoton absorption cross section given by [50]:

$$\sigma^{(N)}(\omega, \rho) = \sum_{k,l,m...p} \frac{d_{ik}d_{kl}d_{lm}...d_{pE}}{(\omega_{ki} - \omega)(\omega_{li} - 2\omega)(\omega_{mi} - 3\omega)...(\omega_{pi} - (K-1)\omega)}, \tag{2.17}$$

for the case of linear polarisation, where the summation covers both the bound and continuum states. The detunings from resonance for each transition are given in the denominator.

The process of MPI can be viewed schematically in Figure 2.1 b). The binding potential experienced by the electron (black) is drawn slightly perturbed from the undressed state (light grey) reflecting the small distortion induced by the intensity of the field required for multi-photon ionisation to occur. The perturbations to the bound potential are periodic with the oscillations of the dressing field.

If the number of absorbed photons matches in energy with an allowed real energy-state transition,

resonance enhanced multi-photon ionisation (REMPI) can occur [51], where the longer-lived real electronic state can enhance the ionisation rate compared with MPI progressing through virtual states alone. For the case of REMPI, the demoninator in equation 2.17 will become zero, and the multiphoton ionisation rate must be calculated differently.

In addition, if the intensity of the dressing field is increased, a critical intensity will eventually be reached where deviations from the power law given by equation 2.15 occur [39, 52]. This is because the ionisation will saturate when the entire sample is ionised.

2.2.1.3 Above Threshold Ionisation

Above threshold ionisation (ATI) extends the concept of MPI and corresponds to multi-photon ionisation events where greater than the required N number of photons are simultaneously absorbed. ATI was first observed by Agostini *et al.* in 1979 [53], and coined ATI by Gontier *et al.* in 1980 [54]. Assuming an additional S photons interact, the ionised electron born into the continuum will, for a weak dressing field, have an energy corresponding to [39]:

$$E_{ATI} = (N + S)E_{photon} - Ip. \tag{2.18}$$

Similarly, the rate of ionisation for the ATI process will be given by [38]:

$$\Gamma_{ATI} \propto \sigma_{N+S} I^{N+S}. \tag{2.19}$$

A schematic diagram of ATI can be seen in Figure 2.1 c). The ATI process requires even higher dressing field intensities than MPI to enable the additional continuum-continuum transitions to occur. Often the ATI process can still be treated perturbatively [54], however at the higher dressing field intensities, distinct strong-field effects start to play a role. In 1983, Kruit *et al.* [55] observed a reduction in amplitude of the lowest ATI peak for a 19-photon absorption in a Xenon target. The increased dressing field intensity required to access such high order nonlinear interaction [56] caused the amplitude change through the AC Stark shifting [57] of the effective ionisation threshold, increasing the threshold with increasing dressing field intensity until such a point that the lowest ATI peak energy was no longer sufficient to ionise an electron. These experiments highlight the overlap between the perturbative and strong field response for high order ATI.

The AC Stark induced shift of the Ip leads to an additional term required in the energy equation to account for the change. More will be said about the AC Stark shift later on in this Chapter however the result is that the Rydberg states of an atom shift to higher energy values with an energy difference given by approximately the ponderomotive energy, Up [39]. The ponderomotive energy will also be discussed in more detail later on in this Chapter, but corresponds to the cycle-averaged kinetic energy gained by a free electron accelerating in a electromagnetic field. The equation for the

ATI energy can be written [39]:

$$E_{ATI} = (N + S)E_{photon} - (Ip + Up), \tag{2.20}$$

however due to an equal energy gain from the force on the electron due to inhomogeneity as it exits the laser focus [58], the actual energy peaks of the ATI signal do not change with the increasing intensity and ponderomotive energy, but remain at fixed energy positions [56]. This is true assuming the intensity of the interacting laser pulse varies slowly compared with the time taken to extract the photoelectron from the laser focus.

To get a sense of the size of the pondermotive shift we can expect we can consider some typical experimental parameters. For an 800 nm field focused to a peak intensity of 1×10^{13}W/cm^2, a ponderomotive energy of $\sim$0.6 eV is provided by the field. As we will see in equation 2.34, the ponderomotive energy scales linearly with intensity, and quadratically with wavelength, and so can become very large under certain experimental conditions.

There are many review articles covering a more detailed history of perturbative, and non-perturbative ionisation. Further information can be found in the following review articles, and the references therein [38, 39, 59].

2.2.2 Strong Field Regime

In the strong field regime, the intensity of the dressing field is such that it can strongly distort the bound potential of the valence electrons. The periodicity of the distortion is determined by the periodicity of the dressing field, with the result that the binding potential of the electron distorts in one direction, then the other, presenting the electron with a finite barrier twice per optical cycle as the electric field vector of the dressing laser reverses direction. A schematic of this can be seen in Figure 2.2. The largest distortion to the bound potential occurs when the peak of the dressing field intensity interacts with the target.

As the effective potential barrier is lowered twice per optical cycle, for high dressing field intensities it becomes probable that a portion of the electron wavepacket can quantum mechanically tunnel through the classically forbidden barrier, and emerge into the continuum [40]. This process is known as tunnel ionisation and will be discussed in the following section.

2.2.2.1 Tunnel Ionisation

Tunnel ionisation can occur when the dressing field is sufficiently intense to distort the bound electron potential to the extent where appreciable ionisation through the classically 'forbidden' potential barrier occurs. The potential, $V(x,t)$, experienced by the bound electron will be a combination of the binding potential from the nucleus, and that from the time-dependent dressing field, expressed

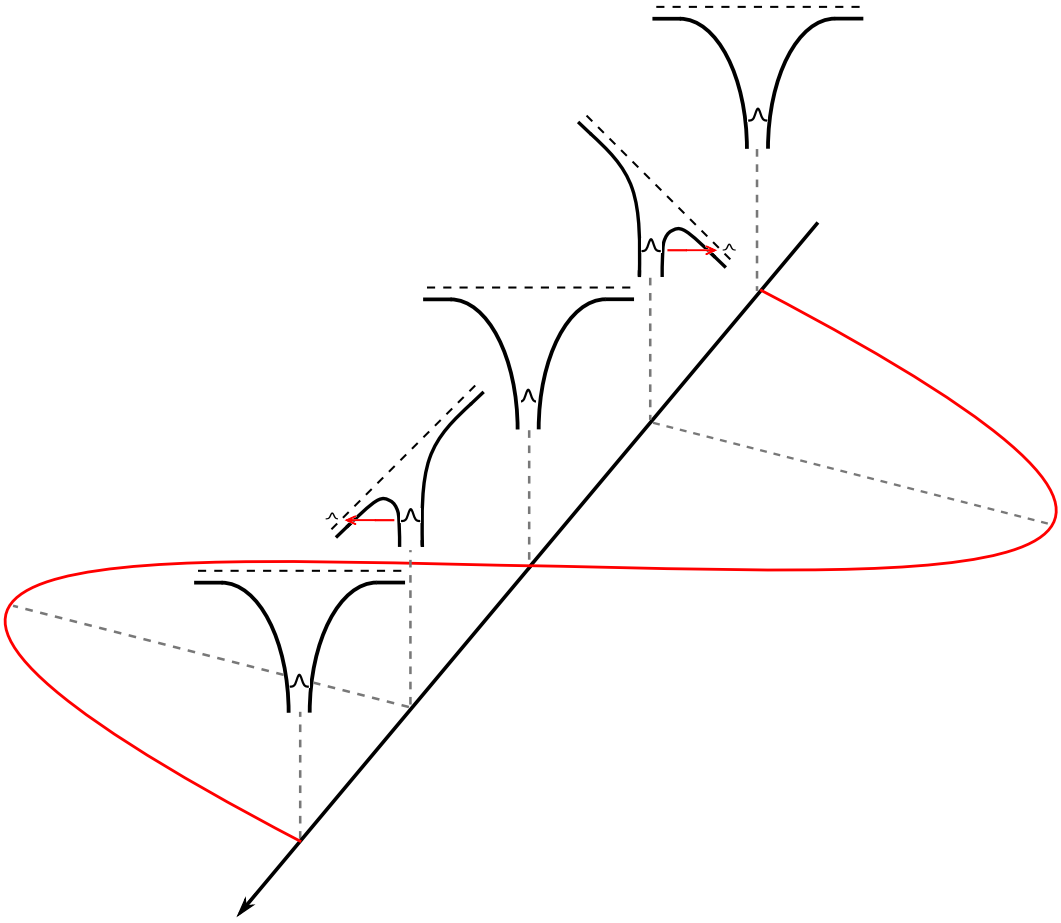


Figure 2.2: Schematic diagram of the large distortions that occur to the potential experienced by bound valence electrons in the presence of a strong dressing field.

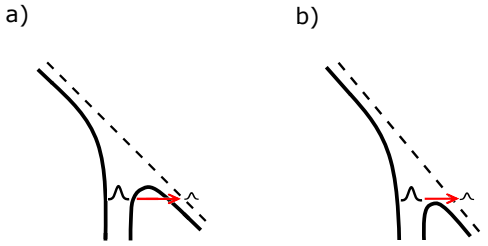


Figure 2.3: Strong-field regime ionisation mechanisms: a) Tunnel ionisation, and b) over-the-barrier ionisation.

as:

$$V(x,t) = -\frac{Ze^2}{4\pi\epsilon_0 x} - exE_0\cos(\omega t), \tag{2.21}$$

where Z is the charge state of the target, e is the charge on the electron, ϵ_0 is the permittivity of free space, x is the distance from the electron to the atomic centre, E_0 is the electric field amplitude, ω is the laser central frequency and t is time.

The rate of tunnel ionisation, Γ_{tunnel}, depends on the exact shape of the bound potential and the properties of the dressing laser field. For an alternating field, the tunnel ionisation rate was calculated by Ammosov, Delone and Krainov [60], and the theory is known as ADK. They determined an exponential dependence for the tunnelling rate, given in atomic units ($\hbar$=m_e=e=1) by the following equation [61]:

$$\Gamma_{tunnel} \propto \exp^{-\frac{2(2I_p)^{\frac{3}{2}}}{3E(t)}}, \tag{2.22}$$

where $\hbar$ is the reduced Planck constant, m_e and e are the electronic mass and charge respectively, I_p is the ionisation potential and $E(t)$ is the electric field amplitude.

The exponential dependence on the electric field amplitude for the tunnelling rate determines that tunnel ionisation can only occur with significant probability for a small window around the peak of the laser field intensity. In addition, it dictates that the least bound electrons presented with the smallest barriers due to experiencing the most significant distortion to their binding potential will be the most likely to tunnel ionise [32]. A schematic diagram illustrating the process of tunnel ionisation can be seen in Figure 2.3 a).

2.2.2.2 Over the Barrier Ionisation

If the interacting field becomes so intense that the potential barrier is suppressed to a level below the ground state of the bound electron, over the barrier ionisation (OTBI) occurs and the electron ionises freely into the continuum with no tunnelling required. A schematic diagram illustrating the process of OTBI can be seen in Figure 2.3 b). At intensities above the OTBI threshold the

ionisation rate is no longer time dependent since the potential barrier suppression is greater than the binding potential of the valence electron. The threshold intensity for which OTBI occurs can be calculated by considering the potential experienced by the valence electron. This is comprised from the Coulomb binding and the potential from the peak electric field, where the symbols have the same meanings as for equation 2.21:

$$V(x) = -\frac{Ze^2}{4\pi\epsilon_0 x} - exE_0. \tag{2.23}$$

The threshold (minimum) intensity required for OTBI is found by setting to zero the differential of the potential with respect to position, obtaining the extremum position, x_{max}, for which the rate of change of potential with distance (the force) is minimum. At, and beyond the x_{max} position the electron is completely removed from the core and no longer feels any force due to the Coulomb binding.

$$\frac{dV(x)}{dx} = \frac{Ze^2}{4\pi\epsilon_0 x_{max}^2} - eE_0 = 0, \tag{2.24}$$

$$x_{max} = \sqrt{\frac{Ze}{4\pi\epsilon_0 E_0}}. \tag{2.25}$$

Substituting x_{max} into equation 2.23 and evaluating that OTBI will occur if this potential is greater than the ionisation potential, Ip, for the bound electron, we find the threshold equation:

$$\sqrt{\frac{Ze^3 E_{OTBI}}{\pi\epsilon_0}} = Ip, \tag{2.26}$$

where E_{OTBI} is the electric field amplitude required to reach the OTBI threshold. Recalling the relation between peak intensity and electric field amplitude, equation 2.2, we find the OTBI threshold intensity I_{OTBI} is given by

$$I_{OTBI} = \frac{c\pi^2\epsilon_0^3 Ip^4 n}{2Z^2 e^6}. \tag{2.27}$$

It should be noted that for multi-electron atoms (Z >1 in the neutral state) electron shielding will alter the effective Coulomb potential experienced by the bound electrons [62]. This modifies the threshold intensity required for OTBI to occur.

2.2.3 Ponderomotive Energy

Following ionisation of an electron into the continuum, interaction between the electromagnetic field and the electron persists, and the electron is accelerated by the field. The cycle-averaged kinetic energy gained through acceleration of the electron in the laser field is known as the ponderomotive energy, Up. Assuming the only force acting on the continuum electron is that from the strong laser field, an equation for the Up can be derived by equating Newton's second law with the Lorentz force

$$\mathbf{F} = m\mathbf{a} = -e(\mathbf{E(t)} + \mathbf{v} \times \mathbf{B(t)}), \tag{2.28}$$

where m is the mass of the electron, $\mathbf{a}$ is the acceleration, e is the charge on the electron, $\mathbf{E(t)}$ and $\mathbf{B(t)}$ are the electric and magnetic field vectors, and $\mathbf{v}$ is the velocity of the electron.

Derived from Maxwell's wave equations for electromagnetic radiation, the following equation relates the electric and magnetic fields [63]:

$$\mathbf{E} = c\mathbf{B}, \tag{2.29}$$

where c is the speed of light. Since for the field intensities used in this thesis the electron speeds are well below the relativistic limit, the magnetic field component of the Lorentz equation can be considered negligible, simplifying greatly equation 2.28.

Assuming we are in what is known as the slowly varying envelope approximation (SVEA), where the laser pulse envelope can be considered constant during any given full laser cycle, we can treat the electric field amplitude, E_0, as a constant. For an electric field vector accelerating the electron along the x-axis, the acceleration can therefore be written as:

$$\ddot{x} = -\frac{eE_0}{m}\sin(\omega t). \tag{2.30}$$

Recalling that the kinetic energy is given by:

$$KE = \frac{1}{2}mv^2, \tag{2.31}$$

integrating equation 2.30 once with respect to x gives an equation for the velocity of the electron as a function of time:

$$\dot{x} = \frac{eE_0}{m\omega}(\cos(\omega t)) + C, \tag{2.32}$$

where ω is the fundamental frequency of the driving laser field. It is assumed that the electron is born into the continuum with zero velocity so the constant, $C = 0$.

Since the ponderomotive energy, U_p, is defined as the cycle-averaged kinetic energy, it can be expressed as:

$$U_p = \frac{1}{2}m\left\langle \dot{x}^2 \right\rangle = \frac{e^2E_0^2}{2m\omega^2}\left\langle \cos^2(\omega\tau_{cycle}) \right\rangle, \tag{2.33}$$

where τ_{cycle} corresponds to the period of the driving laser field. This results in a value of the ponderomotive energy being given by:

$$U_p = \frac{e^2E_0^2}{4m\omega^2}. \tag{2.34}$$

Rearranging equation 2.2 relating the peak intensity of a field to the electric field amplitude, and substituting this into 2.34 we find an equation relating the energy gained to the peak intensity and wavelength of the driving field:

$$U_p = \frac{e^2 I}{2mc\epsilon_0\omega^2 n} = \frac{e^2 I\lambda^2}{8m\pi^2 c^3\epsilon_0 n}, \tag{2.35}$$

where the symbols have the same meanings as previously defined.

The ponderomotive energy has importance in understanding strong field interaction and the process of high harmonic generation. Equation 2.35 is therefore very useful since it relates parameters that are measurable in the laboratory to the ponderomotive gain. The fact that the Up has linear dependence with intensity but a quadratic dependence with wavelength of the driving field will prove to be interesting for the generation of high order harmonics.

2.2.4 Keldysh Parameter

So far we have discussed ionisation processes associated with weak-field response, and those associated with strong-field response. At the boundary between the perturbative and strong field regimes a mixture of ionisation processes occur. Derived by Keldysh in 1965 [40], the Keldysh parameter, γ, can be used to determine the dominant ionisation mechanism for a given set of experimental parameters. Physically the parameter compares the two timescales involved in tunnel ionisation: the time taken for an electron to quantum mechanically tunnel through the forbidden barrier, T_{tunnel}, and the period of the driving laser field, T_{laser}, which will determine the rate at which the barrier height is changing. If the tunnelling time is large compared with the period of the laser field, little tunnelling can occur and the ionisation will be dominated by multiphoton effects. For tunnelling times much shorter than the changing barrier time, tunnelling is more probable and will dominate the ionisation.

Considering the parameters that can be measured experimentally in the laboratory, most usefully the Keldysh parameter can be written in the following form relating the ionisation potential, I_p, and the ponderomotive energy, U_p, of the system to give a value defining the regime of dominance [40]:

$$\gamma = \sqrt{\frac{I_p}{2U_p}} = \frac{T_{tunnel}}{T_{laser}}. \tag{2.36}$$

When $\gamma >> 1$, the ionisation is dominated by multiphoton effects as the Coulomb interaction is much larger than the ponderomotive energy. For $\gamma << 1$, the reverse is true and the magnitude of the ponderomotive energy is much larger than the ionisation energy, with the result that tunnel ionisation is dominant. Theoretical calculations performed in the region around $\gamma = 1$, where much of the work presented in this thesis falls, tunnel ionisation is still found to dominate [64]. A detailed review of the Keldysh theory can be found in reference [65].

2.3 The Effect of Matter on Light

Now we have considered the effect of light on matter, we can also consider the corresponding effect of matter on light.

2.3.1 Dispersion

The refractive index of a material, $n(\omega)$, determines how light interacts with the medium. The refractive index is both frequency dependent, and complex, leading to both wavelength dependent behaviour, and the possibility for attenuation respectively [66].

When a pulse propagates through a dispersive medium, the individual frequency components comprising the pulse wavepacket will behave differently according to their wavelength. The phase velocity, $v_p = \frac{\omega}{k}$, defines how each individual frequency comprising the wavepacket behaves, where ω is the angular frequency, equivalent to the rate of change of phase with time, $\frac{\partial \phi}{\partial t}$, and k is the angular wavenumber.

The quantity that defines how the entire wavepacket propagates is the group velocity, $v_{group} = \frac{\partial \omega}{\partial k}$. Using the equation relating k and ω, $\omega = \frac{ck}{n(\omega)}$, an equation related to the group velocity can be found:

$$\frac{1}{v_{group}(\omega)} = \frac{1}{c}\left(n(\omega) + \omega \frac{dn(\omega)}{d\omega}\right). \tag{2.37}$$

Since speed = distance/time, equation 2.37 defines the effective group delay for a unit distance.

Differentiating this once more with respect to ω defines the rate of change of group delay with angular frequency, or the spread of the group velocity with ω per unit length. This value is known as the group velocity dispersion (GVD) [67] and is given by:

$$GVD = -\frac{1}{v_{group}^2}\frac{dv_{group}}{d\omega}. \tag{2.38}$$

The magnitude of the GVD will determine how much spread will occur as the pulse propagates, and the sign of the GVD determines the direction of the induced frequency dependent spread of the light, known as the chirp. For the chosen sign convention, if the GVD is positive, the chirp is positive and the red light precedes the blue in the pulse. If the GVD is negative, the chirp is negative and the red light lags behind the blue in the stretched pulse. For any given optical element, the rate of change of group delay with ω is known as the group delay dispersion (GDD), with units of fs^2 [61].

GVD is particularly important for short pulses since short pulses inherently have large bandwidths containing a broad range of frequencies. The relationship between bandwidth and pulse duration is governed by an uncertainty relation named the time-bandwidth product:

$$\Delta\omega\Delta t \geqslant K, \tag{2.39}$$

where $\Delta\omega$ and Δt represent the full width at half maximum (FWHM) of the bandwidth and temporal duration respectively, and K represents a factor whose exact value depends on the pulse profile [68]. K is determined to be 0.441 for a Gaussian pulse profile, compared with 0.315 for a sech^2 pulse, or 0.142 for a Lorentzian [69]. If this expression reaches equality we refer to the pulse as transform or bandwidth limited.

The relationship between phase velocity and group velocity is of particular importance for single cycle or few-cycle pulses. When the pulse envelope is of a similar duration to the single cycle pulse length, the exact phase of the modulation relative to the envelope will closely determine the properties of the resultant pulse, for example if the phase modulates symmetrically as a cosine function around the central peak of the envelope (CEP = 0°), a single peak of maximum field amplitude is observed. Focused to sufficient intensity, this can be used to generate isolated attosecond pulses [17, 70] for which more will be said in the High Harmonic Generation section later in this Chapter. Alternatively, if the same pulse phase instead modulates anti-symmetrically around the central peak of the wavepacket envelope (CEP = 90°), two equal amplitude peaks are observed which would lead to a train of two pulses if used to create high harmonic generation. The relationship between the modulation phase and the phase of the envelope is known as carrier envelope phase, CEP. A schematic of the the CEP scenarios discussed can be seen in Figure 2.4 for an assumed dressing field intensity $1{\times}10^{14}\text{W/cm}^2$, and wavelength 800 nm.

When using a single cycle or few cycle pulse, maintaining a constant phase relationship between the carrier wave and the envelope is important to ensure the same characteristics are produced for each attosecond pulse [71]

2.3.2 Effects of Nonlinear Interaction

When an atom interacts with an electric field, the oppositely charged electrons and nucleus displace forming an electric dipole moment, $\mathbf{p} = q\mathbf{x}$, where q is the point charge and $\mathbf{x}$ is the displacement vector. Considering the effect of light matter interaction in a macroscopic medium, the polarisation of the material is given by the sum of the induced dipole moments over volume, $\mathbf{P} = \sum_{i=1}^{N} q_i\ \mathbf{x}_i$. The polarisation of a material determines how light propagates through the material. Considering just the linear term, this can be written as:

$$\mathbf{P}(t) = \epsilon_0 \chi^{(1)} \mathbf{E}(t), \tag{2.40}$$

where ϵ_0 is the permittivity of free space, $\mathbf{E}(t)$ is the time dependent electric field vector, and $\chi^{(1)}$ is the first order nonlinear susceptibility, related to the refractive index through $n = \sqrt{1 + \chi^{(1)}}$ [68].

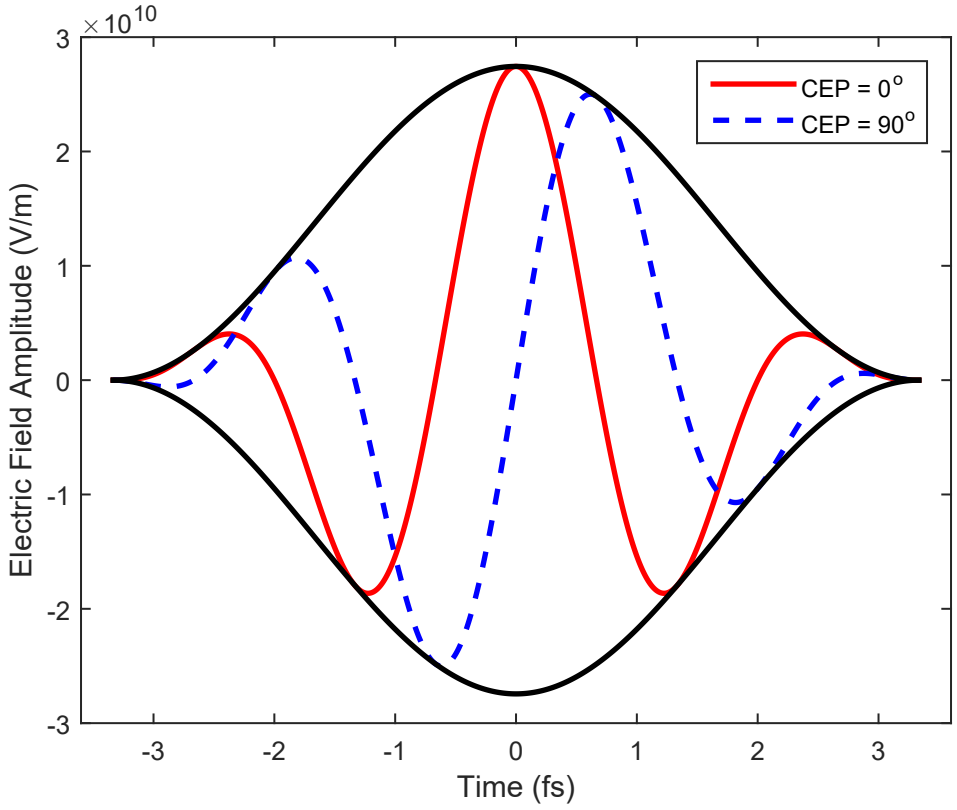


Figure 2.4: Schematic diagram of carrier envelope phase. The red line shows the CEP phase to generate a single peak. The blue dashed line shows the CEP for two equal electric field amplitude peaks. The values shown assume an 800 nm field at intensity 1×10^{14}W/cm^2.

Equation 2.40 assumes a linear response to the electric field. For intense electric fields, nonlinear components become increasingly important. The nonlinear components can be included into equation 2.40 through a power series expansion of the polarisation

$$\mathbf{P}(t) = \epsilon_0(\chi^{(1)}\mathbf{E}(t) + \chi^{(2)}\mathbf{E}^2(t) + \chi^{(3)}\mathbf{E}^3(t) + ...), \tag{2.41}$$

where each successive nonlinear term includes an associated n^{th} order nonlinear susceptibility, $\chi^{(n)}$ [68].

This expansion can be used to understand many of the nonlinear phenomena that occur within the perturbative regime. Several of the effects related to the work presented in this thesis can be found below. For each instance, the electric field is considered to be a cosine within the slowly varying envelope approximation, so the time dependence on the electric field can be neglected.

2.3.2.1 The Pockels Effect

With the application of an external electric field, the refractive index of a non-centrosymmetric material can be modified through a second order nonlinear effect. This behaviour can be exploited to form an effective voltage controlled waveplate, which if used in conjunction with a polariser, can create a pulse picker, switching out selected pulses by quickly rotating the polarisation of the pulsed light. By varying the applied voltage to the birefringent crystal, selected, linearly polarised laser pulses will be transmitted through the polariser, with the remaining orthogonally polarised pulses absorbed.

The frequency and quality of the pulse selection will be limited by the rise time of the applied voltage, and the extinction ratio of the polariser. The Pockels cells used in the Red Dragon laser system (see Red Dragon section in Chapter 4), are switched to select pulses for a 1kHz frequency output to match the frequency of the pump lasers in the amplification stages.

The dependence of the refractive index on the applied field amplitude can be extracted from the polarisation expansion shown in equation 2.41 by adding an additional stationary term, A_0 into the applied electric field, E [68]:

$$E = A_0 + A_1\cos(\omega t - kx). \tag{2.42}$$

Substituting equation 2.42 into equation 2.41, and considering terms in $A_1\cos(\omega t - kx)$ up to the second order, the refractive index is found to change with the applied electric field to be:

$$n = \sqrt{1+\chi^{(1)}} \quad \rightarrow \quad n = \sqrt{1+\chi^{(1)}+2A_0\chi^{(2)}}. \tag{2.43}$$

2.3.2.2 Third Order Nonlinearities - The Optical Kerr Effect

Following the same procedure as for the Pockels effect, however this time considering the expansion substitution up to the third order nonlinearities, we can explore the intensity dependent change to the refractive index, the optical Kerr effect, by identifying the third order terms dependent on $A_1\cos(\omega t - kx)$. Following the substitution of equation 2.42 into equation 2.41 as before, the relevant expansion components are found to be [68]:

$$P = \epsilon_0(... + 3\chi^{(3)}(A_0^2 + \frac{1}{4}A_1^2)A_1\cos(\omega t - kx) + ...). \tag{2.44}$$

Identifying that $A_1^2 = \frac{2I}{c\epsilon_0 n_0}$ (recall equation 2.2), where A_1 is amplitude of the electric field, I is the intensity, and c, ϵ_0 and n_0 are the speed of light, the permittivity of free space and the linear refractive index respectively, the intensity dependent refractive index can be found [68]:

$$n = n_0 + n_2 I \propto n_0 + \frac{3\chi^{(3)}I}{2n_0^2\epsilon_0 c}. \tag{2.45}$$

The intensity dependent refractive index arising from the laser field interaction is known as the optical Kerr effect. Two key effects transpire from the intensity dependent refractive index: self focusing of the laser light, and self phase modulation (SPM). Both these effects are important for those working in ultrafast optics.

Self Focusing

Self focusing can be understood by considering a beam with a non-uniform spatial intensity, for example a Gaussian beam, propagating through a material with refractive index $n(\omega)$. The positions in the beam profile with highest intensity, the centre in the case of the Gaussian, will cause a larger change to the nonlinear refractive index than the lower intensity beam edges. The increased effective refractive index at this central position will affect the phase fronts of the propagating wave. For the case of a Gaussian beam, the effect is to form curved wavefronts, with the beam focusing down upon itself. As the beam focuses, the intensity in the central part increases further, amplifying the effect. This can cause catastrophic damage to optics within a laser system if left unchecked. A discussion on self focusing and review of nonlinear optics can be found in reference [72].

Self Phase Modulation

Another consequence of the intensity dependent refractive index is the possibility for self phase modulation (SPM), where the temporal variation in the refractive index of the medium due to the presence of the intense laser field leads to additional frequencies being generated within the laser pulse. This is beneficial for producing increasingly shorter duration pulses, where an already transform limited pulse may be reduced in duration further by the addition of extra bandwidth through SPM and subsequent pulse compression.

The spectral broadening through self phase modulation was first explored by Shimizu, Brewer

and Cheung *et al.* in the late 1960s [73–75]. Today SPM is typically exploited through hollow core fiber pulse compression [24] to produce few cycle pulses for direct experiment, or in turn used to generate isolated attosecond pulses (IAPs), for example in reference [71].

2.4 High Order Harmonic Generation

High order harmonic generation (HHG) is a highly non-linear process that converts photons of one frequency, ω_1, the fundamental, into higher energy photons. By focusing an intense ($> 10^{14}\,\mathrm{W/cm^2}$) laser pulse into an atomic or molecular target, energy from the laser field can be transferred to the sample, and ultimately to the generation of high energy photons. The specific properties of the high harmonic spectrum will depend on many experimental parameters including the focused laser intensity [76, 77], pulse duration [16, 17] and wavelength [78, 79], as well as the target material [80], backing pressure [76], position with respect to the focus of the light [77, 81, 82], and so on.

In 1977, Burnett *et al.* observed the first high harmonic spectra [83] using a $10.6\,\mu$m CO_2 laser and the plasma plume from laser-ablated aluminium targets. The first presentation of HHG from atomic samples was not until a decade later, with McPherson *et al.* [80] in 1987. In 1988, Ferray *et al.* [84] pushed towards an increasingly extended cutoff, observing a clear plateau region in the harmonic spectrum. This characteristic plateau behaviour was investigated further by Li *et al.* [76], and the exhibited behaviour allows scaling of the high order harmonic generation photon energies whilst still maintaining signal levels up to the onset of the cutoff.

The process of HHG can be understood by considering separately the microscopic and macroscopic effects that occur, that is, the effects occurring on the single atom level (microscopic), and the combined response of many interacting atoms (macroscopic). The macroscopic effects include interference and re-absorption of generated harmonic light, and will be discussed in more detail in the Phase Matching section later in this Chapter. First, however, we will consider the response of the single atom in the context of the semi-classical three-step model for HHG.

2.4.1 Semi-Classical Three Step Model

The semi-classical three step model for describing HHG was proposed by Paul Corkum in 1993 [85], based on work by Krause *et al.* [86] performed the previous year. The model describes the process of HHG through three distinct steps: (1) ionisation of an electron, (2) acceleration of the electron by the laser field, and (3) recombination of the electron with the parent ion. This model comprises both quantum-mechanical (steps 1 and 3) and classical (step 2) physics. A fully quantum description of HHG was developed in 1994 by Lewenstein *et al.* [87], making some important approximations that would later come to be known as the Lewenstein model, based on the strong field approximation (SFA) [88]. We will revisit SFA later on in this section. A schematic of the semi-classical three step

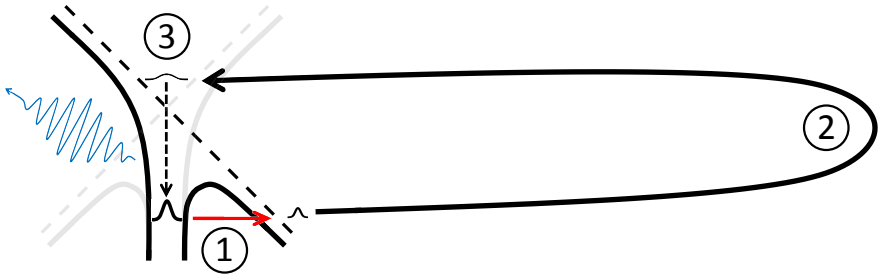


Figure 2.5: Schematic diagram of the semi-classical 3-step model for high harmonic generation. The electron tunnel ionises through the classically forbidden region, step 1. It is accelerated in the laser field, step 2. There is a probability that it can collide back with the parent ion and recombine resulting in the emission of high energy light, step 3.

model can be seen in Figure 2.5.

When an intense laser field interacts with an atom, the large electric field component can distort the binding potential of the valence electrons to such a degree that tunnel ionisation occurs with a high probability. The distortion to the potential varies periodically with the incident field, presenting a maximum twice per laser cycle corresponding to the times of maximum laser intensity. As the rate of tunnel ionisation depends exponentially on the potential barrier (recall equation 2.22), the majority of tunnel ionisation occurs around the peaks of the laser intensity.

Following the ionisation step, the charged electron wavepacket is accelerated by the intense laser field, driven initially away from, and then back towards the parent ion as the direction of the electric field reverses. The acceleration of the electron wavepacket is treated classically within this model. Depending on the phase of the driving laser when the electron was ionised, this will determine the path, or trajectory, of the subsequent motion. One assumption of SFA is that the only force felt by the electron during the acceleration is that from the laser field; the attraction from the ionic core is considered negligible. This is a reasonable assumption since the majority of continuum electrons born through tunnel ionisation arrive into the continuum around the peak of the field intensity, leading to high initial acceleration of the electron, with the result that the electron spends little time in close proximity to the ionic core. Similarly, when the intensity of the laser field equals zero the assumption is still valid since at this time the electron is now assumed to be far from the charged nucleus, and again its influence negligible.

If the electron is born into the continuum after the peak of the laser field, it is possible that it can be steered back to the parent ion where it can recombine with a defined probability. Upon recombination of the accelerated wavepacket with the ground state wavefunction, an oscillating dipole moment is produced, releasing a continuum of high energy light. Trajectories that follow paths

enabling recombination are known as returning trajectories. For continuum electron wavepackets ionised before the peak of the electric field, the field cannot steer them back for recombination with the parent ion and instead they follow non-returning electron trajectories resulting in no harmonic generation, just contribution to the ionisation fraction of the target. Figure 2.6 shows a selection of calculated classical electron trajectories. Returning trajectories are shown in blue to red with a non-returning trajectories shown in black. The trajectory corresponding to the maximum energy gained in the field is known as the cutoff trajectory, and is shown in green dashed. The energy corresponding to the cutoff trajectory E_{cutoff} [86] is given by the equation:

$$E_{cutoff} = I_p + 3.17U_p, \tag{2.46}$$

where the I_p is the ionisation energy of the valence electron, and U_p is the ponderomotive energy. This is verified through the classical trajectory calculation shown in Figure 2.6.

The classical electron trajectories are calculated by equating Newton's second equation with the Lorentz force as in equation 2.28. Recalling that the magnetic component in the Lorentz equation can be neglected since the speed of the ionised electrons considered in this thesis are much lower than the speed of light, and assuming that the electric field vector accelerates the electron along the x-axis, we can integrate twice with respect to x to obtain equation 2.47 defining the position of the electron as a function of time [39]:

$$x(t) = \frac{-eE_0}{m\omega^2}(\sin(\omega t) - \sin(\omega t_0) - \omega(t - t_0)\cos(\omega t_0)), \tag{2.47}$$

where t_0 is the time of birth of the electron wavepacket in the field, and t is the sampling time of the electron trajectory. Again we have assumed that the electric field amplitude of the driving laser is constant i.e. that we are in the SVEA limit.

The electron trajectories can be divided into two regions: the long and the short trajectories corresponding to the paths resulting from electrons ionised before and after the cutoff trajectory. As can be seen from the Figure 2.6, each energy (except the cutoff) emitted on recombination can occur through two different pathways: one short and one long trajectory. Looking at the phase of the electron trajectory return, it is observed that the short trajectories spend less time for a given energy gain in the continuum than the long trajectories. Since the cutoff trajectory lies between the long and short paths, the time-dependent frequency emission (attochirp) for the long and the short trajectories also have opposite signs. Inherently this will lead to different macroscopic optimal conditions to enhance the long or short trajectory components. Again, more will be said on this subject in the Phase Matching section later on in this Chapter.

For each half-cycle peak of the laser field, a continuous spectrum of different energy photons are emitted up to the cutoff. If the incident laser pulse consists of just a single or few laser cycle(s), the

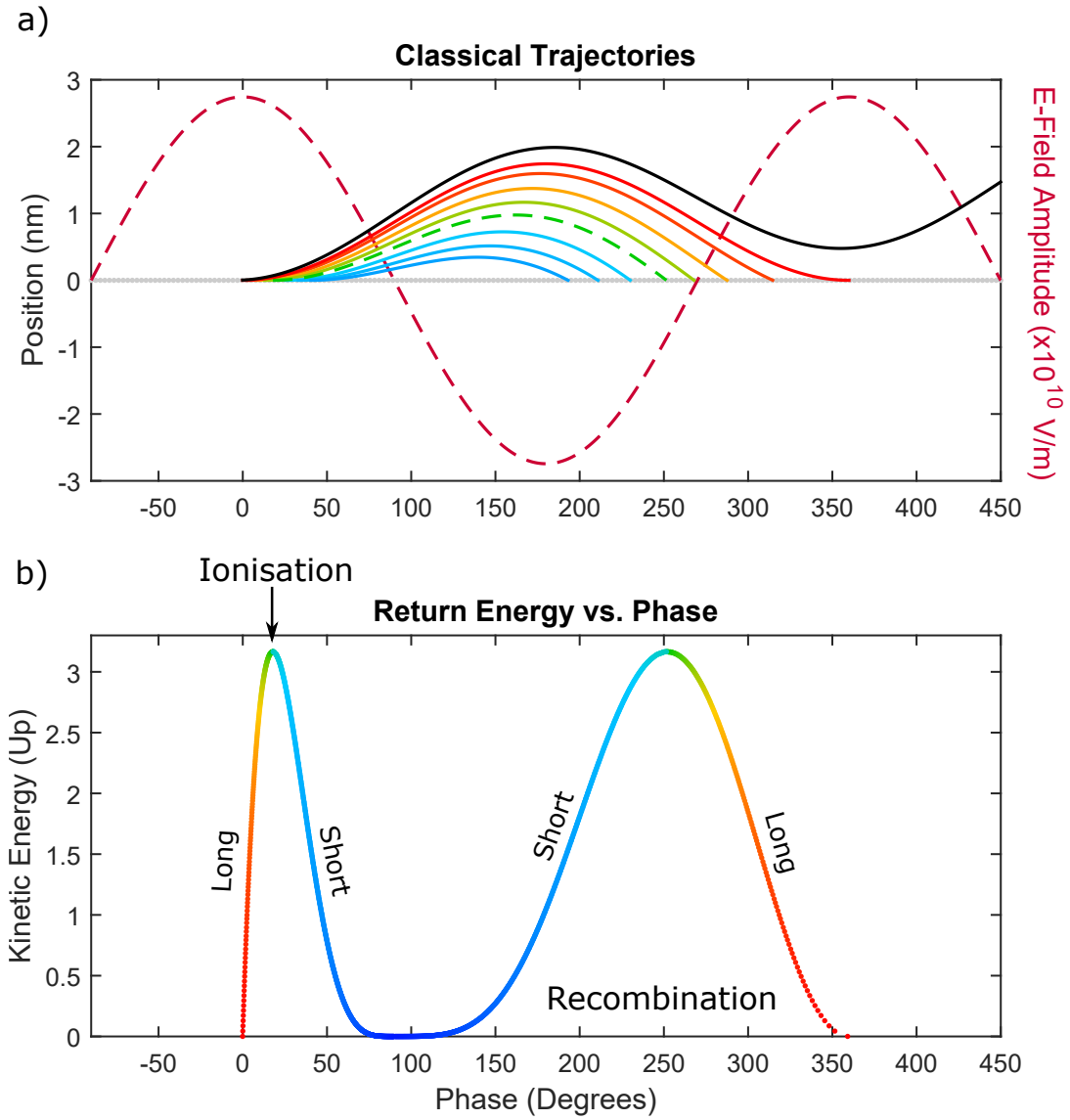


Figure 2.6: a) A selection of the calculated returning (blue to red) and non-returning (black) classical electron trajectories for high harmonic generation, along with the cutoff trajectory (green dashed) representing the highest field energy gain by any electron trajectory in the HHG process. The driving field (800 nm, 1×10^{14}W/cm^2) is depicted by the dashed dark-red line. b) Corresponding ionisation phase and recombination phase for the range of calculated returning trajectories shown in a).

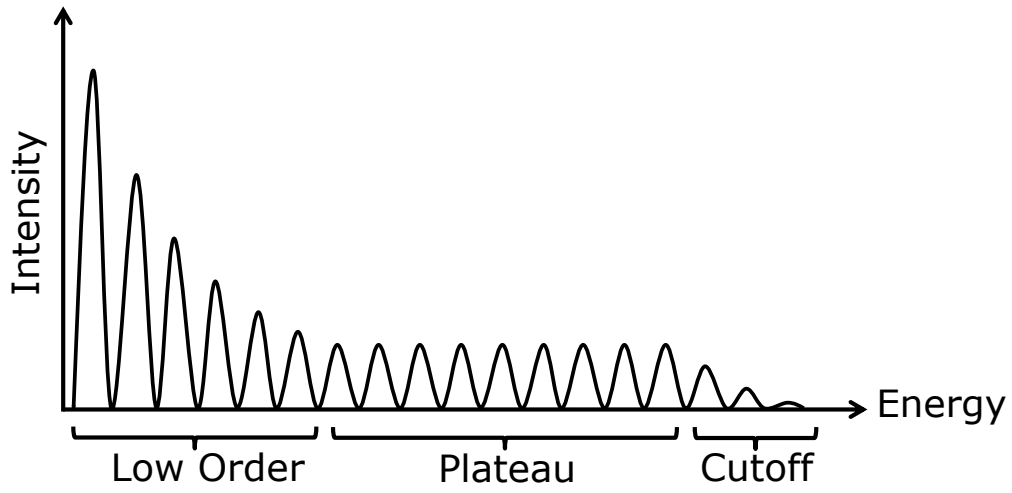


Figure 2.7: Cartoon picture of a typical high harmonic generation spectrum produced from a many-cycle pulse indicating the key profile characteristics: exponentially decaying low order harmonics, equal intensity plateau harmonics and the sharp high energy cutoff.

produced spectrum is continuous and the broad, chirped bandwidth can be windowed to form isolated attosecond pulses (IAP) [17]. More usually, the interacting laser pulse is longer, consisting of several optical cycles or more, resulting in interference between the spectra produced for each half-cycle peak of the laser intensity. This gives rise to the characteristic discrete harmonic spectrum [76, 84], as illustrated in Figure 2.7. If the pulse is many cycles in length, the slowly varying envelope approximation (SVEA) may be applied, where it is assumed that the electric field amplitude within a single optical cycle does not change.

For a centrosymmetric target, for example an atom which is symmetric upon reflection in each of its axes, the interference of the spectra produced at each half-cycle results in a spectrum consisting of only odd harmonic orders of the fundamental frequency (the even harmonic orders destructively interfere). This can be understood by considering the effect of reversing the direction of the incident laser field. For a centrosymmetric medium, the result is identical, so reversing the electric field vector in equation 2.41 will reverse the sign of the polarisation vector too. This implies that for even harmonic orders, the emission from subsequent half-cycles interferes destructively, resulting in zero signal produced for the even components of the nonlinear expansion. The longer the incident laser pulse, the sharper the odd harmonics will be as the destructive interference at the even orders is compounded. A schematic of a typical harmonic spectrum can be seen in Figure 2.7. This illustrates both the characteristic odd harmonic comb structure, as well as the typical shape of the emission with the exponentially decaying amplitude low order harmonics, the extended plateau of approximately equal amplitude harmonics, and the high energy sharp cutoff.

The different regions of the high harmonic spectrum can be understood from the harmonic generation process. Low order harmonics can be generated through both tunnel and multi-photon

ionisation pathways. The probability for multi-photon ionisation will be higher for lower energy harmonic orders where fewer photons are needed to interact. The reduction in probability for increasingly high harmonic orders can be understood from the multiphoton ionisation rate 2.15. The plateau exists since for each half-cycle of the laser, a spectrum covering the whole continuum up to the cutoff is produced. Therefore nothing differentiates the probability of one frequency in the continuum being produced more readily than another. At the cutoff frequency, a sharp drop in amplitude is observed where higher frequencies cannot be produced.

By breaking the symmetry of the system, production of both even and odd harmonic orders is possible. This can be achieved using either a non-symmetric laser field, for example through the addition of a second colour field [29], or a non-centrosymmetric target [89], for example a heteronuclear diatomic molecule.

The wavelength of the field used to generate the harmonics is a key parameter in defining the resultant harmonic spectrum. We have already established there is a λ^2 dependence of the harmonic cutoff energy, recall equations 2.46 and 2.34, however there is an additional, highly unfavourable λ^{-5} to $\lambda^{-6.5}$ scaling with the generated harmonic intensity [78, 79], resulting in significantly lower flux generated for longer driving wavelengths. We will revisit this in the Chapter 6 Discussion since the wavelength scaling is highly relevant when considering results produced using an 800 nm driving laser, and those produced using a 1400 nm driving laser.

2.4.1.1 Time-frequency Mapping

Since the appearance of discrete harmonic orders is generated through interference of the half-cycle continua, and the different harmonic orders correspond to different generated frequencies, because of the inherent chirp across the continuum produced for each half-cycle, there will also be an associated chirp across the produced harmonics. This is named the attochirp. As described earlier, the sign of the attochirp for the long and short trajectory pathways is opposite, and this is illustrated by Figure 2.8 [90], where the return time as a function of harmonic order is plotted for two different intensity, 800 nm wavelength fields: 3.8×10^{14}W/cm^2 in red, and 1.2×10^{14}W/cm^2 in blue.

2.4.1.2 Strong Field Approximation

Different theoretical techniques exist to calculate the interaction of light and matter. The time dependent Schrödinger equation (TDSE) can be used to calculate exact solutions for the simplest of atoms and molecules within the single active electron (SAE) approximation [88], however the numerical calculations are computationally heavy and time consuming.

Approximations exist to simplify the calculations, and one such model is the strong field approximation (SFA) [40, 91, 92]. When SFA is applied to the process of high harmonic generation, this is more usually referred to as the Lewenstein model [87], developed by Lewenstein *et al.* in 1994. The

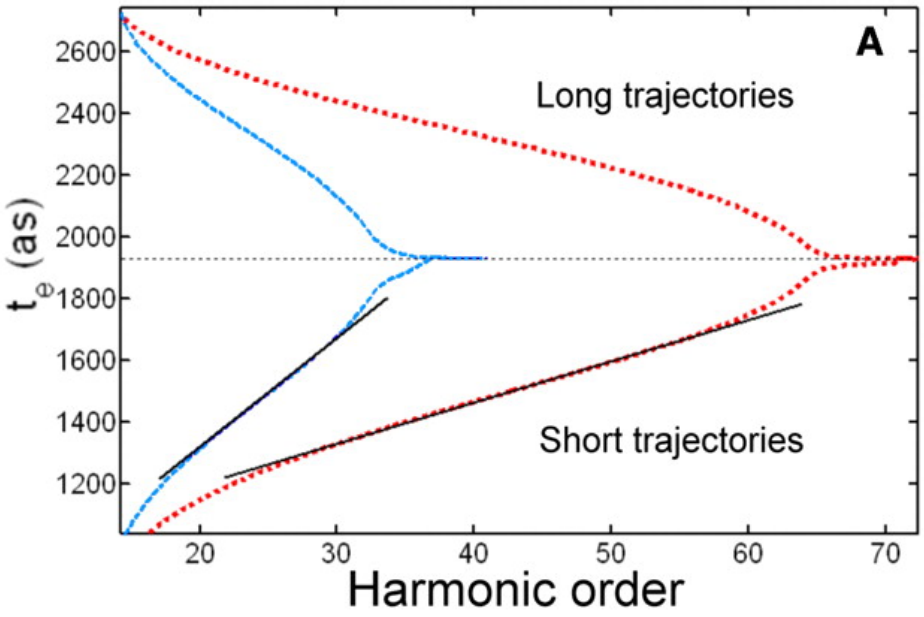


Figure 2.8: Plot showing the relationship between the high harmonic generation order and the emission time for the short and long trajectories at two different 800 nm generation laser field intensities: 3.8×10^{14}W/cm^2 in red, and 1.2×10^{14}W/cm^2 in blue. The peak intensity of the generating laser field occurs at time = 0 as. This plot has been reproduced from [90]. Reprinted with permission from AAAS.

key assumptions of the SFA model are as follows:

- Continuum electrons born through tunnel ionisation have zero initial kinetic energy.
- Acceleration of the continuum electrons is entirely a result of the interacting laser field with no influence from the parent ion core.
- All electrons ionise from the ground state.
- The ground state does not become depleted.
- Single active electron (SAE) approximation, that is that only a single electron participates in the interaction, with all additional electrons in the system remaining in their respective ground states.

Many of the assumptions of the strong field approximation have already been discussed in this Chapter. The main drawback to the SFA model is the accuracy, however the scalability of the method to calculate both simple and complicated systems with reduced computational requirements [88] makes this method widely used.

Many papers and review articles examine closely the history and derivations of SFA, for example a detailed description of SFA and other related developments can be found in [88, 93] and references therein.

2.4.1.3 Wavepacket Spreading

Due to the position momentum uncertainty relation, recall equation 2.11, since the ionised electron wavepacket is born into the continuum with a well defined position, the wavepacket will be comprised of a large spread of momenta. The momentum spread perpendicular to the dressing field is unaffected by the field oscillations and so will continue to spread throughout the duration of the wavepacket acceleration. For the long trajectory paths, the accelerated electron wavepacket spends greater time in the continuum resulting in a larger transverse spreading than for the short trajectory paths. The probability of recombination is proportional to the overlap integral of ionised and ground state wavefunctions and so a larger transverse spreading of the ionised electronic wavefunction will lead to a reduction in the recombination probability, resulting in lower efficiencies for the long trajectory harmonic components.

Considering just the single atom case, the long trajectory components still appear strong since the long trajectory paths are ionised closer to the peak of the field intensity than the short trajectories, resulting in higher ionisation rates. This helps to compensate for reductions in the recombination probability. The short trajectory components however are only ionised after approximately 17° phase of the driving laser where the ionisation rate is lower.

2.4.2 Macroscopic Effects

We have now established the single atom response to an intense laser field for both the single cycle and many cycle limits. In understanding experimentally produced high harmonic generation, we must also understand the macroscopic effects that occur as the incident light interacts with, and propagates through the entire target length.

The technique for ensuring signal constructively adds throughout the target length is known as phase matching and will be discussed in the section below.

2.4.2.1 Phase Matching

When considering the macroscopic response of many target emitters, the strength of the output signal will depend on the number of emitters for which the output light interferes constructively. In the simplistic case of a monochromatic output, if half of the emitters produced light exactly in antiphase with the other half, the result would be zero signal. Similarly, if all the emitters produce light in phase, the result will be maximum signal. Although the concept of phase matching is quite simple: minimise the phase slip between the different emitters to maximise the total number of emitters contributing constructively to the interference, in reality it can be difficult and complicated to achieve.

For ultrafast systems, the light to be phase matched is not monochromatic, and the frequency dependent refractive index of the target will lead to dispersion of the different frequency orders throughout the propagation length. The idea of phase matching has already been introduced in this thesis through the flux improvements made by Maker *et al.* [10] to the first experiment demonstrating second order harmonic generation performed by Franken *et al.* [9] in 1961. By exploiting the fast and slow axes of the nonlinear crystal, phase slip between the fundamental light, ω_1, and the generated second order light, $2\omega_1$, was minimised by selecting an appropriate angle of the crystal with respect to the fundamental beam to compensate the dispersion. Ensuring the fundamental and generated second order remain propagating in phase, energy continues to flow from the fundamental into the second order, and emitters throughout the target length can contribute constructively to the output signal.

Considering just the fundamental, ω_1, and the second order generation, ω_2, one can define the phase mismatch parameter, Δk, to be [68]:

$$\Delta k = k_2 - 2k_1, \tag{2.48}$$

where k is the angular wavenumber.

In this way the length over which the different frequencies remain adding constructively in phase is called the coherence length, and it is given by [68]

$$L_{coherence} = \frac{\pi}{|\Delta k|}. \tag{2.49}$$

When phase matching the high harmonic generation process, many different frequencies are generated, however the same basic principles for phase matching apply. In the production of HHG, the beam must be focused tightly to ensure sufficient intensity in the focal spot to enable tunnel ionisation to occur. This leads to gradients in the phase matching [82, 94] due to the focusing geometry. Considering equation 2.48 in vector form to account for off axis generation we can define [95]:

$$\Delta \mathbf{k}_q = q\mathbf{k}_1 - \mathbf{k}_q, \tag{2.50}$$

where $\Delta \mathbf{k}_q$ is the wave vector mismatch between the q^{th} order harmonic and the fundamental.

In total there are four different components that contribute towards the phase matching conditions, and these are:

- **Gouy phase** or **geometric phase**. This is a π phase shift associated with a Gaussian beam passing through a focus. The origin of the Gouy phase can be viewed in Figure 2.9. The form of the Gouy phase is given by:

$$\phi_{foc}(r, z) = \arg\left[\frac{1}{b + 2iz} \exp\left(-\frac{kr^2}{b + 2iz}\right)\right], \tag{2.51}$$

  where the cylindrically symmetric beam propagates along the z axis, k is the wavenumber of the driving laser and b is the confocal parameter, described in Figure 2.9. This equation can be found in various forms in many textbooks and papers. This particular form was found in reference [82].

- **Atomic dipole phase**. This is the phase associated with the ionisation, propagation and recombination of the electron in the high harmonic generation process. Since the atomic dipole phase plays a factor in the phase matching equation, experimental parameters can be used to select between phase matching the long or short trajectory components in the HHG process [81]. The form of the atomic dipole phase can be written as:

$$\phi_{atomic}(r, z) \propto -\frac{\alpha_j Up}{\omega_1}, \tag{2.52}$$

  where j defines the trajectory of the proportionality constant, α, dependent on the acceleration time spent in the continuum, Up is the ponderomotive energy and ω_1 is the associated return energy of the electron wavepacket. This particular form has been taken from the review article [96], and the equation is given in atomic units.

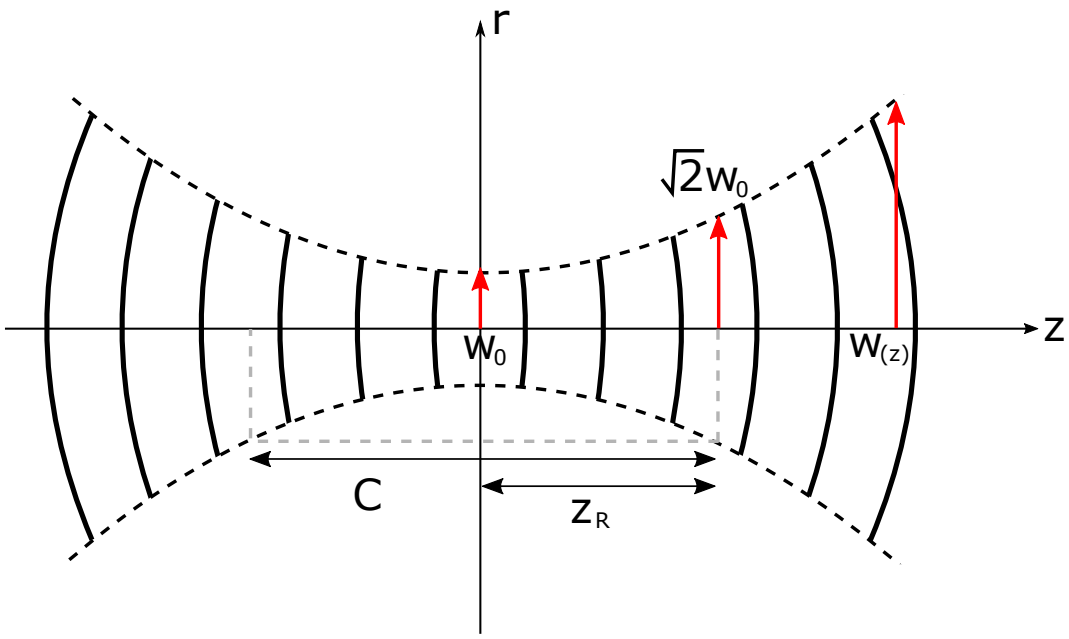


Figure 2.9: Schematic diagram illustrating the Gouy phase through a Gaussian beam focus. As the phase front passes through $z = 0$, the phase front curvature is mirrored indicating a π phase shift at the focus. Positive z indicates the direction of travel of the beam, w_0 is the $1/e^2$ radius of the beam waist, z_R is the Rayleigh range, defining the propagation distance for the beam waist to increase by a factor of $\sqrt{2}$ and consequently the peak intensity to drop by a factor of 2, and C is the confocal parameter, twice the Rayleigh range centred around the beam waist.

- **Phase from the neutral fraction**. This is the phase associated with the non-interacting target emitters.

- **Phase from the ionised fraction**. This is the phase associated with the ionisation fraction of the target. Increasing the ionisation fraction can lead to harmonic saturation and plasma defocusing, for example as explored in reference [97]. The ionisation phase has the opposite sign to the Gouy phase and neutral phase.

The wave vector mismatch associated with the neutral and ionised fraction is related purely to the change in the frequency dependent dispersion associated with different gas densities and ionisation fractions. By balancing the phase associated with each of these effects for a given range of frequencies, coherent build up of signal can be generated throughout the target length.

Overall the phase mismatch terms can be written as [95]:

$$\Delta\mathbf{k}_q = -\Delta\mathbf{k}_{Gouy} + \Delta\mathbf{k}_{Ionisation} - \Delta\mathbf{k}_{Neutral} \pm \Delta\mathbf{k}_{Atomic}. \tag{2.53}$$

By varying different experimental parameters, optimised phase matching can occur for different sets

of trajectories. Practically one can achieve this experimentally by adjusting parameters including: the target backing pressure, the laser peak intensity, the target position relative to the focus and the dimensions and design of the target itself. In fact, it has been shown that modifying the geometry of the focal propagation through the use of capillary targets can increase the harmonic flux by 2-3 orders of magnitude [98]. It is found that positioning the target gas after the focus of the field favours the short trajectory, on-axis generation, whereas positioning the target before the focus leads to better phase matching for the long trajectory, off-axis generation [81].

In addition to phase matching considerations, as a beam propagates through a target length, interaction between the beam and the medium will lead to propagation effects including spectral reshaping [99], and blueshifting of the generated harmonic orders due to the trailing portion of the pulse experiencing a higher ionisation fraction that the beginning of the pulse [100]. A detailed overview of the macroscopic response for high harmonic generation can be found in reference [96].

2.5 Pump-Probe Experiments

Pump-probe experiments are used to extract dynamical information about a system by first preparing the target with the pump pulse into some given state, before a probe pulse extracts information about the time evolved state for a given delay. Strictly speaking, the technique of high harmonic generation itself can be described as a pump-probe experiment, where the 'pump' is the act of ionising the electron wavepacket into the continuum, and the return of the electron wavepacket to the parent ion 'probes' the system for the given delay determined by the chirp of the return trajectory times, recall Figure 2.8. This has been used to study, for example, nuclear dynamics in molecules using the PACER technique [31], however the return times for the different trajectories and hence the interaction window of observation are fixed by the driving laser properties. Isolating the probe delay from the pump timing using separate pump and probe pulses enables precise control over the pump-probe delay, allowing longer duration widows of interaction to be investigated, and removing the requirement for a strong field pump or probe: the pump no longer needs to be sufficiently intense to drive tunnel ionisation. When pump-probe is referred to in the remainder of this thesis, it is assumed that the pump and probe are two separate pulses.

Pump-probe experiments have been used to study both resonant and non-resonant phenomena over a range of dressing field intensities. At the lower intensity end, studies of coherent, resonant phenomena have been investigated, demonstrating effects such as Autler Townes splitting [101, 102] and electromagnetically induced transparency [66, 103]. In general the measurement of light transmitted through a target is known as transient absorption spectroscopy, and by using sufficiently short pump and probe pulses, dynamical information can be resolved about the evolution of the electronic state by scanning the delay between the pump and probe pulses.

If the pump and the probe are derived from the same laser pulse, this ensures an inherent synchronicity between the two pulses [104], allowing for precision control over the pump-probe delay. In this section I will describe two key pump-probe experiments pertinent to the work presented in this thesis: attosecond transient absorption spectroscopy (ATAS) and XUV initiated high harmonic generation (XiHHG). For each of these techniques the basic experimental setup is the same, however differences arise through the applied dressing field intensity, and the understanding of the absorption mechanisms. Although XiHHG was not observed in this work, understanding the XiHHG process helps us to reason its absence.

2.5.1 Attosecond Transient Absorption Spectroscopy

Transient absorption spectroscopy is an all-optical technique to measure dynamical information about a system by recording the transmission of light through the sample. Photons with energies matching available transitions within the target can be absorbed and so by monitoring the transmission for different frequency components, information about available transitions in the sample can be understood. Using a single beam, static information can be gained about a sample, for example as in reference [105], however by including a precise delay controlled second input pulse, one can instead perform pump-probe experiments, accessing dynamical information about the target [18, 106–108].

In attosecond transient absorption spectroscopy (ATAS) the pump pulse is used to excite or ionise the system, and by probing the electronic distribution through absorption of a delayed probe pulse at a series of delay intervals, time dependent changes of the electronic state of the target can be revealed. Using a broadband probe such as an isolated attosecond pulse (IAP) or an attosecond pulse train (APT) allows direct measurement of both above and below ionisation energy (Ip) behaviour to be simultaneously probed [20]. This differs from techniques recording photo-electrons [109], or ion fragments [110].

The versatility of the transient absorption technique makes it particularly powerful. The ability to probe the bound state response in addition to the above ionisation threshold behaviour extends the range of information recorded for a single measurement. The separate pump and probe pulses also enables direct control over the excitation and ionisation timing independent of the dressing field phase, extending the range of interaction that can be probed. If the probe pulse consists of an isolated attosecond pulse, the probing window can extend beyond the laser half-cycle period. In addition to this, the technique of ATAS can be used both at low (perturbative regime) and high (strong field regime) dressing field intensities. When performing ATAS with perturbative dressing fields, information about the coupling between individual bound states can be observed [20, 104, 111–113]. Studies into the effect of varying the transient absorption dressing field polarisation have also been performed for low intensity dressing fields ($\sim 10^{12}\mathrm{W/cm^2}$) [114, 115]. When investigating ATAS using strong dressing field intensities however, resolving individual states becomes impossible.

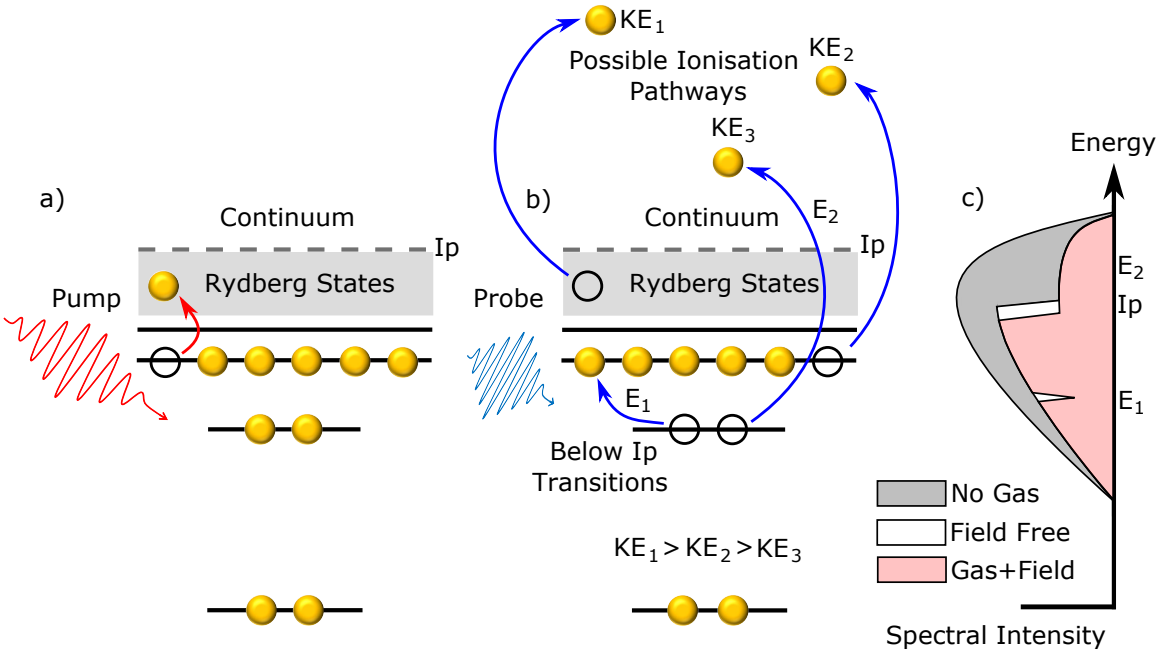


Figure 2.10: Schematic diagram of the principles of attosecond transient absorption spectroscopy. a) The pump pulse prepares the target system, b) the broadband probe excites or ionises the system, and c) the recorded spectrum changes with the addition of target gas and the dressing (pump) field.

A schematic of the technique of ATAS can be seen in Figure 2.10, where example pump and probe steps are shown in a) and b), and c) shows an example spectrum with no target gas, grey, with target gas, white, and with both gas and pump field, pink.

When the target gas is added, the frequency dependent cross section will determine the absorption profile of the probe spectrum, and the target density and length will determine the magnitude of the absorption. When the dressing field is applied, different effects occur that act to shift, split and broaden the bound states of the target. These effects depend on the intensity of the dressing field, and lead to modulations in the recorded delay dependent absorption spectra. The different modulation mechanisms will be described in the following sections.

2.5.2 Modulation Mechanisms

When recording the transmission of a pulse probing a laser dressed system, if transition pathways are available through either single photon or multiphoton absorption, this will result in a reduction in the transmission for that particular frequency. When the delay between the pump and the probe pulses is varied, this will affect the available transition pathways and hence the recorded transmission intensity. Multiple different effects occur in a laser dressed system that result in periodic variation in the transmitted signal, and these will be discussed in the following sections.

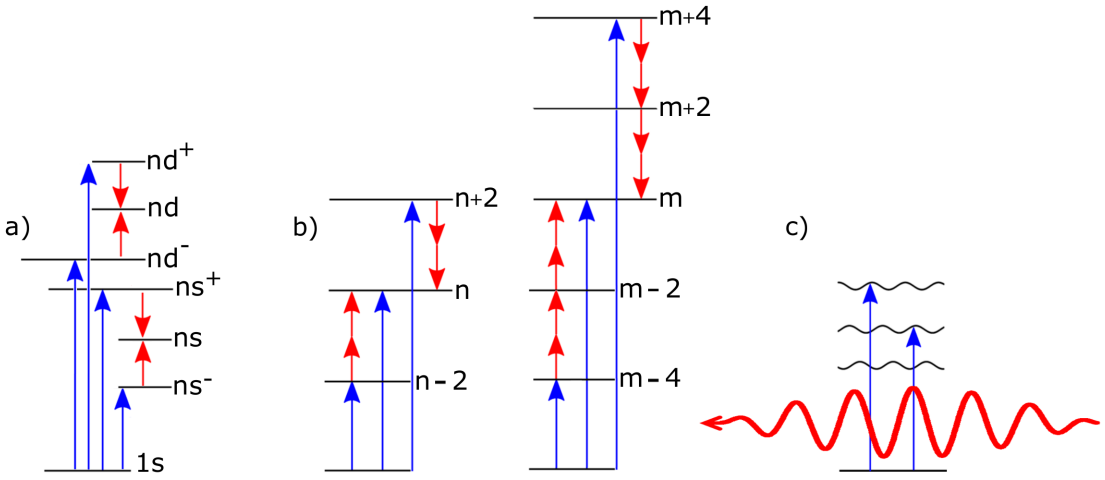


Figure 2.11: Schematic diagram of the mechanisms involved in producing modulation in the detected harmonic signal. a) Light induced states (LIS) appear as previously dipole forbidden transitions become available via multiphoton transition with the addition of the laser dressing field. b) "Which way" interference occurs with transitions via different excitation or ionisation pathways resulting in the same final state. For a discrete harmonic spectrum, coupling between different harmonic orders allows detection of modulations at frequencies equivalent to the number of IR photons difference between the pathways i.e. the n^{th} order harmonic coupling with the $(n-2)^{th}$ order +2IR photon will produce a modulation in the transmission signal at $2\omega_1$. c) AC Stark effect where shifting, splitting and broadening of the bound states occurs in the presence of the intense laser dressing field.

2.5.2.1 Light Induced States

With the inclusion of an additional dressing field, previously dipole forbidden single XUV photon transitions can become available via XUV+nIR multiphoton transitions via virtual states. When probing with an isolated attosecond pulse, modulations are observed in the recorded transmission signal separated by nIR photons from the field-free states. These levels are commonly referred to as virtual states [20] or light induced states (LIS) [114] in the literature, which refer to the laser dressed states of the atom [111, 112].

Cast in another light, the transition via virtual states is very similar to stimulated electronic Raman transitions [116], where the broadband probe covers the necessary frequencies to resonantly excite to a virtual state.

A schematic of the phenomenon of light induced states can be observed in Figure 2.11 a), where the laser dressed states $nd^{+/-}$ and $ns^{+/-}$ are each separated by 1IR photon from their respective field free nd and ns bound levels.

2.5.2.2 "Which Way" Interference

"Which way" interference occurs when excitation or ionisation via two different quantum paths arrive to the same final state and interfere [20, 117, 118]. This results in modulations occurring in the detected delay dependent absorption measurement with frequencies related to the nonlinear

order difference between the quantum paths. An example of this could be the interference between a transition caused by a single n^{th} order harmonic photon, and a $(n-2)^{th}$ order harmonic photon +2IR multi-photon transition to the same state. This would result in a dynamic modulation frequency of $2\omega_1$. Similarly, interference between the m^{th} order harmonic, and a $(m-4)^{th}$ +4IR multi-photon transition would result in a modulation frequency at $4\omega_1$. A schematic illustrating different "which way" interference schemes can be seen in Figure 2.11 b).

2.5.2.3 AC Stark Shift

The Stark shift is the electrical equivalent of the (magnetic) Zeeman effect [119], where energy states of an atom or molecule become split and shifted in energy due to the application of an external electric (magnetic) field. When considering an alternating (AC) electric field, the effect of the AC Stark shift on the energy levels changes depending on the intensity and wavelength of the laser dressing field. First observed in 1969 by Bonch-Bruevich *et al.* [57], for a low frequency dressing field, the response of the system can follow the instantaneous applied electric field [120], adiabatically adjusting the level of the energy states. For higher frequency dressing fields, the general response is no longer instantaneous, and instead the energy levels shift according to the envelope of the dressing electric field [120]. This is known as the dynamic Stark effect.

The nonperturbative, nonresonant dynamic Stark effect shifts both the bound and continuum states in the target [121], modulating also the linewidth of the bound states [122]. The magnitude of the state specific shift results in an intensity dependent variation of the effective ionisation energy [123, 124], increasing for higher intensity fields. This arises since the most tightly bound states are affected less by the intense dressing field than the outer states, reducing the effective Stark shift for these inner states [124]. For the loosely bound Rydberg levels, the shift in energy due to the Stark effect is given approximately by the cycle-averaged energy a free electron would gain oscillating in the intense dressing field, the ponderomotive energy, Up [124].

Since the more tightly bound states shift less in energy than the outer states, this leads to a shift of the relative energy spacing between different electronic states [125]. This can lead to a de-tuning of pump-probe resonant effects, or a shifting of previously nonresonant transitions into resonance [121, 124]. In addition, this also means that the ionisation energy of a dressed atom is always larger than the field free case [123].

When probed with sufficient temporal resolution, instantaneous response of the bound electronic states can be observed through sub-cycle modulation in the transient absorption of an isolated attosecond pulse [122]. This modulation appears in addition to the intensity dependent cycle averaged shift, and constitutes one of the mechanisms for generating sub-cycle modulation in the transient absorption experiments.

Much theoretical and experimental work has been undertaken investigating the dynamic Stark

effect, and more information can be found in the references (and references therein) already cited. As the dressing field intensity increases, the splitting, shifting and mixing of the bound states leads to a breakdown of the conventional dressed atom picture. In this regime describing transitions between states using a multiphoton picture is no longer feasible [123].

2.5.3 XUV initiated High harmonic Generation

XUV initiated High harmonic Generation (XiHHG) extends the standard HHG process by decoupling the steps of ionisation and acceleration. Through the use of a separate, high photon energy pump pulse such as a broadband APT of IAP, one can ionise the target through SPI, with the acceleration and recombination completed, as before, with the probing IR field [19, 126, 127], see Figure 2.12 a). The experimental setup for XiHHG is the same as for ATAS, however XiHHG experiments require high dressing field intensities (for example $5{\times}10^{13}\mathrm{W/cm^2}$ [19]), to ensure the ionised electron wavepacket can be returned to the parent ion. At the higher dressing field intensities, observed modulations in the recorded transmission can no longer be described using simple multiphoton transitions, and instead a field-picture for the interaction is used, similar to that used to describe the HHG 3-step model. A schematic of the multiphoton and field pictures can be seen in Figure 2.12 b) and c) respectively.

The use of SPI as the pump step allows direct access to core and inner valence electronic states which would otherwise be inaccessible through the standard HHG process. This is because SPI is a linear process and so ionisation will occur even for very weak pump fields. If a tightly bound state were to be ionised through the highly nonlinear process of tunnel ionisation, very strong field intensities would be required. With lower intensity pump and probe fields, distortion to the electronic structure of the target is reduced.

Another difference to the standard HHG picture is that due to the separate pump and probe pulses with controllable delay, ionisation can occur at any point within the phase of the probe field. The tunnel ionisation rate for standard HHG is highly dependent on the size of the potential barrier, equation 2.22, and as such the majority of the ionisation occurs around the peak of the laser field. This limit does not apply for single photon ionisation where ionisation can occur at all points within the dressing field laser cycle. By controlling the delay between the pump and probe pulses, one can effectively control when in the cycle the ionisation occurs, and both “uphill” and “downhill” trajectory components can be launched [128]. This is important since the probability of return for the “very-short” trajectories presented in reference [128] is significantly higher than for the standard short and long trajectories we normally observe. The “very-short” trajectories are understood to originate through ionisation of the electron at a phase of the probe field where the electron is driven straight back into the parent ion. The length of time spent by the “very-short” trajectories in the continuum is therefore small, resulting in very little wavepacket spreading and a higher probability

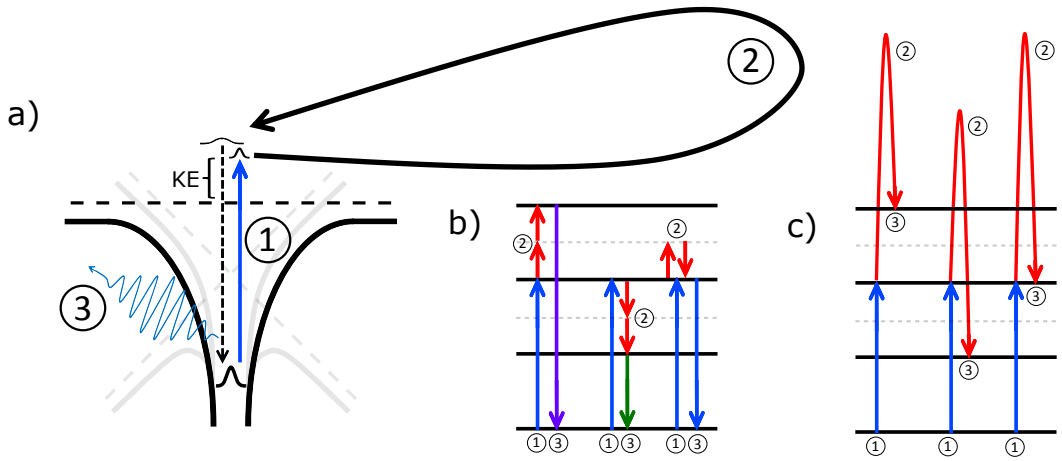


Figure 2.12: a) Schematic diagram of the technique of XUV initiated high harmonic generation. The electron is ionised by a single, high energy photon into the continuum: step 1. The probe field accelerates the electron wavepacket in the continuum: step 2, before the possibility for recombination with the emission of a high-energy photon: step 3. b) and c) depict the multiphoton and field pictures associated with ATAS and XiHHG schemes respectively.

of recombination and emission. Although the energy gained accelerating in the continuum is also small, for a long wavelength probe field, these "very-short" trajectories could play a significant role in any XiHHG process.

If we recall from equation 2.12, an electron ionised through SPI will be born into the continuum with an energy equal to the energy of the XUV photon minus the IP of the electron. For this reason, electrons ionised in the XiHHG process will not be born into the continuum with zero kinetic energy. Therefore there will only be a certain window of energies for which the probing IR field will be able to return an ionised continuum electron to the parent ion for recombination and emission of an XUV photon, leading to a level of probe selectivity.

To detect an XiHHG signature, the recorded spectral intensity following transmission through the target must be enhanced relative to the input spectrum. Due to the levels of absorption of the input light in the target, to observe an XiHHG signature for a harmonic order present in the original pump spectrum, one would need to generate sufficient XiHHG photons to more than compensate for the level of initial absorption in the target gas to observe enhancement. Instead, if one can produce photons at a frequency not present in the initial input spectrum, any detected signal will be evidence of XiHHG, and the recorded signal will be on a zero background [19].

Chapter 3

Ultrafast Light Sources: Generation and Characterisation

Different types of ultrafast light source exist, ranging from simple femtosecond pulse length table-top laser systems, that can be used in isolation, or amplified to millijoules of energy per pulse, to flexible, fiber lasers, offering compact designs and high output power and beam quality. Another technique for generating ultrashort pulses is through multi-kilometer length research facilities such as the linear coherent light source (LCLS) free electron laser (FEL) in California, USA, producing high brilliance, soft and hard x-rays through the entirely different mechanism of electron bunch acceleration [129]. Although FELs can produce x-ray pulse intensities many orders of magnitude greater than typical high harmonic generation based table-top systems [130], at the present, pulse durations are limited to around a few femtoseconds duration [131]. Different techniques exist to perform pump-probe experiments with FELs [132, 133], including the ability to create two different pulse energies [134]. Despite this, the current limitations on the pulse duration prevent this technique from competing with high harmonic generation in the sub-femtosecond regime. In addition the cost of such large scale facilities requires enormous investment, resulting in only a handful of FELs in existence around the world. Acquiring time on one of these facilities requires the submission of a successful application, so beamtime is often short and infrequent.

The mechanism for x-ray production in FELs also introduces its own unique problems when considering pump-probe experiments, where due to the stochastic nature of the generation process, significant temporal and energy jitter can occur between the pump and probe pulses. Without precision control between the pump and probe pulses, as can be achieved using HHG based x-ray pulse generation systems derived from the same input laser pulse, each individual laser shot must be characterised and sorted post acquisition [135]. This results in very large data files requiring huge amounts of data processing to extract results.

During my PhD I took part in two different campaigns at the LCLS FEL facility [136,137], related to the work presented in this thesis through the pump-probe nature of the underlying experiments. The everyday accessibility, affordability and, at the present time, the achievable pulse durations of HHG based table-top laser systems however makes this the ultrafast x-ray production method of choice for the work presented in this thesis. Therefore in the remainder of this section I will concentrate on laser systems used to generate HHG.

In this Chapter I will describe in detail the lasers used to perform the experiments presented in this thesis. I will cover the basic requirements that must be met to achieve a state of lasing, as well as the techniques that are employed to produce high power, short pulsed lasers required to perform ultrafast pump-probe transient absorption experiments. I will finish the Chapter describing the methods used to characterise the ultrashort pulses used to perform the experiments in this work.

3.1 Laser Basics

Lasers are optical devices based on the phenomenon of amplified stimulated emission. They can demonstrate many desirable characteristics including high flux, high directionality and high coherence. The frequency of the light emitted by a laser is defined by the energy of the lasing transition, and depending on the design of the laser, the output can range from essentially monochromatic to broadband. For continuous lasing to occur three main criteria must be met:

1 There must be an amplifying medium that can reach a state of population inversion. Population inversion occurs when there are more electrons in the upper electronic state of the lasing transition than in the lower level. When population inversion is maintained, gain is enabled in the system, and light can be amplified.

2 There must be some mechanism for pumping energy into the amplifying medium to cause the population inversion. For high-power, short-pulse lasers like those used in this work, this is usually achieved with a continuous (CW), or pulsed, high power pump laser tuned to excite electrons from the ground state into a energetically close state to the upper lasing transition level. Considering the process using a simplified 4-level system, see Figure 3.1, fast decay of this excited state ($|2\rangle$), usually via non-radiative means to the longer lived upper lasing level, $|l_2\rangle$, enables population inversion to be quickly achieved and easily maintained. Ensuring the lower lasing state ($|l_1\rangle$) quickly decays back to the ground level, $|1\rangle$, population inversion can be achieved with just a single exciting photon to the upper lasing state. In real systems, the process is more complex but follows the same principles.

3 The pumped amplifying medium must be enclosed by some sort of reflective cavity to provide optical feedback, allowing for sufficient build-up of signal to occur to enable stable lasing. The

cavity usually includes two concave mirrors, focussing the light back and forth into the gain medium, increasing the gain with each pass until saturation. By ensuring one of the cavity mirrors is less than 100% reflective, a portion of the light can be coupled out of the system. This setup is commonly known as an oscillator and forms the first stage of any ultrafast laser system.

The initial lasing process usually starts through spontaneous emission of a photon from the upper to the lower lasing level. As this photon is resonant with the lasing transition, when it passes back through the gain medium it can cause stimulated emission from the population inverted system. This results in the release of a further identical photon, whose electric field is in phase with the stimulating photon. Again each of these photons can repeat the process, and quickly a high flux of identical photons is built up, giving rise to the many desirable properties characteristic of laser emission mentioned above.

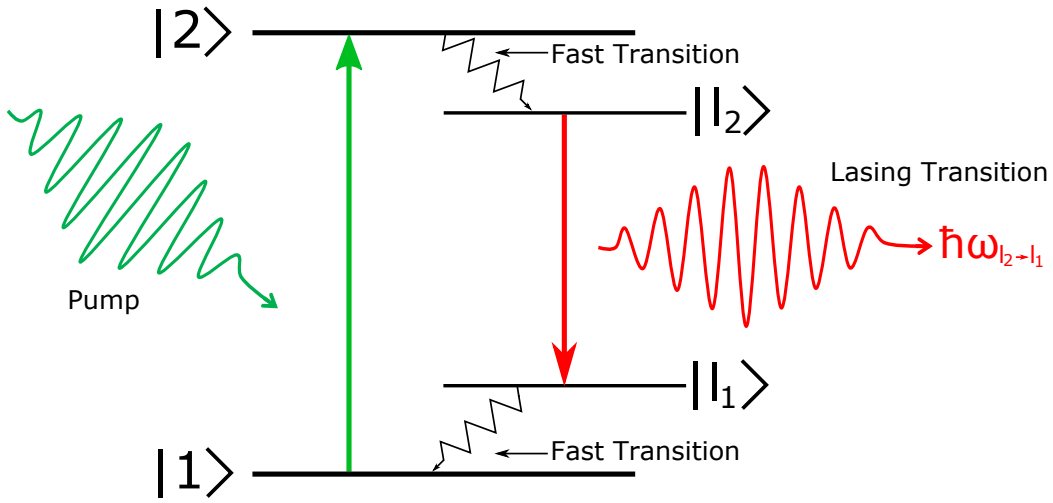


Figure 3.1: Schematic diagram of a simplified four-level system illustrating the key components required for efficient lasing to occur.

Due to the profile of the amplification medium gain response curve, successive passes through the medium can lead to a reduction in bandwidth as the central frequencies within the profile are amplified by a greater amount each pass compared with frequencies at the edges. Care must be taken to minimise this effect, ensuring sufficient bandwidth remains to support the short duration output pulses, as well as preventing damage to optics within the laser system. Both of these effects are discussed later in this Chapter.

3.2 Femtosecond Light Sources

Many different types of lasers exist, amplifying light using a variety of different gain media, in gaseous [138, 139], liquid [140] and solid [8, 12, 141, 142] phase. The specific characteristics required for the output will determine what type of laser will be used, for example: the wavelength, achievable peak power and pulse duration will all be specified by the selected gain medium of the laser.

In the field of ultrafast spectroscopy it is important that the driving laser can produce high energy, short pulses to initiate and probe the resultant dynamics. This means that the gain medium must support a broad bandwidth to achieve the correspondingly short temporal duration pulse. In addition one must be able to extract sufficient energy from the gain medium to produce high power pulses, either through efficient conversion, or hard pumping of the gain medium (or both).

In 1982 the Titanium-doped Sapphire (Ti:Sapph) laser was first presented [143], redefining the limits for short pulse generation. The Ti:Sapph (Ti^{3+}:Al_2O_3) crystal supports the broad emission bandwidth necessary for short pulse generation, and also displays many other desirable characteristics. The broad, conveniently situated absorption bandwidth of the Ti:Sapph crystal enables efficient pumping using common, high power, frequency doubled Nd:YAG or Nd:YLF pump lasers centred at 532 nm and 527 nm respectively. This well established technology can deposit high energy loads into the Ti:Sapph crystal, maintaining population inversion and producing a high amplification gain leading to higher pulse powers. The broad fluorescence bandwidth also enables scope for tuning the central output wavelength of the Ti:Sapph [12, 144]. To compliment its spectral qualities, the Ti:Sapph crystal has good thermal conductivity [144] enabling heat deposited by the pump lasers to be efficiently removed, allowing for harder pumping and higher gain. For these reasons a large quantity of modern ultrafast research has been undertaken using Ti:Sapph lasers in some form. The absorption and emission spectra for the Ti:Sapph laser can be seen in Figure 3.2 [144].

The laser used to undertake the experiments produced in this thesis exploits a Ti:Sapph crystal in each stage of the amplification process to produce the high energy, short pulsed output.

3.2.1 Modelocking

To achieve a high power, short pulsed laser output, the oscillator must operate under modelocking. The technique of modelocking, and how it is achieved is described in this section below.

In theory, an oscillator cavity could support an infinite number of longitudinal modes, however given there is only a limited range of frequencies within the fluorescence window of any gain medium, this will determine the maximum range of cavity modes supported by the oscillator. The range of frequencies comprising a laser pulse is known as the bandwidth, $\Delta\omega$. If there is no phase relationship maintained between the different cavity modes, constructive and destructive interference occurs between the interfering EM radiation across the length of the the cavity round trip path length

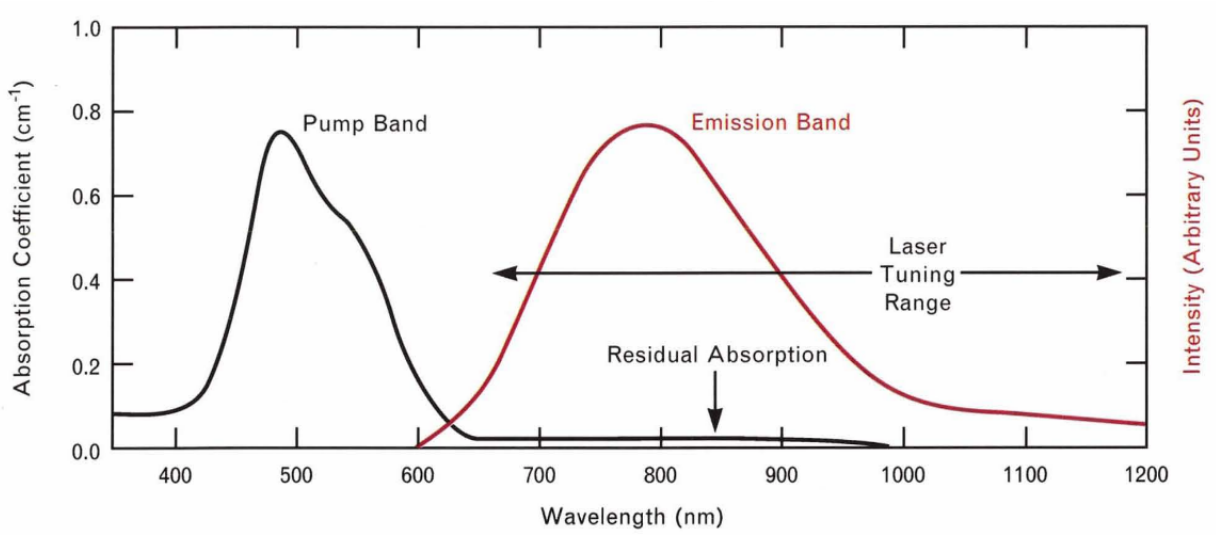


Figure 3.2: Absorption and emission spectra for Ti:Sapph laser [144]. Reprinted with permission courtesy of MIT Lincoln Laboratory, Lexington, Massachusetts.

leading to a continuous, averaged output intensity known as continuous wave (CW) operation.

As an example, 6 theoretical cavity modes are shown in Figure 3.3 a) and b), where the modes are randomly phased with respect to each other in a), and have a fixed phase relationship in b). The resultant electric field amplitude for each set of cavity modes can also be seen in Figure 3.3 c) and d). By forcing the cavity modes to have a fixed phase relation, i.e. all the cavity modes interfere constructively for a single point in space-time ($\phi_n = \phi$), much higher peak powers can be achieved as the energy is concentrated into short pulses of light occurring once every round trip of the laser cavity. The destructive interference between the instances of constructive overlap effectively suppress the signal output between the pulses. This effect is enhanced for a larger number of contributing modes, N, and results in a narrower temporal pulse duration and increased discrimination between the constructive peak and suppressed, destructive interference. Fixing the phase relation of the cavity modes in this way is known as modelocking (ML), and lasers employing this technique are known as modelocked lasers.

Since intensity is proportional to the square of the electric field, mathematically we can write this as:

$$I_{CW} \propto \left| \sum_{n=1}^{N} E_n e^{i(n\omega_0 t + \phi_n)} \right|^2, \tag{3.1}$$

where I_{CW} is the intensity of the CW output, n are the supported cavity modes of which there are N in total, ω_0 is the central frequency of the fundamental mode in the cavity, E_n and ϕ_n are respectively the electric field amplitude of the n^{th} order mode and random phase associated with the n^{th} order mode. Because of the fixed phase relation, for ML lasers the intensity will depend on N^2.

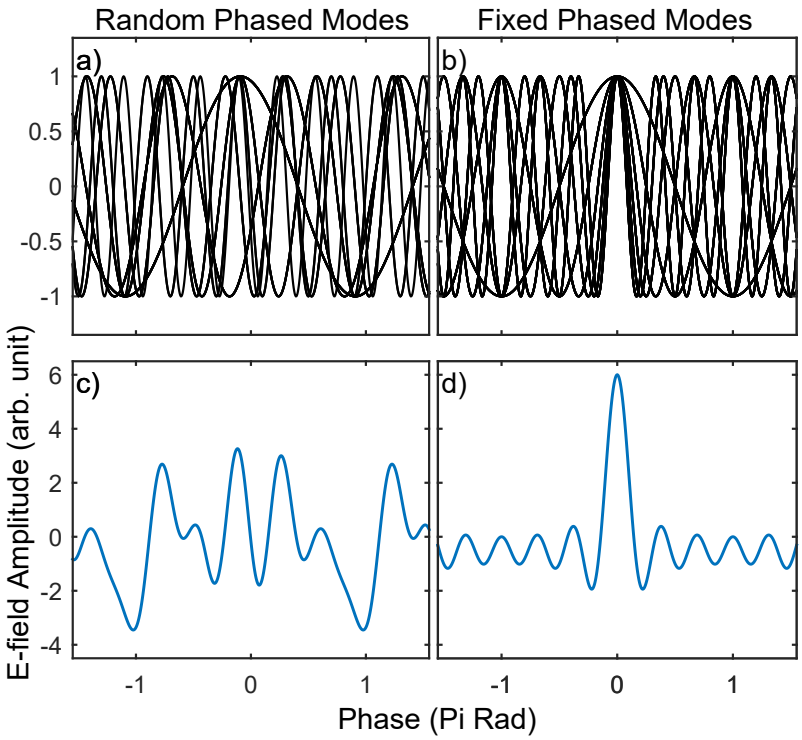


Figure 3.3: Illustration of the technique of modelocking. A selection of 6 possible cavity modes are shown with random phase, a), and with fixed phase, b). The corresponding sum of the individual random phase and fixed phase modes are shown in c) and d) respectively.

3.2.1.1 Modelocking Methods

The state of modelocking can be achieved via different methods. Broadly these can be categorised into two groups: active and passive. Active methods include, for example, the use of an acousto-optical modulator (AOM) [11]. AOMs can be used to actively modulate the amplitude and phase of the cavity light, periodically modifying the cavity losses to produce a pulsed output. Careful matching of the modulation period must be maintained for this technique, and the requirement for active input renders the active modelocking methods often less attractive than their passive counterparts. Passive modelocking instead exploits the natural physics and geometry of the setup to provide a pulsed output.

The technique employed in the oscillator for the Red Dragon laser system (see Figure 3.6) uses Kerr-lens passive modelocking in the Ti:Sapph crystal to produce a pulsed result. By focusing the Verdi pump beam to illuminate just the central fraction of the seed light in the Ti:Sapph crystal, for each round trip, only the brightest, central, on-axis seed modes are amplified. The spatial restriction limits the off-axis amplified mode variation and maintains a well-defined phase relationship between the amplified frequencies. The resulting amplified bandwidth therefore interferes constructively only

for a single point within the oscillator. As the light bounces back and forth within the oscillator cavity, a pulse is produced at a frequency related to the round trip path length of the oscillator. The produced pulse frequency, f, can be determined using the equation:

$$f = \frac{c}{2L} \tag{3.2}$$

where c is the speed of light, and $2L$ is the round-trip path length of the oscillator cavity.

Similar passive modelocking can alternatively be achieved by placing a hard aperture into the optical cavity, blocking the outer parts of the seed light. Caution must always be exercised when placing any hard aperture into a high power optical system however due to the possibility of diffraction and interference induced optical damage occurring. Soft aperturing using the pump beam as a natural smooth window is therefore often preferable.

In general, a lasing oscillator will require a sharp change in the lasing conditions to force it to modelock. To ensure stability in the system, positive discrimination must be maintained between the output power when modelocking compared with in CW operation. To achieve modelocking in the Red Dragon laser system oscillator, we quickly jolt one of the prisms in the prism pair, see Figure 3.6, to disrupt the lasing output. Assuming the oscillator conditions are correctly optimised, modelocked oscillation is energetically favourable and the oscillator proceeds with a pulsed output.

The technique of modelocking was theorised by Lamb in 1964 [145], and demonstrated experimentally later that year by Hargrove *et al.* [11], who actively modelocked a 633 nm helium neon laser using a periodically modulated fused quartz block. Producing a pulsed laser output through modelocking has been a key development in the production of high intensity laser pulses required for the study of ultrafast electron dynamics.

3.2.2 Chirped Pulse Amplification

By the 1980s improvements to the attainable laser pulse intensity had plateaued, recall Figure 1.2 [14], limited by the damage threshold of the optics used. To overcome this limit, Strickland and Mourou devised a method in 1985 to safely amplify pulses to higher peak intensities [13]. This technique stretches the broadband pulse in time as a function of frequency before amplification, lowering the pulse peak intensity by spreading the total energy over a longer pulse duration. Amplification of the stretched pulse can be performed to similar below damage threshold peak intensities as before. The total energy in the temporally stretched pulse now, however, is much larger. Upon re-compression of the stretched, amplified pulse, much higher peak intensities can be achieved as the total energy is concentrated back into the short duration pulse.

This technique exploits the phenomenon of dispersion to spatially separate the different frequency components comprising the broadband pulse, forcing them to travel along different length paths.

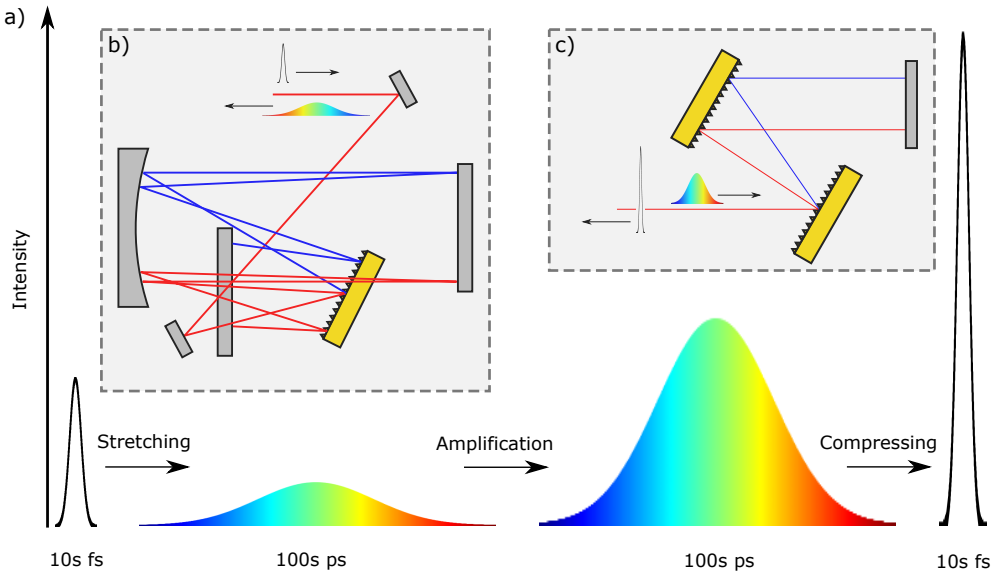


Figure 3.4: Schematic diagram of the technique of chirped pulse amplification (CPA). The effect on the pulse chirp and duration can be seen in a), with schematic diagrams of the stretcher and compressor used in the laboratory illustrated in b) and c) respectively. In both b) and c) the return pulse is offset in height as compared with the input pulse.

Incorporating the dispersive optics into particular geometries translates the spatial separation into a temporal separation, spreading the pulse in time as a function of wavelength. This can be achieved using prisms, or more commonly for short pulses, a reflective diffraction grating. The frequency dependent temporal spreading of the pulse is known as a chirp, and as such this technique was named chirped-pulse amplification (CPA). Typically pulses can be stretched by up to 10^3 times or more in duration before the amplification stage, leading to gains in peak intensity of many orders of magnitude. A schematic of the CPA technique can be seen in Figure 3.4.

3.2.3 The KM Labs Red Dragon

The laser used for the work presented in this thesis is a KM Labs Red Dragon, two stage amplified Ti:Sapph system. The whole setup consists of three stages: the oscillator which generates the seed light, and two amplification stages to increase the peak pulse energy. The pulses produced in the oscillator are referred to as the seed or seeding light since when resonant photons of particular characteristics are injected into a population inverted system, the amplification will no longer be centred around a stochastic spontaneous emission process. Instead the seed light properties will dominate the amplification. A schematic overview of the laser system can be seen in Figure 3.5, indicating the order and specifics of the different stages, along with the position and details of the subsidiary pump lasers. An overview of each laser stage can be found in the sections below.

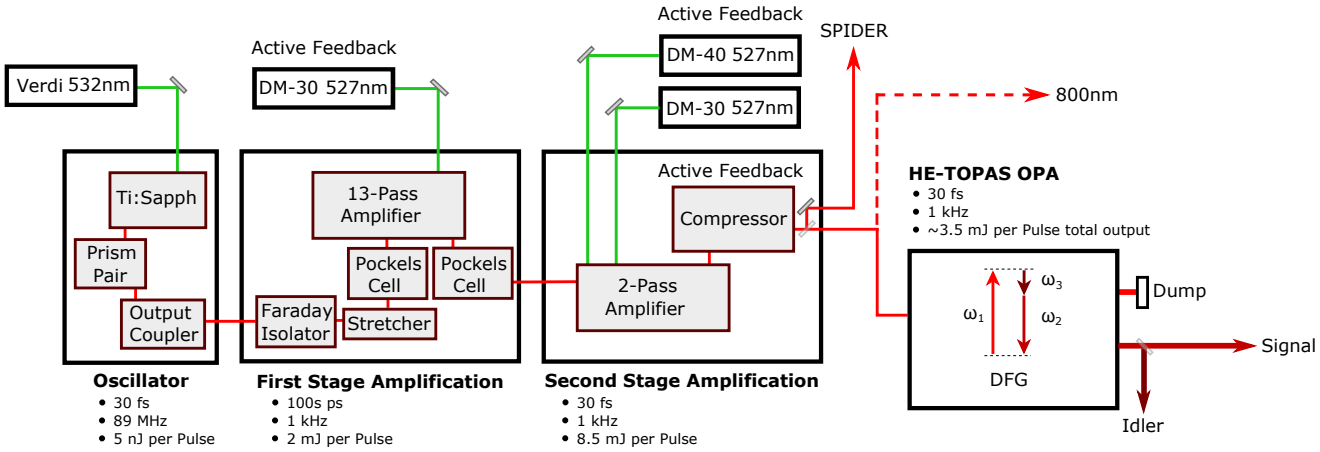


Figure 3.5: Schematic diagram of the Red Dragon laser set-up, and associated additional lasers.

3.2.3.1 The Oscillator

The oscillator is the first stage of any ultrafast laser system. This is the point where laser pulses are first produced, and the output forms the seed for the amplification stages that follow. The oscillator we use is a KM Labs Griffin, and is typical of many ultrafast laser systems, containing several important components that allow tunability and stability of the output to be maintained. A schematic of the oscillator used in the laboratory can be seen in Figure 3.6.

A lens focuses the 5.4 W Coherent Verdi frequency doubled ND:YAG pump laser into the Ti:Sapph amplification crystal. Two focusing mirrors enclose the crystal, focusing the generated light back down for each round trip of the light in the cavity. The extended cavity provides a mechanism to pass the light many times back and forth to increase the gain. Within the cavity length, a linearly adjustable prism pair enable control over the group velocity dispersion introduced by the amplification crystal, in addition to providing a level of control over the output central frequency and bandwidth of the seed pulse. The extended cavity mirrors define the cavity path length, and consequently the pulsed repetition rate when the laser is modelocked. The partial transmission of the output coupler allows a portion of the seed light to escape the oscillator and go on to be amplified in the remaining stages of the Red Dragon laser system.

The typical output power of the oscillator is 400 mW in continuous wave (CW) operation, rising to 430 mW when modelocked (ML). The cavity path length is approximately 1.7m leading to a repetition rate around 89MHz when modelocked. This results in a typical energy of 5nJ per pulse, with bandwidth of the order of 50 nm. As with all oscillators, it is common that a compromise must be made between power, bandwidth and stability, where often two of these three requirements for stable, high quality lasing are easily achieved, though compromise is required for the third.

Since the oscillator provides the seed beam that is amplified throughout the remainder of the laser system, the temporal and spatial qualities of the beam are of utmost importance. Furthermore,

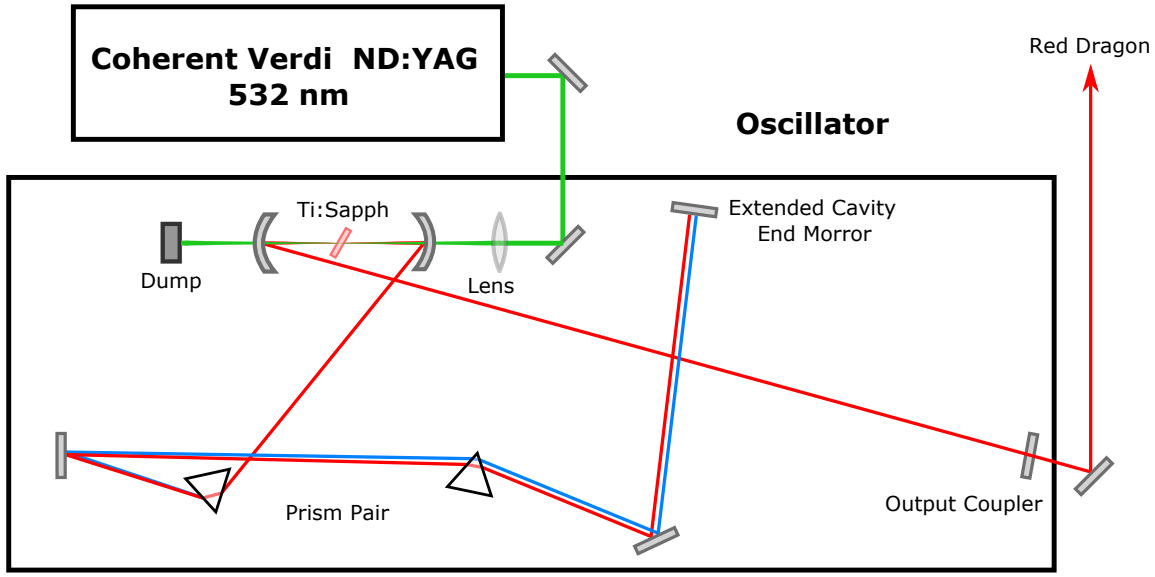


Figure 3.6: Schematic drawing of the Oscillator set-up.

to ensure gain saturation in the following amplification stages, sufficient power must also be achieved from the oscillator. To prevent risking significant damage to the optics within the laser system, it is important that the bandwidth of the modelocked system is maintained above approximately 45 nm. This enables sufficient frequency dependent temporal stretching to be applied to the pulse prior to amplification (recall Chirped Pulse Amplification section), maintaining the peak pulse energy below the damage threshold of the optics. For all of these reasons it is clear that a good quality oscillator pulse is of vital importance to achieving a good quality laser output, and much time and care must be spent ensuring all the requirements are met before proceeding to the amplification stages.

3.2.3.2 The First Stage Amplification

The seed pulse enters the first stage of amplification, passing initially through a Faraday isolator to prevent any back reflections and minimise any amplified spontaneous emission (ASE) from re-entering the oscillator. The seed is temporally stretched from 30 fs to a few hundred picoseconds using a double-pass grating stretcher prior to amplification, see Figure 3.4 b). The resultant beam propagates through a Pockels cell voltage controlled waveplate and polariser which acts as a pulse-picker, reducing the repetition rate down to 1kHz. This is the frequency at which the pump lasers operate. Finally the reduced repetition rate seed enters the first amplification stage: a 13-pass butterfly design, with each successive pass fractionally offset from the previous on the ring cavity mirrors. The foci of each of the passes overlap with the focused pump beam at the amplification crystal.

The Ti:Sapph amplification crystal is cryogenically cooled for efficient heat removal. It is pumped using a Photonics Industries DM-30, frequency doubled Nd:YLF laser, with central wavelength of 527 nm. A notch filter placed inside the ring path minimises bandwidth narrowing during amplification. The filter interrupts the path of the first four passes, and possesses a transmission spectrum approximately inverse to the amplification gain curve of the Ti:Sapph crystal. This actively reduces the enhanced amplification of the central gain curve frequencies, maintaining a broad bandwidth pulse, and consequently the ability to produce short temporal duration pulses. A mask is used to aid the alignment procedure, ensuring even spatial separation of each of the ring passes, and improve the quality of the beam by aperturing the edges. Following the final pass, the beam is picked off and sent to a further Pockels cell and polariser to remove any pre- or post-pulses that could have been amplified. Typical pulse energies at the exit to the first amplification stage are 2 mJ per pulse.

3.2.3.3 The Second Stage Amplification

The second amplification stage consists of a two-pass bow-tie arrangement where a further cryogenically cooled Ti:Sapph amplification crystal is pumped using both a Photonics Industries DM-30 frequency doubled Nd:YLF laser, similar to that for stage one, and a DM-40 frequency doubled Nd:YLF laser, with central wavelength 527 nm. The gain achieved in stage two pushes the pre-compression pulse energy up to 14 mJ per pulse. A grating compressor to compensate the stretcher in amplification stage 1 temporally compresses the stretched pulse back down to 30 fs, achieving typical pulse energies at the output of the laser system of around 8.5 mJ per pulse. A schematic diagram of the compressor can be seen in Figure 3.4 c).

This beam can be used as produced to perform experiments such as those presented in Chapter 5 with an 800 nm field, or alternatively it can be used to drive a Light Conversion HE-TOPAS optical parametric amplifier (OPA), down converting the high intensity 800 nm light into two lower photon energy beams. Either of the higher or lower photon energy beams, known as the signal and idler respectively, can be used for experiments. Examples of using the TOPAS OPA signal 1400 nm wavelength field can be found in Chapter 6.

Maintaining a good spatial beam quality at the output of the Red Dragon laser system is often as important as ensuring high output power. In addition, ensuring good stability of both temporal and spatial properties of the beam profile is paramount. This is particularly applicable when using the Red Dragon to pump the TOPAS OPA, where any small changes in the driving laser will be amplified through the nonlinear OPA process. Active feedback for the Red Dragon pump laser currents and compressor grating linear position are therefore employed to try to minimise any long-term fluctuations in the system arising through thermal drifts and daily evolutions of the laser conditions. The feedback systems were implemented by Dr Dane Austin. The feedback for the pump laser current adjustment is obtained using photodiodes situated at the exit of each of the

amplification stages. Monitoring the amplitude of the output light from a pickoff in each stage, the pump laser currents can be adjusted automatically to maintain a constant power level. Similarly, by monitoring the pulse duration using a SPIDER (see SPIDER section later on in this Chapter), if the measured pulse duration falls outside a certain range, the compressor grating linear position is automatically adjusted to correct for the drift.

With these feedback mechanisms in place, the stability of the Red Dragon, and by extension the TOPAS output, is improved.

3.2.4 Optical Parametric Processes

For a process to be parametric, the medium with which the optical field interacts must remain in the same quantum state, that is to say no overall energy, momentum or angular momentum can be transferred from the field to the material during the interaction. Optical parametric processes include sum frequency generation, (SFG), and difference frequency generation, (DFG), where DFG can be thought of as the inverse process of SFG. In SFG, two low energy photons can combine to produce a single, high energy photon, of total energy equivalent to the sum of the two constituent photons. A common, special example of SFG is second order generation, where two identical ω photons add to produce a single output photon of frequency 2ω. As standard, however, SFG and DFG do not require the constituent photons to be identical. When adding two photons of known energy, it is clear what the sum total will be. When dividing a single photon in to two lower energy photons however, in theory there are an infinite number of possibilities for the division. Depending on the particular phase matching conditions for the DFG process, the energy splitting will be favoured for a particular ratio. This ratio can be strengthened by seeding the process with one of the desired output wavelengths. SFG is commonly referred to as 'up-converting' the light, whereas DFG is commonly referred to as 'down-conversion'.

3.2.4.1 The TOPAS

The HE-TOPAS is a three-stage optical parametric amplifier (OPA), down-converting the input 800 nm light into two, lower energy beams, prior to amplification. The system is both pumped and seeded through a single input, splitting portions of the input energy to form the seed and the pump beams for each amplification stage. The TOPAS is optimised for an input power of 8 W from the Red Dragon laser, and operates considerably worse for lower input powers. Maintaining a steady 8 mJ per pulse input is therefore paramount for ensuring a high degree of TOPAS output stability.

Initially, the input beam is divided using a beamsplitter, directing over 90% of the input energy to form the pump beam for the final amplification stage. The remaining portion is divided twice further to create the pump beams for stage 2 and stage 1 amplification, with the remainder forming the seed light for the OPA process. For each splitting, up to 80% or more of the remaining energy is

channelled to form the various pump beams. In each stage of the TOPAS, a motorised amplification crystal and delay stage allow fine control over the amplification process. The temporal overlap of the pump and seed pulses can be adjusted by controlling the delay stage settings, and the angle of the amplification crystal will influence the phase matching of the amplification process.

In the first stage of the TOPAS, the remaining seed light is focused into a sapphire plate generating a stable white light continuum. A dispersive plate spreads the different frequencies in time, chirping the pulse and allowing the selected wavelength to be amplified through fine control over the delay between the pump and seed pulses in the amplification crystal. The angle of amplification crystal 1 is set to maximise phase matching for the selected signal output wavelength. The pump and seed beams propagate noncollinearly, overlapping at the focus, but enabling the removal of the residual pump, idler and other sum-frequency and difference-frequency wavelength components using a precisely positioned block. The angle of the different energy components is not the same due to the addition of the different k-vectors used to form each output frequency.

Following this, the signal wavelength seed is focused onto the second amplification crystal where it is overlapped collinearly by the second stage focused pump. Again, the delay of the pump can be adjusted to match the arrival time of the seed pulse. The rotation angle of crystal 2 is again set to maximise the phase matching of the signal wavelength. Since the seed and pump are now collinear, the signal and idler propagate collinearly towards the amplification stage 3. A dichroic mirror is used to remove the co-propagating residual pump.

A further dispersive plate separates the signal and idler wavelengths in time, allowing either of these pulses to be amplified in the final stage. The selection of the stage 3 pump delay determines this. Again amplification crystal 3 is set to maximise phase matching for the particular conditions. The pump and seed enter the final amplification crystal collinearly, resulting again in a collinear output containing signal and idler wavelength components, as well as residual pump, and many other low power sum frequency and difference frequency components of the amplified wavelengths. The residual 800 nm pump is filtered from the beam using a further dichroic mirror, and exits the TOPAS box separately into a beam dump.

The final output energy is typically as high as 3.5 mJ for the combined signal and idler pulses, with a fairly even split in power obtained between the two. Using a dichroic separator at the exit of the TOPAS box, the collinearly propagating signal and idler beams can be separated, and each can be used simultaneously. For all the TOPAS results presented in this thesis, the signal beam was transmitted through the dichroic mirror, with the idler beam reflecting. All of the experiments using the TOPAS presented in Chapters 5 and 6 of this thesis have been performed using the signal output, tuned each time to approximately 1400 nm. The output pulse length of the TOPAS is similar to that of the Red Dragon, around 30 fs.

3.2.4.2 TOPAS Stability

The necessity for high stability throughout the laser system to produce a good quality laser output has already been discussed. An additional demand on the stability requirements, however, is made through the method employed to divide the input beam in the generation chamber (see Figure 4.1), creating the separate pump and probe pulses to perform time-resolved ultrafast transient absorption experiments. By spatially separating the beam profile using a 45° annular drilled mirror, any small non-uniform change in the beam power or spatial profile will disproportionately affect the pump and probe pulses. Alternative splitting methods such as using a beamsplitter would minimise the effect of many of the beam profile fluctuations since changes would occur proportionately for each beam path. To maintain versatility of the setup, and minimise pump power losses upon recombination, the annular mirror spatial separation method was used. More details on the beamline setup can be found in The Beamline section in Chapter 4.

The overall quality of the TOPAS signal beam profile is poor, exacerbating the instabilities and problems with the day-to-day reproducibility of the spatial splitting by the generation chamber entrance annular mirror. To understand this better, we investigated the effect of fractionally changing the TOPAS internal stage 3 delay setting whilst monitoring the splitting ratio between the light forming the pump and probe beams. By doing this we wanted to better understand the sensitivity and limitations of the current system.

The ratio of light in each beam was measured directly after the dividing annular mirror in the generation experimental chamber (see Figure 4.1). With the chamber at atmospheric pressure, we placed a power meter in each arm and adjusted the setting of delay 3 in the TOPAS. The units of delay 3 are steps, where nominally 1 step is equivalent to 200 nm, or 0.67 fs delay. For scale, it was typical that the peak power measured in the signal beam could be convincingly determined within approximately 15 steps of delay 3. Since delay 3 does not greatly affect the wavelength selection for the ultimate TOPAS output, the usual daily procedure would be to optimise delay 3 for maximum output power. We wanted to test what effect this daily, and often sub-daily change of a few steps in the delay 3 setting actually meant for the pump probe pulse generation process.

Recording the power in each of the reflected and transmitted portions of the spatially separated input beam interchangeably with a recorded profile image of the TOPAS signal output, we could trace the changes occurring in both the splitting ratio and beam profile simultaneously. The spatial profile was recorded on a Logitec HD720p webcam pixel array using a de-magnified image of the beam from an insertable pickoff before the entrance to the first experimental chamber. The result of the scan can be seen in Figure 3.7 a), where the number in the top-left corner corresponds to the number of delay steps set away from the determined peak power (zero) setting. The scan both starts and ends at zero so this set position is displayed twice. The first zero position image is shaded to give an idea of the approximate spatial splitting for the experiment. This was achieved by closing an

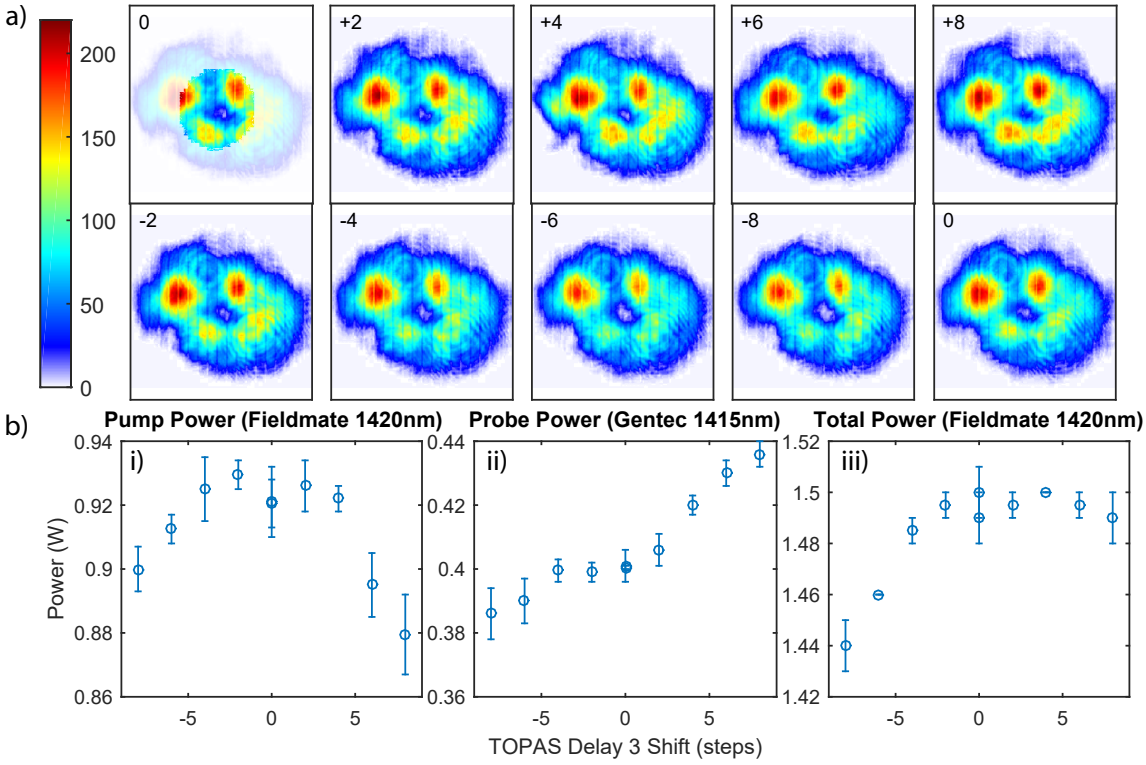


Figure 3.7: Comparing the ratio change of pump-probe power and TOPAS signal beam profile as delay 3 of the TOPAS is adjusted. Recall that nominally 1 step is equivalent to 200 nm, or 0.67 fs delay. a) Images of the TOPAS beam profile as a function of delay 3, and b) corresponding power measured in the pump (i), probe (ii), and total (iii) beam paths measured directly after the splitting annular mirror (pump/probe), and before the generation chamber (total) respectively.

iris at the entrance to the generation chamber to approximately match the diameter of the splitting annular mirror, 4 mm. The difference between the two zero positions indicates a degree of hysteresis in the delay adjustment, or a change in total beam power across the time period required to obtain the measurements. Figure 3.7 b) shows plots of the recorded powers in each of the pump (i), probe (ii) and total signal (iii) beams. The values were measured using either a Coherent PM10 power head connected to a Fieldmate power meter, or a Gentec UP 19K-30H-VR-D0 power meter set to the wavelengths indicated. The TOPAS signal power was measured separately following the initial scan due to the limited number of power meters in the lab. The error bars show the maximum and minimum powers recorded for each TOPAS delay 3 setting.

It is apparent that with little observable change in the spatial profile of the signal beam, a large variation in the splitting ratio could be obtained. This is unsurprising since the profile of the TOPAS beam is far from Gaussian, and thus using a spatial separation method such as an annular mirror to divide such a non-uniform profile can inevitably lead to problems arising from the non-uniformity. If profile changes in the Red Dragon or the TOPAS cause a hot-spot to drift from a position previously reflecting from the annular mirror to one transmitting, abrupt changes can result

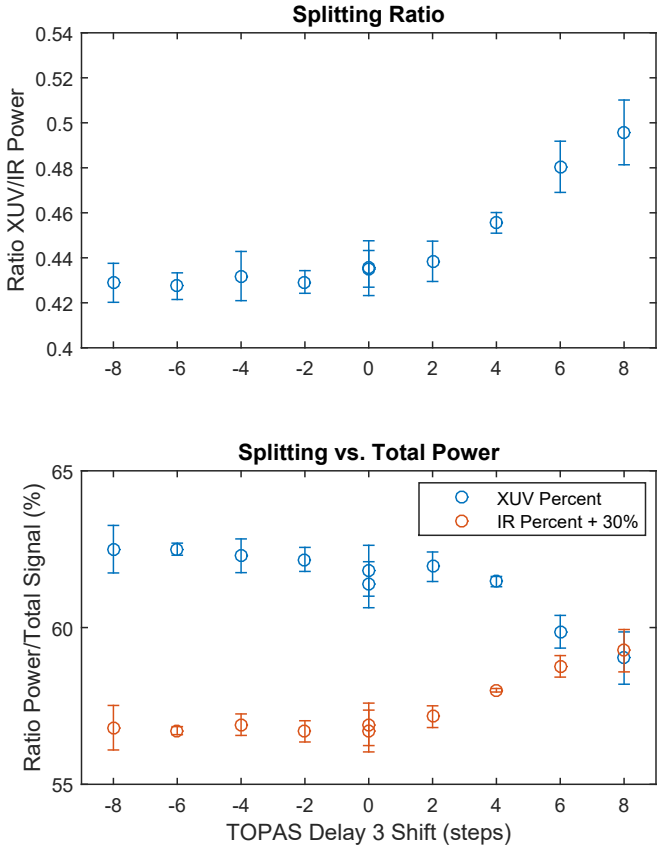


Figure 3.8: Comparison of the splitting ratio between the pump and probe powers as the TOPAS delay 3 is adjusted.

in the relative splitting ratio. Although this was expected to a degree, the level of sensitivity to the daily laser evolution was high, and as shown in Figure 3.7 a), even marginal changes in the profile reference could lead to significant changes in the relative pump-probe powers.

Within the range scanned the variation in the dressing field recorded power is only ∼5%, and the generation beam power ∼11%. The difference in shape of the response between the two recorded beam powers, and the sharp drop in power for the dressing field beam at higher step numbers when the total output power remains approximately constant indicates how significant variation in the splitting powers could arise each time the TOPAS is adjusted if only the TOPAS output power is considered. A plot showing the splitting ratio, along with the (scale adjusted) percentage ratio of each arm compared with the total recorded signal can be seen in Figure 3.8.

Of particular significance is the day-to-day repeatability of selecting similar pump probe splitting ratios. When the chamber is under vacuum, only indirect measures of the splitting ratio can be

performed. One measure is the power of the pump beam recorded using the insertable offline diagnostic. In addition the probing harmonic intensity produced in the generation chamber gas target can give an indication of the relative generation beam power, however this nonlinear process is also dependent on many other external parameters including: the target gas pressure, the gas target position, phase matching etc. which may also drift depending on the experimental conditions.

3.3 Pulse Characterisation Techniques

Accurately measuring the pulse duration and characteristics of ultrashort pulses can be challenging. To resolve temporal information for an event one generally needs to probe the dynamics at time intervals shorter than the process of interest. When the event of interest is already on the femto- or attosecond timescale this becomes problematic, and alternative methods must be explored to measure the temporal properties. Different methods exist to characterise the ultrashort pulses in question, with each providing a different level of final information about the pulses for varying amounts of measurement complexity. Simple techniques such as autocorrelation can give a quick and easy estimate of the pulse duration, however to completely characterise the pulse properties, more complex measurements must be performed such as spectral phase interferometry for the direct electric field reconstruction (SPIDER) technique [146], or attosecond streaking [147].

In this section I will concentrate on the techniques used by myself during the course of this work to characterise the pulses required to perform the experiments presented in Chapters 5 and 6.

3.3.1 Frequency Resolved Optical Gating (FROG)

The technique of frequency resolved optical gating (FROG) expands upon the simple technique of autocorrelation, extracting additional spectral information about the pulse to compliment the retrieved intensity measurement. To perform an autocorrelation, one uses a replica of the ultrashort pulse to temporally gate itself. This can be achieved by focusing both the pulse and its replica noncollinearly into a nonlinear crystal, and recording the resultant nonlinear response on a camera. Controlling the relative intensity of the pulse and its replica, the nonlinear interaction can be fixed to only occur for delays corresponding to pulse-replica temporal-spatial overlap in the crystal. Measuring the intensity distribution of the nonlinear response on the camera, one can therefore estimate the temporal duration of the pulse following deconvolution. Replacing the camera with a spectrometer allows additional spectral information to be recorded, transforming the setup from an autocorrelator into a FROG. Without a second, spatial dimension to the spectrometer, a delay stage must be incorporated into one arm of the interferometer to allow the nonlinear spectrum to be recorded as a function of delay between the two pulses. This is known as a scanning FROG.

A typical scanning FROG setup can be viewed in Figure 3.9. For ultrashort pulses, transmissive

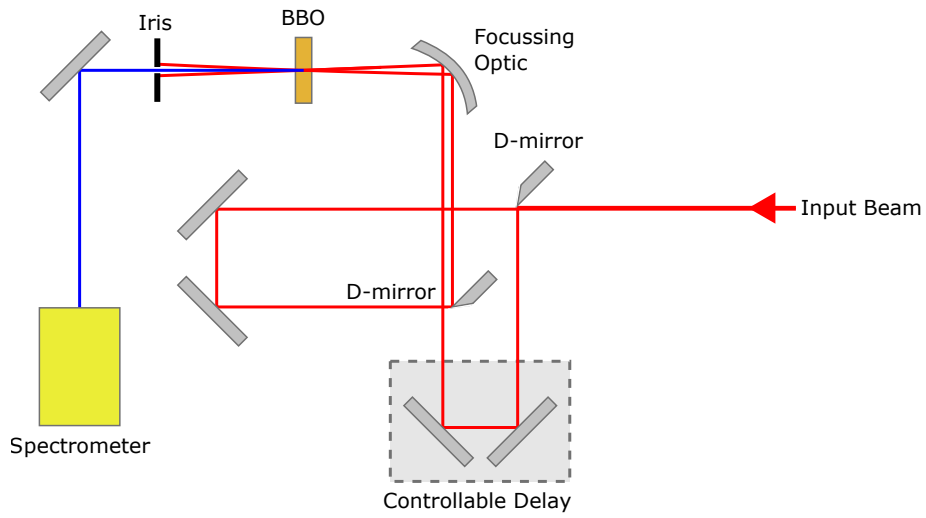


Figure 3.9: Schematic diagram of a typical scanning FROG setup.

optics can introduce large group delay dispersion, distorting the characteristics of the pulse in question. Unless the beamsplitter is very well characterised and any effects can be removed following the measurement, to prevent GDD the pulse can instead be spatially divided using D-shaped mirrors. This also allows easier control over the angle set between the two pulses which enables isolation of the nonlinear signal from the residual intense pulse and replica light. Spatially separating the pulse does however assume some degree of spatial homogeneity across the beam profile for the second pulse to be considered a replica of the first.

A delay stage is set in one arm of the interferometer to precisely control the delay between the pulse and replica light. As already mentioned, the two beams propagate noncollinearly, overlapping at their foci in the nonlinear crystal. In this way the residual light from each beam separates following the nonlinear generation, leaving the up-converted light to propagate in a direction dependent on the k-vectors of the photons used to generate it. Assuming the nonlinear crystal is a second order crystal, the nonlinear result will propagate at an angle directly between the two generating pulses. Setting an iris to block the pulse and pulse replica residual light, but transmit the second order response, the intensity and spectral properties can be measured on a zero background.

To resolve the spectral information, an iterative algorithm is applied to the recorded spectrogram to reconstruct the phase information given the recorded intensity profile. The algorithm works by trying to guess the correct phase profile associated with the measurement by iteratively comparing the known intensity distribution with the improved phase guess until some threshold is met. Different algorithms exist, implementing the optimisation in different ways. The final FROG result gives spectral and temporal information about the measured pulse, though is limited in that since the ultrashort pulse gates itself, asymmetric pulses cannot be resolved.

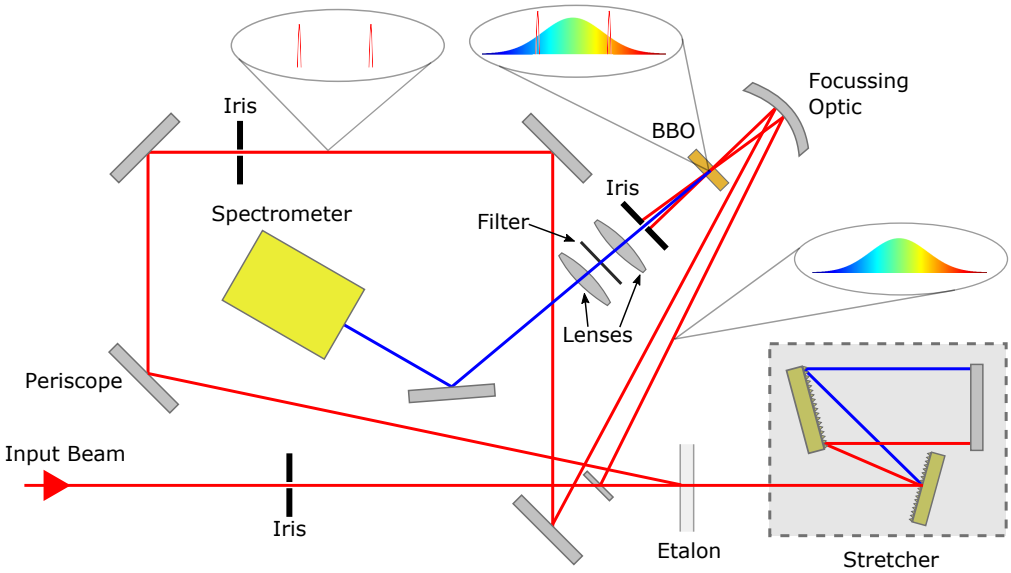


Figure 3.10: Schematic diagram of the technique of spectral phase interferometry for direct electric-field reconstruction, based closely on the schematic provided with the APE SPIDER used in the lab [149].

The FROG technique was first demonstrated by Kane and Trebino in 1993 [148], and is now used as a standard ultrafast characterisation technique in ultrafast labs around the world. FROG measurements were recorded in our laboratory on a daily basis for the 1400 nm studies presented in Chapter 6.

3.3.2 Spectral Phase Interferometry for Direct Electric field Reconstruction (SPIDER)

The spectral phase interferometry for direct electric field reconstruction (SPIDER) technique takes ultrafast pulse characterisation one step further still, resolving the exact shape of the electric field enabling characterisation even of asymmetric pulse shapes. The SPIDER technique again uses pulse replicas to temporally gate the measurement, however instead of measuring spectral intensity as with FROG, the SPIDER technique relies on interference to extract the required information.

The input pulse to be characterised is divided twice, producing two replicas of the original. The front and back reflections from an etalon direct two, precisely delay separated pulses along one beam path, with the transmitted portion entering a stretcher. The short pulse is chirped, stretching the pulse in time as a function of frequency. As for the FROG technique, the double replicas and chirped pulse are overlapped noncollinearly at their foci in a second order nonlinear crystal. Again, the relative beam intensities are adjusted so as just to produce a nonlinear signal when spatial and temporal overlap is achieved. Again this allows spatial separation of the nonlinear

signal from the residual generation light. In the SPIDER setup however, up-conversion through sum-frequency generation will occur between each of the delayed replicas overlapping with the chirped pulse. Due to the chirp, each replica will up-convert with a different frequency resulting in a small frequency difference between the two up-converted pulses. The spectral interference between the time delayed up-converted replicas is recorded, along with an interference reference with the chirped pulse blocked. Provided an accurate calibration of the SPIDER setup is known, the full electric field can be extracted from the recorded interferograms through algorithms. This type of technique using chirped pulses for characterisation is known as spectral shearing.

The SPIDER technique was first demonstrated by Iaconis and Walmsley in 1998 [146]. Since the complete electric field is retrieved using this technique, it allows information about the pulse duration, pulse shape and phase to be understood.

SPIDER measurements were recorded frequently in the laboratory to characterise the Red Dragon pulse. For the experimental work undertaken using the TOPAS signal wavelength, presented in Chapter 6, the SPIDER was run continuously, and the linear translation of the compressor grating in the second stage amplification of the Red Dragon setup was automated to provide feedback for the SPIDER measurement. This was implemented by Dr Dane Austin to minimise long-term drifts in the laser temporal properties.

Chapter 4

Experimental Methods

A significant portion of time and work during this PhD has been dedicated to developing and characterising the transient absorption beamline to perform ultrafast pump probe experiments on the sub-femtosecond timescale. From the delivery of the main experimental chamber in May 2013, several versions of the beamline setup were tested. Some elements remained the same throughout, with the largest differences usually manifesting in the beam paths taken by the generation and dressing field arms in the high harmonic generation chamber. In this Chapter I will describe the general experimental setup, the experimental methods used to determine day-to-day alignment of the beamline as well as how we ascertained certain experimental parameters. I will then move on to discuss more detailed specifics for each of the experiments performed. General data acquisition and data processing methods will be described for the 800 nm and 1400 nm wavelength work.

4.1 The Beamline

The transient absorption beamline setup is comprised of a series of five interconnected vacuum chambers. These contain optics used to create both the pump and probe beams, and to propagate the beams to the detector. The entire beamline was maintained under vacuum for several important reasons:

1. To prevent unwanted nonlinear effects occurring from the propagation and focusing of the intense dressing and probe fields at atmosphere e.g. self focusing.

2. To enable the propagation of the generated high energy high harmonic photons that otherwise interact within a very short distance in air.

3. To prevent contamination of the target sample being probed.

A schematic of the general beamline setup can be seen in Figure 4.1, adapted from [37]. I will

cover the important features along with any variations to the beamline configuration below. The beamline presented in Figure 4.1 [37] approximates that used for the 1400 nm TOPAS work. The exact layout of the generation chamber did change a little between experimental runs, however the general principles were the same.

The majority of the beamline optics are contained within the first chamber. I will refer to this as the generation chamber, so called since it houses the optics used to generate the pump and high harmonic probe beams.

4.1.1 The Generation Chamber

The generation chamber forms the entrance to the transient absorption beamline. The chamber itself is very large, with dimensions $1.0 \times 1.4 \times 0.56\,\mathrm{m}^3$, corresponding to a volume of $0.78\,\mathrm{m}^3$. The physical size affords this chamber a high degree of versatility, with lots of space to test different pump-probe configurations, and easily accommodates additional control optics for the pump-probe beams.

The input laser beam enters the generation chamber through a thin, 3 mm ultra-violet fused silica (UVFS), entrance port window. It is initially divided using a 45° drilled annular mirror, spatially splitting the beam into two. The reflected, outer portion forms the dressing field beam and will be discussed later in this section. The transmitted portion is used to generate the probing high harmonic pulse train and is described directly below. In earlier 800 nm dressing field work, a thicker entrance window was used. Given all of the experiments presented in this thesis are performed using multi-cycle (>30 fs) pulses, this should make little overall difference.

4.1.1.1 The Generation Beam

Following spatial separation, the generation beam is magnified using a reflective telescope. Depending on the particular experiment being performed, the size of the aperture for the splitting annular mirror and the telescope magnification varied. Table 4.1 indicates the different parameters used for the different experiments presented in this thesis. Different values were used to tailor the generated harmonic spectrum to the desired experimental requirements.

Wavelength	Generation Gas	Target Gas	Splitting Annular Mirror Aperture	Telescope Mag.
800 nm	Kr	He	4 mm	×2
1400 nm	Xe	He	4 or 3 mm	×1.875
1400 nm	Ar	Kr	4 mm	×5

Table 4.1: Generation beam optics selected for the different experiments.

After magnification the generation beam propagates along a beam path containing a near normal incidence piezo (Physik Instrumente S-310) controlled mirror. This can be used to introduce up to

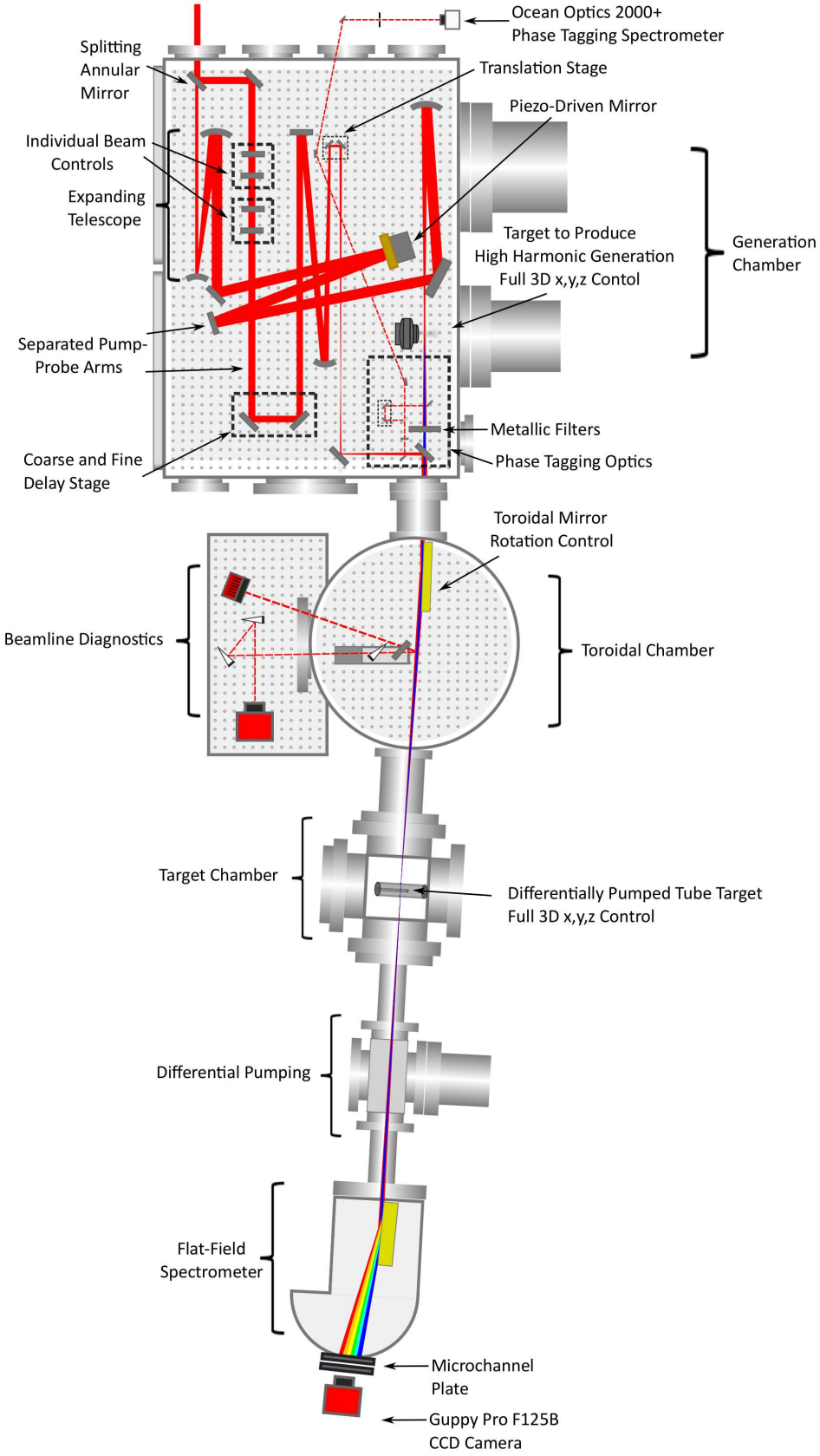


Figure 4.1: Schematic of the beamline used to perform ATAS from laser dressed helium at 1400 nm. Modified with permission from SPIE [37].

40 fs delay between the pump and probe pulses. The beam is then focused using a 50 cm focal length mirror into the generation target gas to produce the high harmonic attosecond pulse train used to probe the target atom. The generation target is mounted on a fully motorised, x,y,z controlled 3D manipulator allowing precise control over the target position under vacuum. The specifics of the generation target again depended on the particular experiment being performed. For the earlier experiments using 800 nm laser dressed helium, the probing harmonics were generated using an effusive, 100 μm orifice gas jet formed from a laser drilled Swagelok cap. For the longer wavelength, 1400 nm dressing field studies however, an adhesive taped, laser drilled, 2.3 mm diameter tube target was mounted on the orthogonal translation assembly. This increased the generation target length, increasing the generated signal through different phase matching conditions.

The co-propagating residual IR light was separated from the high harmonic beam using thin metallic filters. The particular experimental requirements determined what spectral filtering was applied. To study the first ionisation edge in helium required probing harmonic photons around 20-30 eV. A thin aluminium filter was therefore an appropriate choice to remove the 800 nm or 1400 nm residual IR light, but still provide an appropriate harmonic spectrum at a flux sufficient to perform a transient absorption experiment. Similarly, when considering the transient absorption from the 3d edge in krypton with ionisation threshold around 95 eV, filtering through a silicon-zirconium foil will remove the residual IR light whilst transmitting the required range of harmonic energies. Examples of the spectral filtering applied for the different experiments performed can be found in the Spectral Filtering section later in this Chapter.

Prior to filtering, a small portion of the residual IR light is removed using a further 45° annular mirror positioned in the generation beam path for the 1400 nm work, or a D-shaped mirror for the 800 nm studies. Since the divergence of the generated harmonics is less than that of the residual IR, the harmonics pass unaffected through the centre of the annular pickoff, though some residual IR reflects at the edges. The reflected IR light is used to form one beam of the phase tagging temporal correction interference which will be described in detail in the Phase Tagging Temporal Correction section later in this Chapter.

Finally the filtered high harmonic beam exits the generation chamber through a further 2 mm, 45° annular mirror positioned at the end of the generation chamber. It is at this point that the dressing and high harmonic beams are recombined to propagate co-linearly towards the target atom. Once again, the harmonic beam passes through the central hole of the annular mirror, with the dressing field reflecting. Throughout the remainder of this thesis, when referring to the source harmonic spectrum or the source harmonics, it is this spectrally filtered, high harmonic generated spectrum to which it is referenced.

All the mirrors used in the generation arm are silver coated, increasing the versatility of the setup due to the broad-band high reflectivity achieved with a silver coating (>97.5 % average reflectance

for the wavelength range 450 nm to 2 μm [150]).

4.1.1.2 The Dressing Field Beam

The light reflected from the splitting annular mirror forms the dressing field beam. In the IR pump, XUV probe experiments forming the work presented in this thesis, the wavelength of the pump pulse remained the same as that of the incident driving laser. The generation chamber design however would allow for a further high harmonic generation target to be installed in the dressing field beam path enabling the possibility for future VUV pump, XUV probe, or XUV pump, XUV probe experiments to be attempted.

Following this, the dressing field beam passes through a series of control optics allowing the properties of the field to be manipulated. The specific control optics in place depended on the requirements of the particular experiment being performed, for example: studies looking at the effect of changing the relative linear polarisation of the dressing field compared with that of the XUV field required a half waveplate in the pump beam path to rotate the dressing field linear polarisation accordingly. Wavelength specificity of these control optics determined that different control optics were required for each experiment performed using a different driving laser field wavelength. A list of the type of optics used to perform the experiments presented in this thesis is as follows:

- Half waveplate: Used to control the relative linear polarisation of the dressing field compared with that of the XUV field.
- Polariser: Used to transmit a single polarisation state of the dressing field arm. When used in conjunction with a half waveplate, this formed a method of intensity control for the dressing field.
- Iris: Motorised apertures were used in both the dressing and generation beam paths as a fine control over the beam power. Unlike the waveplate polariser combination, adjusting the beam size to control the beam power also affects the focal spot diameter, changing the effective dressing field intensity in multiple ways.

The IR pump beam path includes two 45° mounted mirrors on a delay stage manifold comprising a coarse translation stage (Physik Instrumente M-403.4VP) positioned below a further fine translation stage (Physik Instrumente P-622.1UD). These delay stages can, in addition to the piezo controlled mirror in the generation arm, precisely control the set delay between the pump and probe pulses. The translation range of the coarse stage is 10 cm, offering a beam path control of twice that value. This stage is used to obtain initial, coarse, pump-probe pulse overlap following any changes made to the relative pump-probe beam paths. The fine delay stage has a translation range of 250 μm, and can be used to control the delay between the pump and probe pulses for transient absorption experiments.

The pump pulse is focused using a 1 m focal length mirror, before reflecting from the recombining annular mirror at the exit of the generation chamber. Recombining with the filtered harmonic flux, the two pulses can propagate collinearly to the next stage of the beamline. A further delay stage was added following the focusing optic for the 1400 nm work to more easily be able to adjust the focal position of the dressing field along the direction of beam propagation. The addition of an extra mirror in the dressing field arm however unbalanced the parity of the mirrors in each of the pump and probe beam paths.

To minimise power loss in the dressing field beam, the hole for the splitting annular mirror was imaged onto that used for recombination. In this way, no additional dressing field light was lost through the recombination hole as it would be, for instance, if the splitting was instead performed using a beamsplitter. As for the generation arm, silver mirrors were used throughout the dressing field beam path to increase the versatility of the setup. Irises positioned throughout each of the generation and dressing field beam paths enabled good alignment of the system.

4.1.2 The Toroidal Chamber

After exiting the generation chamber, the collinearly propagating pump and probe beams enter the toroidal chamber. The foci of each of the dressing and generation beams in the generation chamber are situated 1 m from the central plane of the toroidal mirror, ensuring 1:1 (2f-2f) imaging of the foci onto the target atoms, also positioned 1 m from the toroidal mirror. The toroidal mirror surface is uncoated gold on a fused silica substrate, with radii of curvature 11470 mm and 87 mm for the long and short radii respectively. The physical dimensions are 2 cm by 20 cm, and it is aligned at 85° grazing incidence, displaying a 10 mm x 10 mm effective usable area. The mirror itself is mounted on a motorised assembly allowing translation and rotation control along and around each of the x, y, z axes except translation along the direction of the beam propagation, z, where manual control can be performed with the chamber at atmosphere. Gate valves either side of the toroidal chamber allow independent venting of the chambers. The intensity of the focused dressing field could be increased by magnifying the dressing field beam, however ultimately the maximum dressing field beam size is limited by the physical dimensions of the toroidal mirror. Measurements of the dressing field focal spot size indicate that the toroidal operates close to the diffraction limit.

In addition to the toroidal mirror, the toroidal chamber also houses a mirror and glass wedge mounted on to a motorised translation stage, positioned after the toroidal reflection. These optics can be inserted into the beam path to perform offline referencing and alignment procedures. More details will be given in the Offline Diagnostics section later in this Chapter.

4.1.3 The Interaction Chamber

Following refocusing of the pump and probe beams using the toroidal mirror, the imaged foci are spatially and temporally overlapped in the target gas jet. This is the position in the beamline where the transient absorption experiment is performed. The target gas jet has full 3-dimensional translation control from an orthogonal arrangement of translation stages. For the earlier 800 nm dressing field work, the differentially pumped, 2.6 mm diameter tube target was mounted on a manual manipulator for 3D target position control. The target gas jet and mounting assembly was upgraded for the 1400 nm dressing field studies. The upgraded setup consists of a differentially pumped, nominally 6 mm tube target mounted on fully motorised x,y,z controlled translation stage stack. This is comprised of two SmarAct SLC-2475 translation stages controlling the horizontal and beam propagation direction movements, and a Thorlabs MTS 25 translation stage controlling the vertical position. Motorised stages enable more precise movement of the interaction target gas jet, as well as the opportunity for automation. The effective target length is reduced fractionally by small recesses created following the removal of burring at each end of the new target, and the aperture diameters for the outer jacket and inner tube were 500 μm and 300μm respectively.

The resultant transient absorption signal exits the interaction chamber and propagates towards the detector. Differential pumping holes are mounted at the entrance and exit of the interaction chamber to minimise pressure leak to the surrounding chambers.

4.1.4 The Flat Field Spectrometer

A flat field spectrometer detector was used to record the transient absorption data. A concave, aperiodic, 1200 lines/mm Hitachi grating mounted at 87° grazing incidence dispersed the broadband incident light along the energy axis, enabling capture of spatial (divergence) and spectral information about the detected harmonics. A Photonis Chevron imaging micro channel plate (MCP) detector was used to amplify the high photon energy signal. Coupling this with a P46 phosphor screen, the detected harmonics could be imaged using an Allied Vision Guppy Pro F125B CCD camera. The pore size of the micro channel plates was 10 μm, with pitch factor 12 μm, and blaze angle 8°. The active area of the MCP was 8 cm, and the plates were uncoated. High voltages are required for both the MCP plates and screen to amplify the signal through the electron cascade process. Typical voltages used for the plates and screen ranged from 1.5-1.9kV and 3.1-3.8kV respectively. On the inside of the spectrometer setup a zero order block is in place to prevent the zero order light reflected from the grating from saturating the MCP signal.

Flat-field spectrometers are designed to produce a flat focal plane of the focused harmonic light, appropriate for the flat MCP detector. Our spectrometer design allowed rotation of the detector flange with the chamber at atmosphere to vary the detected energy range of the harmonic spectrum.

At the time of the experimental runs presented in this thesis, only vertical control of the grating could be performed under vacuum. As such, alignment of the grating and adjustment of the observed spectral energy range had to be performed at atmosphere, resulting in a non-trivial procedure particularly due to the long pumping requirements and voltage ramping for atmosphere-exposed MCPs prior to use.

A stage of differential pumping between the interaction chamber and the flat field spectrometer reduced the base pressure in the detector chamber. An additional gate valve directly before the detector chamber allows isolation of this chamber when venting or pumping the interaction chamber.

Data acquisition software was used to record the transient absorption signal and control the various hardware within the beamline. The data acquisition framework was upgraded between the 800 nm dressing field studies and those performed using the 1400 nm dressing field beam. This will be described in more detail in the 800 nm and 1400 nm Specific Methods sections later in this Chapter.

4.2 Spectral Filtering

Spectral filtering is applied to the generation beam for two key reasons:

1. To remove from the beam the residual IR light used to generate the high harmonics.

2. To actively filter the high harmonic spectrum, removing the high intensity, low order non-plateau harmonics, and windowing the transmission if required.

The co-propagating residual IR light must be removed from the generation beam to prevent it from interfering with the dressing field IR light in the interaction chamber. This would modify the effective dressing field intensity experienced by the target atoms. The residual IR light would, in this case, be phase-locked with the generated harmonic pulse train, leading to a complicated effective dressing field response as the true dressing field pump pulse is delayed in time with respect to the XUV probe and residual IR fields.

In addition, removing high intensity, low order, non-plateau harmonic orders from the probing XUV pulse train ensures that all interaction with XUV photons is linear. The conversion efficiency of the phase matched high harmonic process is typically very low, resulting in a prohibitively low harmonic flux for probable nonlinear interaction to occur. The low energy, exponentially decaying, non-plateau harmonic orders however can be orders of magnitude more intense [80].

As already mentioned, aluminium filters are particularly useful when investigating around the first ionisation potential of neutral helium (24.59 eV). Aluminium acts as a band-pass filter for XUV photons, cutting sharply any photons below ∼15 eV and above ∼72 eV with a discrimination dependent on the thickness and quality of the filter. Typically, aluminium filters used in the lab for this purpose are between 100-200 nm. Thicker filters are less fragile and can produce higher

discrimination between the transmitted and blocked photon energies, however overall they transmit less of the incident light. Careful filter selection is therefore paramount to ensure good quality experimental results are obtained. We used a 150 nm aluminium filter for the work presented in this thesis looking at transient absorption from laser dressed helium at both 800 nm and 1400 nm.

The transmission window of aluminium as given by the CXRO x-ray database [151] can be seen in red in Figure 4.2 a) linear axis, and b) log scale. To account for the rapid oxidation for both surfaces of the aluminium filter, a more realistic transmission is achieved using an aluminium-aluminium oxide composite filter shown in blue on the same plot. An oxidation thickness layer of 10 nm was estimated for each surface of the filter corresponding to 10s of atoms of oxidation depth. Assuming an 800 nm central wavelength driving laser, the positions for the associated harmonic orders relative to the aluminium filter transmission are also shown in Figure 4.2 c) in black, with the position of the first ionisation threshold (Ip) of helium in cyan. For our experimental measurements (Figure 4.3), we observe that contrary to the CXRO data, harmonic 11 was also heavily attenuated by the aluminium filter. Since the harmonic generation was performed by a many-cycle, but still relatively short, ∼30 fs, 800 nm pulse, the individual harmonics measured on the MCP had significant spectral widths. This in conjunction with the possibility of the central wavelength of the driving laser being slightly red-shifted from 800 nm could in part account for the observed results.

In Figure 4.3 we see an image of a typical spectrum measured on the MCP with the aluminium filter both removed from and blocking the generation arm XUV light. We observe that the experimentally measured transmission efficiency is slightly higher (up to around 50%) compared with the transmission predicted assuming 10 nm of oxidation for each face of the 150 nm aluminium foil (closer to 15-20%). This indicates that either the oxidation layer formed on the surface of the foil is actually thinner than 10 nm for each surface, that the filter itself is thinner than the quoted 150 nm, or that the CXRO data underestimates the transmission for the aluminium or aluminium oxide (or a combination of the above).

Similarly, to investigate transient absorption around the 3d edge in krypton, spectral filtering whilst providing harmonic photons in the energy range 85-105 eV is required. A 400 nm silicon, 200 nm zirconium composite filter was selected to produce the desired spectral characteristics to probe this transition. The combination of the transmission characteristics of each of these materials windows the spectrum, removing the undesirable residual IR and low energy harmonic orders, and the sharp silicon edge around 100 eV truncates the high photon energies, allowing for the possibility to explore XiHHG from the laser dressed krypton 3d edge.

The transmission spectrum for this composite filter taken from the CXRO x-ray database [151] can be seen in red in Figure 4.4 a) linear axis, and b) log scale. Accounting for approximately 50 nm of oxidation in the zirconium layer, the silicon zirconium zirconium-oxide composite filter as taken from CXRO is plotted alongside in blue. In Figure 4.4 c) we observe a magnified region of the

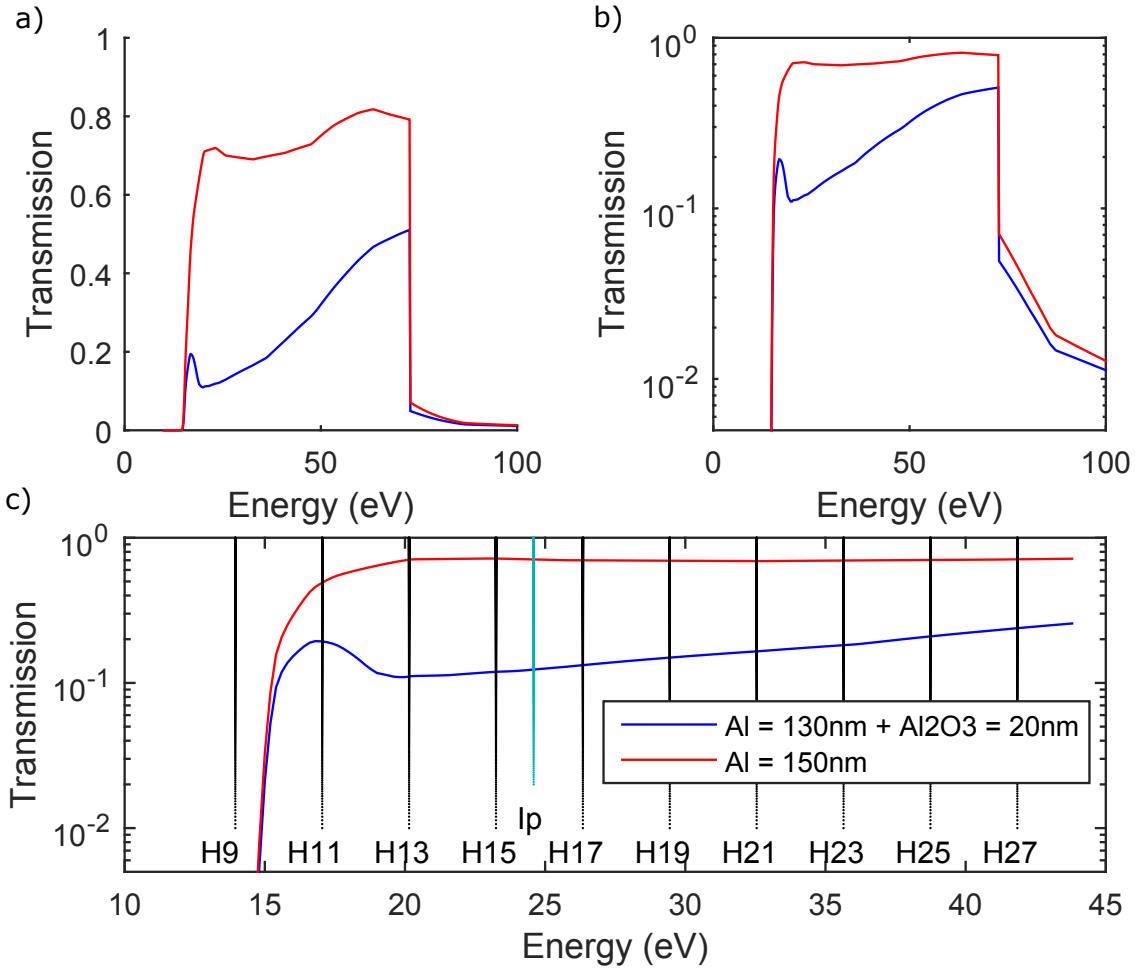


Figure 4.2: Transmission spectrum of a 150 nm aluminium foil presented on a linear scale (a), and a logarithmic scale (b) indicating the spectral windowing that can be achieved by both a pure 150 nm aluminium foil, as well as a more realistic 130 nm aluminium, 20 nm aluminium oxide composite foil. c) Magnified transmission spectrum of the energy range of interest, spanning the first ionisation energy of helium around 24.6 eV. The black lines indicate the positions of the harmonics for an 800 nm driving laser central wavelength. 100% transmission would correspond to 1 on the transmission axis. The transmission data is obtained from the CXRO database [151].

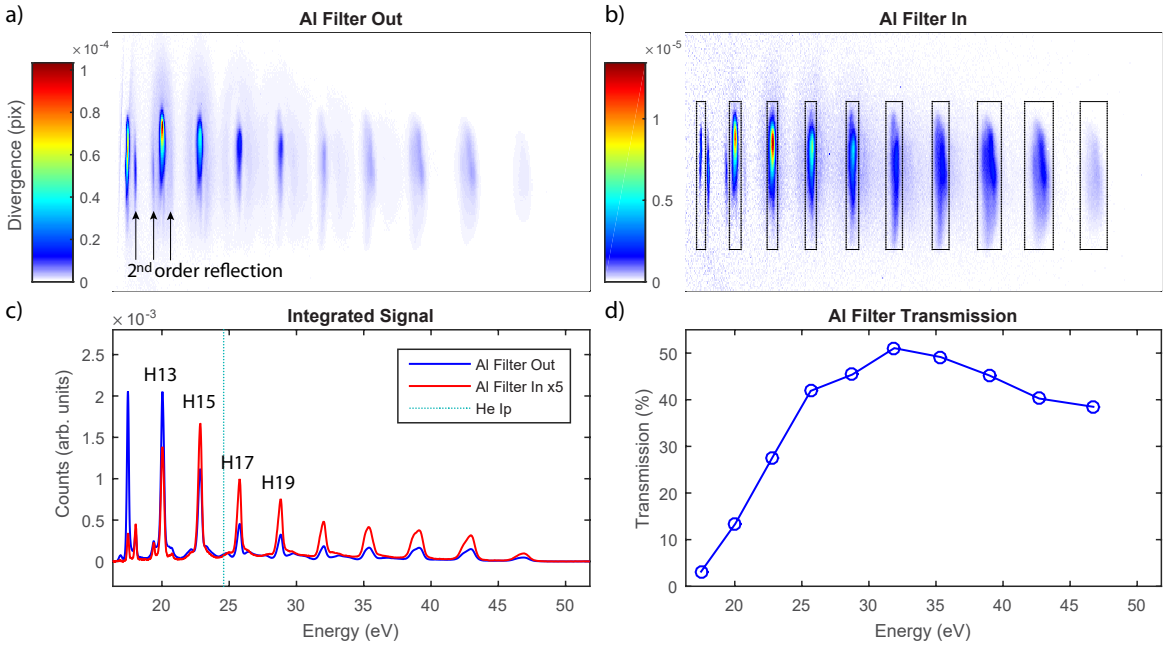


Figure 4.3: Comparison of typical experimentally measured spectra both unfiltered (a) and filtered (b) using a nominally 150 nm aluminium filter in the beam path. Summing the signal along the divergence axis, the integrated signal with (red) and without (blue) the filter is shown in c). The approximate percentage transmission calculated by comparing the integrated harmonic signal within each black box shown in b) can be seen in d). It should be noted the energy width of each of these boxes is not the same. The energy axis of the MCP has been rescaled to be linear, and the signal amplitude corrected accordingly.

spectral filtering around the energy range of interest. The black vertical lines represent the labelled harmonic orders assuming a 1415 nm driving laser wavelength. The 95 eV ionisation edge of the 3d state in krypton is shown in cyan. It is noticed that to observe an XiHHG signal from laser dressed krypton above the silicon edge one would need to generate and detect photons above 100 eV.

Comparing the harmonic spectra from the generation target with and without the silicon zirconium filter in the beam, Figure 4.5, we can see the resultant spectral shape change and the transmission percentage for the filter. It is observed that the measured transmission amplitude and shape of the harmonic flux through the filter is similar to that predicted by the CXRO silicon zirconium zirconium oxide values. We do however observe a sharp rise in the recorded signal around 50 eV in the experimental result. This is attributed to the detection of light on the MCP from the second order reflection of the grating. The shape of this part of the spectrum therefore mirrors that of the first order silicon edge. The filters were mounted in motorised filter mounts enabling their insertion and removal under vacuum.

The visible second order reflection light was useful during experiments as an energetically well known calibration aid. In addition, due to the $1/\lambda$ scaling for the energy axis of the detector, it was found that the energy resolution of the second order reflection light was actually better than its corresponding first order component. All of the experiments probing the krypton edge presented in this thesis therefore use the response of the second order reflection light, rather than the typical first order, to determine the harmonic modulation response. Care must be taken for instances where harmonics were generated by the dressing field beam in the target gas.

4.3 Stabilisation

For such a large and complex beamline, many forms of stabilisation are required to attain the required pump-probe delay precision, pump-probe spatial overlap, and laser stability to perform good quality transient absorption scans.

4.3.1 Laser Stability

As already described in the Red Dragon section in Chapter 3, the Red Dragon output power and compression are both actively stabilised to maintain a more constant output. Although this functionality was not available when the first 800 nm dressed helium experiments were performed, experiments undertaken using the TOPAS beam demanded a higher Red Dragon stability since any changes in the Red Dragon output are magnified through the nonlinear OPA process.

For the 1400 nm experiments, the input pointing of the TOPAS beam was actively stabilised. This was implemented because of concerns regarding small changes in the beam pointing causing large changes in the splitting ratio at the first annular mirror due to the highly non-uniform TOPAS

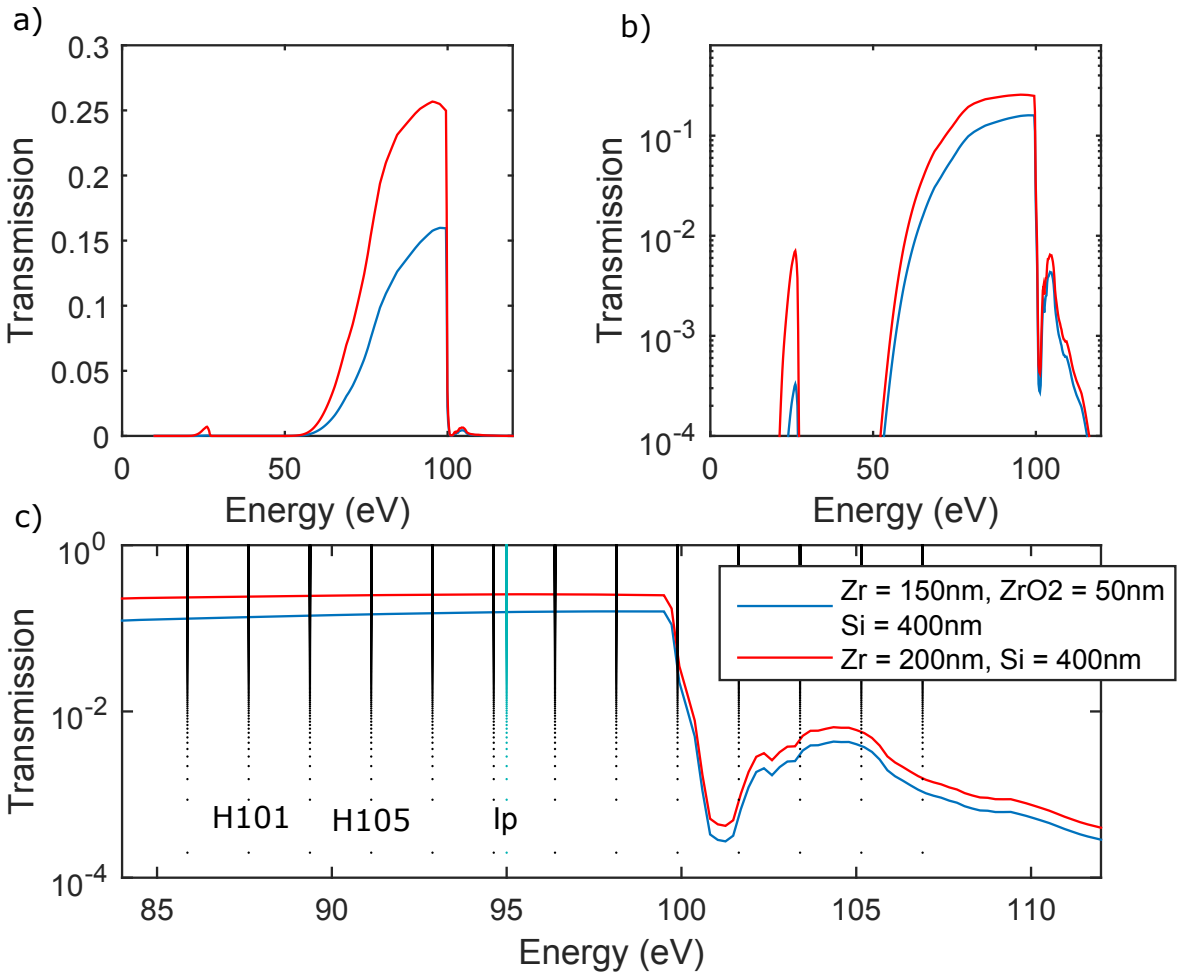


Figure 4.4: Transmission spectrum of a 400 nm silicon 200 nm zirconium composite filter presented on a) a linear scale, and b) a logarithmic scale indicating the spectral windowing that can be achieved by both a pure 400 nm silicon 200 nm zirconium composite filter, as well as a more realistic 400 nm silicon 150 nm zirconium 50 nm zirconium oxide composite foil. c) Magnified transmission spectrum around energy range of interest, spanning the 3d ionisation edge of krypton around 95 eV shown in cyan. The black lines indicate the positions of the harmonics assuming a 1415 nm driving laser central wavelength. 100% transmission would correspond to 1 on the transmission axis. The transmission data is obtained from the CXRO database [151].

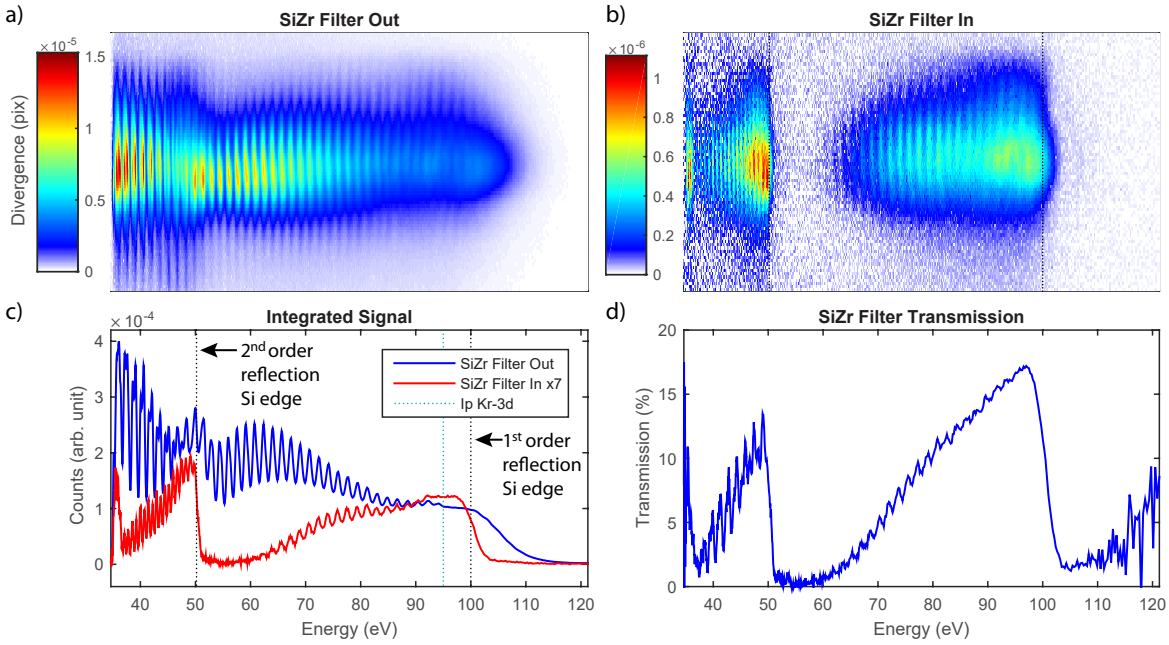


Figure 4.5: Comparison of typical experimentally measured spectra both unfiltered (a) and filtered (b) using a nominally 400 nm silicon 200 nm zirconium composite filter. The edge appearing at 50 eV corresponds to light from the 2^{nd} order reflection of the grating corresponding to the silicon edge around 100 eV. Below this value (or higher for the case of SiZr filter out where the cutoff energy is higher), the MCP signal will be contaminated with second order signal and so is not representative of the true values. The silicon edge observed with both the 1^{st} order (100 eV), and 2^{nd} order (50 eV) light reflected from the grating is indicated by black vertical dotted lines in c), where the spectral response with (red) and without (blue) the SiZr filter are shown by integrating along the divergence axis in a) and b). The 3d Ip (∼95 eV) is marked in cyan. The calculated percentage transmission for the filter is presented in d). Again, the signal below 50 eV is contaminated with light from the second order reflection of the diffraction grating. The energy axis of the MCP has been rescaled to be linear, and the signal amplitude corrected accordingly.

beam profile. As such, the experiments performed using the 800 nm driving laser field would have been less affected as a result of a more uniform Red Dragon laser beam profile.

4.3.2 Generation Chamber Stability

With such a large chamber, stability is always going to be a challenge. The choice to use a non-collinear pump-probe geometry means easy control over the characteristics of the pump pulse, however it also requires both beam paths to propagate using a separate set of optics, spanning different regions of the vacuum chamber. The separated path length within the generation chamber is around 4 m, requiring a selection of stabilisation techniques to be used.

First, the entire breadboard inside the generation chamber is mounted directly to the optical table below using double-bellows. This independence of the beam path optics from chamber walls and frame vibrationally isolates the breadboard from any of the turbo and roughing pumps attached to the chamber, whilst maintaining vacuum inside the generation chamber.

Even with this design, due to the size of the chamber, long term thermal drifts and relaxations associated with evacuation of the chamber from atmosphere can cause the breadboard to extend and warp, which in turn causes drifts and instabilities in the pump-probe spatial and temporal overlap. Motorised control using Newport picomotor actuators of two steering mirrors in each of the pump and probe beam paths allows fine alignment control following evacuation of the chamber. Post acquisition temporal correction provides pump-probe delay accuracy better than 150 as. The method for doing this is described in the following section.

4.4 Phase Tagging Temporal Correction

As described in the Beamline Section above, a small portion of driving laser light was picked off from each of the pump and probe beams at the end of the generation chamber. The two pick-offs could then be recombined spatially using a beam splitter in a miniature Mach-Zehnder style interferometer situated at the end of the generation chamber. With spatial and temporal overlap of the pulses, the spectral interference pattern could be monitored as a function of delay. Additional delay could be added between the two beams using a further delay stage positioned in one of the pick-off interferometer arms. This enabled control over the fringe separation measured in the spectrometer. The recombined beams were directed out of the generation chamber through a further window port. Focusing the light into an Ocean Optics USB2000+ spectrometer, the resultant spectral interference pattern could be monitored, with any shifts in the relative delay between the pump and probe light manifesting as a shift in phase of the interference fringes. An iris positioned before the spectrometer entrance allowed some control over the relative pick-off contributions from the pump and probe beams. Balancing the contributions from the pump and probe light provided the best visibility

interference fringes.

As data was acquired over the course of each scan, the spectral interference from the auxiliary interferometer was also simultaneously recorded, enabling each data point to be 'tagged' with the true relative delay time between the pump and probe pulses. This was often found to vary from the chosen set delay time selected in the software. The deviation between set and true delay values could be quite large, changing the overall length of a long delay scan by many femtoseconds, or varying throughout the scan leading to a changing sampling rate across the scan duration. An example of differing set and true delay values can be seen in the dressing field polarisation study performed using 1370 nm dressed krypton, see Figure 6.2. The set delay steps were chosen to be 0.2 fs using the fine delay stage control, however the true delays steps as recorded using the phase tagging were actually measured to be closer to 0.13 fs, meaning the set delay range of 270 fs to 380 fs was greatly reduced.

The measured true delay was extracted from the interference spectra by applying a Fourier transform to the recorded interferogram, and windowing the Fourier component corresponding to the interference modulation frequency. By inverse Fourier transforming the filtered result back to the time domain, information on the relative position of the interference peaks could be extracted from the phase. Images showing the spectral interference phase tagging steps can be seen in Figure 4.6.

Calculating the root-mean-squared (RMS) value of the recorded phase tagging data with a smoothed fit to the data, the resolution of the phase tagging was measured to be better than 150 as. Since the spectral interference was recorded simultaneously with each data set, each scan could be individually corrected for any drifts in the pump-probe delay. It should be noted that only relative delays can be recorded using the setup. The absolute delay is unknown. To avoid any ambiguity in the spectral shifts, the true delay increments used must therefore be smaller than the delay induced from a step size corresponding to $\lambda/2$, where λ is the wavelength of the fundamental dressing field.

4.5 Offline Diagnostics

The insertable pickoff optics situated in the toroidal mirror chamber allow offline measurements of the dressing field beam power, focal position and focal spot size. In addition, by removing the metallic filters blocking the generation beam residual IR, an approximate XUV focal spot position can also be recorded. The recombining annular mirror heavily apertures the generation beam IR light, forcing the measured focal spot diameter and Rayleigh range to be much larger than for the unapertured case. For a perfect Gaussian beam, the central position of this IR focus should correspond to the central position of the generated XUV focus. For the real beam profiles however, this was not always found to be the case.

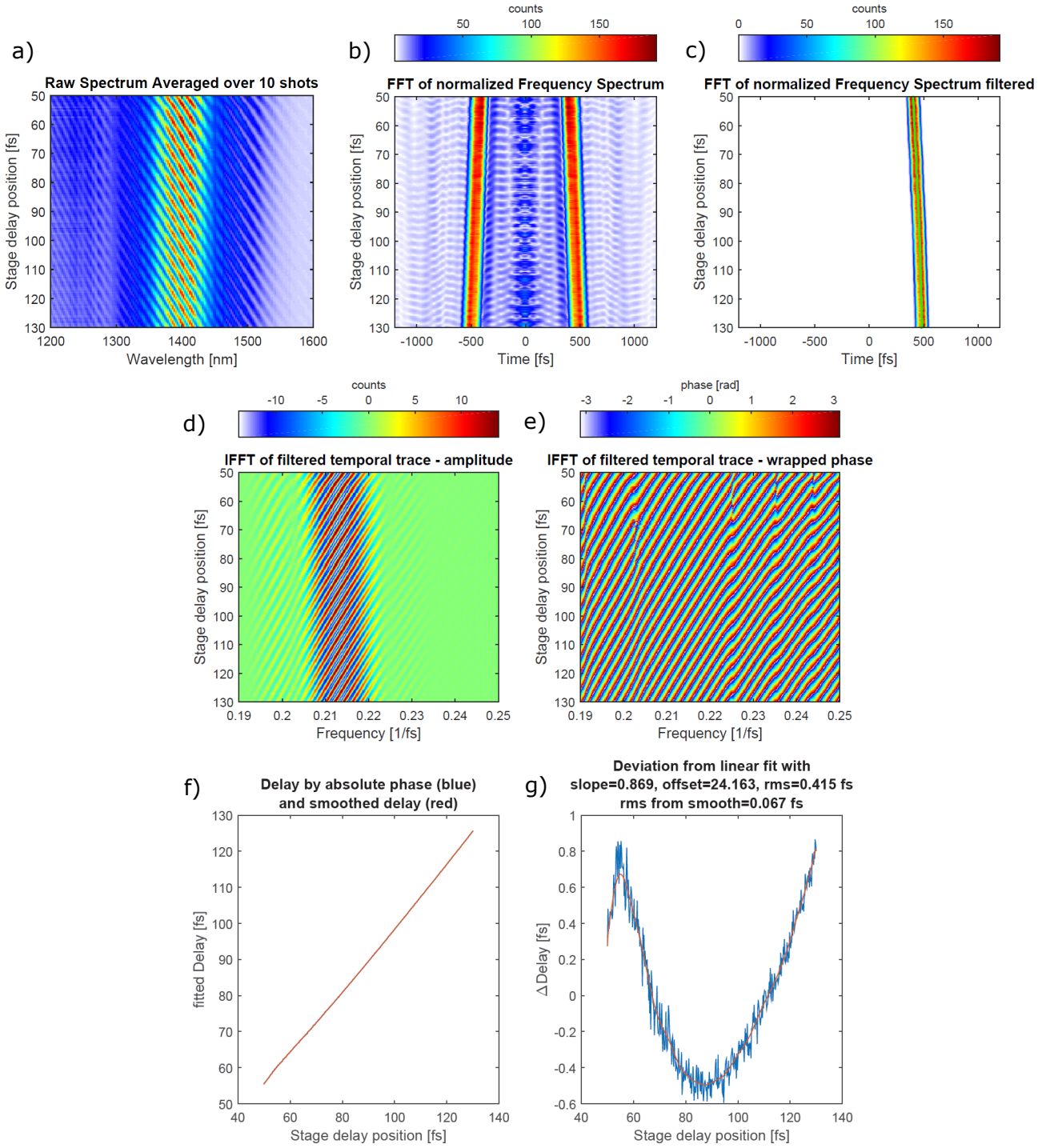


Figure 4.6: The key steps associated with phase tagging the relative pump-probe delay. a) The raw recorded spectrum measured by the spectrometer for each pump-probe delay. b) The Fourier transform of the delay-dependent spectra. c) Windowed Fourier component corresponding to the fringe spacing for each delay. d) The amplitude and e) the phase of the inverse Fourier transform of the filtered signal. f) The extracted and smoothed phase delay. g) The deviation of the recorded phase delay from a linear response as a function of the set pump-probe delay.

4.5.1 Focus Measurements and Overlap

To record the dressing field focal position and size, the glass wedge mounted on the pickoff diagnostics translation stage in the toroidal chamber is inserted into the beam path. The reflectivity of glass is only a few percent, reducing the power of the reflected beam. This is necessary to prevent nonlinear effects from occurring in the glass window port used to extract the light from the vacuum chamber assembly. With two further reflections from mounted glass wedges outside the vacuum assembly, the extracted beam can be imaged using an Allied Vision Guppy F503B CMOS camera. Neutral density filters further attenuate the focusing beam to prevent damage to the camera chip. For the 1400 nm TOPAS signal, an additional long pass filter (Thorlabs FEL 1100 nm or FEL 1150 nm) is used to remove the intense, visible green, sum frequency generated light propagating collinearly with the signal. If this light is not filtered it would saturate the camera response since the sensitivity of the camera at 1400 nm requires interaction via a two-photon process. For the majority of the 800 nm work presented in Chapter 5, the focal spot imaging was performed using a Logitech HD 720p webcam. In general, fewer references were recorded for the earlier work, however for the 1400 nm results presented in Chapter 6 referencing was performed daily.

The daily focal overlap alignment procedure relies on the images from the offline diagnostics camera. The day-to-day drift in temporal overlap was found to be of the order of 10 s of femtoseconds. The procedure would therefore be to first check the spatial overlap of the pump and probe foci using the pickoff wedge and camera, then confirm the exact temporal overlap by varying the dressing field delay. Blocking the generation beam and imaging the dressing field focus allowed focal scans to be performed by sliding the camera along a fixed ruler aligned parallel with the beam propagation direction and recording images at different planes throughout the focus.

Determining the focal plane by fitting a curve to the recorded beam profile effective area, the camera could be repositioned at the focus in preparation for pump-probe focal overlap. With any filtering removed, heavy aperturing of the generation beam by the annular exit mirror following the gas target in the generation chamber reduces the beam size of any diverging IR light propagating along the generation beam path to 2 mm diameter. The result is that trying to perform a similar focal scan using the generation arm IR light yields no clear result since the focal spot size and effective Rayleigh range are very large. An image at the focus can, however, be recorded, and the dressing field focus aligned to match centrally.

Overlap of the foci is achieved by steering the dressing field focal spot using the two motorised Newport picomotor actuators mounted on the recombination annular mirror located at the exit of the main chamber. Small adjustments of this mirror should not affect the transmission of the generation beam, however it will have a large effect on the position and quality of the dressing field focus. An additional motorised mirror mount one optic back in the dressing field beam path can be controlled to allow for far-field corrections in the position if necessary under vacuum. Similarly,

two optics in the generation beam path can also be controlled under vacuum for fine tuning of the generation beam focus and position. Since the generation beam defines the line of the whole experimental setup, these controls are rarely used.

If the input beam was a perfect Gaussian, overlapping the central position of each recorded focus should ensure perfect overlap of the dressing field with the generated XUV APT. Given the poor quality of the TOPAS beam profile, this assumption was not always valid. Fine adjustments of the recombining annular mirror were often made looking at the experimental absorption interaction effect as feedback for the optimal pump-probe overlap.

The measured focal position of the dressing field beam using the pickoff camera should roughly correspond to the position of the target in the target chamber. When performing a full alignment of the beamline, the recombining annular mirror was removed, and the position of the generation arm IR light focus determined on the pickoff camera. Ensuring the position of the camera matched the approximate target position in the target chamber, a mapping between the true focal position and recorded focal position with respect to the camera ruler could be made. With the recombining annular mirror replaced, the focusing of the dressing field arm could be adjusted to match that of the generation and target positions.

4.5.2 Power Measurements

Inserting the pickoff translation stage mirror in the toroidal chamber into the beam path directed the whole beam power through the window port and out of the vacuum assembly. Using a power meter (either a Coherent PM10 or Gentec UP 19K-30H-VR-D0) positioned close to the window port, measurements of the dressing field beam power could be recorded. Beam quality was not important for the power measurements so long as all the light could be collected on the power meter head. Due to the heavy attenuation in the generation beam path, power measurements of the generation beam residual IR were meaningless, and the XUV photons inaccessible outside the vacuum chambers. With measurements of the dressing field power and focal spot profile recorded, estimations of the dressing field peak intensity could be made.

4.5.3 Intensity Measurements

From the focal images obtained and the power measurements recorded, we could estimate the peak intensity of the dressing field. The recorded images were cropped, background subtracted and thresholded to account for camera noise and scattered light. For the 1400 nm wavelength work, since the Guppy camera is designed to work at optical wavelengths, a square-root factor was applied to all the images to account for the two photon process. Normalising the pixel values to a unitary maximum and multiplying by the sum by the pixel area to give an effective total focal area, A, we could calculate an approximate peak intensity, I_{peak}, using the equation:

$$I_{peak} = \frac{E}{A\tau}, \tag{4.1}$$

where E is the energy per pulse obtained by the power measurement from the pickoff mirror, and τ is the estimated pulse duration. This value is dependent on the level of thresholding applied. For the 800 nm work, the camera response was linear and so thresholding was less important. For this reason, the thresholding was limited to setting all negative values following background subtraction to zero to enable the gamma factor correction necessary for 800 nm light on the Logitech webcam. In addition, the power measurements for the 800 nm work were compensated for a measured approximate 10% total loss upon front and back reflections from the window output port. For the 1400 nm work, the intensities presented in this thesis assume a 1% camera dynamic range threshold to account for camera noise, and a 3% peak signal value threshold to account for other residual background. For each threshold value, all pixels with values lower than the threshold within the camera image are set to zero.

Plotting the peak intensity as a function of position, Figure 4.7 b), we can also verify the approximate Rayleigh range of the focus assuming a Gaussian beam profile for the calculated area. For the particular scan shown, we find from the estimated intensity values the Rayleigh range is approximately 6.6 cm. This has a corresponding FWHM focus of 200 μm, shown as a red circle in Figure 4.7 a), calculated from the fit shown by the dashed line in Figure 4.7. Due to the spatial separation of the pump and probe beams with the annular mirror, the dressing field beam is not Gaussian, and instead resembles a doughnut shape. The focus is therefore also not Gaussian, and instead a significant portion of the beam energy falls in a ring outside the main peak. The ratio of central to outer energy varies depending on the quality of the focus, though for the example shown in Figure 4.7 a), approximately 36% of the total power falls outside the FWHM ring. The central portion of the dressing field focus is still larger than the XUV focus, so we can assume a fairly uniform intensity across the probed sample.

4.6 Calibration of HHG Spectra

To calibrate the nonlinear energy axis into equally spaced energy increments requires a minimum of two, well known energy reference points within the recorded image, or applicable image set. Assuming the line separation of the grating, d, can be approximated by the central value, the grating disperses the light as a function of wavelength following the well known grating equation:

$$d(\sin\theta_i + \sin\theta_r) = m\lambda \tag{4.2}$$

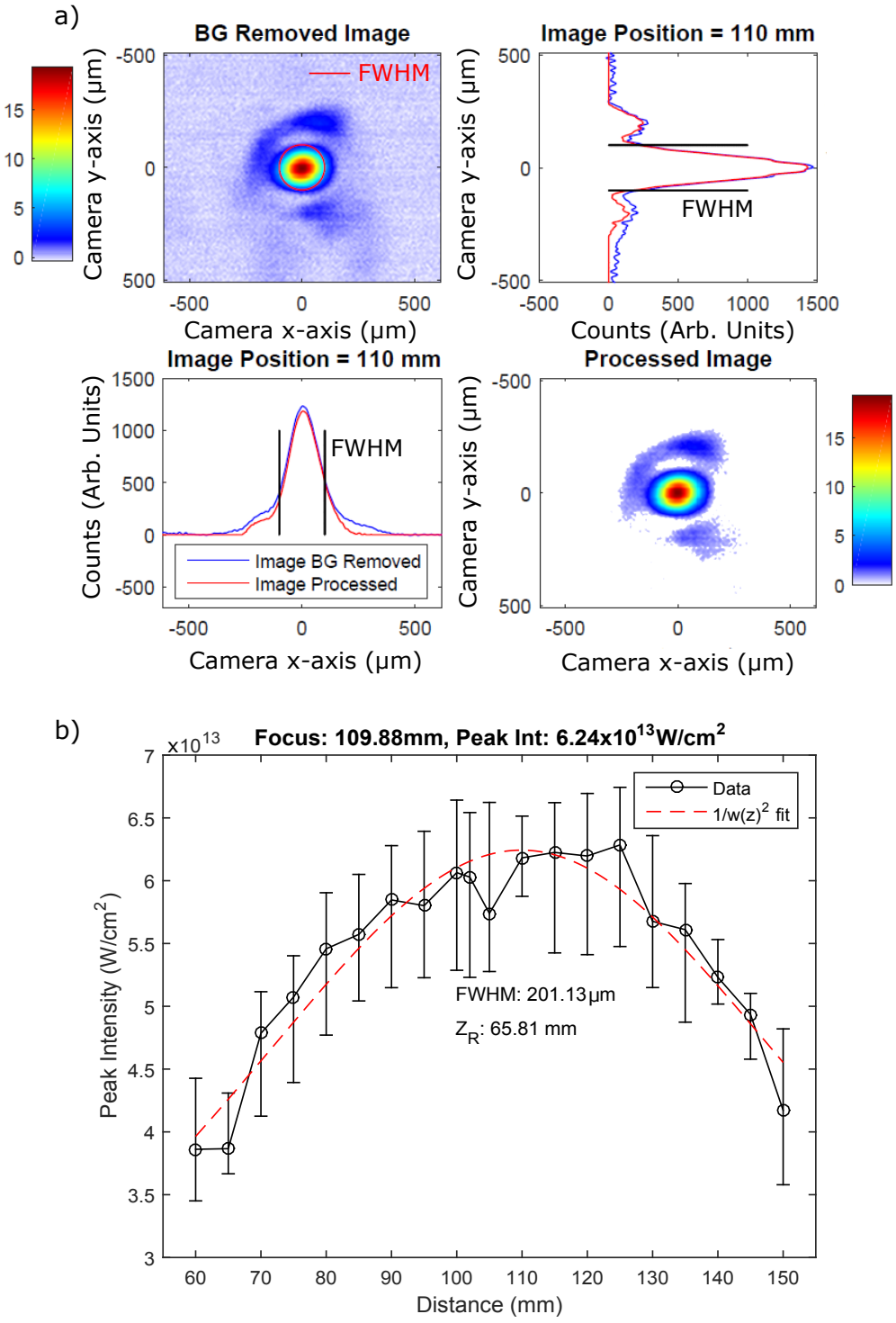


Figure 4.7: a) Image of the focal spot position as determined from the fit in b), where the level of thresholding can be observed by comparing the background (BG) removed with the BG removed and thresholded (processed) images. The red circle in the top-left panel, and black parallel lines in the top-right and bottom-left panels indicate the calculated FWHM assuming a Gaussian beam profile using the determined effective area. b) Peak intensity plotted as a function of camera position for the dressing field beam indicating the approximate Rayleigh range and FWHM assuming a Gaussian beam profile and using the calculated effective area.

where $\sin\theta_i$ and $\sin\theta_r$ are the angles of incidence and refraction of the incident light with respect to the normal, d is the line separation of the grating, m is the order of refraction and λ is the wavelength of the light. Using the small angle approximation, the distance axis is linear with wavelength, and so proportional to $\frac{1}{E}$ where E is energy. Using the equation relating energy and wavelength:

$$E = \frac{hc}{\lambda} \tag{4.3}$$

the linear wavelength axis can easily be transformed into a linear energy axis, and interpolated onto even spacing.

To correct the nonlinear intensity, a Jacobian must be applied to the data to rescale the intensity along the calibration axis. The Jacobian can be found by differentiating equation 4.3 with respect to λ to determine the relationship between an increment in energy and an increment in wavelength. Dividing each wavelength increment by the differential rescales the intensity for the linear energy axis.

For the transient absorption experiments around the 3D krypton edge, the close spacing on the MCP of the argon produced high energy harmonic orders allows calibration of the energy axis to be performed using the sharp silicon edge around 100 eV, and the corresponding second order reflection light from the grating showing the same edge profile around 50 eV. These reference positions provide the two good energy reference points required for calibration. For the transient absorption experiments performed around the helium Ip, the large separation on the MCP of the xenon or krypton produced harmonic orders means that although the harmonic orders can be easily identified using the aluminium filter, direct calibration from the filter edge is not possible (unless a harmonic order happened to exactly match the filter edge). Since this was not the case, the harmonic orders themselves were instead used as the calibration reference points, determining the energy for each harmonic from the known harmonic order and central wavelength of the input laser light. Given that in the high harmonic generation process, the harmonics themselves can become shifted in energy, for example see reference [100], in general, using well known edges from filters is preferable to calibrating using the high harmonic peak positions. For each set of experiments, the final check was adding the target gas to the target chamber and observing that the absorption edge falls as expected on the calibrated axis. Again this was more clearly observed for the closely spaced high energy harmonic orders recorded for the krypton transient absorption work.

4.7 800 nm Specific Methods

4.7.1 Data Acquisition

For the work presented in Chapter 5, the data acquisition automation was limited to perform 2D scans in a linear manner: recording an automated individual delay scan for each position of a second scan parameter, for example a delay scan was recorded for each selected polarisation of the dressing field. References could be recorded at the beginning and end of the full 2D scan. Alternatively, the second scan parameter could be performed manually, for example scanning the intensity of the dressing field where specific references were required for each parameter setting. Effectively this was just recording a series of 1D delay scans.

Frequent referencing was important to understand any changes in the conditions of the experiment, as well as to be able to monitor and correct for slow temporal drifts. In this earlier work we were limited to reference at most at the beginning and at the end of each scan since no automated referencing was enabled throughout. The references recorded, and corresponding nomenclature used in the remainder of this thesis includes:

- Source Harmonics Reference (SH): The spectrally filtered, high harmonic spectrum used to probe the dressed target. This reference was obtained by creating the XUV APT in the generation target, removing all gas from the transient absorption target chamber and blocking the dressing field light with the motorised beam block (BB).

- Static Absorption Reference (SA) or field free (FF) transmission: The spectrum of the remaining source harmonic signal following field-free absorption in the undressed target gas. Gas is present in the target jet, however the dressing field beam remains blocked with BB. The term static absorption reference is used interchangeably with field free reference in the remainder of the thesis.

- Dressing Field Blocked and Unblocked Backgrounds (BG-IR in/out): With the generation beam blocked, there should be no signal recorded by the detector. A small amount of background stray light and 'hot' pixels on the camera will, however, always remain that require removal. Although there is a block in place in the flat-field spectrometer to remove the zero order light and prevent the strong IR dressing field saturating the response on the MCP, backgrounds with and without the dressing field present were recorded in case of any dressing field scatter reached the detector. These are referred to as BG-IR in and BG-IR out respectively. Each respective background could then be subtracted from the applicable data. Under most circumstances these backgrounds were similar so if one was not recorded for whatever reason, the same BG-IR in/out would be used for all data sets.

The exposure time per image for the references was kept the same as that for the data, 1 s, so the

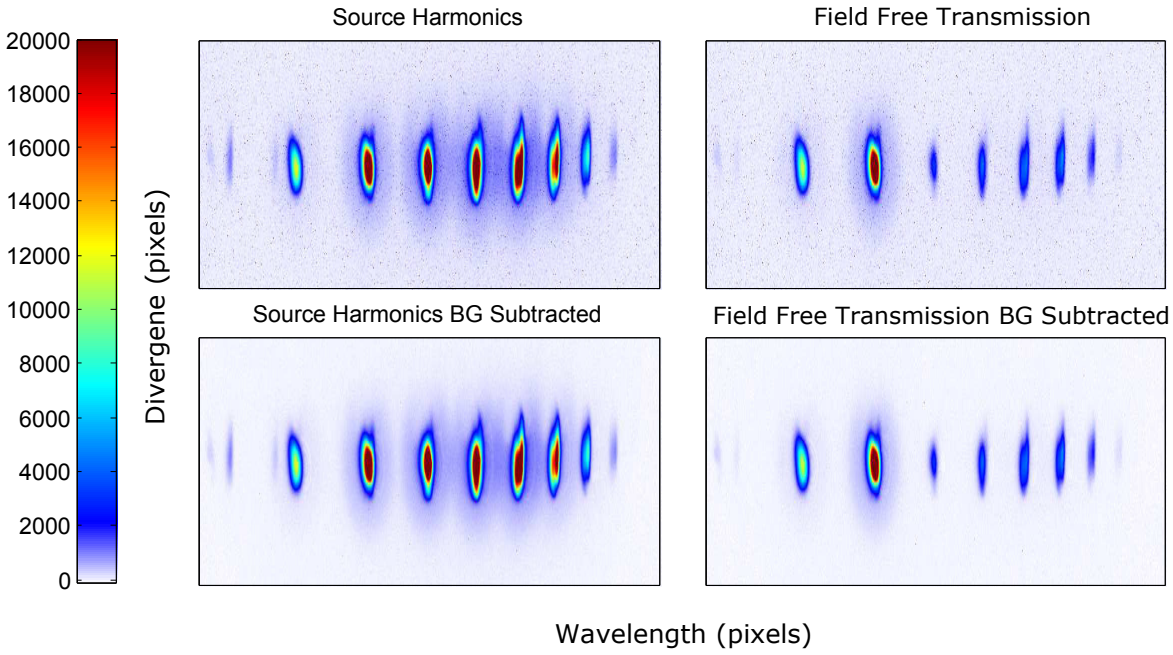


Figure 4.8: Images showing the source harmonics and static absorption (field free transmission) raw harmonic spectra compared with the corresponding background subtracted versions. The colour scale has been chosen to deliberately saturate to highlight the flux levels for the field free transmission measurements.

two values could be directly compared. To ensure the references were representative, typically a larger number of images were averaged over for the references compared with the data. This number ranged from from 20 to 50. Averaging so many images for each data point would have made the scan durations prohibitively long. Figure 4.8 shows a typical source harmonics and static absorption reference with and without background BG-IR out subtraction. For each panel, the mean of the recorded images is presented.

This early work focused on recording predominantly short scans of approximately 6 fs duration, covering nominally just over two full modulations of the 800 nm driving wavelength. This allowed quick comparison of parameters to be made, minimising the effect of any drifts in the laser system and experimental setup. Typically the procedure was as follows:

- We would observe the whole envelope of interaction by running a long, sparsely sampled, scan to determine the delay corresponding to central overlap of the pump and probe pulse envelopes, t=0. An example of this can be seen in Figure 5.3.

- We would select the particular delay range over which to run the shorter, finely sampled, scans. This was done by observing the response of the different harmonic orders across the envelope of interaction, and choosing the position containing the largest apparent modulation

depth in the above Ip harmonic signal. Often this would coincide closely with or around the approximate t=0 delay.

- If multiple parameters were scanned, we would set the same nominal delay range for each recorded scan. For each delay scan the phase tagging monitored the real delay introduced between the pump and probe pulses. Due to long-term drifts in the setup, the real delay and the set delay differed. For scans run using the same set delay, the real delay would differ slightly between the scans as well.

- Attempts were made to reference the phase of the XUV pulse relative to the peak of the incident dressing field. This was done by removing the aluminium filter from the generation beam, along with any gas in the generation target, so that just 800 nm light propagated down each of the pump and probe beam-paths. By inserting a lower Ip gas into the interaction target, such as argon or krypton, effectively a nonlinear IR-IR autocorrelation measurement could be recorded, generating and detecting harmonics produced by the interfering IR-IR fields in the interaction target. The harmonic generation signal was maximised for the delays corresponding to constructive interference between the two IR field peaks. For the delays resulting in destructive interference, the harmonic generation signal was suppressed. Recording the delay dependent signal alongside the phase tagging result allowed us to relate the phases in the IR-IR autocorrelation to the phases of the experimental results. The delay axes for data presented in Chapter 5 have therefore been corrected for this factor. It should be noted however that this method does not take into consideration any phase difference between the IR used to generate the APT and the spectrally filtered XUV light actually probing the response. For this reason, in addition to not precisely knowing the absolute t=0 delay, one cannot compare the absolute phase between experiment and theory, or between two different experimental scans in the delay dependent data presented in Chapter 5.

4.7.2 Data Processing

Following the data acquisition, data analysis was performed to extract information about the dynamics of the system by monitoring the changes in the harmonic signal throughout the delay scans. In this section I will give an overview of how the data was treated for presentation in Chapter 5. To begin, boxes were selected around the brightest region of each high order harmonic to capture the majority of the on-axis, short trajectory, signal. The size of the boxes was chosen observing the average signal for each harmonic across the delay scan, with additional insight also gained by reviewing the standard deviation of the individual harmonic signals for the scan image stack. The total signal within each of these boxes was summed to give a value for that harmonic order per delay point. Equivalent boxes selected for the corresponding references and backgrounds could be

compared and subtracted respectively. A typical box selection is shown in Figure 4.9, where the selected boxes (similar between the panels) are shown with respect to the mean of the harmonic signal across the scan and the standard deviation. Selecting a box with finite spectral width averages together a small range of different frequencies. Harmonic 11 is seen to be greatly attenuated by the aluminium filter.

The lower panels in each image show the magnified box selections, normalised to the maximum pixel value for each box, and smoothed to enable more informed selection. It should be noted that since the background subtraction was performed once the boxes were selected, any hot pixels on the camera falling within a selected box made the task of selecting the brightest region of the harmonic more difficult. A 3x3 median filter was therefore used to smooth the panels as a visual aide for automation of the colour axis selection. A 3x3 median filter scans pixel to pixel in an image, comparing the central pixel in the 3x3 block to its nearest eight neighbours. By resetting the value of the central pixel to the median of the nine pixel values compared, this acts to smooth the data by removing any extreme values, whilst maintaining general trends.

Following summation of the individual pixel contributions within the selected boxes to form the signal data points for each delay step, the set temporal axis was corrected using the recorded phase tagging information. The result is an unevenly sampled delay axis. The data must therefore be interpolated to recover an evenly sampled axis to allow Fourier transformation to be performed in Matlab, extracting the frequency components comprising the recorded delay-dependent absorption modulations. To ensure the cleanest extraction of the frequency components, care has to be taken in the way the data is treated, particularly for shorter delay scans where there will be low resolution in the Fourier domain.

In addition to a regularly spaced time vector, careful attention must also be paid to the data range selection when the number of recorded modulations is small. Ensuring the data is trimmed and scaled to present only a whole number of $2\omega_1$ modulations ensures that when the fast Fourier transform is applied in Matlab there is no artificial contamination in the frequency domain from stitching artefacts. Ensuring there is no large jump in the data signal from the first point to the final point of the selected modulation range will prevent any step function in the data which following Fourier transformation would generate signal at all frequencies in the Fourier domain. By ensuring a whole, even number of sampling points is chosen for each cycle, this also forces the Fourier components to fall exactly at $2\omega_1$ and $4\omega_1$ etc. rather than at points around these values. Given the low resolution afforded in the Fourier domain from the short scan duration, by doing this we also ensured there was only one Fourier domain point corresponding to each frequency component for these scans. The cycle length was scaled to ensure that when the data was stitched together to perform the Fourier transform in Matlab the correct overall frequency was maintained. These data analysis considerations were particularly important for the theoretical data for which only a

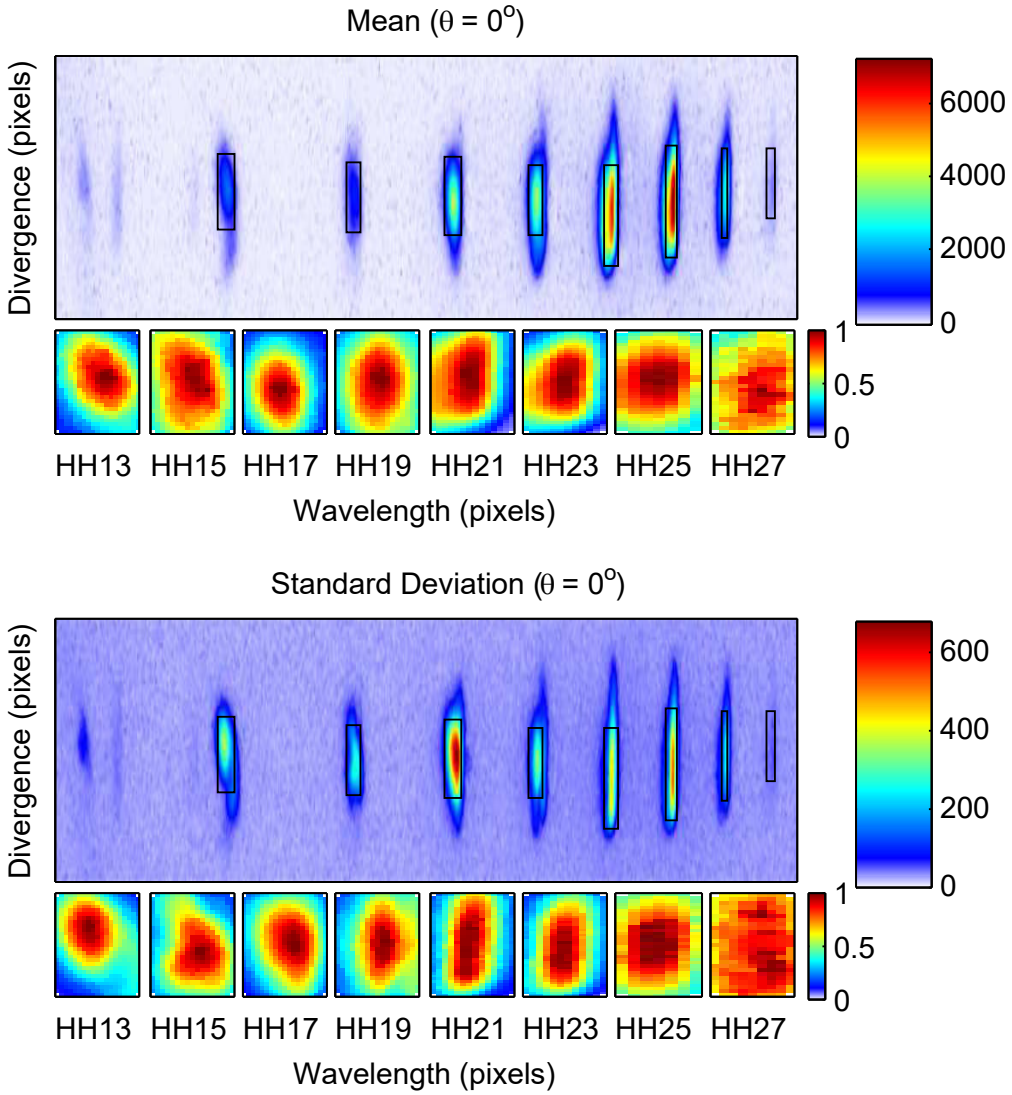


Figure 4.9: Typical box selection for the harmonics using the mean signal of the delay scan and standard deviation of the image stack as guidance. The lower panels in each image show magnified versions of the selected boxes shown in black with the corresponding harmonic order label. The magnified images have been smoothed using a 3×3 median filter as a visual aid.

single oscillation was calculated. In the experimental work we usually selected as a minimum $1.5\omega_1$ modulations (corresponding to 3 full $2\omega_1$ modulations, 6 full $4\omega_1$ modulations etc.).

The pulse duration was estimated using SPIDER measurements recorded intermittently throughout the experimental run, and a model approximating the dispersion difference between the pump and probe beam paths. The optimal pulse compression at the SPIDER setup differs from that at the generation target due to propagation differences between the two beam paths. By maximising the signal of the measured harmonics whilst optimising the compressor grating linear position in the Red Dragon however, we could fine-tune the optimal pulse compression at the generation target using the sensitive harmonic signal as feedback. It was understood that maximum harmonic signal coincided closely with the position for shortest pulse compression at the generation target. Understanding the pulse duration is important for obtaining an accurate peak intensity value for the dressing laser field. Given that optimisation of the pulse compression at the generation target does not automatically guarantee optimisation of the pulse compression in the dressing field unless the beam paths pass through an identical amount of glass and air, a thick ($\sim$10 mm) glass plate was placed in the dressing field arm to compensate GDD between the beam paths. Using a model to approximate the remaining GDD difference between the beam paths, an approximate temporal duration of the dressing field pulse was determined to be 50 fs in duration. This is significantly longer than the $\sim$30 fs optimal pulse duration measured at the SPIDER.

It was observed that when using high MCP voltages with gas present in the target chamber, some background-like signal due to scatter from the generation arm was created on the MCP. This signal could not be accounted for in any standard background subtraction. For this early data we therefore subtracted an additional estimated 'background' from each averaged image to account for this scatter. We determined the value of this additional factor by calculating the difference in signal value from the summed boxes surrounding harmonics 13 and 15 in the source harmonics and static absorption references. Since both of these harmonics fall below the ionisation threshold of helium, we would expect the difference in signal to be zero. No light should be absorbed at these frequencies by the undressed target gas. Since the static absorption reference also requires gas to be present in the target chamber, instead of the difference being zero, the subtracted value instead reflects the amount of scatter recorded on the MCP within the boxes selected for the below Ip response. By dividing each value by the number of pixels contained within the corresponding harmonic box, and averaging the result, an approximate average value per pixel could be obtained to correct, in part, for this extra scatter factor. We could test how well the additional background accounted for the scatter by considering the signal summed in the boxes for the source harmonics and static absorption references as shown in Figure 4.10.

In Figure 4.10 we observe that by taking into account this extra scattering factor, the value of the summed harmonic 13 and 15 boxes for each of the source harmonics and static absorption references

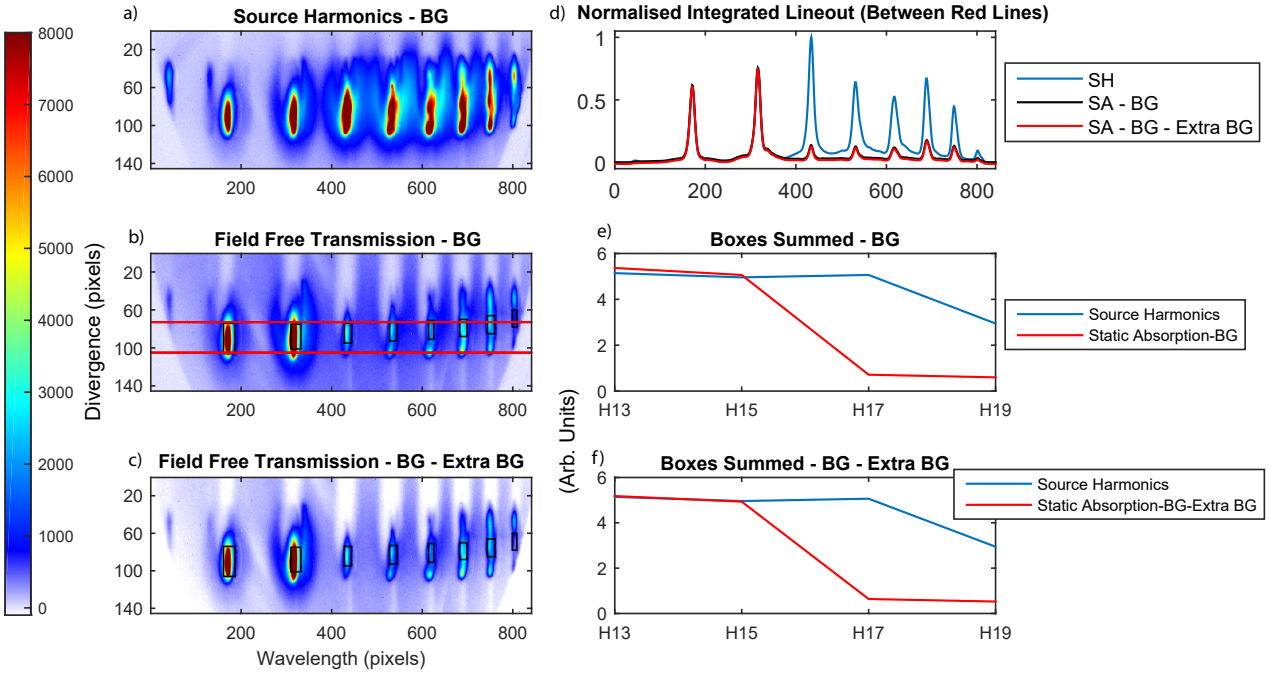


Figure 4.10: Determining the effective extra background due to scattered generation arm light in the presence of the target gas for high MCP voltages. The background subtracted source harmonics and background subtracted field free transmission harmonics are shown in a) and b) respectively. The field free transmission harmonic response with the additional determined 'extra' background removed can be seen in c). Integrating along the divergence axis between the red lines indicated in b), d) shows the normalised spectral intensity for the data presented in a) (blue), b) (black), and c) (red). Summing the contents of the selected boxes shown in black in both b) and c), the total summed signal for the below Ip harmonics (H13 and H15) can be compared e) for the cases with, b), and without, a) the target gas. These values should be equal. Following the same procedure for e) however including the removal of the 'extra' background for the field free transmission we find f). Here the values for the below Ip harmonic orders are more similar.

agrees much closer than for when this extra factor is not applied. The close agreement between the corrected values implies this correction factor is appropriate. Assuming a linear correction factor across the MCP, the above Ip harmonic order values are also corrected using the same factor.

Also visible in Figure 4.10 is the extent to which we had damaged the MCP phosphor screen. The white stripes observed above the harmonic orders correspond to 'burnt' regions on the phosphor screen. These 'burnt' regions are positions of reduced sensitivity on the screen due to long exposure to high XUV flux, and general photo-induced degradation and ageing. The damage appears as stripes since to utilise the whole active area of the MCP detector, the harmonics have, over time, been actively shifted in height on the detector to strike fresh positions on the MCP. The burns are particularly clear in these images due to the conditions resulting in the extra scatter from the generation arm.

For 2-dimensional scans, the boxes were selected to ensure summation of the brightest signal for each delay scan whilst maintaining the same box selection throughout. This often led to a larger box selection for the multi-dimensional scans where the likelihood for the harmonic position or divergence to change throughout the scan duration was increased.

4.7.2.1 Converting Transmission into Absorption Cross-Section

To relate the measured relative absorption to real physical units, a conversion of the recorded transmission into absorption cross section was performed. By recording both source harmonics and a static absorption reference spectra, the density length product, η, of the tube target could determined from the known field-free absorption cross section, σ_{FF} [152], and the diameter of the tube target, 2.6 mm.

Splitting the total delay dependent absorption cross section, $\sigma(\tau, \lambda)$, into two components arising separately from the laser dressing field, $\sigma_D(\tau)$, and the known field free static absorption cross section, σ_{FF} [152], the transmitted intensity at delay τ, I(τ), can be found using the following Beer-Lambert equation:

$$I(\tau) = I_0 e^{-\eta\sigma(\tau,\lambda)} = I_0 e^{-\eta(\sigma_{FF}+\sigma_D(\tau))}. \tag{4.4}$$

where I_0 is the measured source harmonic reference signal.

The Beer-Lambert law for static absorption is:

$$I_{FF} = I_0 e^{-\eta\sigma_{FF}}, \tag{4.5}$$

where I_{FF} is the measured static absorption reference signal, resulting in equation 4.4 becoming:

$$I(\tau) = I_{FF} e^{-\eta\sigma_D(\tau)}. \tag{4.6}$$

Rearranging this for $\sigma_D(\tau)$, the total absorption cross section can be written in terms of measurable quantities:

$$\sigma(\tau, \lambda) = \eta^{-1} \log\left(\frac{I_{FF}}{I(\tau)}\right) + \sigma_{FF}. \tag{4.7}$$

This technique could also be applied to the 1400 nm work for future analysis of the data since all of the relevant references were recorded.

4.7.2.2 Theoretical Methods

Theoretical results were calculated by Dr Marco Ruberti at Imperial College London to compare with the 800 nm dressing field experimental results presented in Chapter 5. The theory employed the recently developed *ab initio*, single atom time dependent B-spline algebraic diagrammatic construction (ADC) method [153], using the full-dimensional time dependent Schrödinger equation (TDSE) to numerically calculate the cross section values to compare with the polarisation and intensity dependence scans.

The method assumed a single excited electron, truncating the ADC hierarchy to 1. This assumption was valid since the cutoff energy of the experimental source harmonic spectrum was lower than the energy threshold for double ionisation, around 60 eV [154]. The frequency dependent generalised absorption cross section was found using the equation [99]:

$$\sigma(\omega; \tau_D) = \frac{4\pi\alpha\omega S(\omega, \tau_d)}{|\tilde{E}_X|^2}, \tag{4.8}$$

where α is the fine structure constant, ω is the frequency, $\tilde{E}_X$ is the Fourier transform of the incident XUV field and $S(\omega; \tau_d)$ is the frequency dependent absorption. The absorption was found using the following equation:

$$S(\omega; \tau_d) = -Im[\tilde{E}_X^*(\omega)\langle\tilde{z}(\omega; \tau_d)\rangle], \tag{4.9}$$

where $\langle\tilde{z}(\omega; \tau_d)\rangle$ is the expectation value of the Fourier transformed dipole moment, and $\tilde{E}_X^*(\omega)$ is the complex conjugate of the incident XUV frequency. Further detail on the theoretical method can be found in reference [35].

4.8 Advances in the Beamline

Between the 800 nm work presented in Chapter 5, and the investigation into transient absorption from 1400 nm dressed helium and krypton in Chapter 6, many advances to both the beamline and laser setup as a whole were made. The key changes implemented were as follows:

- The Red Dragon power control feedback was refined. The power control program recorded any changes to the Red Dragon amplification using photodiodes positioned at the end of each of the amplification stages. Fluctuations in the power could be controlled through fine adjustment of the pump laser currents, affording a more long-term stable output power of the Red Dragon beam.

- Multiple cameras were positioned inside the Red Dragon laser system to more reliably track drifts in the setup. In addition, a more reproducible alignment procedure could also be performed.

- The beam path geometry for the generation beam was altered, varying the setup slightly to minimise the reflection angles for near-normal incidence reflections, reducing aberrations and increasing the quality of the focus.

- The beam path for the dressing field was adjusted to accommodate the change in path length of the generation beam. An additional mirror and delay stage were added to the dressing field beam path following the focusing optic to enable easier adjustment of the dressing field focus position along the direction of beam propagation.

- Input beam stabilisation was implemented at the entrance to the generation chamber to correct for any long-term drifts in the TOPAS beam pointing or position. This also enabled easier adjustment of the TOPAS beam profile to allow monitored selection of the beam profile region sent to each of the generation and dressing field beam paths by the dividing annular mirror.

- The gas tube-target in the target chamber was upgraded from a 2.6 mm laser drilled, differentially pumped tube on a manual manipulator, to a nominally 6 mm purpose-built, differentially pumped tube target mounted on full x, y, z 3D motorised orthogonal translation stage assembly.

- The gas target in the generation chamber was changed from a 100 μm orifice, effusive laser drilled Swagelok cap to a 2.3 mm diameter tube target, adhesive taped and laser drilled. The longer target length enabled a larger interaction volume and consequently a higher generation flux to be achieved. The adhesive tape allowed easy laser drilling of the target hole, maximising ease of alignment with minimum load on the turbo vacuum pumps used to maintain vacuum in the generation chamber. Typically the tape would need to be replaced every few days.

- The linear position of the compressor grating was automated using feedback from the SPIDER, minimising any long-term drifts in the pulse duration, and improving the long-term stability of the setup.

– The magnification of the telescope in the generation arm was modified from 2x magnification for the 800 nm work, to 5× magnification for the krypton work at 1400 nm, and 1.875× magnification for the helium work at 1400 nm. For each arrangement the generation beam needed to be realigned, and the length of the dressing field beam path adjusted accordingly.

– The MCP was rotated by approximately 70° to move the burnt stripe in the MCP phosphor screen to cover just one small band of photon energies, rather than covering the whole harmonic transmission.

4.9 1400 nm Specific Methods

4.9.1 Data Acquisition

A new data acquisition framework was developed to record data taken using the TOPAS signal wavelength as the input laser beam. The primary objective was to provide more versatility in the data recording, allowing for more frequent referencing and more control over the data acquisition process.

This was particularly important when using the TOPAS signal driving laser since any drifts in the Red Dragon output are magnified by the additional non-linear OPA process. In addition to increased referencing, we also automated and logged more experimental parameters such as the chamber pressures, compressor grating linear position, Red Dragon pump powers and the beam input steering. Monitoring each of these throughout the scans afforded us better insight into how drifts in particular parameters effected the end result.

The acquisition framework enabled the user to select the scan parameters including: the delay range, delay step size, and the frequency and type of references required. Due to the non-automation of the gas flow, source harmonic references could only be performed at the beginning and end of each scan along with their relevant backgrounds. Automated beam blocks inside the chamber enabled static absorption references to be taken throughout the scan, and background references for these were recorded at the beginning of each scan. The background was assumed to remain constant throughout the scan duration. The ability to select multiple sampling resolutions within the same scan allowed a coarser sampling step to be selected for the edges of the overlap envelope, reducing the overall duration of a scan, whilst retaining high resolution for the modulations around the central overlap position.

If multiple parameters were varied within a single scan, for example comparing the parallel ($\theta = 0°$) and perpendicularly ($\theta = 90°$) aligned dressing field and XUV polarisation directions, the scan duration was minimised by ordering the processes to reduce the number of instructions required. For example, a typical instruction sequence for the polarisation scans could be:

1. Move to delay position 1.
2. Acquire image with parallel dressing field polarisation.
3. Rotate waveplate controlling polarisation of the dressing field to set polarisation to perpendicular.
4. Acquire image with perpendicular dressing field polarisation.
5. Move to delay position 2.
6. Acquire image with perpendicular dressing field polarisation
7. Rotate waveplate controlling polarisation of the dressing field to set polarisation to parallel.
8. Acquire image with parallel dressing field polarisation.
9. Move in dressing field beam block.
10. Acquire static absorption reference.
11. Move out dressing field beam block.
12. Move to delay position 3.
13. ... etc.

where the different dressing field polarisation states to be compared were interleaved to improve the comparison between them.

In reality, there were also many other processes required to control the parameters in the different scans, for example due to the polarisation dependent reflectivity coefficients for non-normal reflection from silver and gold surfaces, the IR dressing field intensity calculated for the perpendicular aligned polarisations compared with the parallel alignment was reduced. For each polarisation scan we would therefore calibrate the motorised iris in the dressing field arm for the parallel alignment to compensate for the energy lost in the perpendicular case. In doing this, an additional process of moving the dressing field iris to calibrated size is therefore required before each new acquire image with parallel dressing field polarisation instruction. Conversely, an open dressing field iris instruction is also then required before each acquire image with perpendicular dressing field polarisation instruction as well. A schematic of a typical polarisation scan instruction sequence can be seen in Figure 4.11.

To reduce the size of the recorded scan data, cropping of the detector camera array was implemented. This was particularly important for the 1400 nm data since in the new acquisition framework, all of the recorded data images were saved rather than just the average and standard deviation as for the earlier 800 nm work.

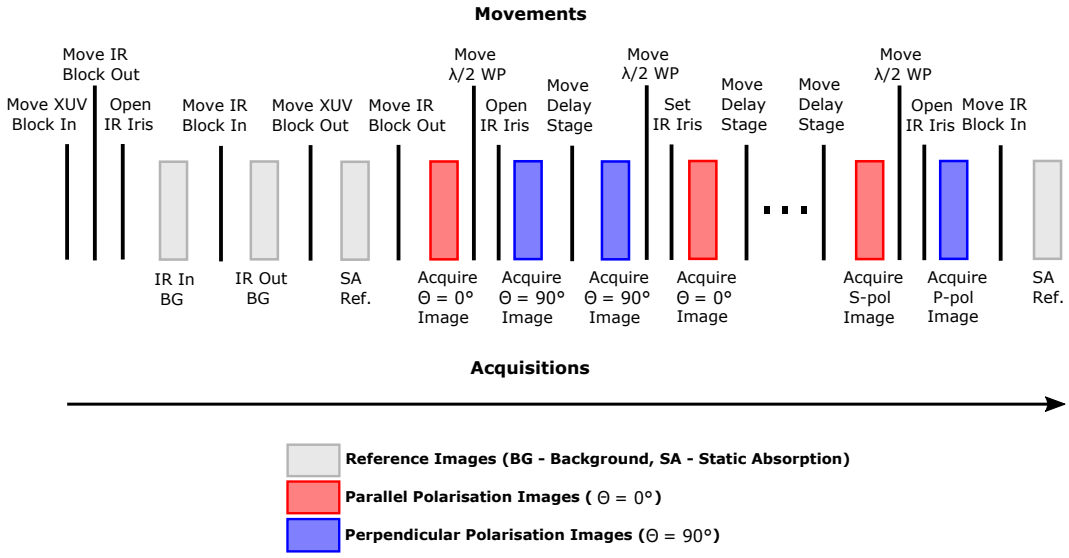


Figure 4.11: Schematic of a typical scan procedure used to perform the 2-dimensional polarisation dependence transient absorption scans.

An additional acquisition control implemented for the 1400 nm work was the ability to pause the delay scan, and re-start the acquisition a short while later. This was particularly useful for instances where sudden, known changes occurred in the setup such as a sudden spike in the generation target backing pressure. If identified quickly, the scan could be paused, the pressure corrected and the scan resumed with only a small interruption in the recorded data.

4.9.2 Data Processing

The same data processing principles used for the 800 nm work were required to process the 1400 nm wavelength scans. For the majority of the longer wavelength work, long duration scans covering large portions of the pump-probe interaction overlap were recorded, relaxing the requirement for careful modulation matching of the data prior to Fourier transform since the resolution in the Fourier domain was much higher.

The energy spacing of the krypton edge harmonics was such that box selection was impossible. All the 1400 nm wavelength data is instead presented on delay vs. photon energy 2D plots, with corresponding Fourier frequency vs. photon energy 2D maps to explore the comprising frequency components. As before, the phase delay temporal correction was applied requiring interpolation onto a linear delay axis prior to the Fourier transformation. Isolating and removing the zeroth order component allowed mean-free data to be presented.

Options to select the range of the divergence axis of the imaging MCP allowed control over the amount of on-axis and off-axis signal summed for each data point. In general smaller divergence

regions were selected to try to isolate effects occurring just from the on-axis harmonics.

Due to the increased referencing, normalisation was performed using both the recorded static absorption (field-free transmission) reference scans, interpolated to correct for slow drifts in the apparatus and changes to the spectral profile of the source harmonics, as well as intensity normalised using a slice of the spectrum where no delay dependent modulations occur. The intensity normalisation region selected depended on the target gas, with higher order above ionisation threshold non-modulating harmonic(s) selected for the helium work, and a lower order below ionisation threshold harmonic range selected for the krypton studies. Figure 6.17 a) shows an example of the intensity normalisation range selected for a helium scan, with the normalisation value for each delay point given by the range summed between the two vertical black lines. In Figure 6.17 b) the improvement to the raw data acquisition through normalisation can be observed.

For the longer delay range scans, analysis of the Fourier components could be performed by sliding a filter window across the delay range, Fourier transforming just the modulations within the window rather than using the whole delay range. The window was chosen to be a 6th order super-Gaussian, 15 fs FWHM in the temporal domain so as to select a sufficient number of oscillations to allow good resolution in the Fourier domain, whilst still enabling fine sampling across different regions of the scan envelope. Smooth attenuation of the edges of the filter window reduces artefacts in the Fourier domain. Using a 1400 nm driving laser wavelength, a full ω_1 cycle period corresponds to $\sim$4.7 fs. The 15 fs temporal window therefore samples approximately three full laser cycles corresponding to six $2\omega_1$ modulations, twelve $4\omega_1$ modulations and so on. When considering the scan in its entirety, since some dynamics may only be present for short durations i.e. only around the peak overlap of the dressing field envelope, sampling small temporal and spectral windows is important for observing modulations that may otherwise not be resolved above the noise. In addition, since full interaction envelope scans can take in excess of 2-hours to perform, sampling smaller temporal windows across the delay range ensures any effects due to long-term drifts in the system are minimised.

As explained previously in the Calibration section, the experiments performed using the 1400 nm field with the krypton target were evaluated using the second order light visible on the MCP due to the increased resolution it provided. The energy axis was therefore scaled back to the correct energy values following the data processing.

Chapter 5

Transient Absorption from 800 nm Laser Dressed Helium

In this Chapter I will present the results obtained by studying the transient absorption from field-dressed helium using an 800 nm wavelength dressing field. I will present results observing the effects on the delay dependent modulation amplitude as the dressing field polarisation and intensity are varied as a function of delay. Our results expand upon the current literature, pushing the intensity of the laser dressing field beyond that typically studied before, extending the understanding of the strong field response of laser-dressed helium at sub-cycle timescales.

The work presented in this Chapter expands upon work previously published in reference [35]. Many similar observations, discussions and conclusions are therefore made as compared with reference [35].

There were several important reasons for choosing helium as the target atom for the early studies. These were:

- Helium is a stable, inert gas. Technology to insert gaseous samples into vacuum is well established, and the properties of helium make it easy to handle and dispose of safely.
- Helium is the simplest multi-electron atom. Laser-dressed absorption studies are a convenient way to commission and characterise a beamline. In addition, it is convenient to use a simple target for which much is already known.
- Helium possesses the highest first ionisation threshold of any atom (24.59 eV). To generate high order harmonics directly from helium one therefore requires extremely high dressing field intensities. Approximating the OTBI threshold from equation 2.27 we find the field intensity required to OTB ionise helium is $\sim 1.5\times10^{15}\,\mathrm{W/cm^2}$. This approximate value is verified experimentally by the literature [155] using a picosecond, 1.053 μm laser. Full barrier

suppression is not required for harmonic generation however, and it is found that the onset of tunnel ionisation occurs with intensity fields from mid-10^{14} W/cm^2 [156]. Due to the magnitude of the intensities required for direct high order harmonic generation from helium we can be confident that the dressing-field intensities used for our experiment will always be lower than this threshold. This prevents additional signal being produced and detected alongside that from the transient absorption process. It should be noted however that at the dressing field intensities investigated, the possibility for XUV initiated high harmonic generation (XiHHG) exists [19, 128, 157]. For an XiHHG event the ionisation occurs through a single XUV photon process, removing the requirement for strong field tunnel ionisation.

- The energy separation between first and second ionisation thresholds is large (54.42 eV). Following ionisation of the first electron, the second ionisation threshold is significantly separate in energy not to warrant concern about doubly ionising the system if careful selection of the probing harmonic spectral shape is applied. Since the conversion efficiency of high harmonic generation is very low, one can assume interactions with the low flux APT are linear. This means so long as the cutoff energy for the probing APT falls below the energy requirement for double ionisation, ~79 eV, and double excitation, ~60 eV [154], each interaction between the XUV and the helium results in single excitation or ionisation.

- The overall energy required to ionise the ground state is low. Although the first Ip of helium is high, overall the spectral energy requirements demanded from the APT are modest i.e. the cutoff only needs to extend to a few harmonic orders beyond the first Ip of helium. When probing core states in larger atoms, much higher energy photons are required to ionise the tightly bound electrons.

- For the reasons already stated, helium was used also in other laser-dressed transient absorption studies at lower dressing field intensities which we can use as a benchmark of our results before pushing towards new studies using higher intensity dressing fields [35].

Figure 5.1 depicts the lowest ten singlet electron energy levels in helium (S=0), as well as a typical probing source harmonic spectrum. The electronic configuration of the ground state of neutral helium is $1s^2$, with both of its two electrons residing in the innermost, closed electronic shell. This closed shell structure gives rise to its characteristics: atomic, inert and high Ip. Since photons carry an angular momentum of $\ell = \pm 1$, this restricts the single photon transitions that can occur between bound states of the helium atom. To excite an electron from one atomic state to another, angular momentum must be conserved, limiting any single photon process from the ground state in helium to excite to a p-orbital. The rules governing the conservation of quantum numbers are commonly referred to as the selection rules for transitions. It is observed that each of the helium

excited states can be reached via appropriate sequential or non-sequential multiphoton transitions, provided the angular momentum is conserved.

For the reasons already highlighted above, there are many advantages to studying the transient absorption from laser dressed helium atoms, and consequently much previous work has already been performed investigating different aspects of the laser dressed helium response [19, 20, 104, 111–115, 117, 122, 159, 160]. What differentiates the work presented in this Chapter from many of the previous studies is the peak intensity of the laser dressing field. The work presented here focuses on the strong field response of helium atoms probed through transient absorption, investigating effects up to peak dressing field intensities of 2.4×10^{14} W/cm^2 [35].

5.1 Response to Varying the Pump-Probe Delay

We probed the strong-field dressed helium target using the precisely delayed source harmonic spectrum. Recording the transmitted XUV signal as a function of delay we were able to map out the sub-cycle response of the laser dressed helium target. Summing the divergence axis to produce a spectrum for each delay point, we could plot 2-dimensional delay-photon energy maps where each column represents a different pump-probe delay slice. An example can be seen in Figure 5.2 a). Following interpolation of the phase corrected delay axis, one can then Fourier transform along the length of each row to extract a 2D Fourier map of the constituent frequencies (Figure 5.2 b). Both Figure 5.2 a) and b) have been rescaled to be linear along the energy axis. A Jacobian has been applied to correct the rescaled amplitude [161]. This data was recorded by averaging five images of 1 s exposure each per delay point. The interaction was sampled every 200 as using the fine delay stage. The interaction target helium backing pressure used was 50 mbar.

Representing the data in this form allows the dissemination of large amounts of information direct from a single plot. For example information about the phase variation across the spectrum can be observed directly, with sub-harmonic phase differences manifesting as a slant to the harmonic modulation. This can be observed for the below Ip harmonics (harmonics 13 and 15). Additionally, the higher modulation depth in harmonic 13 towards the right hand side of the plot indicates that we have scanned over one edge of the interaction envelope. This means there will be an inherent dressing field peak intensity variation across the scan, with the intensity decreasing from left to right. The low frequency components have been removed from each row of the presented data so the modulations are shown around a zero offset. The phase delay has been smoothed using a third-order polynomial fit, and both the energy and delay interpolation have been performed using a piecewise cubic polynomial.

Towards the central overlap of the pump-probe envelopes (the negative end of the presented delay axis) we estimate a peak intensity to be 2.4×10^{14}W/cm^2. At this intensity we did not detect any

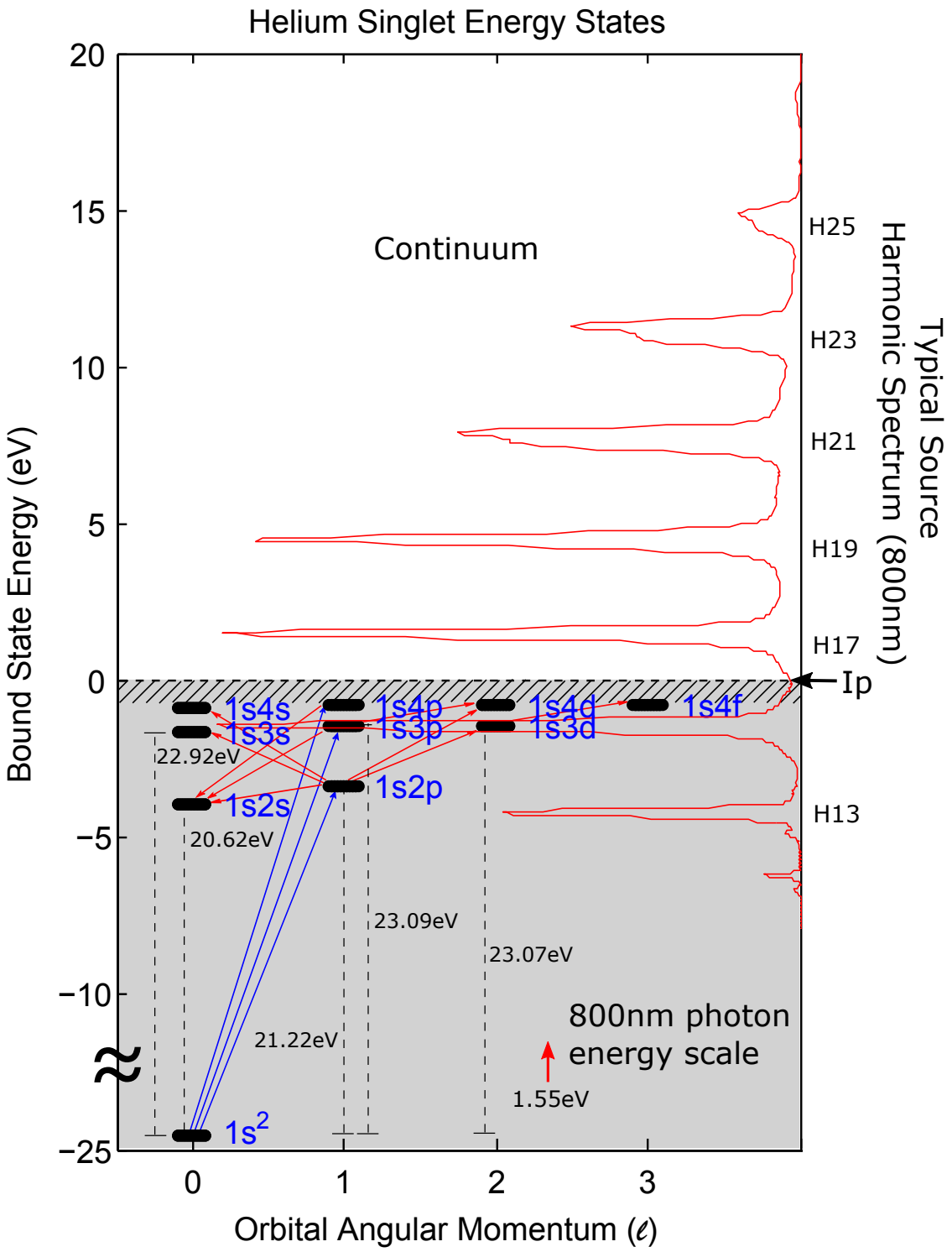


Figure 5.1: The ten tightest bound helium singlet energy states as a function of orbital angular momentum and binding energy. Some of the available excitation pathways have been highlighted with arrows representing photon absorption or emission. The singlet electronic shell energies were taken from the NIST catalogue [158]. The energy separation of some of the states are also highlighted. The overlay shows a typical APT probe spectrum for 800 nm, indicating the position of the different harmonic orders with respect to the undressed helium states. An 800 nm IR photon is also drawn for scale.

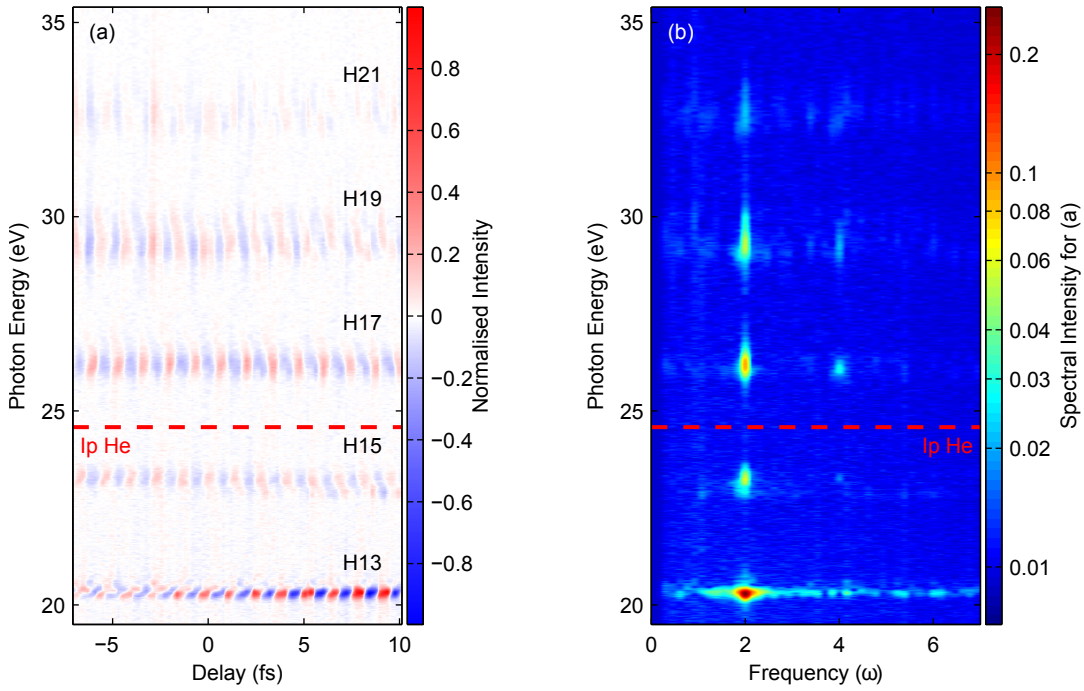


Figure 5.2: a) Transient absorption signal as a function of delay for a dressing field intensity 2.4×10^{14}W/cm^2. The background free data has been presented following high-pass filtering of the delay axis. b) Fourier map of the delay scan shown in a) indicating the different frequency components comprising the modulations in a). This Figure has been reproduced from reference [35]. © IOP Publishing. Reproduced with permission. All rights reserved. CC BY 3.0.

harmonic orders produced directly from high harmonic generation in the helium target. It is clear from Figure 5.2 b) that modulations at both $2\omega_1$ and $4\omega_1$ are present in the recorded delay dependent absorption data, where ω_1 is the frequency of the driving laser. Modulations at $2\omega_1$ appear in all the harmonic orders, indicating a coupling between all adjacent harmonics, where modulation in the absorption at $2\omega_1$ arises through the modulation mechanisms described in Chapter 2.5.2. We describe the harmonics as being coupled since light absorbed at harmonic n with the addition or subtraction of m IR photons will interfere with light present at harmonic $n+m$ or $n-m$ respectively. In this way the behaviour of one harmonic can influence the detected signal of another harmonic and vice versa. The idea of coupled harmonics is discussed in both reference [104] and [113], among others. Modulations at $4\omega_1$ appear strongest in the above Ip harmonic orders 17 and 19. As noted in Figure 4.3, harmonic 11 is blocked by the aluminium filter and so the entire $2\omega_1$ contribution in harmonic 13 must arise from coupling with harmonic 15. Modulations with a frequency of $4\omega_1$ indicate a coupling between harmonic orders separated by one odd harmonic.

Presenting data as 2-dimensional plots is particularly effective for long delay scans where many cycles of the driving laser are covered. Scans covering many modulations improves the resolution in the Fourier domain, and relaxes the effects of stitching artefacts introduced through selection of an arbitrary length delay period before performing the Fourier transform.

For the majority of this early work the individual delay scan durations were short to minimise drifts in the setup over the course of the scan time. Usually delay scans were recorded over nominally 6 fs delay, spanning over two full periods of the 800 nm cycle length. At 800 nm a single cycle period corresponds to 2.67 fs. This ensured that in almost all scans, four full $2\omega_1$ periods were recovered following rescaling adjustments from the phase tagging. For the universal analysis framework, three full $2\omega_1$ cycles were selected for each delay scan to ensure all data sets could be processed with the same code. With such short scans, selecting appropriate delay lengths and interpolation parameters becomes more important since the resolution in the Fourier domain is reduced. The methods used to select the data are discussed in more detail in the 800 nm Specific Methods section in Chapter 4. The result, however, was to select small spectral-spatial boxes around the central region of each harmonic order, summing the contents to give a value of the harmonic signal for that particular delay. This method presented additional benefits such as being able to plot real-time updates to the measured signal with the available software at the time, as well as minimising effects of detector damage issues which were also discussed in Chapter 4.

With boxes selected around the brightest, central region of the detected harmonics, the recorded delay dependent data could be presented such as in Figure 5.3. Here we see a typical non-phase corrected delay scan over the majority of the central overlap of the pump-probe envelopes. The peak intensity of the dressing field was estimated to be $1.9\times10^{14}\mathrm{W/cm^2}$, and three images of 1 s exposure were averaged per delay point. The interaction was sampled every 300 as, with a backing pressure of

~50 mbar helium in the interaction target. The probing XUV signal was generated by focusing the 800 nm generation arm light into a 100 μm krypton effusive gas jet. Krypton was used to generate the XUV probe harmonics for all of the 800 nm helium transient absorption results.

We observe in Figure 5.3 that as the dressing field envelope is scanned with respect to the APT, the below ionisation threshold harmonics are strongly modulated. This is because although the below Ip harmonics are insufficiently energetic to single photon ionise the helium target in isolation, both harmonics 15 and 13 can excite or ionise the strongly-dressed helium target via the different mechanisms presented in Chapter 2, Figure 2.11. For particular experimental runs we observed a clear reduction in absorption of the above ionisation threshold harmonic signal with respect to the undressed absorption. This can also be seen in Figure 5.3. Here we observe a clear reduction in absorption of harmonic 19, well above the undressed absorption level which is approached towards the 60 fs edge on the delay axis. The increased transmission (reduced absorption) of the below Ip harmonics towards each edge of the scan clearly indicates the range of the interaction envelope. For this reason the signal values around 60 fs can act as an approximate field-free reference value for the above ionisation threshold static absorption. A separate static absorption reference spectrum was not acquired for this particular scan.

The relative increase in harmonic 19 signal could be indicative of an XiHHG process occurring; locally more light is being recorded for the laser-dressed target at this frequency than was estimated for the field-free absorption. For a net gain in HHG signal however, more light would need to be detected for a given frequency following interaction than was initially incident on the target, i.e. one would need to record more light at a particular frequency than was present in the source harmonics reference. A simple way to do this would be to produce light at a harmonic order not present in the incident source harmonic spectrum. Only a small signal would be required since this light would automatically be generated on a zero background. This would, however, be impossible for the experimental conditions presented in Chapter 5, where the harmonic cutoff extends beyond the edge of the MCP detector area. The alternative way to prove an XiHHG signal is to detect more light at the output than in the source harmonic spectrum for a harmonic present itself in the source spectrum. We observed however that often as much as 80% or more absorption of the incident signal would occur in the static absorption reference alone. This ensured that by using this method it was also impossible to detect an XiHHG signal with the experimental conditions used in Chapter 5.

An alternative explanation arises by considering the AC induced Stark effect. If we recall from the AC Stark Shift section in Chapter 2, the effective ionisation energy varies with the intensity of the dressing field. The Stark shift of the Rydberg states approximates that of the continuum levels, the ponderomotive energy, Up, whereas the tightest bound states shift very little [124]. For an 800 nm wavelength laser field at an intensity of 1.9×10^{14}W/cm^2, the ponderomotive energy is found to be 11.6 eV. For the undressed atom, harmonic 19 falls 4.9 eV above the ionisation threshold, well

below the potential dynamic Stark shift applied to the ionisation threshold. If this result were due to the AC Stark shift, one might expect to see a similar reduction in absorption for the harmonic 17 response as well. Since the AC Stark shift does not affect each bound state equally, it is possible that reduced absorption occurs only for harmonic 19.

One point to note here is that due to the linear process of single photon ionisation, both helium within the tube target length, and low levels of background helium within the target chamber will contribute to the total level of static absorption recorded. Helium within the target will be dressed by the intense laser field. Helium positioned away from the target focus will add to the static absorption, but not add to the interaction dynamics, or add with a different phase due to the effect of a lower dressing field intensity. Since we cannot know the different levels of contribution to the total static absorption for the concentrated and residual helium, to minimise this effect, differential pumping was employed around the tube target to lower the immediate background pressure, as well as the operational base pressure of the target chamber, minimising any contribution from residual helium far from the focus.

5.2 Relative Dressing Field Linear Polarisation Response

Scanning further parameters in addition to the delay allowed us to perform 2-dimensional scans, comparing the recorded dynamics as a further variable is adjusted. Of particular interest was comparing the delay dependent absorption modulation response for strong-field dressed helium when the linearly polarised dressing field was aligned either parallel, or perpendicular with respect to the polarisation direction of the probing XUV field. Similar polarisation studies comparing the response due to the relative linear dressing field polarisation direction, as well as the effect of using an elliptically polarised dressing field, had previously been conducted at intensities of the order of $10^{12}\,\mathrm{W/cm^2}$ [114, 115]. Although these dressing fields can appear strong to bound electrons excited by XUV photons, the dressing field alone only weakly distorts the helium ground state. Extending the question of the response to dressing field linear polarisation to intensities approaching the strong field ionisation threshold of the helium ground state, we present in Figure 5.4 i) the comparison between parallel and perpendicular aligned pump-probe linear polarisations for an estimated experimental dressing field intensity of $1.3{\times}10^{14}\,\mathrm{W/cm^2}$. In Figure 5.4 i) a), b), e) and f) we see the experimental results showing the delay dependent modulation depth observed for the above *Ip*, a) and b), and below *Ip*, e) and f), harmonic probes when the dressing field linear polarisation is aligned parallel with (Θ=0°) and then perpendicular to (Θ=90°) the direction of the APT linear polarisation. Theoretical results calculated by Dr Marco Ruberti at Imperial College London using the recently developed *ab initio* single atom time-dependent Schrödinger equation (TDSE) calculation with B-spline ADC [153] are also shown, c), d), g) and h). The theoretical results were calculated

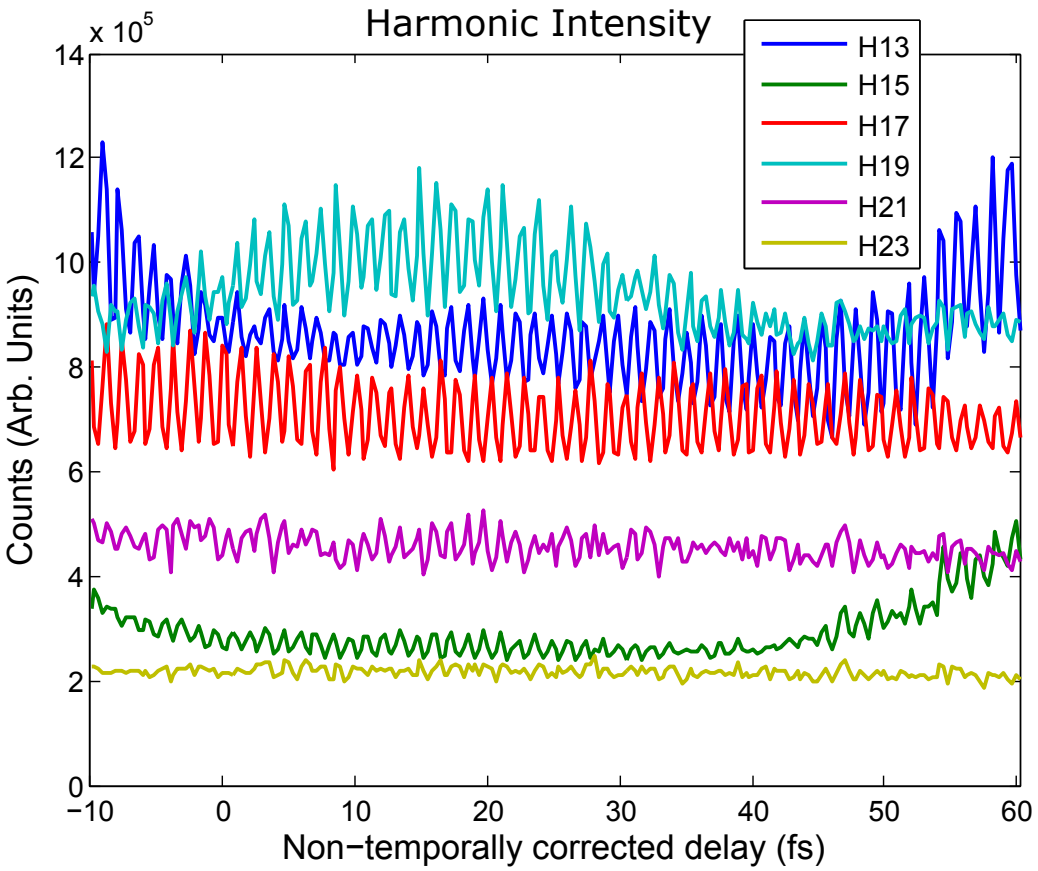


Figure 5.3: Delay scan showing the intensity of the harmonic orders for a large portion of the pump-probe interaction envelope. Increase in the harmonic 19 transmission is observed around peak overlap of the pump and probe pulse envelopes relative to the levels at the edges of the scan. Although the IR field is still present for the extreme edges of the scan, the field magnitude is reduced indicating approach towards the field free absorption levels. The estimated peak dressing field intensity is $1.9\times10^{14}\mathrm{W/cm^2}$.

assuming a similar peak dressing field intensity as that determined for the experimental results, 1.2×10^{14} W/cm^2. A brief overview of the theoretical methods can be found in the 800 nm Specific Methods section in Chapter 4, and a more detailed overview in reference [35].

Observing first the harmonic response of the above Ip probes, harmonics 17 (H17) and 19 (H19), it can be seen that as the linear polarisation of the dressing field is changed from parallel to perpendicular with respect to the XUV field, the amplitude of the observed delay dependent modulations is dramatically reduced. This strongly anisotropic response is mirrored qualitatively by the theory. For the below Ip harmonics however, little effect in the experimental modulation depth is observed as the dressing field linear polarisation changes from parallel to perpendicular. The below Ip theory again qualitatively captures the harmonic 13 (H13) response, but less well captures the change to the harmonic 15 (H15) modulations. The dashed lines shown for the above Ip harmonic orders represent the undressed absorption cross section for helium, obtained from reference [152]. The field-free absorption cross section values for H13 and H15 are both zero since both of these harmonic orders fall below the first ionisation threshold in helium. The absorption cross section for both the experimental and theoretical results is presented in megabarns (Mb).

Qualitative differences in the theoretical results and those obtained through experiment for harmonic 15 (directly below the ionisation threshold) could be attributed to small discrepancies between the theoretically calculated field-free states in helium compared with the field-free values given by NIST [158]. A comparison of the theoretically calculated singlet states along with the NIST singlet values can be seen in Figure 5.5 a), with the energy difference for each singlet state plotted in Figure 5.5 b).

We observe a separation of 0.4-0.5 eV for each of the states compared, with the general trend that the separation reduces as we near the Ip. For the inner-most, well separated states this matters less since the possibility of shifting one of these states through AC Stark interaction with the intense dressing field onto an energy present in the harmonic APT is unlikely. For the densely populated Rydberg states directly below Ip however, small discrepancies in energy can easily change whether a state lies resonant or not with a particular harmonic energy. As such, we understand harmonic 15 falling just below the Ip of helium will be most sensitive to this in the theoretical calculation.

As discussed previously in the Modulation Mechanisms section 2.5.2, the energy shift of the Rydberg states due to the AC Stark effect is approximately equal to the ponderomotive energy, Up. The ponderomotive energy for an 800 nm field with intensity 1.3×10^{14}W/cm^2 is approximately 7.8 eV. This is significantly larger than the 0.5 eV offset.

Since the theoretical calculation is for a single atom response, not taking into account any macroscopic effects such as phase matching or reabsorption, only qualitative comparisons can be made between the experimental results and theory. Understandably the predicted modulation depths for the theoretical calculation are therefore much larger than those measured in the experiment. In

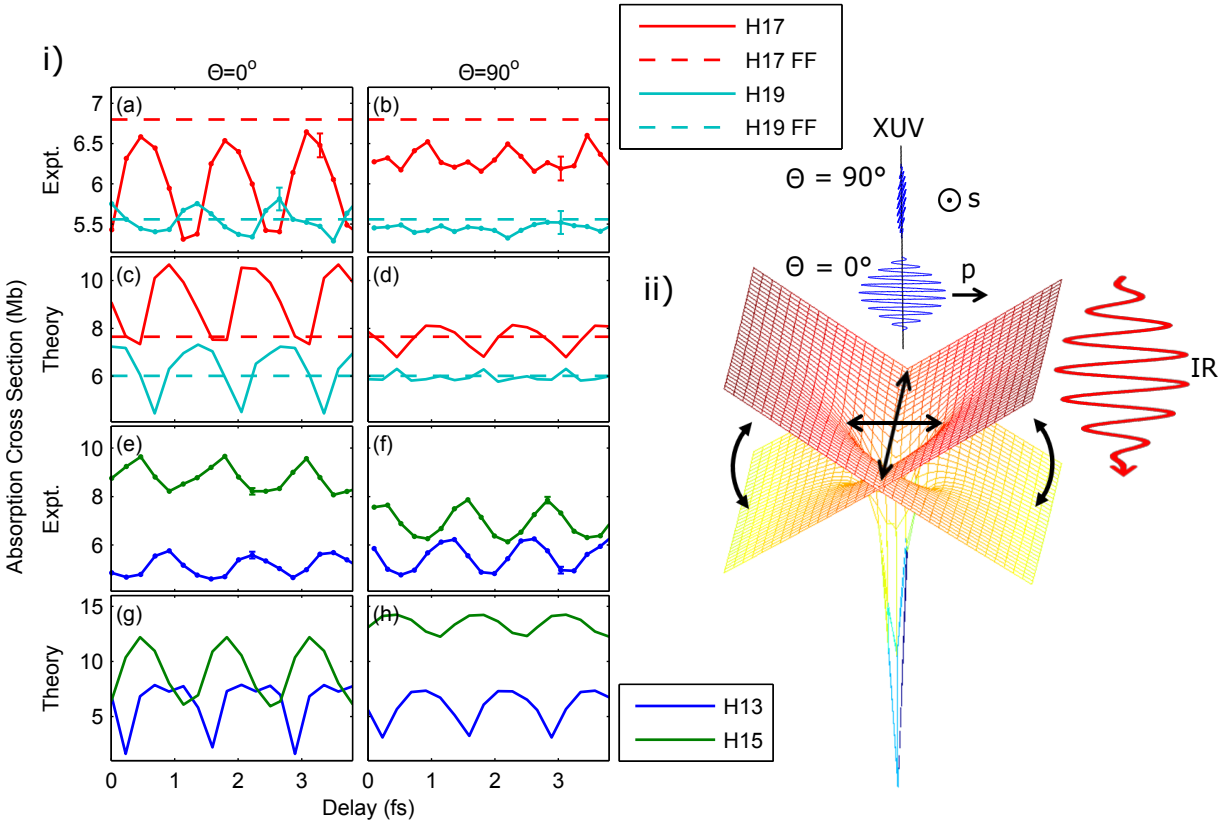


Figure 5.4: i) Experimentally measured delay dependent response of the absorption cross section as a function of parallel, a) and e), and perpendicular, b) and f), aligned pump-probe linear polarisation alignments. Theoretically calculated absorption cross sections, c), g), and d), h), for the corresponding polarisation alignments are also shown. The presented results are split, displaying separately the above (red, cyan), and below (blue, green) *Ip* harmonic order response. The undressed absorption cross sections [152] are shown as dashed lines in a)-d). The dressing field peak intensity was determined to be 1.3×10^{14}W/cm^2. ii) Cartoon to illustrate the geometry resulting in the experimentally observed anisotropy in the recorded absorption modulation amplitude for the above ionisation threshold harmonic orders as the dressing field polarisation is aligned either parallel or perpendicular with respect to the probing XUV polarisation direction. This Figure has been modified from reference [35]. © IOP Publishing. Reproduced with permission. All rights reserved. CC BY 3.0.

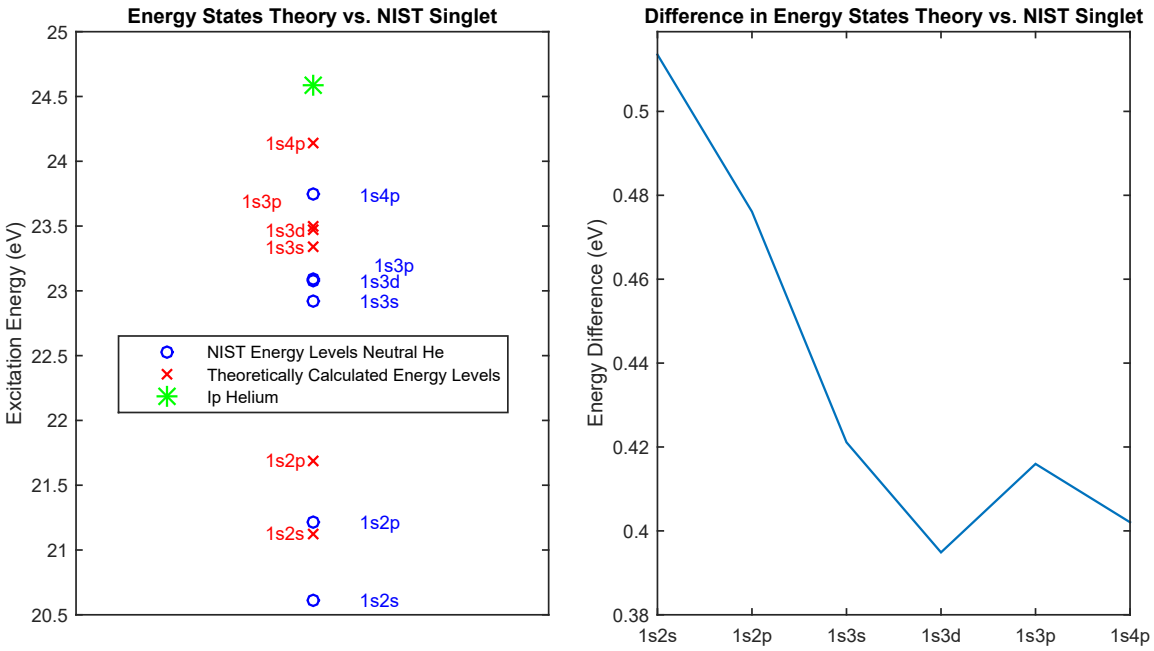


Figure 5.5: a) Singlet energy states of helium from the NIST catalogue [158] compared with the singlet energy states obtained using the theoretical calculation presented in reference [35]. The energy difference between the two sets of states is plotted in b).

addition to macroscopic effects, other experimental factors that could lead to discrepancies between the experimental results and theory include:

- Intensity distribution of the experimental IR dressing field in the interaction target due to finite sized pump and probe foci. The theoretical calculations were performed for a peak dressing field intensity of $1.2\times10^{14}\mathrm{W/cm^2}$, however the spatial energy distribution of the experimental pump-probe foci means that a range of intensities will be probed simultaneously for each stated peak experimental intensity.

- Uncertainty in the peak intensity due to the selection of the 6 fs scanning delay range within the envelope of the IR dressing field. The experimental peak intensities estimated were obtained for the peak overlap of the pump-probe pulse envelopes (often known as absolute time zero, or t=0). When running short delay scans there is no direct reference as to where within the dressing field envelope the scan is occurring.

- Uncertainty in the spatial pump-probe overlap.

- Uncertainty in the actual intensity. Given the points raised above, and errors associated with the intensity calculation, we estimate an error of $\pm50\%$ for all the stated intensity values.

It should be noted that when considering the identification of the t=0 position, even having

observed the full interaction envelope, reference [113] suggests that a better way to locate the exact t=0 value is to consider the central position of any signal modulating at $4\omega_1$, a frequency not present in either the pump or probe pulses. The results presented in reference [113] indicate a symmetric measurement of the $4\omega_1$ modulation response, compared with an inherent asymmetry in the $2\omega_1$ absorption envelope resulting from the difference between the dressing field either preceding, or following the XUV probe. In future experiments a better estimate of the t=0 delay could enable more accurate dressing field intensity determination.

We can understand the vectorial response of the delay-dependent modulation amplitude through consideration of the heuristic model shown in Figure 5.4 ii). When considering the direction of the induced dipole from the XUV APT interaction with the helium, if the dressing field is aligned parallel with respect to the XUV field, the dipole experiences maximum modulation of the strong-field dressed helium target. If instead the dressing field is perpendicularly polarised with respect to the XUV field, minimum modulation of the bound potential is probed.

Absolute time zero was not measured for the experimental data. The absolute delay in the presented figures is therefore unknown. Consequently, absolute phase between experiment and theory, and between the two Θ=0° and Θ=90° experiments cannot be directly compared, however relative phase between the harmonics for each corresponding panel can be (i.e. harmonics obtained within the same delay scan). For example a similar relative phase between harmonics 17 and 19 in the experimental and theoretical results is observed in Figure 5.4.

Attempts to reference the absolute phase were made by performing effective high-order autocorrelation measurements between IR light propagating down each of the pump and probe beam paths and generating harmonics in a low Ip gas in the target chamber. The IR light could propagate along the generation beam-path by removing any gas from the generation target, and removing any subsequent spectral filtering. Modulations in the yield of produced harmonics could be detected with a period of $1\omega_1$ as the dressing field was delayed with respect to the IR light propagating along the generation beam path. The peaks of these modulations correspond to overlap of the electric field amplitude peaks between the pump and probe pulses, referencing the phase of the dressing field to the phase of the light used to generate the APT. The presented experimental delay scans in this Chapter have been shifted along the time axis to match this reference, however this value does not account for any change in phase between the generating IR field and the resultant harmonic pulse train. Additionally, long, high resolution IR-IR autocorrelation scans would need to be performed to accurately determine the exact absolute zero delay which were not done.

5.3 Response to Varying the Dressing Field Peak Intensity

Another parameter we varied as a function of delay was the dressing field peak intensity. Performing scans covering two orders of magnitude (2.3×10^{12}W/cm^2 - 2.3×10^{14}W/cm^2) we extended the intensity range over which previous studies had investigated [111–113]. It is difficult to compare the results from previous studies with those presented here for a number of different reasons including the number of sampling points in common between the different dressing field intensity scans. Considering reference [113], where the $2\omega_1$ and $4\omega_1$ oscillator strengths of harmonics 13 to 17 are compared as a function of dressing field intensity between 2.7×10^{12}W/cm^2 and 1.1×10^{13}W/cm^2 in helium, only approximately three intensity points fall close to, or within this range in our presented results. For these points it is observed that the general qualitative trends within this range do not agree between reference [113] and our presented results, however it is possible that differences in the experimental setup and conditions between the experiments could account for these differences.

Observing the delay dependent modulation amplitude for modulation frequencies $2\omega_1$ and $4\omega_1$ as the peak dressing field intensity is varied, we can gain insight into the effect peak dressing field intensity has on the absorption cross section modulation amplitude. Figure 5.6 shows the $2\omega_1$ and $4\omega_1$ modulation amplitude as a function of intensity, spanning the range 2.3×10^{12}W/cm^2 - 2.3×10^{14}W/cm^2. The experimental results are shown for the $2\omega_1$ response in panel a), with the $4\omega_1$ response shown in panel c). The experimental results are compared with theoretical results obtained using the same method as for the polarisation calculations. The theory is shown in panels b) and d) for the $2\omega_1$ and $4\omega_1$ response respectively.

We can see that qualitatively there are many similarities between the experimental and theoretically calculated results. Starting with the intensity response of the $2\omega_1$ modulation amplitude we observe similar trends between the experimental and theoretical results for each of the harmonic orders. For harmonic 13 the theory reproduces the rise and fall in amplitude with increasing intensity, and for harmonic 15 the double peak in the $2\omega_1$ amplitude is qualitatively reproduced. For the experimental above ionisation threshold harmonic response both harmonics 17 and 19 remain fairly flat across the intensity range. A slight rise in amplitude around 1×10^{13}W/cm^2 is predicted by the theory for harmonic 17, however otherwise the qualitative response is captured well. Similarly, considering the $4\omega_1$ modulation amplitude we again observe some qualitative similarities between the experimental results and theory. The response splits the harmonics into two groups following more similar trends: harmonics 13 and 17, and harmonics 15 and 19, each separated by 4 IR photons giving rise to the $4\omega_1$ coupling between the harmonics. This is observed in both the experiment and theory. Both harmonics 15 and 19 generally display low amplitude response except for a peak in harmonic 15 (and possibly harmonic 19) around 2×10^{13}W/cm^2. Similarly, the amplitude of harmonic 17 increases then decreases across the intensity range, and harmonic 13 rises with increasing intensity, evolving differently at the highest intensities. In addition, the higher intensity onset of the

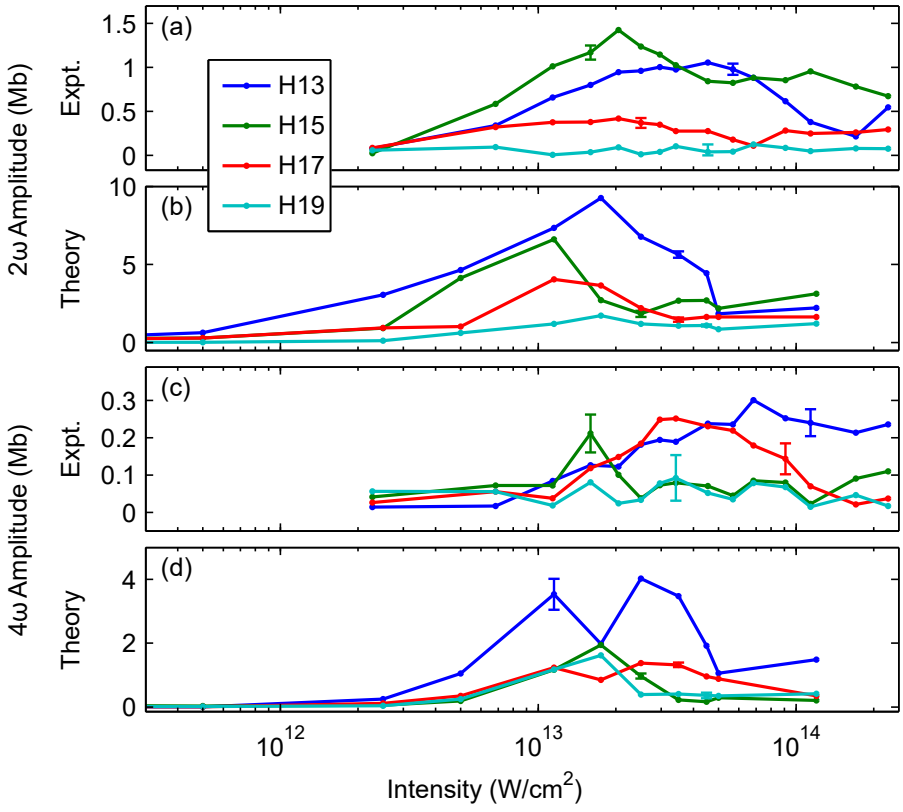


Figure 5.6: Absorption cross section modulation amplitude in megabarns (Mb) for the $2\omega_1$ and $4\omega_1$ frequency components as a function of dressing field intensity. a) and c) show the experimental results for $2\omega_1$ and $4\omega_1$ respectively. b) and d) show corresponding theoretical results. This Figure has been reproduced from reference [35]. © IOP Publishing. Reproduced with permission. All rights reserved. CC BY 3.0.

$4\omega_1$ modulations is also predicted by the theoretical model.

The behaviour of the $2\omega_1$ amplitude response can be understood by considering first the above ionisation threshold harmonic response. Since no additional dressing field is required to enable these harmonics to excite or ionise an electron in the helium target, their response varies little as the intensity of the dressing field is increased above a minimum value to enable the 2IR photon coupling. For the below ionisation threshold harmonics however, excitation and ionisation is only made possible through the dressing of the helium target with the intense IR field. As the dressing field intensity is increased, a steep increase in the modulation amplitude is observed in both harmonics 13 and 15 as their coupling increases. As a higher intensity still is applied to the helium target, many different excitation and ionisation pathways are available to the below ionisation threshold harmonics, complicating the dynamics and reducing the modulation amplitude through different phased responses. The response for the $4\omega_1$ amplitude is more complicated still, and although some understanding can be gained from the pairing of the harmonic orders (harmonics 13 and 17, and harmonics 15 and 19) in their response profiles, little more can be extracted other than the coupling strength between harmonics 13 and 17 seems to increase with dressing field intensity, however that between harmonics 15 and 19 remains around zero.

It was also observed for this particular scan that at the lowest dressing field intensities for particular delay times, the measured absorption cross section of the below Ip harmonic 13 became negative. This means that at these times we were recording more light at the detector for this frequency than was present in the input harmonic spectrum. The delay dependent absorption cross section modulations for both recorded below ionisation threshold harmonics (13 and 15) can be seen in figure 5.7. The absorption cross section modulations are shown for three different low peak intensity dressing field values (2.3×10^{12}W/cm^2, 6.8×10^{12}W/cm^2 and 2.0×10^{13}W/cm^2), spanning the value for which the negative absorption cross section was observed. The possibility for enhancement of the harmonic 13 signal relative to the source harmonic spectrum is discussed in reference [104].

Producing additional light relative to the input spectrum indicates a coupling between the response of different harmonic frequencies through addition or subtraction of a number of IR dressing field photons. By considering the bound states at these low dressing field intensities, it is clearer to understand the processes occurring in a photon picture, rather than using a field picture of the dressing IR.

Considering harmonics 13 and 15 in Figure 5.7 we observe that at the lowest dressing field peak intensity 2.3×10^{12}W/cm^2 neither of the harmonics modulate indicating neither one is coupled with any other harmonic order. The absorption cross section for harmonic 13 resides around zero indicating harmonic 13 does not lie resonant with any laser-dressed bound states. Harmonic 15 however is offset by just over 2 Mb. This absorption is attributed to the available direct excitation channel to the 1s3p state [20, 110]. At 6.8×10^{12}W/cm^2, both harmonics 13 and 15 modulate with

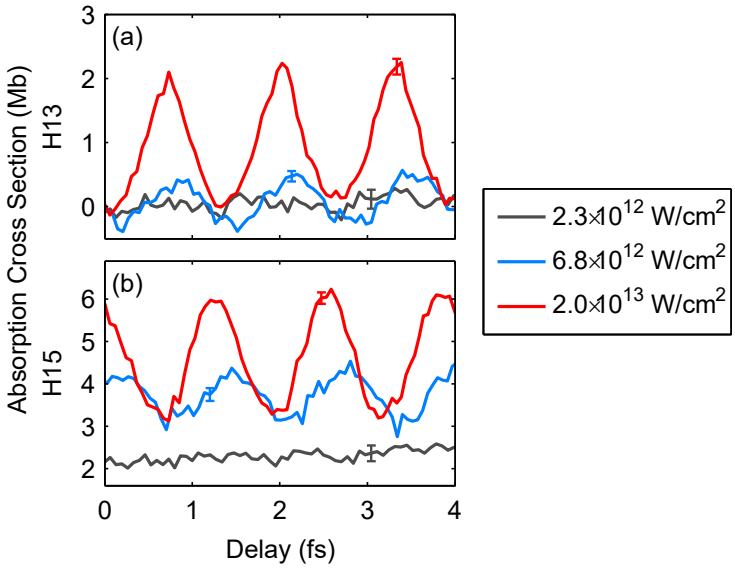


Figure 5.7: Negative absorption cross section obtained for a below ionisation threshold harmonic dressed with low peak intensity field (6.8×10^{12}W/cm^2). The absorption cross section for the below Ip harmonics 13 (a) and 15 (b) is shown as a function of delay between the pump and probe pulses for three different dressing field peak intensities. This Figure has been reproduced from reference [35]. © IOP Publishing. Reproduced with permission. All rights reserved. CC BY 3.0.

a clear $2\omega_1$ component indicating a 2IR photon coupling between the harmonic orders. Harmonic 13 modulates around a zero absorption cross section, indicating a continued lack of available direct or multi-photon excitation or ionisation pathways. By modulating around zero, this periodically provides delay times with negative absorption cross section corresponding to the generation of light twice per laser cycle. Harmonic 15 also modulates with an increased absorption cross section offset of ∼3.7 Mb, attributed to the increase in absorbance with peak dressing field intensity of the resonant 1s3p state [20].

Increasing the dressing field peak intensity further still to 2.0×10^{13}W/cm^2 we observe an enhanced modulation depth for both harmonics 13 and 15 indicative of a strengthening of the coupling between the two harmonic orders. We also observe an absorption modulation offset for harmonic 13 resulting in the entirety of the modulation now being above the zero absorption cross section threshold. Due to the increased shifting, splitting and broadening of the electronic states with increased dressing field intensity arising from the different modulation mechanisms discussed in Chapter 2, as the dressing field intensity increases, the conventional laser dressed atomic picture breaks down and identifying individual pathways becomes impossible. In addition, probing with an attosecond pulse train rather than an isolated attosecond pulse [20, 114] limits the spectral information to the harmonic frequencies rather than probing with a continuum. It was suggested previously [35] that the harmonic 13 offset could possibly be attributed to the availability through laser dressing of the

previously dipole forbidden XUV + 1IR multi-photon transition to the 1s3s bound state (see Figure 6.19 [20]). Another possible transition pathway could be the harmonic 13 XUV + 2IR photon transition to the 1s3p state. Although we understand the coupling between harmonic 15 and harmonic 13, evident at the dressing field intensity 6.8×10^{12}W/cm^2, to be based on the effect of resonant absorption of harmonic 15 with 2IR photon coupling to the harmonic 13 energy, since the harmonic 13 absorption is not directly resonant with any states, it is possible that coupling to harmonic 15 from a harmonic 13 photon + 2IR photons would onset at a higher dressing field intensity, leading to the observed results. The increase in coupling strength as a result of a resonant transition is discussed in reference [104].

5.4 Discussion

Reviewing the data recorded using the 800 nm driving laser field, several important observations can be made. To start, the maximum frequency modulation observed in the recorded transient absorption spectra is $4\omega_1$. With the phase tagging resolution of better than 150 as, this would imply modulations up to $8\omega_1$ should be resolvable if present in the recorded signal. The absence of modulations at this frequency indicates that either they truly do not exist, or that we cannot resolve them due to a further limiting factor. It was observed that the short-term intensity fluctuations of the Red Dragon laser led to considerable noise on the transient absorption scans. The low amplitude of any high order modulations appearing in the detected harmonic signal will make resolving the modulation above the noise from the laser intensity fluctuations very difficult. For future experiments, improved laser stability, referencing and normalisation techniques could help to extract higher order signals.

Another related point of note is the lack of directly observed XiHHG signal. Gademann *et al.* [19] observed a clear XiHHG response for laser dressed helium at an intensity covered within our tuning range, 5×10^{13}W/cm^2. The signal reported in reference [19] corresponds to a minimum coupling separation of $6\omega_1$ photons, indicating coupling between harmonics separated by two further harmonic orders. The signal produced was unambiguously XiHHG in origin since photons were produced at harmonic frequencies not existent in the probing source harmonic spectrum. This was made possible through the detection of the source harmonic cutoff within the detector energy range. Observing a small signal on a zero background is much easier than resolving a small enhancement to an already existent, fluctuating signal. In our experimental setup, the source harmonic spectrum filled the MCP detector, making it impossible to view an unambiguous XiHHG response. Resolving higher order modulation could have been indicative of an XiHHG process, however due to the other modulation mechanisms that can cause delay dependent absorption of the probing harmonics, actual enhancement is the only truly clear method of measurement.

Comparing our relative dressing field linear polarisation results with those obtained by Reduzzi

et al. [114], we find general agreement regarding a strong vectorial response to the changing relative dressing field polarisation direction. With the specifics, however, significant differences are observed which we can attribute to the two orders of magnitude difference in the dressing field intensities under which the experiments were performed. Reduzzi *et al.* probed with an isolated attosecond pulse a dressed helium sample with dressing field intensity $\sim 1\times10^{12}\mathrm{W/cm^2}$. The work concentrated on resolving the bound state response in the multiphoton picture to the parallel and perpendicular dressing and probe field polarisations. With a manifold of p-states populated via single photon absorption of the isolated attosecond pulse, it was observed that in the parallel dressing field alignment there was strong coupling to states with m=0. For the perpendicular alignment however, due to selection rules, coupling was restricted to m=±1, resulting in a significant reduction in the quantity and amplitude of recorded delay dependent absorption modulations.

For our experiment, we dressed the target with an field intensity of $1.3\times10^{14}\mathrm{W/cm^2}$. At these values where we start to approach the strong field ionisation of the helium target, the conventional multiphoton picture of the dressed atom breaks down. With such high intensity, the energy levels become shifted, split and mixed due to the AC Stark effect, making it impossible to assign any below ionisation threshold modulation to the transition between any two particular states. In addition to this, we probed using an attosecond pulse train resulting in non-continuous energy resolution, information was only obtained for certain frequencies corresponding to the harmonic orders. The result is that we observed little change in the delay dependent modulation amplitude of the below ionisation threshold harmonics as the dressing field polarisation was changed from parallel to perpendicular with respect to the XUV probe field. This could be understood through the large number of available pathways for the below ionisation threshold harmonics to become absorbed for both the parallel and perpendicular alignments of the dressing field relative linear polarisation. The above ionisation threshold response was strongly anisotropic however, with a sharp reduction in the modulation amplitude for the perpendicular alignment. This we understood through a heuristic picture of the field-induced dipole shown in Figure 5.4.

It was also observed that for some scans different regions within the individual harmonic orders appeared to modulate with different phase. In Figure 5.8 we see the same box selection as for Figure 4.9, however the data presented shows that for the case of perpendicular relative alignment of the dressing field linear polarisation with respect to the XUV field. Comparing Figures 5.8 and 4.9, as expected we see that there is little change in the appearance of the average of the recorded images as the dressing field polarisation is changed, however an interesting feature is observed in the harmonic 19 response for the standard deviation of the image stack. Although for the simple standard deviation image we cannot empirically differentiate between contributions arising from fluctuations in the harmonic position and flux from those arising from delay-induced modulation in the harmonic signal, any random fluctuations should average out across the scan. We therefore

deduce that the stripe appearing in harmonic 19 in Figure 5.8 standard deviation image must be due to subharmonic changes in the phase. For this reason the standard deviation of the image stack was found to be a useful indicator for highlighting times at which the phase across particular harmonic orders changes.

With two lobes appearing in the standard deviation for the harmonic 19 transmission we investigated further the delay dependent phase response for the different regions within this harmonic order. The results can be seen in Figure 5.9.

Summing the contents of the subharmonic boxes and observing the relative phase of each of the boxes covering harmonics 13 to 19, a) to d) in Figure 5.10, we see that for many of the harmonic orders, there is not perfect synchronisation of phase between the different regions of the selected harmonic. For harmonic 13 in both the parallel and perpendicular polarisation states we find that the lower part of the harmonic is out of phase with the rest. This could be due to selection of more long trajectory components in the lower box which we would expect to have a phase offset with respect to the on-axis, short trajectory components due to the attochirp inherent in the high harmonic generation process. The other harmonic orders may not show this due to the lower box of harmonic 13 selecting only the very lowest portion of the signal, whereas the sub-harmonic boxes for the other harmonic orders select closer the half of the signal within each harmonic order, averaging more. For harmonic 19, it is unclear that there is any obvious phase difference between the left and right lobes as shown in the standard deviation plot in Figure 5.8. It should be noted that by selecting different regions along the horizontal axis on the MCP detector, one is selecting slightly different energy regions, so comparisons between left and right side boxes are for slightly different energies. Due to the nonlinear scaling of the energy axis on the MCP, the difference in energy between each side will vary with the size of the boxes chosen and the position along the energy axis.

A strategy to minimise the effect of selecting different phased light across the harmonic would be to select boxes to only contain one dominant set of trajectories i.e. centre the boxes on the middle, bright region of the harmonics (to observe the short trajectory response), or only select the outer regions to observe the response of the long trajectories.

In addition to observing sub-harmonic phase difference due to different trajectory components in the dressing field linear polarisation scan, it was observed in the standard deviation images of the intensity dependence scan that harmonic 13 also displayed a sub-harmonic change in phase, visible in the standard deviation image for the higher intensity dressing field values, see Figure 5.11. At dressing field intensities above $\sim 3\times10^{13}\mathrm{W/cm^2}$, a clear two-lobe structure could be observed in the standard deviation image.

The general non-symmetric appearance, particularly of the higher order harmonics shown in the mean signal plot in Figure 5.11, is most likely due, at least in part, to the damage on the MCP detector.

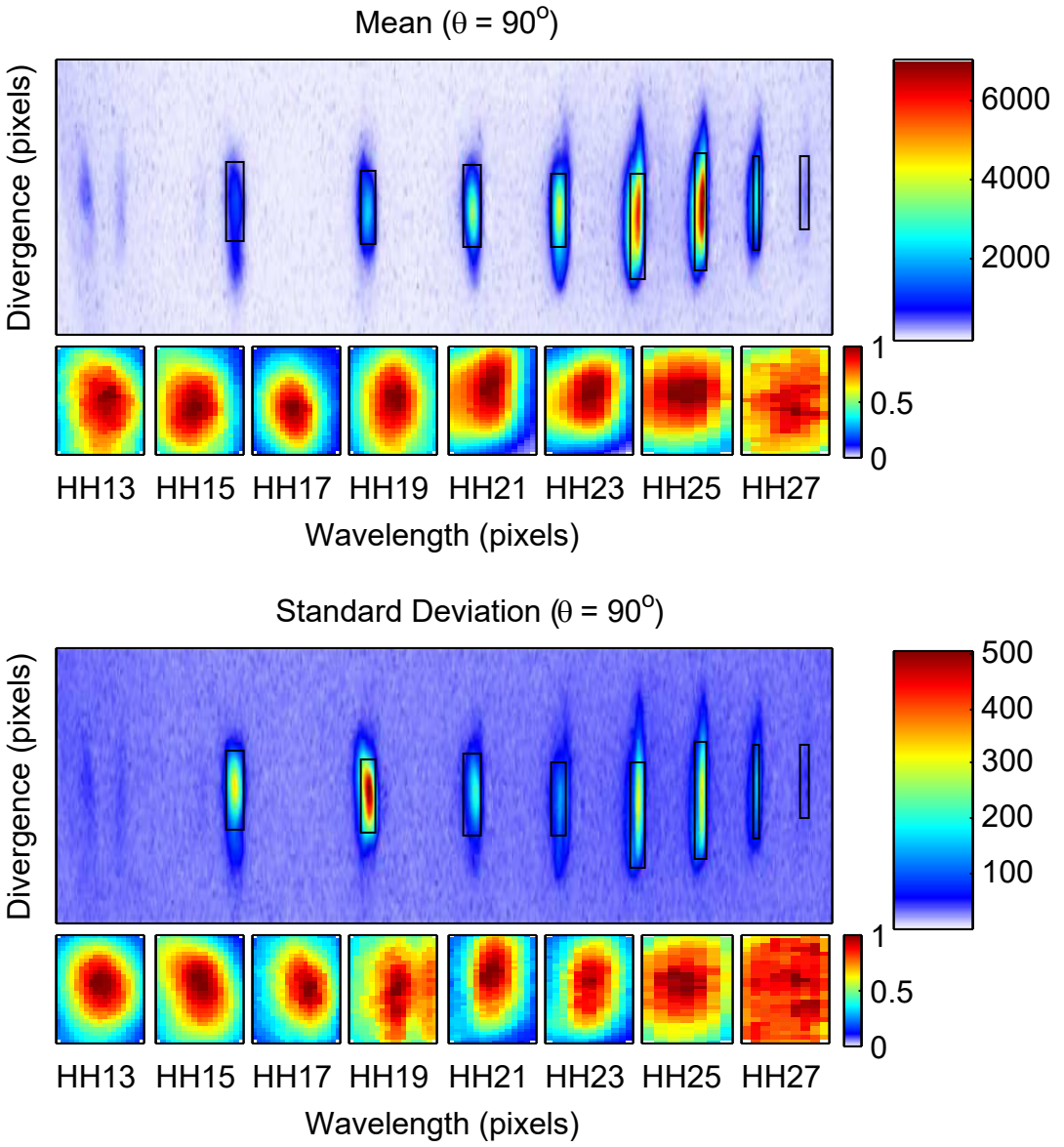


Figure 5.8: Example box selection for detected harmonics using perpendicularly aligned dressing and probing linear polarisations with dressing field intensity $1.3{\times}10^{14}\,\mathrm{W/cm^2}$. The box selection is compared to the average signal in the delay scan and standard deviation of the recorded image stack.

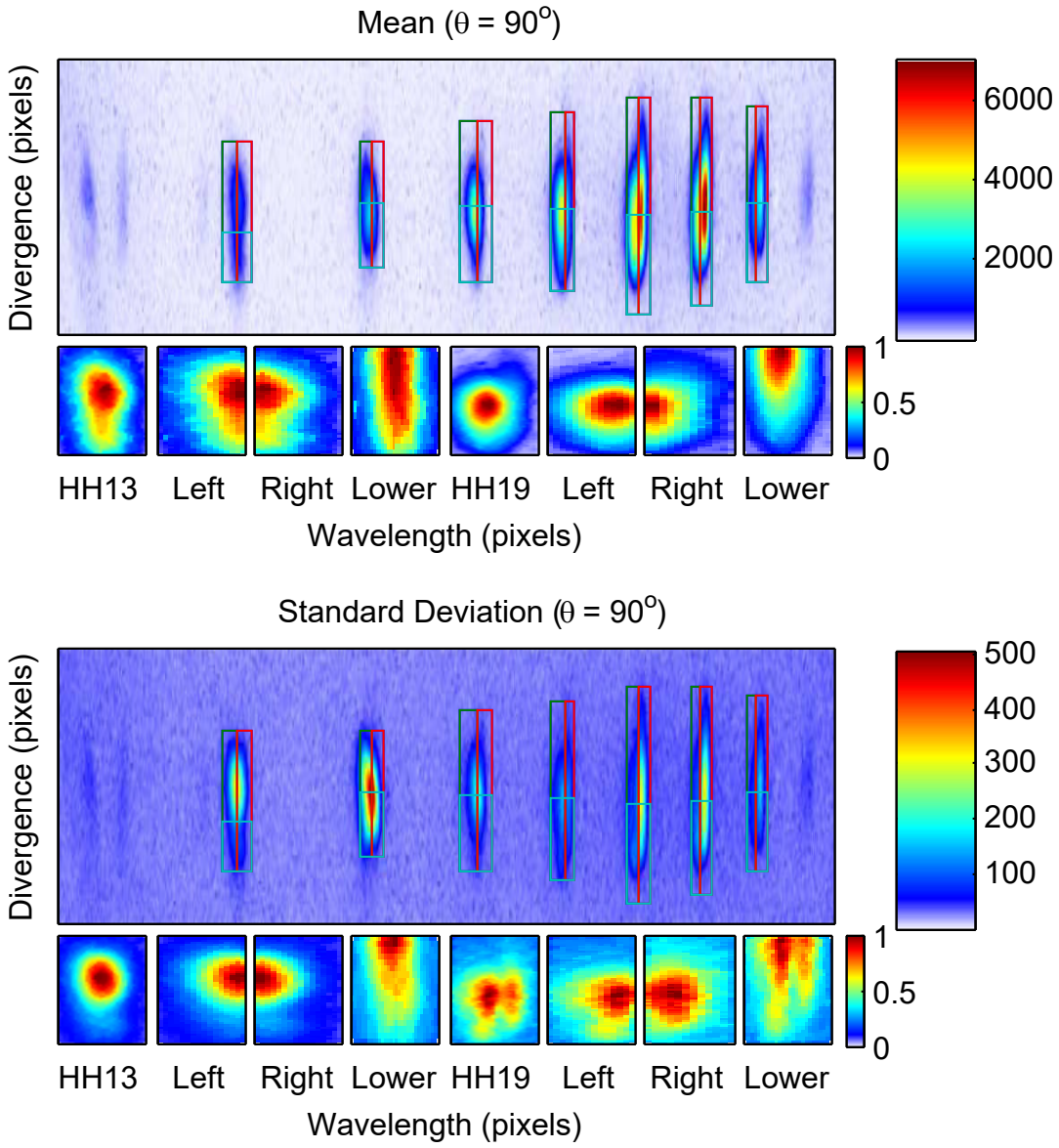


Figure 5.9: Box selection to investigate sub-harmonic phase differences for data presented in Figure 5.8.

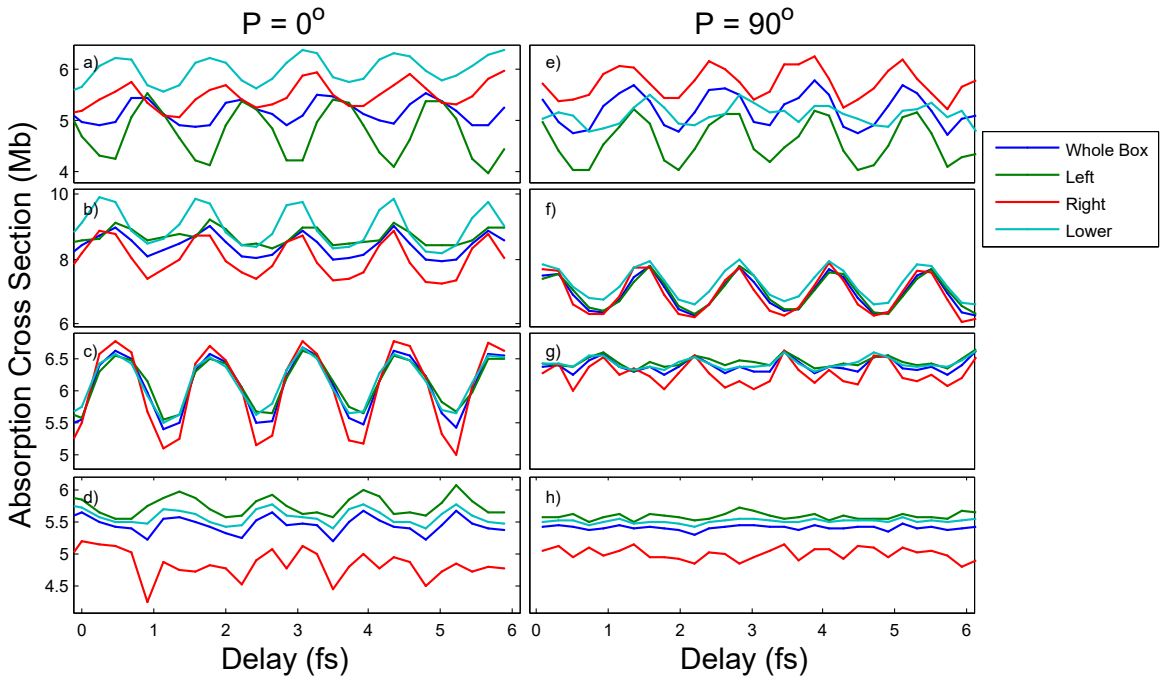


Figure 5.10: Relative phases for the different boxes selected over harmonic orders a) 13, b) 15, c) 17 and d) 19 as shown in Figure 5.9 for parallel aligned linear dressing and probing field polarisations. Panels e), f), g) and h) show the corresponding harmonic 13 to 19 response for the same selected boxes when the dressing field linear polarisation is aligned perpendicular to that of the probing field.

Investigating the phase response of the below ionisation threshold harmonics further, we selected integration boxes over different regions of the harmonics to map out the relative delay-dependent phase between these different regions, see Figure 5.12. In can be seen in Figure 5.13 that as the intensity of the dressing field is increased, the phase of the left side of the harmonic becomes increasingly shifted with respect to the right. Plotting the $2\omega_1$ and $4\omega_1$ phases for each selection box relative to the phase for the box selecting the whole harmonic we observe the results shown in Figure 5.14. It can be seen that in both cases, the right lobe of the harmonic behaves markedly different to both the left-hand side, and to the overall average behaviour of the harmonic. This indicates the general effects of the averaged harmonic phase are dominated by the left-hand side of the harmonic modulation, until the dressing field intensity reaches above 1.1×10^{14}W/cm^2 when the modulation phase from the right-hand side starts to dominate by 1.7×10^{14}W/cm^2. It is possible this averaging is the reason for observing such a steep drop in the H13 modulation depth at the highest dressing field intensities in Figure 5.6 for the experimental data.

We understand the phase response of harmonic 13 to be due to a field-induced resonance shifting in to the energy bandwidth probed by harmonic 13 for the highest dressing field intensities. Given that we do not observe any change in the sub harmonic phase until a dressing field intensity of approximately 6.8×10^{13}W/cm^2 is reached, at these intensities, due to the AC Stark effect splitting,

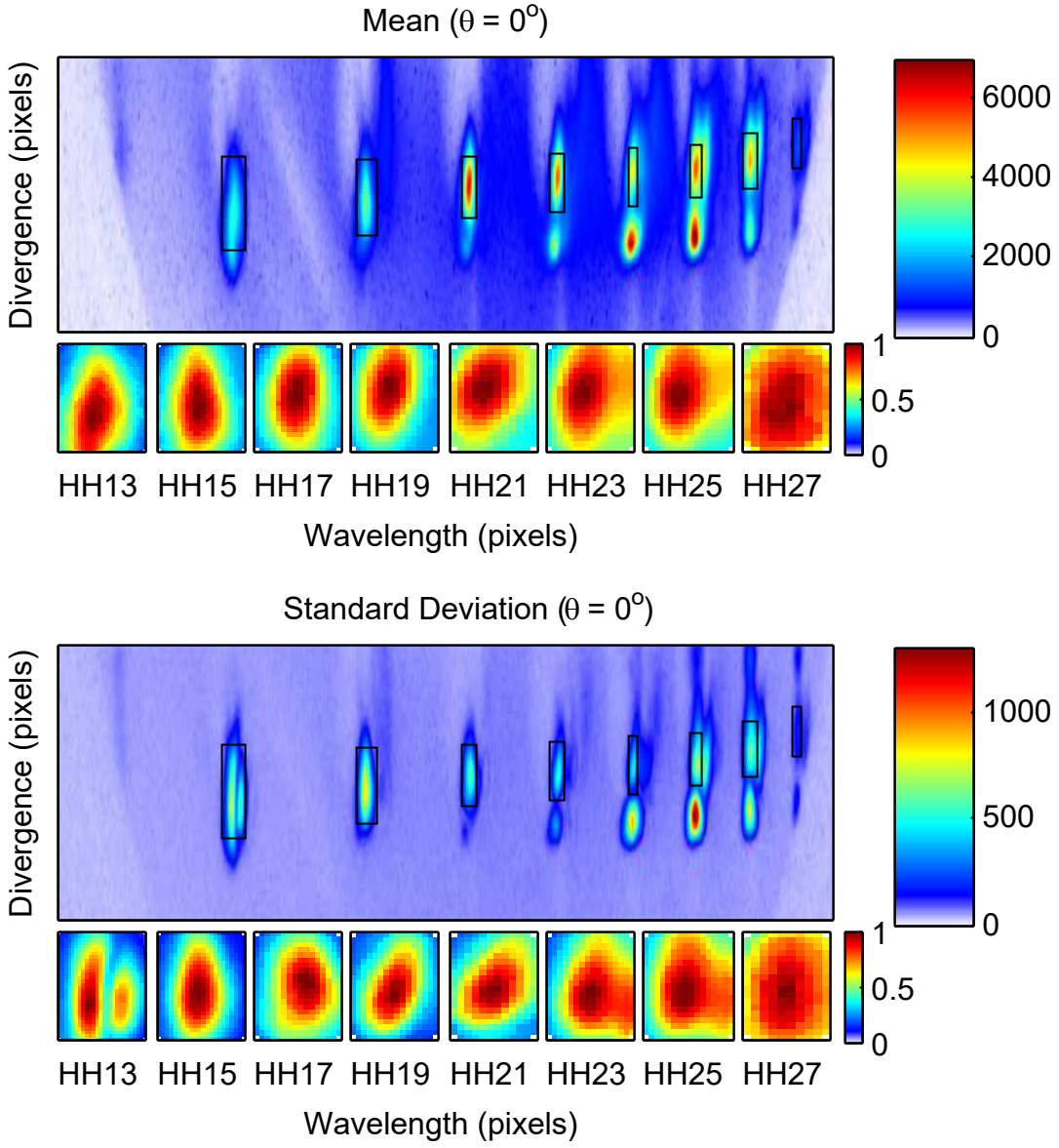


Figure 5.11: Box selection for the harmonic orders using the signal in the delay scan and standard deviation of the image stack as guidance. The data shown is from the dressing field intensity scan (recall Figure 5.6), corresponding to a dressing field intensity of 1.1×10^{14}W/cm^2.

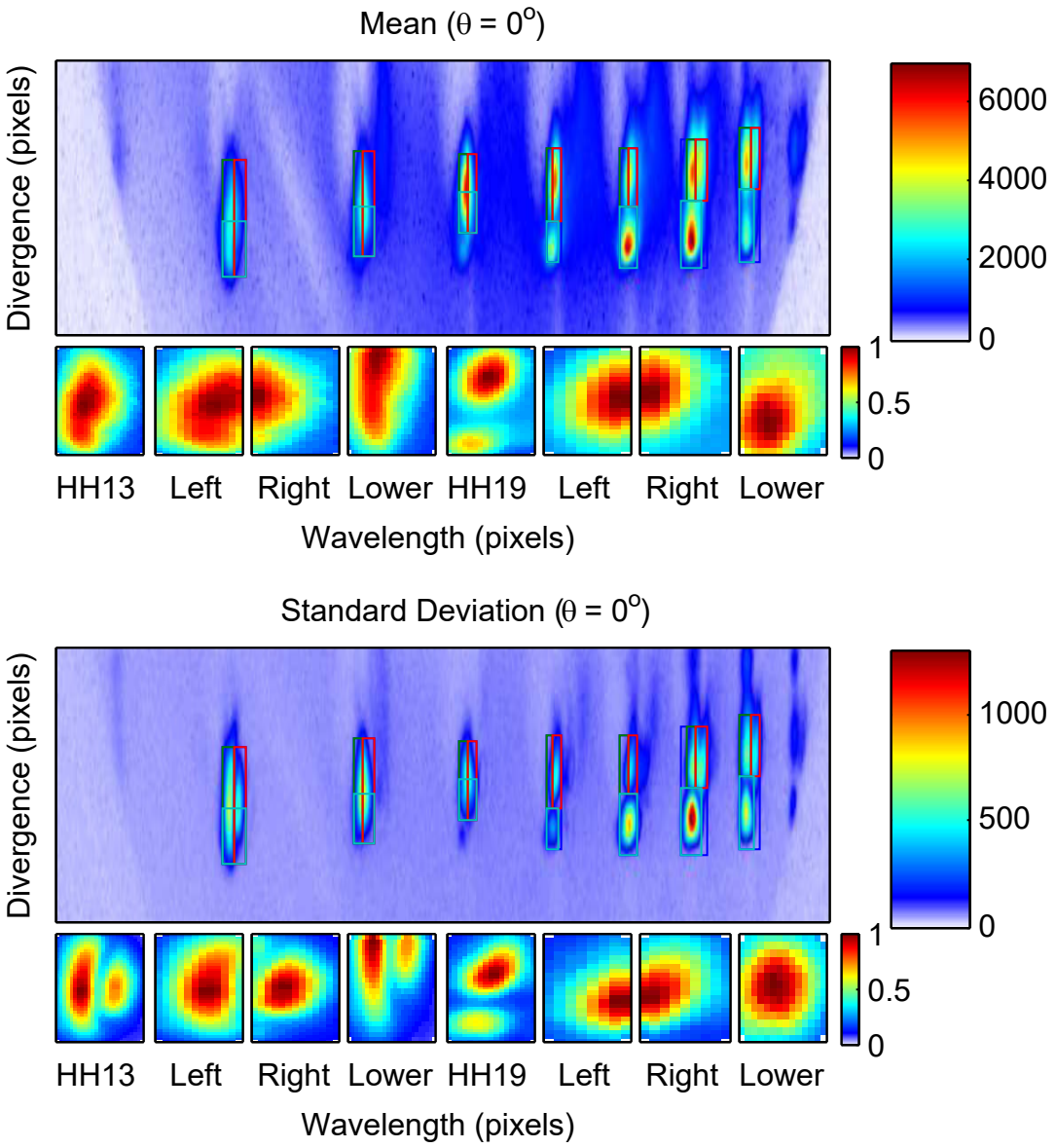


Figure 5.12: Subharmonic box selection to investigate the different phase components within different regions of the harmonics presented in Figure 5.11.

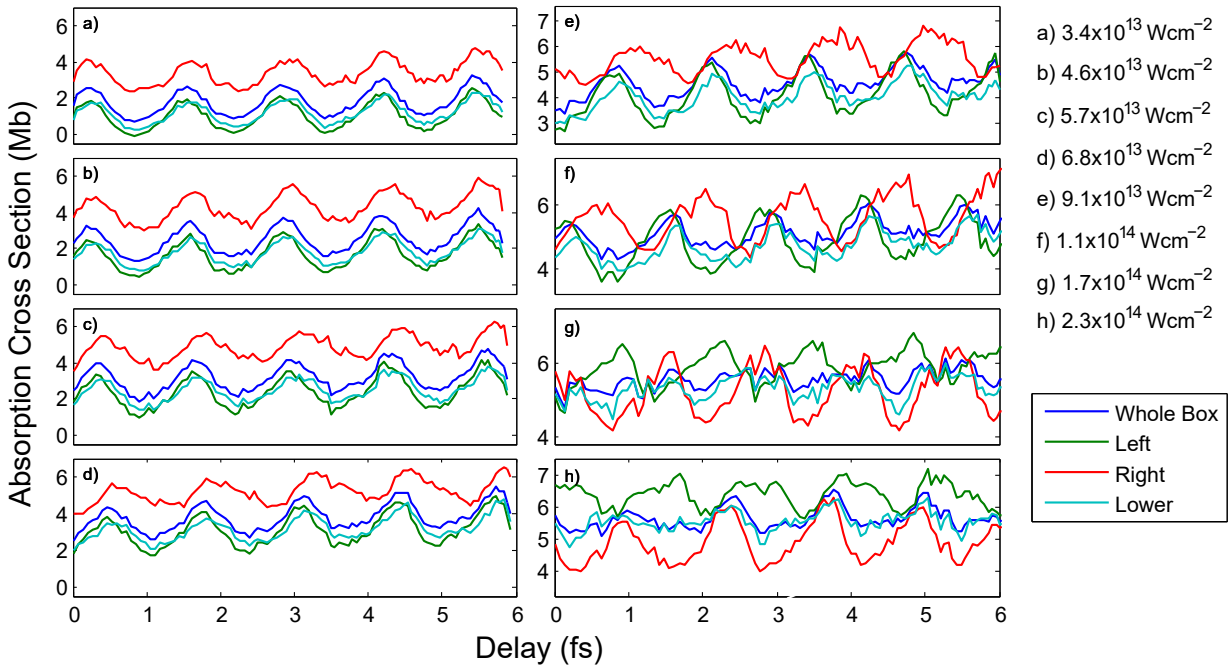


Figure 5.13: Investigating the phase of different regions of harmonic 13 for different dressing field intensities.

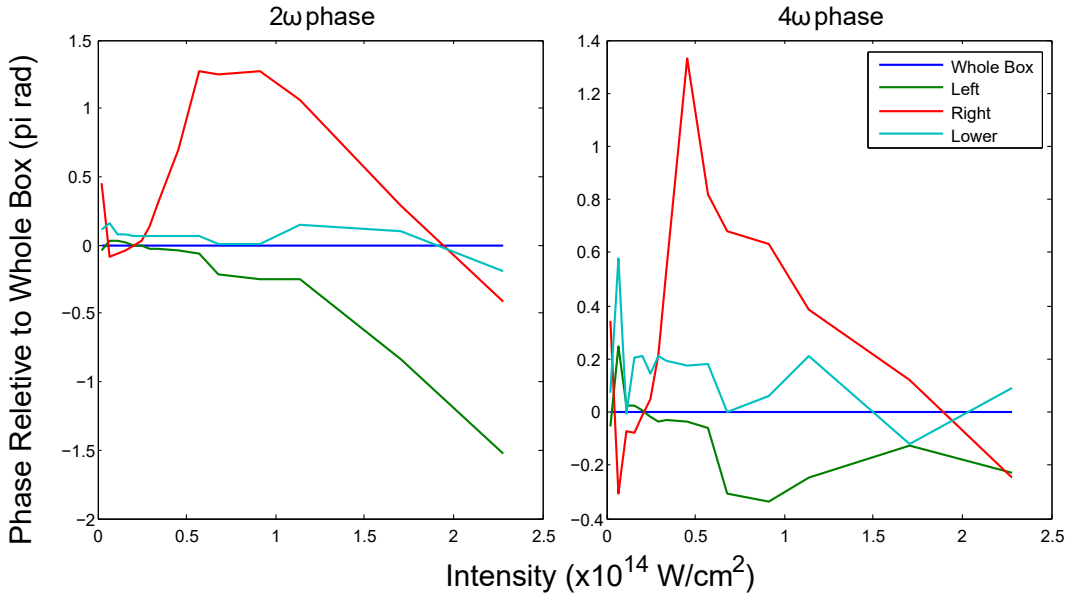


Figure 5.14: Investigating the phase of different regions of harmonic 13 for different dressing field intensities relative to the phase for the box selecting the whole (averaged) harmonic signal.

shifting and broadening the bound levels, it becomes increasingly difficult to isolate single transitions from individual bound states. If we recall from the earlier presented work (Figure 5.7), we observed absorption of harmonic 13 from dressing field intensities as low as $2\times10^{13}\mathrm{W/cm^2}$. For the higher intensity dressing field, the associated ponderomotive energy (corresponding to the approximate energy shift of the Rydberg states due to the AC Stark effect) is $\sim$4 eV, making the assignment of a single transition pathway difficult. If one could extrapolate the coupling behaviour observed at lower dressing field intensity however [114], the fact that the resonance appears for a parallel aligned dressing field polarisation could indicate harmonic 13 + dressing field coupling to a further s-orbital via a multiphoton pathway. In any eventuality, it is clear that more investigation into the box selection could extract deeper information from the delay dependent absorption modulations.

To conclude, to use the box selection method in future, one must take great care in the choice of the boxes selected to avoid missing or distorting the recorded information through the spatial-spectral averaging. Alternatively, by plotting the data as in Figure 5.2 this automatically makes visible any subharmonic phase changes as essentially it is selecting many very narrow (single pixel) photon energy axis boxes, summed across the length of the divergence axis. Sub-harmonic phase changes then appear as slanted harmonics with respect to delay. Coupling this method with an option to trim the divergence axis of the recorded spectra could allow easier separation of long and short trajectory components.

Chapter 6

Transient Absorption Using 1400 nm Dressing Field

Extending the dressing field wavelength to 1400 nm using the signal beam of a Light Conversions HE-TOPAS OPA broadens the range of transient absorption experiments that can be performed. Primarily, increasing the wavelength enables access to higher cutoff energies for the APT probe, recall equation 2.46 [86], allowing direct single photon access to more deeply bound states.

The primary goal of the longer wavelength studies was to probe, through transient absorption, dynamics associated with a laser dressed core electronic state. For core and inner valence electrons, ionisation through a single high energy photon removes the requirement for highly intense dressing fields that, if the state was instead probed through tunnel ionisation, by definition strongly distort the potential of the bound electron. With high energy single photon interaction, lower intensity dressing fields can instead be used, reducing the effect of the field on the states of interest. This results in a cleaner overall measurement. With larger atoms there is also the possibility for more interesting dynamics to occur. It seems logical therefore to extend the spectral range of the probing APT to accommodate these harder to access, and arguably more interesting, inner electronic states.

The two objectives for the longer wavelength study were therefore as follows:

1. Investigate the transient absorption around the 3d ionisation edge in krypton, extending the technique of transient absorption to these inner atomic states.

2. Repeat the transient absorption work around the first ionisation edge in helium previously performed at 800 nm.

6.1 Probing the Krypton 3d State Through Laser Dressed Transient Absorption

The target core state chosen for this experiment was the 3d state in krypton, requiring approximately 95 eV for ionisation. Similar to helium, krypton is a monatomic, inert gas making it easy to handle and use. The similar properties of krypton and helium also enabled direct interchange of the gasses without requiring any modifications to the experimental setup. Through direct single photon absorption, electrons from the krypton 3d shell can ionise or excite to the p-manifold situated approximately 92 eV in energy from the 3d state, or the f-manifold lying just below the ionisation threshold (see Figure 6.1).

When probing the 3d shell there are many available transition pathways and the complexity of the krypton interaction is significantly greater than that of the two-electron helium. To start, the 3d state itself is comprised of two energy separated levels reflecting the range of allowed total angular momentum quantum numbers. These levels are situated at 95 eV and 93.8 eV below the continuum [163], and correspond to the $j = 3/2$ and $j = 5/2$ states respectively. Electrons from either of these levels can ionise to the continuum, or excite to one of a manifold of closely spaced p- and f-orbitals. In addition, ionising or exciting from a core state resulting in a core vacancy opens the door to further dynamics such as Auger decay to the 3d hole. The measured core hole lifetime for the $j = 5/2$ 3d state is found to be $7.9^{+1.0}_{-0.9}$ fs [164], significantly longer than the sub-cycle dynamics investigated in this experiment. This value however is obtained for an undressed krypton sample, and the result may vary for the intensely-dressed krypton target.

6.1.1 Dressing Field Polarisation Dependence In Kr Target

We investigated the effect of changing the dressing field relative linear polarisation from parallel to perpendicular with respect to the probing XUV field as a function of delay between the pump and probe pulses.

Presented in Figure 6.2 a) and b) we observe the difference in delay-dependent transmission amplitude across the extent of the scan range for the case of parallel aligned pump and probe field linear polarisation, $\Theta = 0°$, and perpendicularly aligned polarisation, $\Theta = 90°$, respectively. The displayed signal has been normalised with respect to the interleaved static absorption references and the intensity of each delay position referenced to a lower energy range of non-modulating harmonic orders. The delay range investigated spanned approximately 60 fs following phase tagging correction of the temporal axis over the interaction envelope, with effective delay steps of $\sim$0.13 fs. Five images of 1 s exposure were recorded per delay step, and a static absorption reference was recorded every four delay points. Acquisition of the parallel and perpendicular dressing field orientations were interleaved to allow more direct comparison between the similar experimental delays, minimising

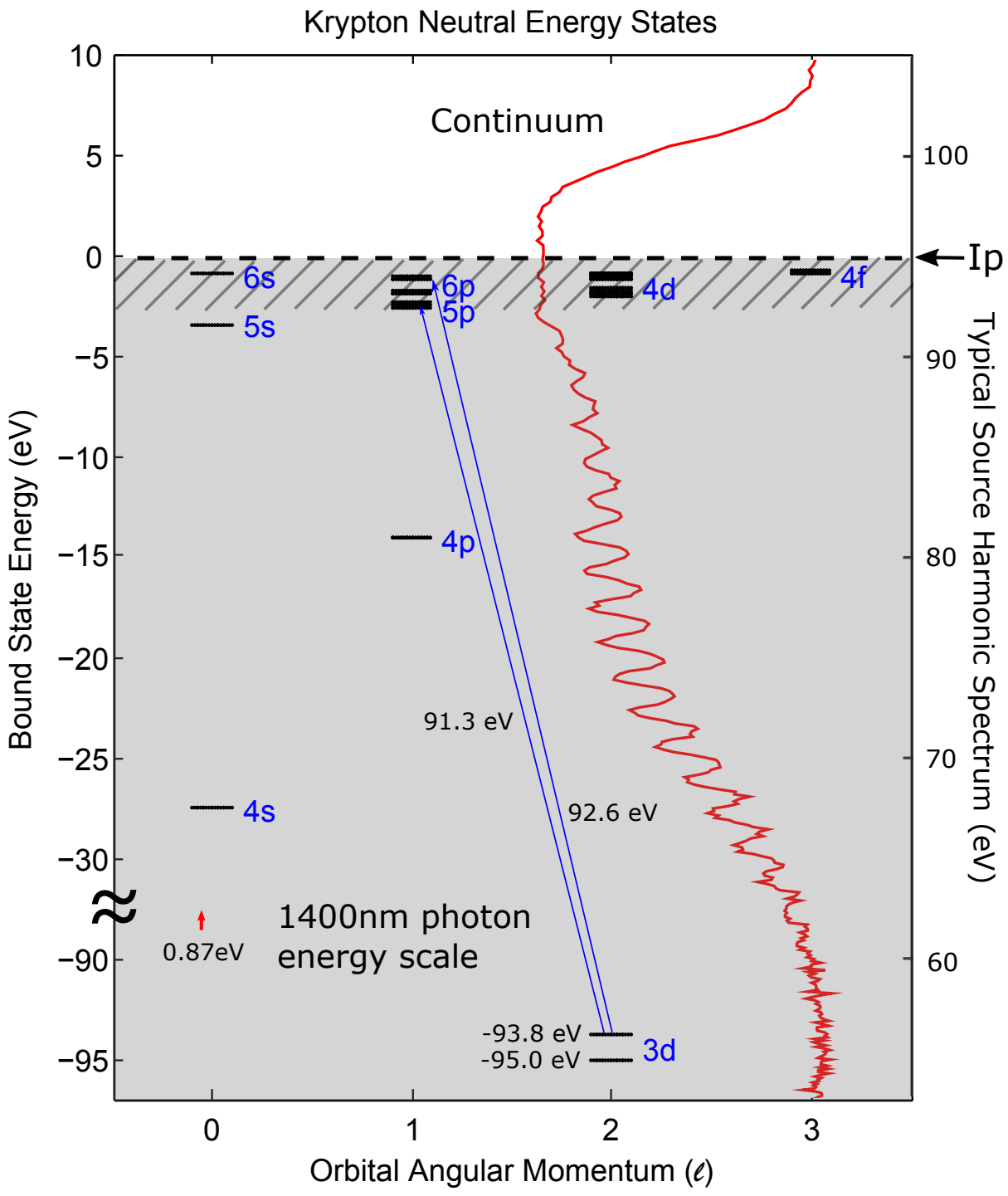


Figure 6.1: Energy level diagram of the krypton atom. Values for the energy states were taken from references [162] and [163]. The overlaid red line indicates a typical source harmonic spectrum for driving wavelength ∼1400 nm, used to probe the krypton target.

effects of long-term drifts in the system. To compensate dressing-field power differences between the parallel and perpendicularly aligned polarisation orientations, the dressing field power was reduced for the parallel alignment using a motorised iris in the dressing field beam path to match that of the full power for the perpendicular case. An iris was used rather than a waveplate and polariser as we used to control the dressing field intensity for the 800 nm work to maximise the total power in the dressing field arm. This change in power for different dressing field polarisations arises through differences in the reflectivity coefficients for the beam path optics for each polarisation orientation. The peak intensity of the dressing field was estimated to be $4.5\times10^{13}\mathrm{W/cm^2}$ at the start of the scan, dropping approximately 12% across the scan duration. The probe harmonics were generated in argon with a backing pressure of 340 mbar, and the krypton target backing pressure was measured to be 150 mbar. The central wavelength of the dressing field was measured to be 1370 nm

A phase shift of approximately pi radians is observed between the peaks of the detected modulating harmonic orders in the parallel and perpendicular results. We attribute this to the rotation of the half waveplate used to vary the polarisation state of the dressing field.

Comparing the resultant delay dependent absorption modulation amplitude from narrow spectral regions selected within the harmonics surrounding the ionisation edge we can understand better any changes that occur between the dressing field polarisation alignments. The selected spectral regions are shown using black vertical lines in Figure 6.2 a) and b). The regions selected are the same between the different polarisation states. Sliding a 15 fs FWHM, 6th order super-Gaussian filter window across the delay axis for these chosen spectral ranges, we can extract the frequency components comprising the modulation within each of the window delay ranges through Fourier transformation. The results are presented in Figure 6.2 c).

It is observed that the majority of the modulation detected occurs in harmonic orders below the 3d ionisation threshold. Strong $2\omega_1$ components are present in all three harmonics situated directly below the 95 eV threshold for both the parallel and perpendicular dressing field polarisation alignments across the extent of the scan range. Possible $4\omega_1$ signal is detected for the parallel aligned case in the harmonic orders sampled around 92.7 eV and 91.2 eV, not present for the perpendicular measurements. To record a $4\omega_1$ modulation, coupling must occur between harmonic orders separated by one harmonic. The lack of corresponding $4\omega_1$ signal for harmonic orders separated by 4-IR photons from either of the harmonics in question however makes it less clear if this signal is real. For the harmonic sampled above 95 eV, hints of $2\omega_1$ modulation are present in parts of the delay range, however the signal at this order barely reaches above the noise. The lowest harmonic signal investigated with spectral range centred around 89.7 eV shows clear $2\omega_1$ modulation only for the central region of the scan range for the parallel orientation, and slightly more extended for the perpendicular polarisation. Figure 6.2 c) has been plotted on a log scale for clarity.

Generally we appear to observe little change in the measured absorption modulation amplitude

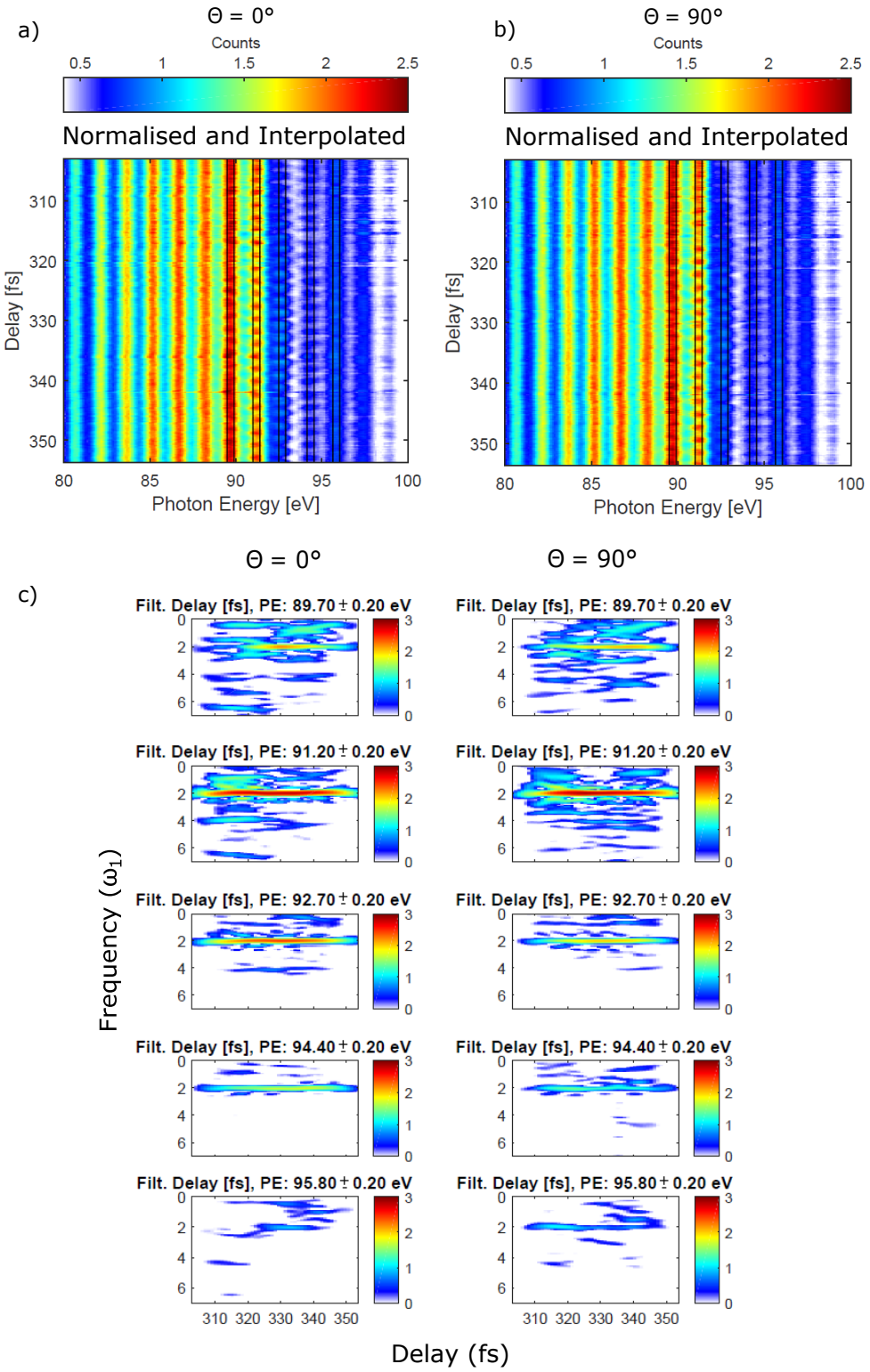


Figure 6.2: Comparison of the transient absorption transmission signal of laser dressed krypton for linear polarised dressing fields aligned a), parallel (θ=0°), and b), perpendicular (θ=90°), with respect to the probing APT field polarisation. c) Log scale Fourier response sampled for discrete energy ranges for each polarisation orientation as a function of delay with respect to a sliding 15 fs FWHM, super-Gaussian window filter. The analysis was performed for the second order light measured on the MCP and rescaled back to the correct energies. The peak dressing field intensity was calculated to be 4.5×10^{13}W/cm^2.

for the different linear dressing field polarisation states for these experimental parameters. Unlike for the 800 nm dressed helium experiment where we observed a strong vectorial response to the polarisation state of the intense dressing field for the above ionisation threshold harmonics, there is little significant change observed in the modulation amplitude between the different polarisation states for this scan. For this measurement however we are mostly probing the below ionisation threshold response in krypton for which we also observed little change with relative dressing field polarisation in the previous 800 nm helium work. No modulation was observed around or above the 100 eV silicon edge from the silicon-zirconium filter.

Identifying individual harmonic orders around the krypton 3D edge is more difficult than for around the helium Ip since the $1/\lambda$ scaling of the MCP energy axis means that the higher order harmonics are much less well resolved than the lower order harmonics. In addition, uncertainty in the energy axis due to the calibration edges and krypton edge spanning several harmonic orders prevents easy identification of the exact harmonic orders observed.

The ω_1 frequency of the Fourier axis was adjusted by eye to ensure the different frequency components are situated at the correct $2n\omega_1$ frequencies. This allows for automatic windowing of the Fourier components in the Fourier domain. For the results presented this corresponds to a central input wavelength of 1263 nm. Reasons for the discrepancy between the recorded input wavelength and the determined wavelength required to match more closely the Fourier components at $2\omega_1$ and $4\omega_1$ could be due to some systematic error in the temporal correction phase tagging resulting in a distorted modulation period. Alternatively, it is possible that the input wavelength was actually bluer than that measured at the exit to the TOPAS box, which could explain, at least in part, the large discrepancy. Another possibility, since the adjustment was just done by eye, is that there is actually a broad range of input wavelengths that result in a similar Fourier spectrum by eye, and that this is not the optimal input wavelength selection. In any eventuality, we know the modulations should occur at even multiples of the driving wavelength, and so have adjusted the input wavelength setting accordingly for each scan. An image of the averaged interleaved field free reference spectra recorded alongside the data can be seen in Figure 6.3 a), along with the generating (argon) and target (krypton) backing pressures as a function of time throughout the delay scan in b).

6.1.2 Dressing Field Peak Intensity Dependence In Kr Target

In addition to the polarisation study, we also investigated the effect on the absorption modulation amplitude as a function of delay as the peak dressing field intensity was varied. The dressing field linear polarisation was aligned parallel, $\theta = 0°$, with that of the XUV probe field for this investigation. The results can be seen in Figure 6.4, where the extracted $2\omega_1$ amplitude components have been interpolated onto a linear intensity axis. We controlled the power of the IR dressing field using a motorised iris in the dressing field beam path, recording the power at the beginning and end of each

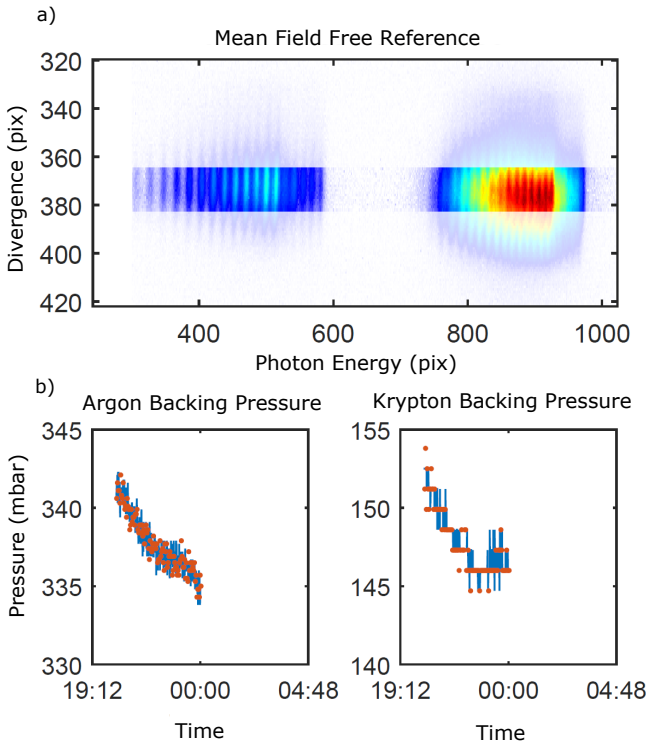


Figure 6.3: a) Mean harmonic spectrum obtained for the interleaved static absorption measurements recorded across the scan delay range shown in Figure 6.2. The selected divergence range is shown in full colour. b) The recorded generation and target backing pressures as a function of delay throughout the scan duration.

delay scan using the insertable pickoff mirror. Again an iris was used to prevent reflection losses from a waveplate polariser pair. Images of the focal spot for each of the dressing field iris diameters used were recorded to enable more accurate peak intensity estimates to be made.

To record this 2-dimensional scan we performed a series of short delay scans spanning nominally 15 fs duration in 0.2 fs delay steps for the different dressing field intensities. Performing short scans allowed us to cover a broad intensity range whilst minimising impact of long-term drifts in the set-up. For each delay step, five images of 1 s exposure were recorded. The central wavelength of the TOPAS signal was measured to be 1400 nm. A static absorption reference was taken every four delay steps. The probing APT was generated in argon using a set backing pressure of 310±10 mbar. The krypton target backing pressure was measured to be 132 mbar at the start of the scan range, and fluctuated slightly throughout. The evolution of the measured dressing field power, estimated krypton target backing pressure and determined peak intensity across the scan range can be seen in Figure 6.5 a), b) and c) respectively. The plotted errors indicate the approximate maximum and minimum values recorded for each power and pressure value. The peak intensity was calculated for the maximum power measured for each scan. This usually corresponded to the power recorded at the start of each scan. One point of note is the jump in the recorded power between scans 6 and 7. This corresponded to the start of a new intensity scan taken immediately following the first.

The mean static absorption (field free transmission) reference harmonic spectrum and selected divergence range (full colour) can be seen in Figure 6.4 c). To ensure a fair comparison across all of the different dressing field intensity scans, a large harmonic divergence range was summed for each delay point to ensure the brightest region of each harmonic was captured, even with small fluctuations in the divergence profile of the probing harmonics over time. The Fourier axis was rescaled to ensure the extracted frequency components matched the $2n\omega_1$ values. The rescaling corresponded to a central input wavelength of 1370 nm.

We observe in Figure 6.4 a) that for higher dressing field intensities (above $\sim 3\times10^{13}\mathrm{W/cm^2}$) $2\omega_1$ modulation is observed more strongly in the harmonic order around 95 eV. For the lower intensity values, significant modulation is observed only for the two lower harmonic orders. In general it appears that increasing the dressing field intensity increases the $2\omega_1$ modulation amplitude for these lower harmonic orders. This seems reasonable since the energy of these harmonics falls below the ionisation threshold in krypton. Dressing the krypton with an increasingly intense laser field could increase the coupling between these states, resulting in an increased $2\omega_1$ response. At the highest dressing field intensities hints of $2\omega_1$ modulation in the harmonic order around 97 eV are also present. In Figure 6.4 b) we see the same intensity response only this time each intensity spectrum has been normalised to its maximum value. In doing this it helps to clarify the changes to the $2\omega_1$ modulation depth at the higher photon energies. The analysis has been performed looking at the second order light on the MCP, scaled back to the correct first order energy.

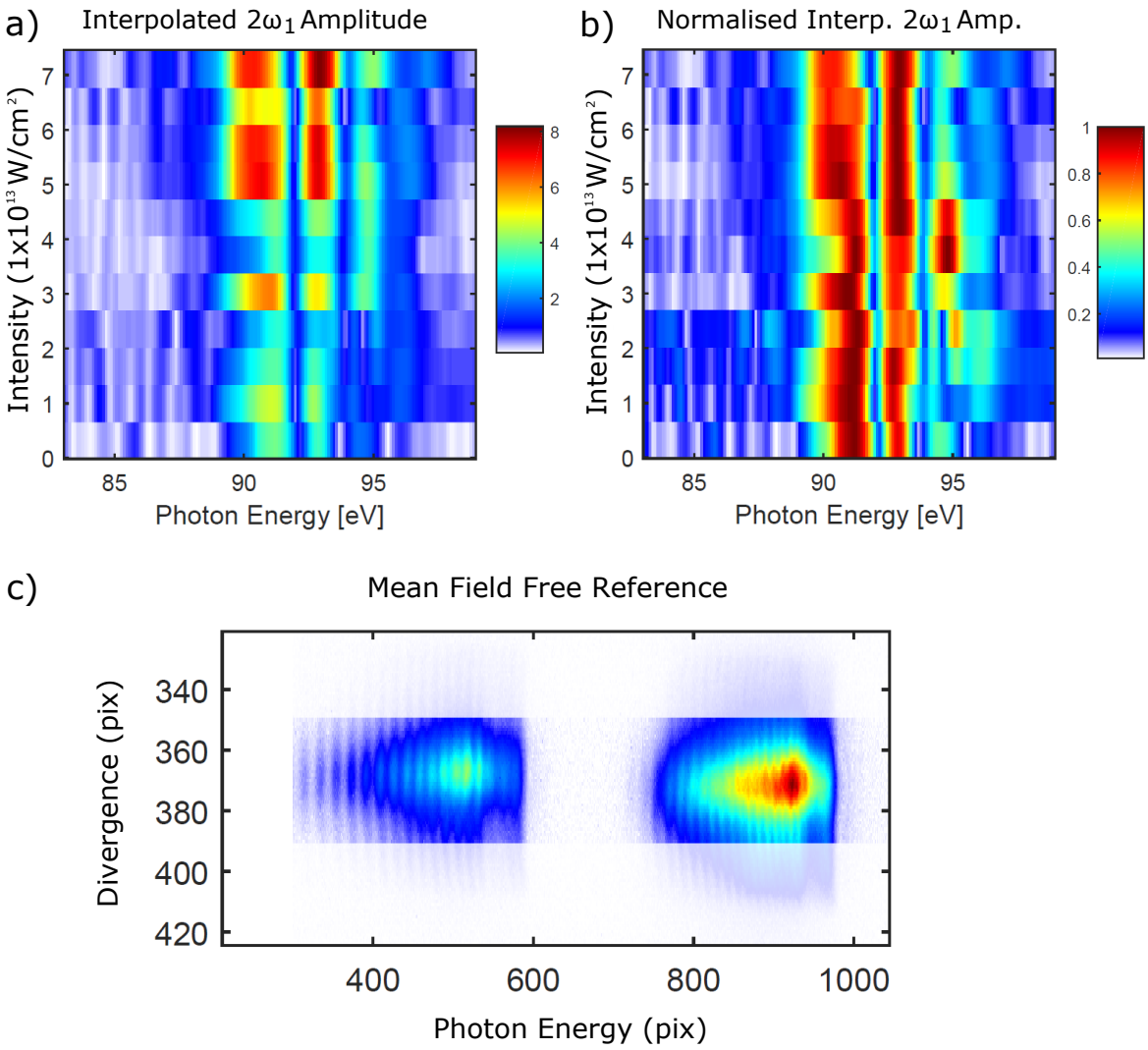


Figure 6.4: $2\omega_1$ amplitude response as a function of dressing field peak intensity, presented as relative amplitude, a), and normalised with respect to the maximum signal for each measured intensity, b). c) Image of the mean harmonic spectrum recorded for the interleaved static absorption measurements across the delay range. The selected divergence range (full colour) was intentionally large to minimise effects occurring from small changes to the source harmonic spectrum across the scan length. The analysis was performed for the second order light measured on the MCP and rescaled back to the correct energies.

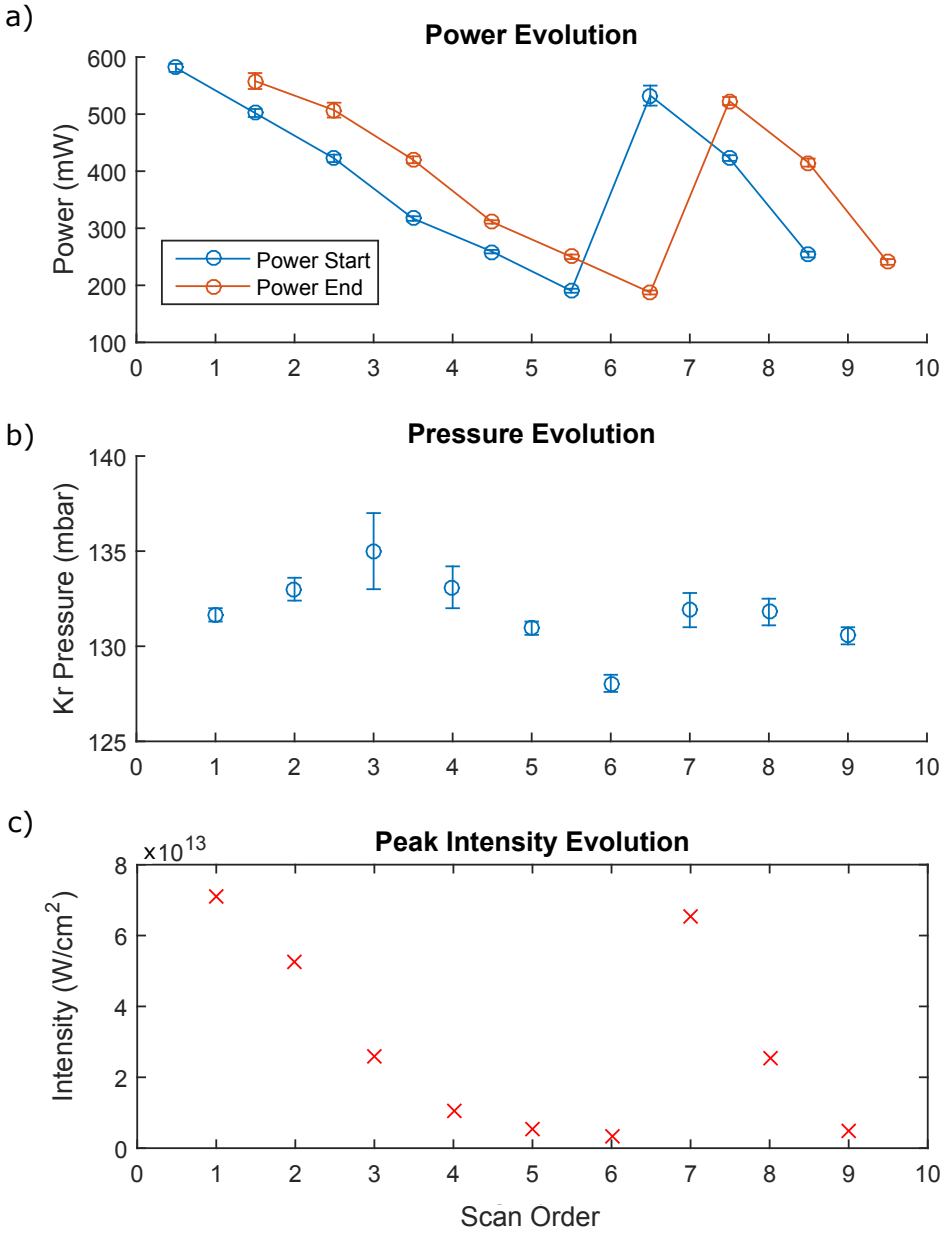


Figure 6.5: Measured dressing field power, a), krypton target backing pressure, b), and peak intensity, c), as a function of scan order for the different dressing field intensity delay scans used to construct Figure 6.4. The jump in power between scans 6 and 7 corresponds to the start of a new power scan, immediately following the first. The dressing field power was recorded at the start and end of each delay scan as presented in a). The peak intensities were calculated using the maximum power recorded for each delay scan and the corresponding dressing field focal spot image recorded for each iris aperture size taken following the entire intensity scan.

It should be noted that by adjusting the pump iris to control the dressing field intensity, this also affects the quality of the spectral interference phase tagging measurement. Since the dressing field contribution to the spectral interference result is selected using a D-shaped mirror from the very outer region of the beam, reducing the dressing field beam size reduces the portion of the dressing field pickoff light sent to the phase tagging interferometer. The visibility of the spectral interference fringes depends on the relative amplitudes of the light interfering from the separate pumps and probe beams. Reducing the intensity by lowering the power across the whole beam profile rather than exclusively from the edges however should therefore improve the deterioration.

In general we can conclude that increasing the dressing field intensity over the range we observed does not change the detected $2\omega_1$ amplitude response significantly. Extrapolating from the observations one conjecture is that at higher dressing field intensities, modulations in higher order (above ionisation threshold) harmonics could potentially be observed provided the coupling continues to increase with dressing field intensity. Due to the power limitations of our laser however, and restrictions on the current experimental setup we cannot at this current time investigate to higher intensity dressing fields. Recalling the $2\omega_1$ modulation response from laser dressed helium at 800 nm however, we observed that increasing the dressing field intensity increased the modulation depth for the below ionisation threshold harmonic orders up a point, but that the above Ip harmonics remained fairly constant above a threshold intensity. It is possible we observe a similar effect here.

6.1.3 Dependence on the Krypton Backing Pressure

Our final 2-dimensional scan investigated the effect on the absorption modulation amplitude of varying the krypton target backing pressure as a function of delay. We did this to better understand the optimal conditions for investigating transient absorption dynamics. Literature suggests that for a select target geometry with a target thickness significantly narrower than ours, anything in excess of ∼20% absorption can lead to spectral reshaping of the probing APT throughout the target length, effectively resulting in different dynamics being probed across the length of the interaction [104]. We often observed that with greater backing pressure however, the modulation amplitude (at least for the below ionisation threshold harmonics) appeared to be larger. Investigating this further we performed a series of 16 short delay scans covering nominally 15 fs delay in 0.2 fs delay steps. The central wavelength of the TOPAS signal was measured to be 1420 nm. We scanned eight different backing pressures, repeating each setting twice in different orders to eliminate any systematic bias. The results of the $2\omega_1$ modulation amplitude as a function of krypton backing pressure can be seen in Figure 6.6 a) and b), where a) shows the absolute $2\omega_1$ amplitude measured for each pressure, and b) shows the same result normalised to the maximum value in each pressure spectral slice. The recorded Fourier amplitudes have been interpolated onto a linear pressure scale for each image. The Fourier axis was rescaled to ensure the extracted frequency components matched the $2n\omega_1$ values.

The rescaling corresponded to a central input wavelength of 1370 nm.

Comparing this result to the averaged field free transmission (static absorption reference) recorded at the start and end of each scan (Figure 6.7 lower panel), we see that the general shape of the measured $2\omega_1$ modulation amplitude follows closely that of the field-free transmission (static absorption) flux around the 3d absorption edge. The field-free transmission plot selects the same broad divergence region as for that presented in Figure 6.6, and is also interpolated onto a linear pressure axis. Once again a large divergence range was selected to ensure fair comparison between the different scans. The static absorption references were individually averaged over 50 images of 1 s exposure. Background subtraction for these references had the dressing field blocked.

The power in the dressing field was recorded at the beginning and end of each scan, and the results are plotted both as a function of scan order, and of krypton backing pressure in Figure 6.8 a) and b) respectively. The plotted error bars indicate the approximate maximum and minimum values recorded for each power. The peak intensity was determined to be $4.0\times10^{13}\mathrm{W/cm^2}$ at beginning of the first scan.

Observing the response of the $2\omega_1$ amplitude as the backing pressure is increased, Figure 6.6 a) and b), we see that at the highest backing pressures, the absolute, a), and relative, b), modulation amplitude of the above 95 eV harmonics is reduced. We observe that the amplitude of the lowest modulating harmonic (around 90.7 eV) increases with krypton backing pressure. Similarly the amplitude of the next highest harmonic order (around 93 eV), increases up to ∼125mbar backing pressure, before reducing in amplitude again. This is most clearly seen in the normalised relative $2\omega_1$ modulation shown in Figure 6.6 b). We observe that at the lowest krypton backing pressures, all of the below ionisation threshold harmonic modulation amplitudes are low due to the reduced target density. At these low krypton backing pressures, however, there does appear to be more convincing evidence of modulation amplitude in the higher (above ionisation threshold) harmonic order around 97 eV.

The reduced $2\omega_1$ modulation amplitude in the higher harmonic orders with increased backing pressure we attribute to re-absorption within the dense target length. The increased modulation amplitude for the lowest modulating harmonic order (∼90.7 eV) we attribute to the discrimination of the krypton 3d edge increasing with increasing krypton backing pressure. With the intense dressing field present, the sub-cycle AC Stark shift will modulate the energy levels of the bound electron states [122]. If the discrimination between signal below and above the krypton 3d absorption edge is large, this will cause substantial changes in the harmonic flux as it modulates. With less backing pressure in the target, the discrimination is lower and the edge less steep, resulting in lower AC Stark shift induced flux modulation.

To understand the levels of absorption we achieve in the target interaction above the 3d edge as a function of krypton backing pressure we can compare the averaged static absorption references

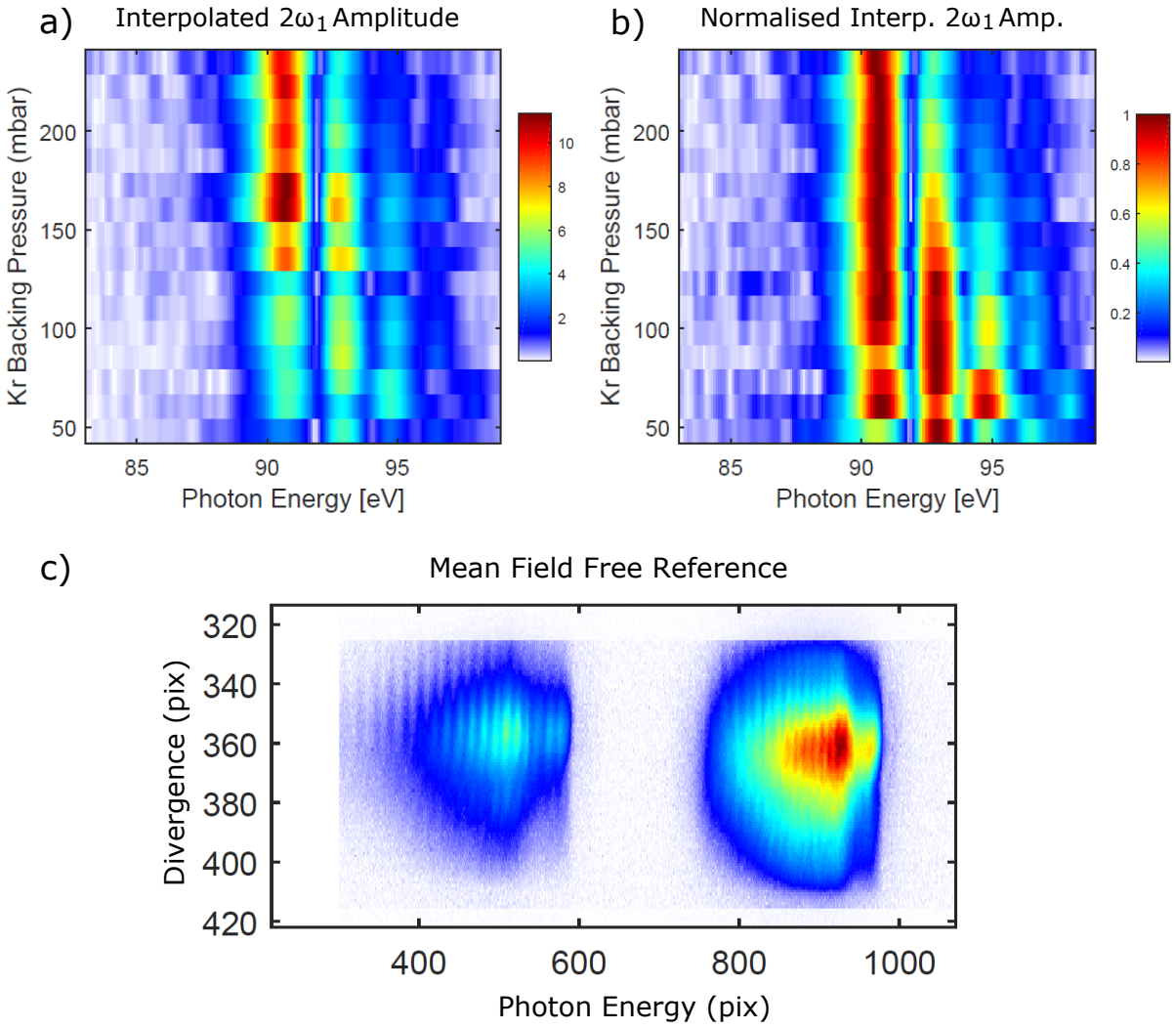


Figure 6.6: $2\omega_1$ amplitude response as a function of krypton target backing pressure for the relative $2\omega_1$ amplitudes measured, a), and those normalised to the peak value at each pressure, b). c) Image of the mean harmonic spectrum recorded for the interleaved static absorption (field free transmission) measurements across the delay range studied. The selected divergence range (full colour) was intentionally large to minimise effects occurring from changes to the source harmonic spectrum across the scan length. The analysis has been performed looking the second order light measured on the MCP, and rescaled back to the correct energies. The dressing field peak intensity for the presented scans was calculated to be $4.0\times10^{13}\mathrm{W/cm^2}$

.

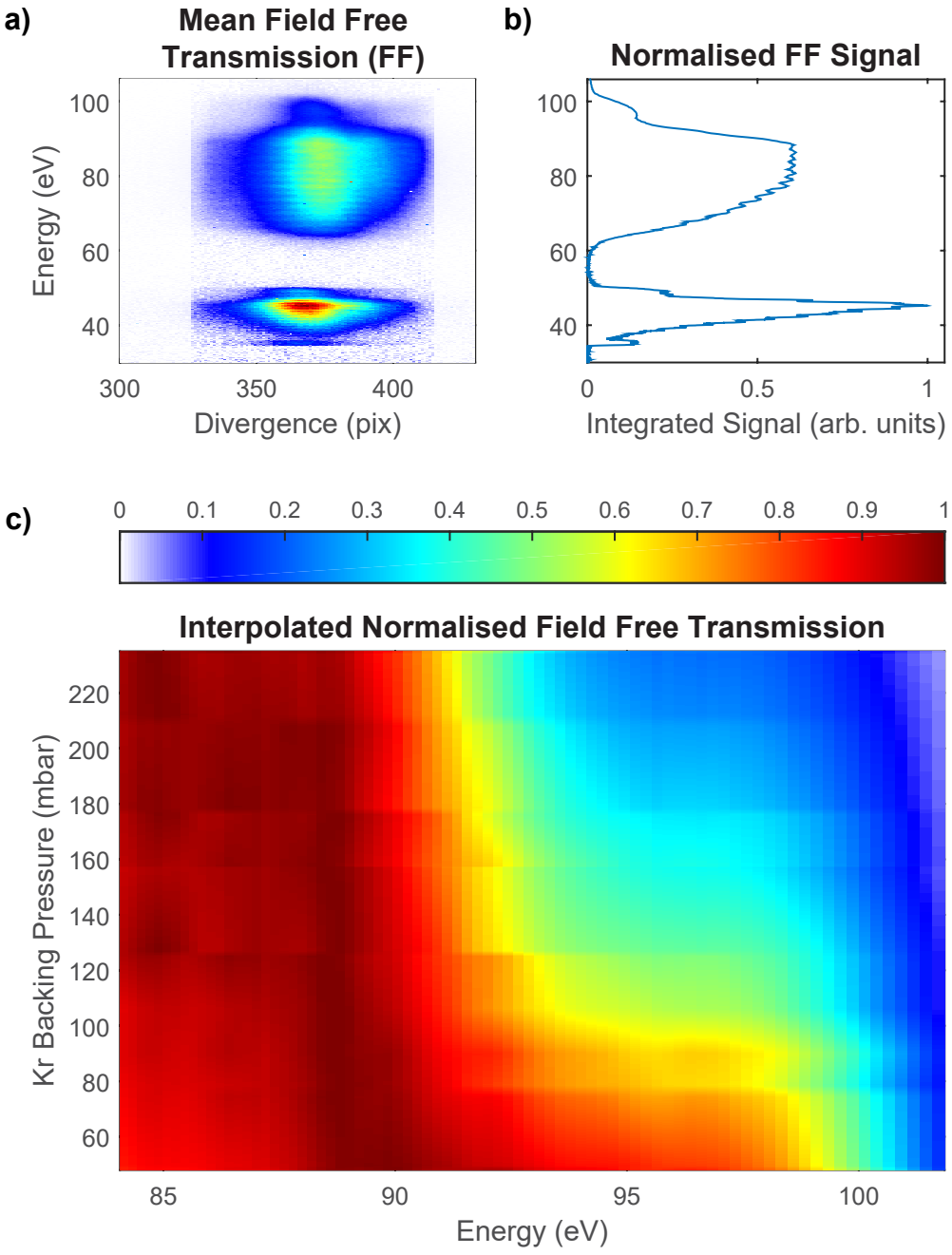


Figure 6.7: Mean field free transmission (static absorption reference) as a function of krypton backing pressure. a) Example mean field free transmission spectrum averaged from measurements recorded at the start and end of each scan. This particular reference was recorded for 235 mbar krypton backing pressure. b) Normalised summation of the field free transmission across the selected divergence axis, shown in full colour in a). c) Summed average field free transmission as a function of krypton backing pressure. The references have been interpolated onto a linear backing pressure axis.

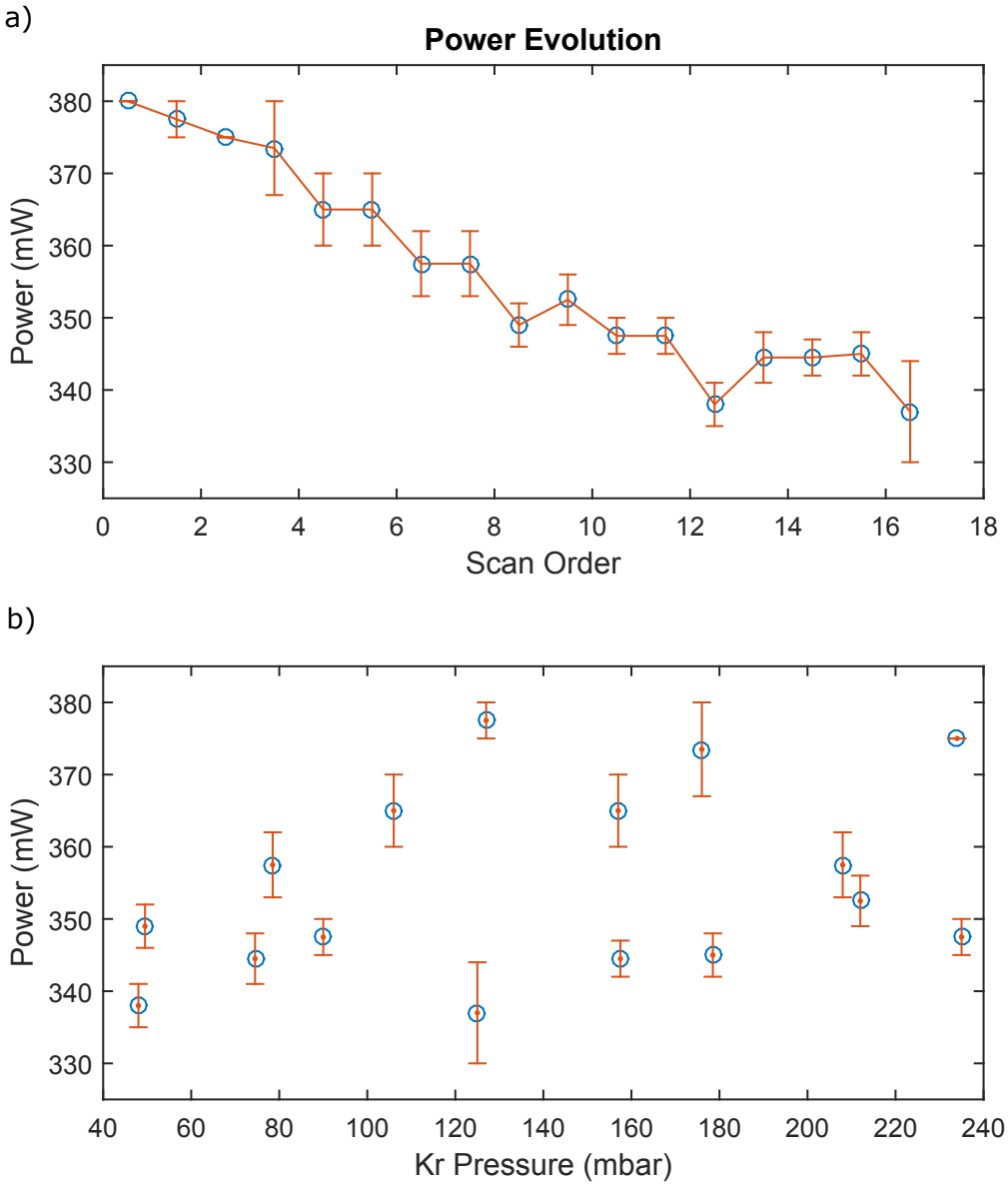


Figure 6.8: Measured dressing field power as a function of scan number, a), and krypton backing pressure, b), for the recorded delay scans at each backing pressure presented in Figure 6.6 a) and b).

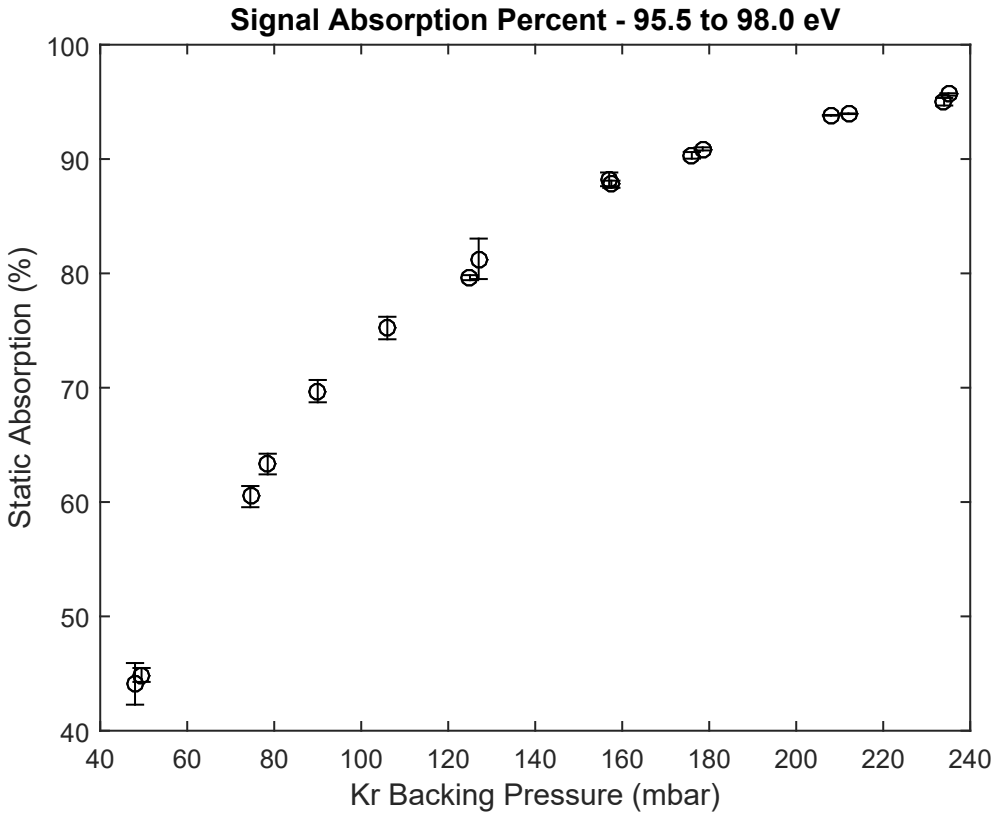


Figure 6.9: Average percentage absorption as a fraction of the total signal measured within the energy range 95.5 to 98.0 eV for each source harmonics reference as a function of krypton backing pressure.

taken at the start and end of each scan to their corresponding source harmonics references. The results can be seen in Figure 6.9. We observe that even at our lowest krypton backing pressures (around 50 mbar), we still achieve approximately 40% absorption in the above ionisation threshold source harmonic signal. The percentage values were calculated considering the change in signal measured in the source harmonics compared with the static absorption measurements averaged over the energy range 95.5-98.0 eV.

In future experiments to operate below the 20% threshold of absorption suggested in reference [104], we would need to use krypton backing pressures significantly lower than 50 mbar. It should be noted that the 20% threshold value is stated for a 0.3 mm target length. This value may differ for the longer, 6 mm target used in this work.

If we recall from Chapter 5, however, the static absorption measurement includes both absorption within the target region, as well as absorption due to diffuse helium within the target chamber, the ratio of which cannot be determined. Depending on the relative contributions from both absorption within the target and diffuse background absorption, improving the differential pumping and base

pressure within the target chamber could help to ensure a more accurate measurement for the interaction signal absorption by minimising any absorption from the diffuse background helium.

6.1.4 Delay Dependence In Kr Target

To investigate the highest order delay dependent modulation frequency components produced, long one-dimensional delay scans were performed to probe the response across the whole interaction overlap. Recording measurements without a second scan dimension significantly reduced the scan duration, minimising the impact of long term drifts in the setup. One such long scan can be observed in Figure 6.10 a). The raw signal was normalised using the same procedure as for the polarisation dependence data, delay corrected using the phase tagging and interpolated onto a linear delay axis, b). The vertical black line on the raw data image indicates the upper-edge of the harmonic range used to perform the intensity normalisation for the data set. The lower edge is beyond the lowest energy value shown on the photon energy axis. To compare the different frequency components observed in the harmonic orders around the ionisation threshold, narrow spectral regions were selected, indicated by the black lines in Figure 6.10 b). The signal was summed along the photon energy axis for each of these regions, and following the same procedure as for the polarisation scan we can extract the frequency component within a 15 fs FWHM super-Gaussian sliding temporal window as it is positioned at different points across the delay range, Figure 6.10 c). The final two spectrogram panels correspond to harmonic orders above the krypton 3d ionisation edge.

We observe a $2\omega_1$ component in all of the sampled harmonics, including the central regions of those above the ionisation threshold. For the four highest harmonic orders we also observe indication of a $4\omega_1$ component around 250-280 fs. The absolute delay offset is unknown. Since a modulation at $4\omega_1$ indicates a coupling between harmonic orders separated by one odd harmonic, this makes sense in the results where the shape of the response around the $4\omega_1$ frequency looks most similar between the spectral regions centred around 92.80 eV and 95.60 eV, and 94.2 eV and 97.00 eV respectively. The Fourier axis was rescaled to ensure the extracted frequency components matched the $2n\omega_1$ values. The rescaling corresponded to a central input wavelength of 1370 nm.

This scan was recorded using coarser resolution sampling at the envelope edges, reserving the finer delay steps for the 120 fs covering the peak interaction overlap. The set fine delay step used was 0.2 fs with the coarse delay step set to be 0.4 fs. Five images of 1 s exposure were recorded for each delay point, with static absorption references recorded every four delay steps. The dressing field peak intensity at the beginning of this scan was determined to be $6.5\times10^{13}\mathrm{W/cm^2}$, with a measured $\sim$3% drop in power across the duration of the scan. The central wavelength of the TOPAS signal was measured to be 1400 nm.

The probing APT was generated in argon using a set backing pressure of 310 mbar. An image showing the mean interleaved field free transmission (static absorption) reference signal on the

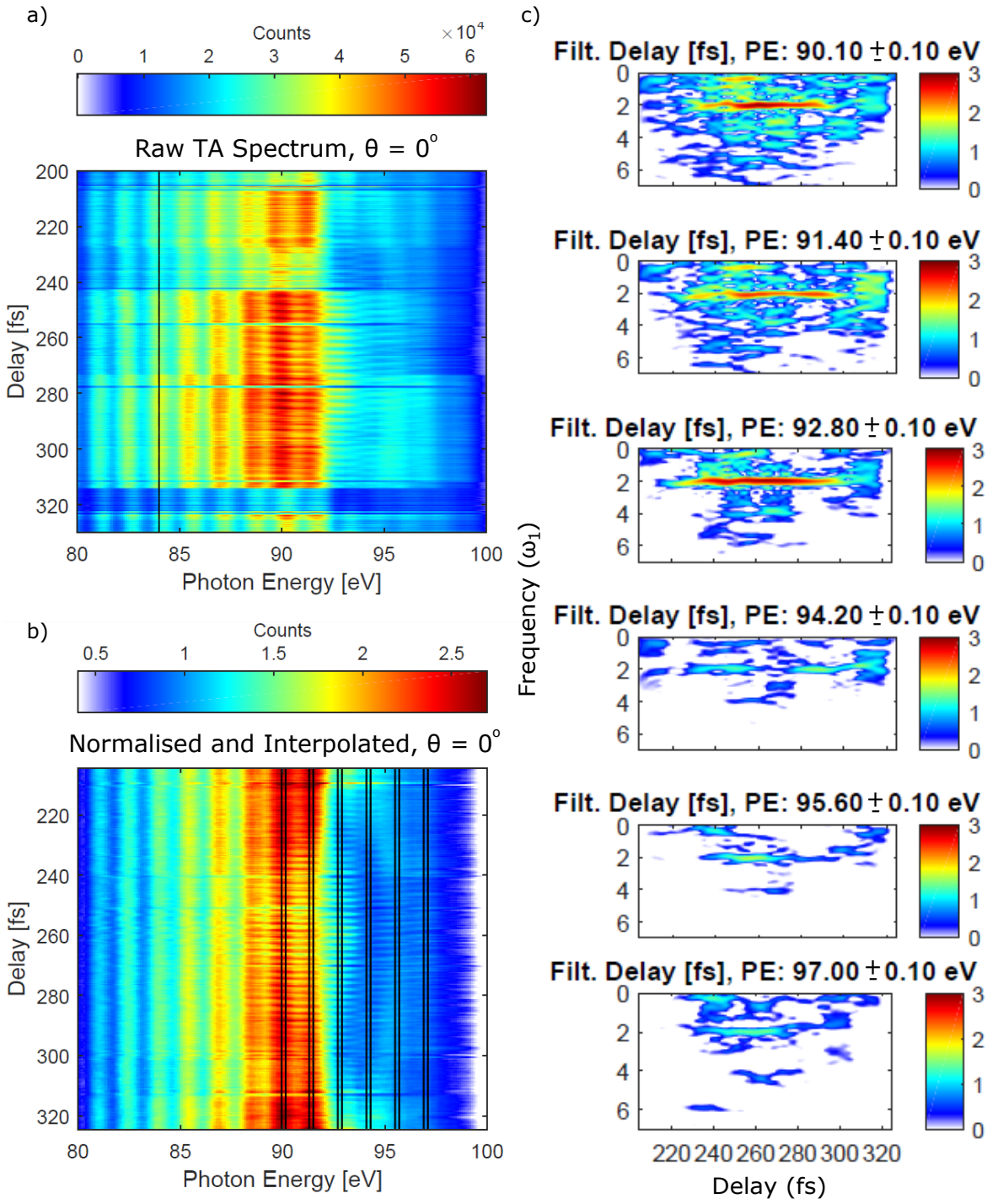


Figure 6.10: Raw, a), and processed, b), long transient absorption delay measurement from laser dressed krypton. The processed scan has been normalised both to the interleaved static absorption references as well as to a non-modulating harmonic energy range, temporally corrected using the phase tagging reference and interpolated onto a linear delay axis. c) Log scale Fourier response at different delays throughout the scan duration obtained by sliding a 15 fs FWHM super-Gaussian temporal window filter across the scan delay axis and recording the resultant Fourier components. The analysis has been performed looking the second order light measured on the MCP, and rescaled back to the correct energies. The dressing field peak intensity for the presented scan was calculated to be $6.5\times10^{13}\mathrm{W/cm^2}$.

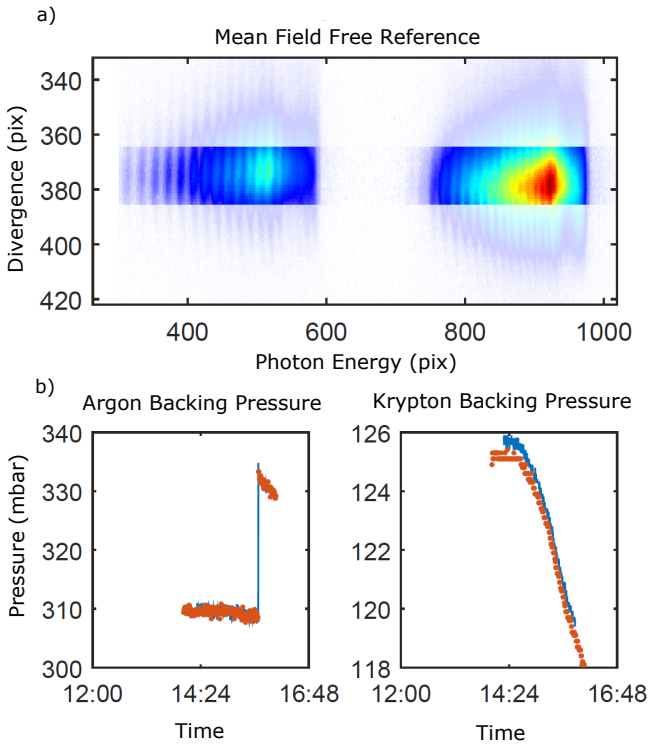


Figure 6.11: a) Mean harmonic spectrum recorded for the interleaved field free transmission (static absorption) reference measurements recorded across the scan delay range shown in Figure 6.10. The selected divergence range is shown in full colour. b) The recorded generation and target backing pressures as a function of delay throughout the scan duration.

detector across the range of the scan can be seen in Figure 6.11 a), along with plots of the generation and target pressures throughout the scan, b). The divergence range selected for this scan was narrower to try to isolate high order modulations that might otherwise fall below the noise floor.

A sharp jump is observed in the argon generation target backing pressure towards the end of the scan. Although such a change in the generation parameters will effect the probing APT, normalisation with respect to both the interleaved static absorption references and the intensity of each delay slice should correct, within reason, for both long term drifts and short term fluctuations.

Considering the whole spectral range whilst sliding a 15 fs FWHM super-Gaussian temporal window filter across the scan duration we can extract slices of the Fourier response centred at different temporal positions within the scan. These are presented in Figure 6.12. Here we observe the evolution of the different frequency components as a function of delay between the pump and probe pulses. We observe the strong $2\omega_1$ signal appearing in each of the harmonic orders probed, but also note that the $4\omega_1$ signal appears less convincing with the Fourier components displayed in this format. The results are presented on a log scale to enhance the lower amplitude components.

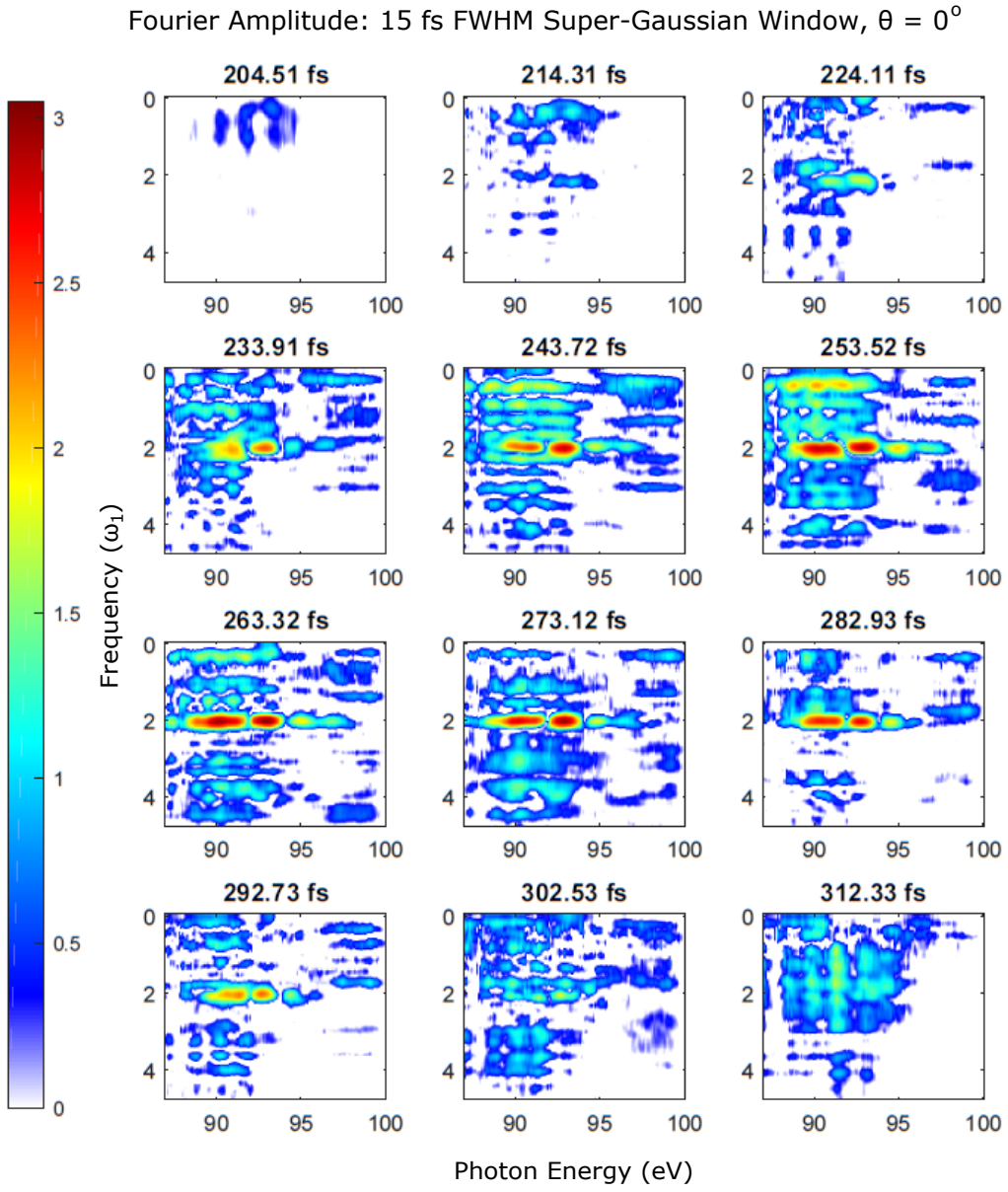


Figure 6.12: Log scale extracted Fourier amplitude components as a function of probing photon energy for the laser dressed krypton transient absorption delay scan presented in Figure 6.10. Each panel corresponds to a different 15 fs FWHM, super-Gaussian temporal window within the scan duration. The central delay for each window is given in the title for each panel.

6.1.5 Discussion

In general, we do not observe strong modulation in many of the above ionisation threshold harmonic orders, including anything around or above the 100 eV silicon edge from the silicon-zirconium filter.

Due to the high photon energies required to probe the krypton 3d edge and the nonlinear energy scaling on the MCP, the spatial separation of the harmonic orders around the krypton 3d edge is very narrow (approximately 10 pixels separation between peaks around 95 eV). Because of this, any significant error in the calibration could change the exact positioning of the harmonic orders with respect to the ionisation threshold. Since the calibration for the krypton work was performed using energetically well known filter edges (the first and second orders of the silicon-zirconium filter silicon edge at 100 eV and 50 eV respectively), the calibration should be more accurate than determining the energy scale from the source harmonic order positions.

As already discussed in the introduction to this Chapter, for the krypton atom there are many different energetically close excitation and ionisation possibilities. With the typical dressing field peak intensities used, I$\approx 6\times10^{13}$W/cm^2, for a 1400 nm input, this gives a ponderomotive energy around 11 eV. The AC Stark effect will shift, split and broaden the bound energy states in the dressed krypton, with the Rydberg levels shifting upwards by approximately the ponderomotive energy, Up, leading to many different possible transition pathways becoming available. To observe the best visibility modulation one should have two equally contributing signals allowing for perfect constructive and destructive interference to occur. If one of the contributing signals is much weaker than the other, the interference contrast will be reduced. In addition, for an increased number of contributing signals, unless they all add perfectly in phase, this will also act to lower the visibility of any single modulation. With the many different ionisation pathways available in the dressed krypton atom from both the 93.8 eV, j = 5/2, and the 95 eV, j = 3/2, it is possible that low modulation above the ionisation threshold arises through the interference of many different ionisation channels, rather than resulting just from weak coupling. One possible way to clarify this is if we could have identified an XiHHG signal above the 100 eV filter edge.

Detecting light above the 100 eV edge would have been a clear indication of higher order processes occurring. As no photons were present at those frequencies in the source harmonic spectrum due to the silicon-zirconium filter, if a signal was detected above 100 eV following transient absorption, it could only have been generated through an XiHHG type interaction, and would have been produced onto a zero background. One reason why we may not have observed such an XiHHG signature is due to the intensity of the dressing field used. Literature suggests that the "very-short" trajectories made available through the ability to ionise both "uphill" and "downhill" trajectories in an XiHHG scheme could play a significant role in any XiHHG measurement [128]. Although standard short and long trajectories can also contribute, the theory predicts a much larger recombination probability for the "very-short" trajectories [128]. Recalling that in the XiHHG mechanism, the electron is assumed

to be born into the continuum with kinetic energy equalling the difference between the ionisation threshold and the energy of the ionising photon, the maximum energy that can be imparted by the dressing field will depend on both the relative delay between the XUV pulse and the phase of the dressing field, as well as the kinetic energy with which the electron is born. For the work presented by Leeuwenburgh *et al.* in reference [128], the Up is approximately 34 eV. The highest intensity XiHHG signal calculated returns the electron to the parent ion with just a small fraction of the Up energy, up to ∼15 eV gain corresponding to approximately $0.44\,Up$. Considering again the typical Up achieved for the krypton work, ∼11 eV, the maximum kinetic energy gain for the "very-short" trajectories would be 4.8 eV. This would not be enough to be visible above the 100 eV edge, and below the edge any signal produced would overlap with light already present from the source harmonics making detection much harder and not conclusive as XiHHG. Future experiments looking at transient absorption of the krypton 3d edge could benefit from the ability to dress the krypton with a higher intensity dressing field in order to be able to look more thoroughly for an XiHHG signature.

6.2 Transient Absorption from Long Wavelength Laser Dressed Helium

With the many improvements made to the beamline setup and acquisition software prior to the longer wavelength studies, we wanted to repeat the transient absorption work from laser dressed helium at this longer wavelength to confirm the previous results, and extend the earlier studies with the upgraded system and longer wavelength pump.

In this section I will present the results we obtained comparing the effect on the delay dependent modulation when we change the relative dressing field linear polarisation from parallel to perpendicular with respect to the probing XUV field. With the improvements made to the setup, the results presented probe the response across the whole envelope of interaction. Specifically, we observe light induced states (LIS) at the interaction envelope edges. These regions correspond to a gradient of effective lower intensity dressing field. I will compare the LIS evolution for the different dressing field polarisation alignments with that from literature [20, 114]. In addition, I will present results looking for high order modulations.

6.2.1 Dressing Field Polarisation Dependence

We observed the response in helium of the delay dependent absorption modulation amplitude as the relative linear polarisation orientation of the TOPAS signal dressing field is rotated from parallel to perpendicular with respect to that of the probing XUV. As for the similar krypton measurement

presented in Section 6.1.1, we follow the same data processing procedures to understand the changes between the two polarisation states. This can be seen in Figure 6.13. Unlike the krypton study, the intensity normalisation for the helium work was performed using higher order, non-modulating harmonic(s) since modulations were visible in many orders below the ionisation threshold. The processed normalised and interpolated data can be seen for each of the parallel ($\theta = 0°$), and perpendicular ($\theta = 90°$) linear dressing field polarisations in Figure 6.13 a) and b) respectively. Again, normalisation was performed using both the interleaved field free (static absorption) references to adjust for slow changes in the spectrum, as well as intensity normalisation to correct for fast changes in the recorded flux.

In Figure 6.13 c) we observe the result of the Fourier components comprising the summed discrete energy regions depicted by the vertical black lines in Figure 6.13 a) and b), for a 15 fs FWHM super-Gaussian temporal window filter slid across the scan delay range. We observe that for the two below ionisation threshold harmonic orders (below 24.59 eV), there is little change in the amplitude of the $2\omega_1$ components for the different dressing field linear polarisation orientations. There are hints of $4\omega_1$ in the energy region centred around 23.89 eV for the parallel aligned dressing field polarisation which are absent from the perpendicularly polarised case. In the directly above ionisation threshold harmonic probed there is a large vectorial response to the dressing field polarisation orientation for the measured $2\omega_1$ frequency. For the case of perpendicular alignment of the dressing field polarisation, the recorded signal appears to be almost zero, markedly different from the clear $2\omega_1$ response recorded from the parallel aligned dressing field alignment. In the highest harmonic order probed, there are hints of $2\omega_1$ and $4\omega_1$ components in the parallel aligned case however these signal values approximate the noise measured around $1\omega_1$.

This strongly anisotropic behaviour for the directly above ionisation threshold harmonics was also observed when probing the laser dressed helium target with the 800 nm dressing field. In addition, for the earlier 800 nm work we also saw minimal change for the below ionisation threshold modulation amplitude which is mirrored in this longer wavelength dressing field study. The results shown in Figure 6.13 c) are presented on a log axis for clarity.

Due to the rotation of the MCP detector between the 800 nm work and the 1400 nm studies, the harmonic order that should lie around 20.5 eV falls directly on the stripe of insensitivity resulting from the 'burnt' phosphor screen. For this reason this harmonic appears very low flux compared with the other harmonic orders.

The scan was performed using a set coarse delay increment of 0.5 fs for the overlap edges (-80 to -50 fs and 50 to 100 fs), with finer delay steps, (0.25 fs), reserved for the central nominally 100 fs overlap position, reducing the overall scan duration. In general following the phase tagging temporal correction, the actual delay increments were reduced a little from their set values. This is indicated by the shorter delay axis observed in Figures 6.13 a) and b). The central signal wavelength for this

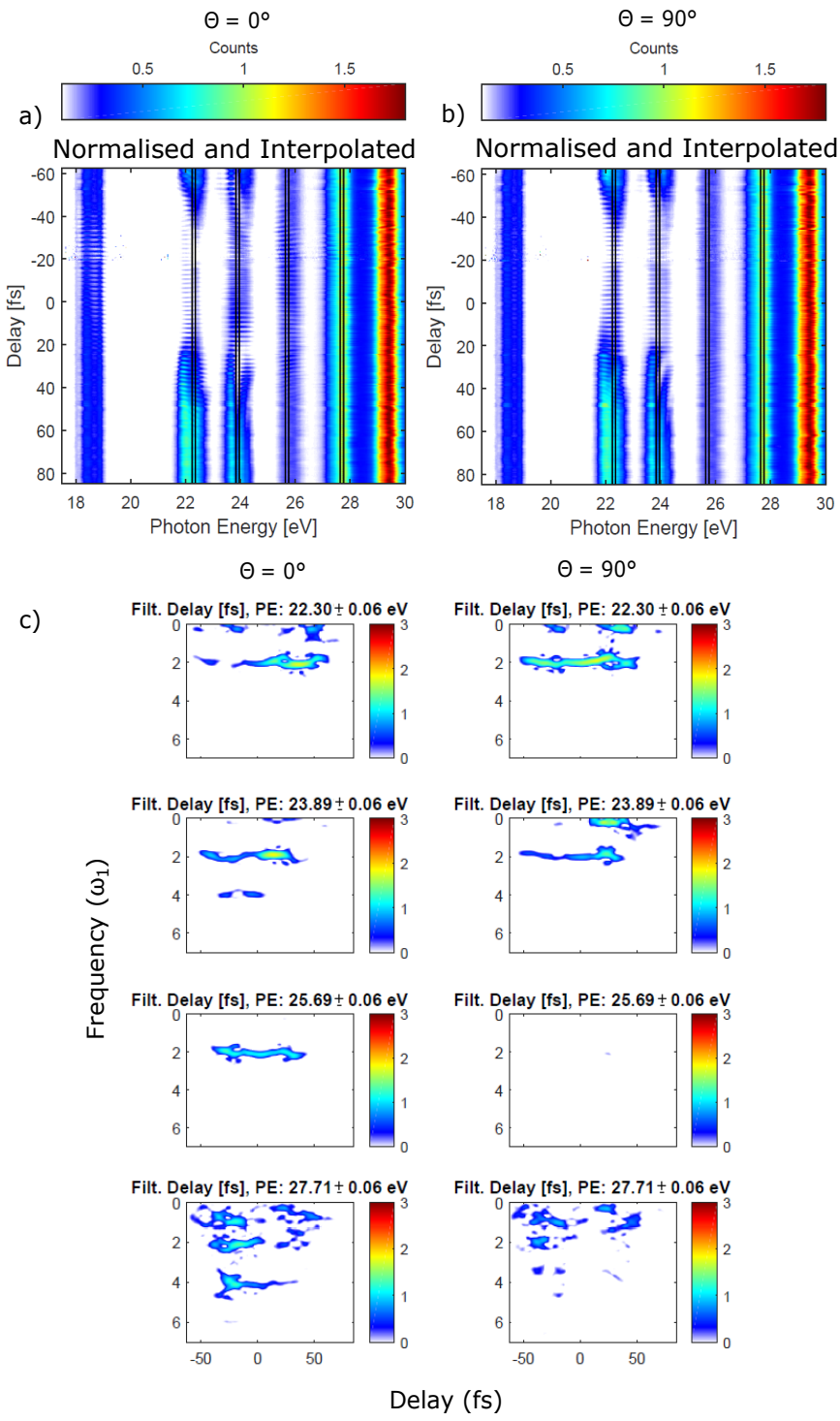


Figure 6.13: Comparison of the transient absorption transmission signal of laser dressed helium for linear polarised dressing fields aligned a), parallel (θ=0°), and b), perpendicular (θ=90°), with respect to the probing APT field polarisation. c) Log scale Fourier response sampled for discrete energy ranges for each polarisation orientation as a function of delay with respect to a 15 fs FWHM, super-Gaussian window filter. The target gas is helium, with probe harmonics generated in xenon. The dressing field peak intensity for the presented scans was calculated to be 6.2×10^{13}W/cm^2.

scan was measured to be 1390 nm, and the peak intensity determined to be 6.2×10^{13}W/cm^2. Five images were recorded per delay step, each with an exposure time of 1 s. The different polarisation states were interleaved to minimise the impact of long term drifts in the setup, and a static absorption reference was recorded every 4 delay steps. The averaged static absorption references interleaved throughout the course of the delay scan can be seen in Figure 6.14 a), along with the divergence region selected for which to sum over to produce the signal for each delay slice. This is indicated by the full colour region of the image. The source harmonics for this scan were generated in xenon, with a typical backing pressure of ∼10.5 mbar. The helium target was backed with a pressure ∼26 mbar. The evolution of both of these parameters throughout the scan duration can be observed in Figure 6.14 c). The Fourier axis was rescaled to ensure the extracted frequency components matched the $2n\omega_1$ values. The rescaling corresponded to a central input wavelength of 1263 nm. Again the reason for such a large difference between the measured input wavelength and that determined to position the Fourier components at exactly $2\omega_1$ and $4\omega_1$ is unknown. Some suggestions however were given in section 6.1.1.

Considering instead the Fourier components extracted for the whole photon energy axis for specific 15 fs FWHM super-Gaussian temporal windows, we can observe the evolution of the coupling amplitudes as a function of delay across the scan duration. This can be seen in Figures 6.15 and 6.16 corresponding to the parallel and perpendicularly aligned dressing field linear polarisations respectively. The central delay positions of the temporal filter window for each of the scans do not exactly match due to the different phase tagging correction applied to each of the parallel and perpendicular aligned data.

Comparing the response to the two dressing field polarisation states we again clearly see an enhanced $2\omega_1$ modulation amplitude for the parallel alignment, particularly in the above, and far below, ionisation threshold harmonic orders, compared with the perpendicular polarisation alignment. We also clearly observe $4\omega_1$ components for both scans, however in general these appear to be stronger, and visible in a broader number of harmonic orders for the parallel polarised dressing field response compared with the perpendicular. An example of this is in the lowest harmonic order observed in the photon energy range displayed (around 19 eV). For the parallel aligned pump and probe field polarisations, a clear $4\omega_1$ component can be observed at this photon energy from -38.4 fs up to 21.8 fs on the delay range. In the perpendicular aligned case only hints of a $4\omega_1$ response can be observed in this range. The strong $2\omega_1$ component in all of the modulating harmonic orders indicates coupling between each of these adjacent harmonics. The modulations appearing at $4\omega_1$ indicate coupling between harmonic orders separated by one order, which are therefore separated by $4\omega_1$ in energy. Since the harmonic order situated around 20.5 eV on the energy scale falls within a damaged region on the MCP detector, it appears much less bright than the other harmonics due to the reduced sensitivity. Lower amplitude modulations in this harmonic could be in part a result

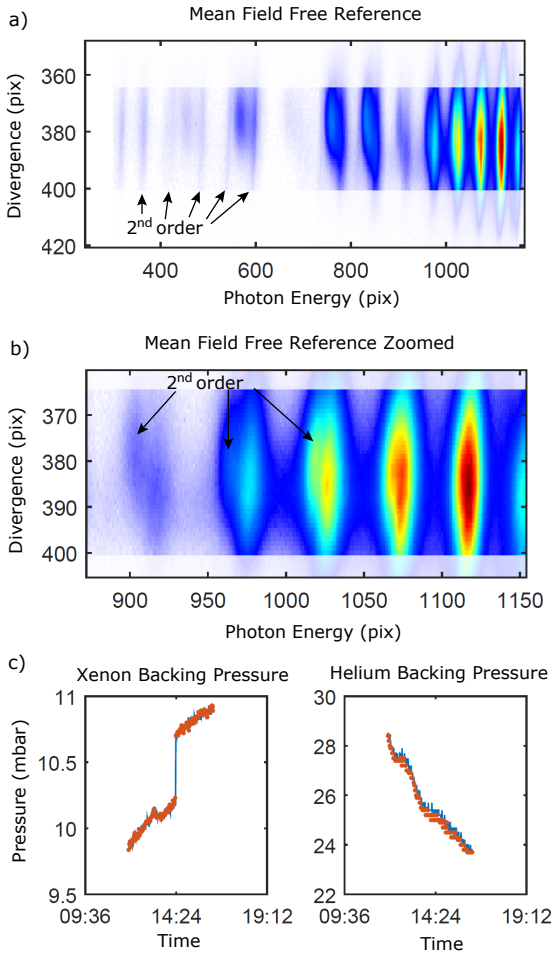


Figure 6.14: a) Mean harmonic spectrum recorded for the interleaved field free transmission (static absorption) reference measurements recorded across the scan delay range presented in Figure 6.13. The selected divergence range is shown in full colour. b) Magnified mean field free transmission reference to highlight the second order harmonic components visible on the detector. c) The recorded generation and target backing pressures as a function of delay throughout the scan duration.

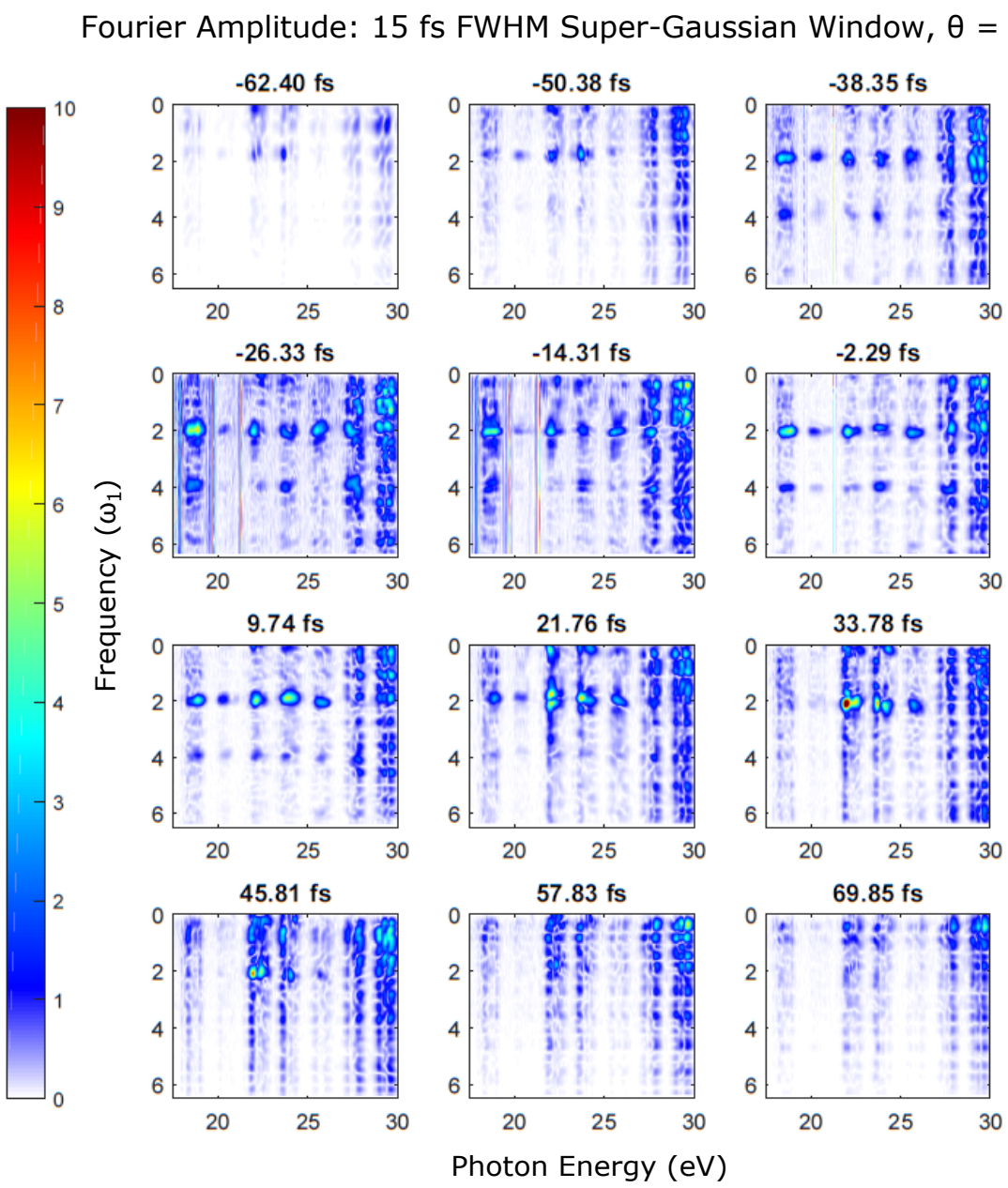


Figure 6.15: Fourier amplitude as a function of probing photon energy extracted from the transient absorption delay scan using parallel aligned dressing and probe field linear polarisations. Each panel corresponds to a different 15 fs FWHM, super-Gaussian temporal window within the delay scan. The central delay for each window is given in the title for each panel.

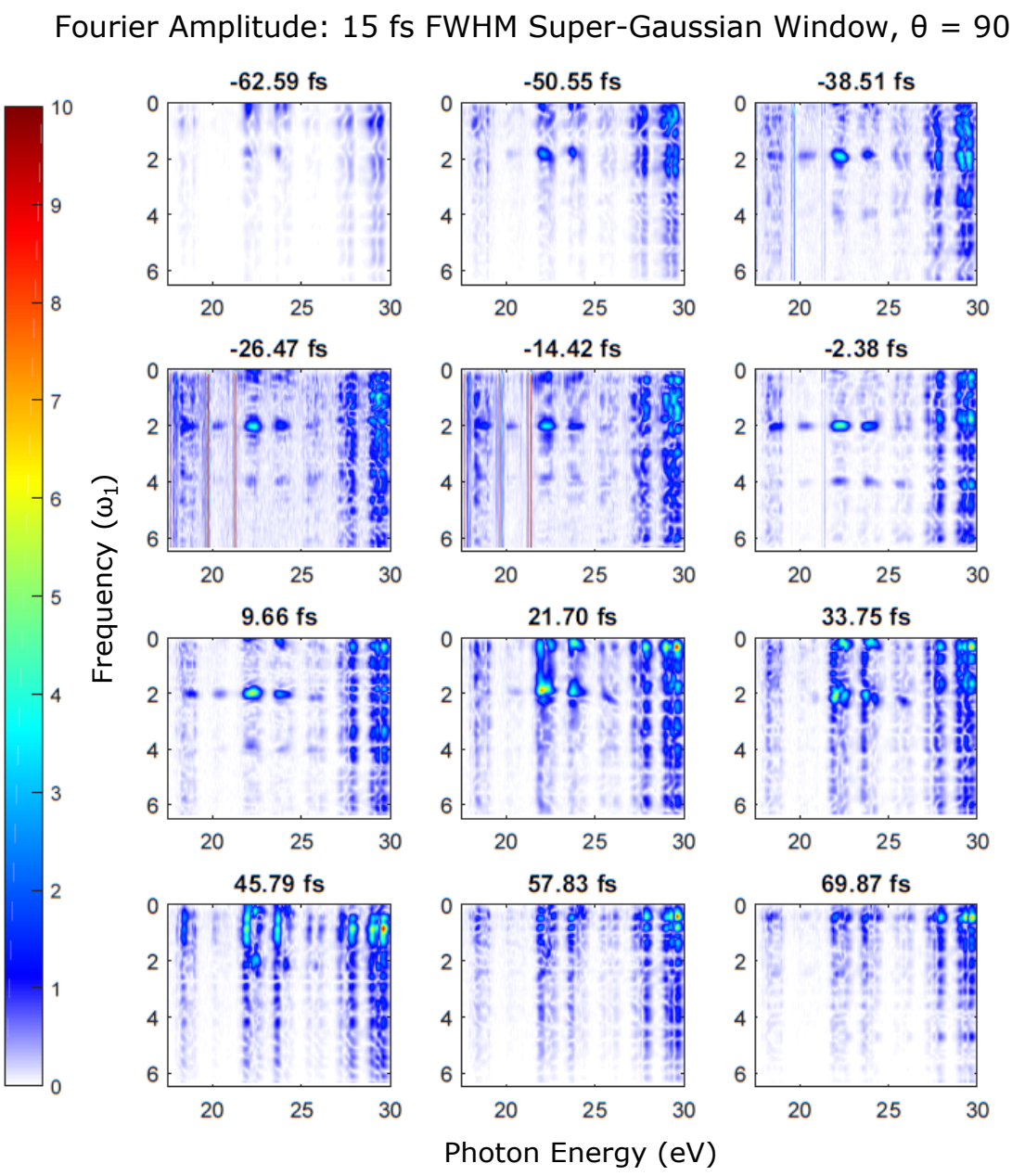


Figure 6.16: Fourier amplitude as a function of probing photon energy extracted from the transient absorption delay scan using perpendicular aligned dressing and probe field linear polarisations. Each panel corresponds to a different 15 fs FWHM, super-Gaussian temporal window within the delay scan. The central delay for each window is given in the title for each panel.

of this damage.

Despite changing the orientation of the laser dressing field in this experiment, it was observed that there was only minimal change in dressing field power as measured after the insertable pickoff mirror when the polarisation was oriented either parallel or perpendicular with respect to the probing XUV field. The difference was only ∼10 mW out of a total measured ∼440 mW, and as such no dressing field IR iris power compensation was used for this scan.

During approximately the first third of the scan delay, the detected signal was observed to drop significantly. This can be seen in the raw signal measured for the parallel oriented dressing field polarisation scan in Figure 6.17 a). At around -28 fs on the processed delay axis the acquisition was paused, and the target gas jet was adjusted vertically and laterally with respect to the pump-probe foci to improve the detected signal strength. With the improved signal following the adjustment, the scan acquisition could be re-started with only a minimal interruption to the recorded scan. Following normalisation, the interface between these two segments is barely visible (compare Figures 6.17 a) and b)). The black vertical lines in the raw image, Figure 6.17 a), indicate the harmonic range used to perform the flux normalisation. Adjusting the position of the target relative to the pump and probe beams should not affect the processed result other than the effective signal to noise ratio so long as the slow drift producing the drop in signal resulted between the target gas jet and the overlapped beams rather than between the two pump and probe foci themselves. If the target slowly drifts relative to the beams it will effectively just slowly cut the XUV signal, but the dressing field intensity probed by the XUV foci will remain constant. If however the cutting of the XUV signal results for the XUV beam slowly drifting relative to the dressing field foci and the target holes, this would change both the overall signal and the probed dressing field intensity peak value and distribution within the target. Given the similarity between the two regions of the scan when the data is normalised, we can assume that generally we are experiencing the former.

Considering the below ionisation threshold delay dependent modulation response towards the edges of the interaction envelope, we observe structure in the harmonic modulation for the two harmonics directly below Ip, Figure 6.18 a). This reduction in transmission was not visible for the static absorption references in the undressed helium target and so must be induced by the laser dressing field. Magnifying this region, Figure 6.18 b) and c), we observe a series of light induced states (LIS) visible within the probing harmonic energies centred around 22.1 eV and 23.9 eV for both the parallel and perpendicular dressing field relative linear polarisations. In addition we observe that the evolution of these states with delay differs between the dressing field polarisation orientations. The data presented in Figure 6.18 c) is the same as that in 6.18 b) however with the zero order modulation component (DC offset) removed so as just to observe the modulations in the transmission around a zero background.

The clearest LIS occurring around 23.9 eV for both $\theta = 0°$ and $\theta = 90°$ appears to broaden

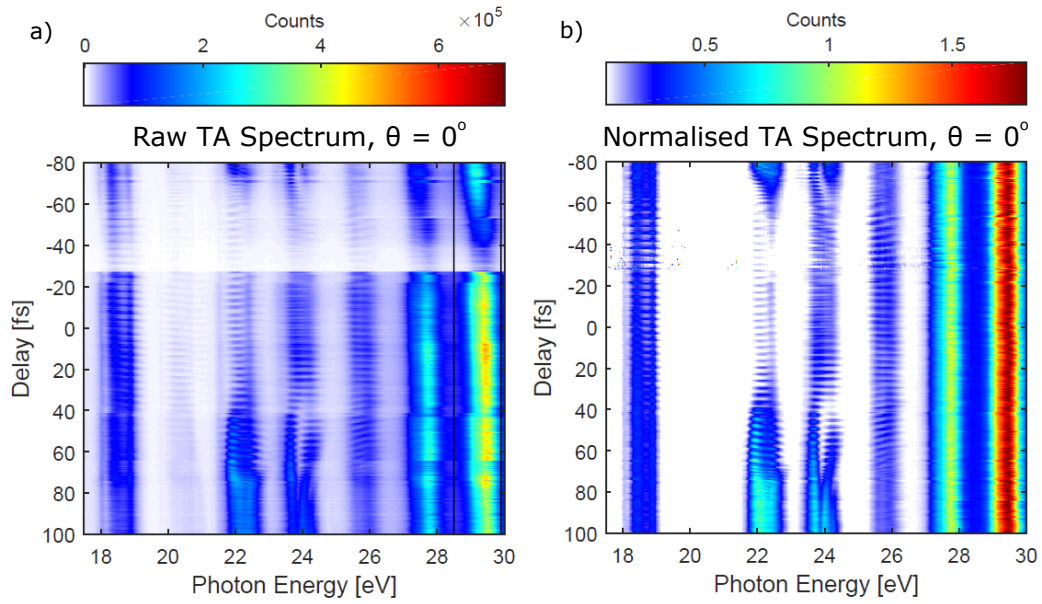


Figure 6.17: Comparison of the recorded raw transient absorption transmission, a), and processed transient absorption transmission, b), for the parallel aligned dressing field linear polarisation. The processed image has been normalised both with respect to the interleaved field free transmission references as well as the flux of the recorded images. Both the processed and raw spectra have been plotted on a similar, temporally corrected delay axis.

and shift out of the probing harmonic energy range at around 24 fs on the delay scale. It looks as though a further LIS appears around a photon energy of 24.25 eV for each polarisation orientation, more easily viewed in the background free images in Figure 6.18 c). This LIS disappears from the harmonic modulation at around 35 fs on the delay scale. For the lower harmonic order, centred around 22.1 eV, two further splittings of the harmonic modulation due to resonances appear to be visible in both polarisation orientations located in energy around 22.15 eV and 22.4 eV respectively. The general evolution with pump-probe delay for these LIS however are visibly different between the dressing field polarisation states, with the splitting in the harmonic response around 22.15 eV much more pronounced in the perpendicularly aligned case.

The energy levels for the undressed helium target presented in Figure 5.1 are recapped in table 6.1, along with the expected LIS energy positions assuming a 1390 nm wavelength with a single dressing field photon energy corresponding to 0.89 eV. This table has been based closely on that presented by Reduzzi *et al.* in [114]. Considering these values one can try to assign possible levels to the observed LIS.

Due to the close separation of many of the different LIS states, it is difficult to assign particular LIS to spectral features with certainty. Recalling the observations of Reduzzi *et al.* to the dressing field polarisation response of the LIS in low dressing field intensities [114], one can infer states

Energy Level	Energy (eV)	Dressed State	Energy (eV)
1s2s	20.62	$2s^-$	19.73
		$2s^+$	21.51
1s3s	22.92	$3s^-$	22.03
		$3s^+$	23.81
1s3d	23.07	$3d^-$	22.18
		$3d^+$	23.96
1s4s	23.67	$4s^-$	22.78
		$4s^+$	24.56

Table 6.1: Expected energy levels for light induced states with dressing field $\lambda = 1390$ nm, corresponding to photon energy of 0.89 eV. This table is based closely on that presented by Reduzzi *et al.* in reference [114]. The field free energy levels are reproduced from reference [114], and confirmed using reference [158].

appearing only with the $\theta = 0°$ dressing field polarisation alignment will be due to two-photon coupling to an s-state, where as LIS appearing in both $\theta = 0°$ and $\theta = 90°$ dressing field polarisation alignments will be due to two-photon coupling to a d-state. Comparing the energy values observed for the measured LIS with those from table 6.1, we can tentatively assign the LIS at 22.15 eV to be the $3d^-$ state, and that appearing around 23.9 eV to be a mixture of the $3s^+$ and the $3d^+$. This could be plausible since the state around 22.15 eV appears strongest for the perpendicular dressing field alignment. If the closely separated $3s^+$ and $3d^+$ LIS both contributed to the structure observed around 23.9 eV this could explain the difference in appearance between the LIS at parallel (dominated by the $3s^+$), and perpendicular (dominated by the $3d^+$) dressing field alignments. Calculated using the field free helium values, these states would be separated by 0.15 eV. By the same argument, the 2^{nd} component of the 3s LIS could also contribute to the observed structure in the modulation around 22.15 eV and the differences observed between the response of the parallel and perpendicular polarisation alignments. The $3s^-$ LIS should appear around 22.03 eV however, which is a little lower than the observed structure in either of the parallel or perpendicular oriented results.

The LIS at 22.4 eV does not closely match any states. One of the closest matches it could be is the $4s^-$, however this should be somewhat higher at around 22.78 eV. Alternatively, if there was a small calibration offset and the features at 22.4 eV and 22.15 eV were instead the $3d^-$ and $3s^-$ LIS respectively, then the structure at 24.4 eV would match more closely in energy to the calibration adjusted $4s^-$ LIS. If we recall from reference [114] however, LIS due to s-state coupling were not present for the perpendicular dressing field polarisation orientation, whereas these states appear to be present for both parallel and perpendicular dressing field polarisation alignments.

The possible LIS appearing around 24.25 eV does not match closely with any states either. It does however match very closely with the 1s6p state, observed in Figure 6.19, reproduced from reference [20]. As the dressing field is applied, this leads to a broadening of the bound states as the lifetime of the states reduces due to additional transition pathways becoming available [20]. The

observed feature at 24.25 eV could therefore actually just be the single photon transition to the 1s6p state becoming visible with the resolution of the detector.

It is observed in the harmonic spectra of the average field free transmission (static absorption) reference scans, Figure 6.14 a) and b), that signal is also detected at energies not associated with expected harmonic orders. This is particularly visible for the lower harmonic orders seen in Figure 6.14 a). We understand this light to be the second order reflection from the diffraction grating resulting from higher energy harmonics not visible on the MCP detector area. We can therefore use this information to estimate the cutoff of our source harmonic spectrum, even though the first order reflection response cutoff appears at a higher energy than we can detect. Considering the magnified image shown in Figure 6.14 b), we estimate the highest visible second order reflection component to be on the left-hand side of the central harmonic shown in this panel. This corresponds to harmonic 33, situated the third harmonic above the ionisation threshold. Considering the energy calibration for this scan, second order light falling around this position would correspond to a cutoff of ∼59 eV. If we recall that double excitation processes become energetically available with single photons energies around 60 eV [154], we are very close to this limit for the source harmonic spectrum used in this scan. With a small error in the maximum second order contribution or energy calibration scaling we could easily find ourselves above this threshold. Around the cutoff energy, the intensity of harmonics falls sharply however meaning that even if we do surpass this threshold with our probing source harmonic spectrum, the flux of light at this photon energy will only be small, and should have little impact on the result. In addition there should not be any coupling between harmonics around 60 eV and those situated around the ionisation threshold, so this should not affect the results presented.

We can however estimate the peak intensity of the focus within the generation target to give such a high cutoff. Recalling equation 2.46, and assuming the cutoff energy is 59 eV, the central wavelength is 1393 nm and we are generating in xenon ($Ip = 12.1$ eV), we can estimate an intensity of the order of 8.2×10^{13}W/cm^2 must be present in the generation target. This is still below the measured saturation intensity of xenon, found at $\sim1.2\times10^{14}$W/cm^2 [165], for an 800 nm laser pulse of 58 fs pulse duration.

To reduce the peak intensity in the generation target, lowering the cutoff energies and moving closer towards a scenario where we may hope to observe an XiHHG signature, we replaced the dividing 4 mm annular mirror with a smaller, 3 mm, replacement, reducing the beam area to a factor of $\frac{9}{16}$. The peak intensity will also reduce by a similar amount, however given that reducing the beam diameter will also increase the focal spot size, this too will play a role in the intensity change. Fine adjustments to the generation intensity could still be made with the generation beam motorised iris, allowing some control over the effective phase matching and generation process. Calculating a new effective cutoff energy with an approximate $\frac{9}{16}$ reduced intensity, we expect to observe cutoff around 38.5 eV following the annular mirror swap, which should be visible around

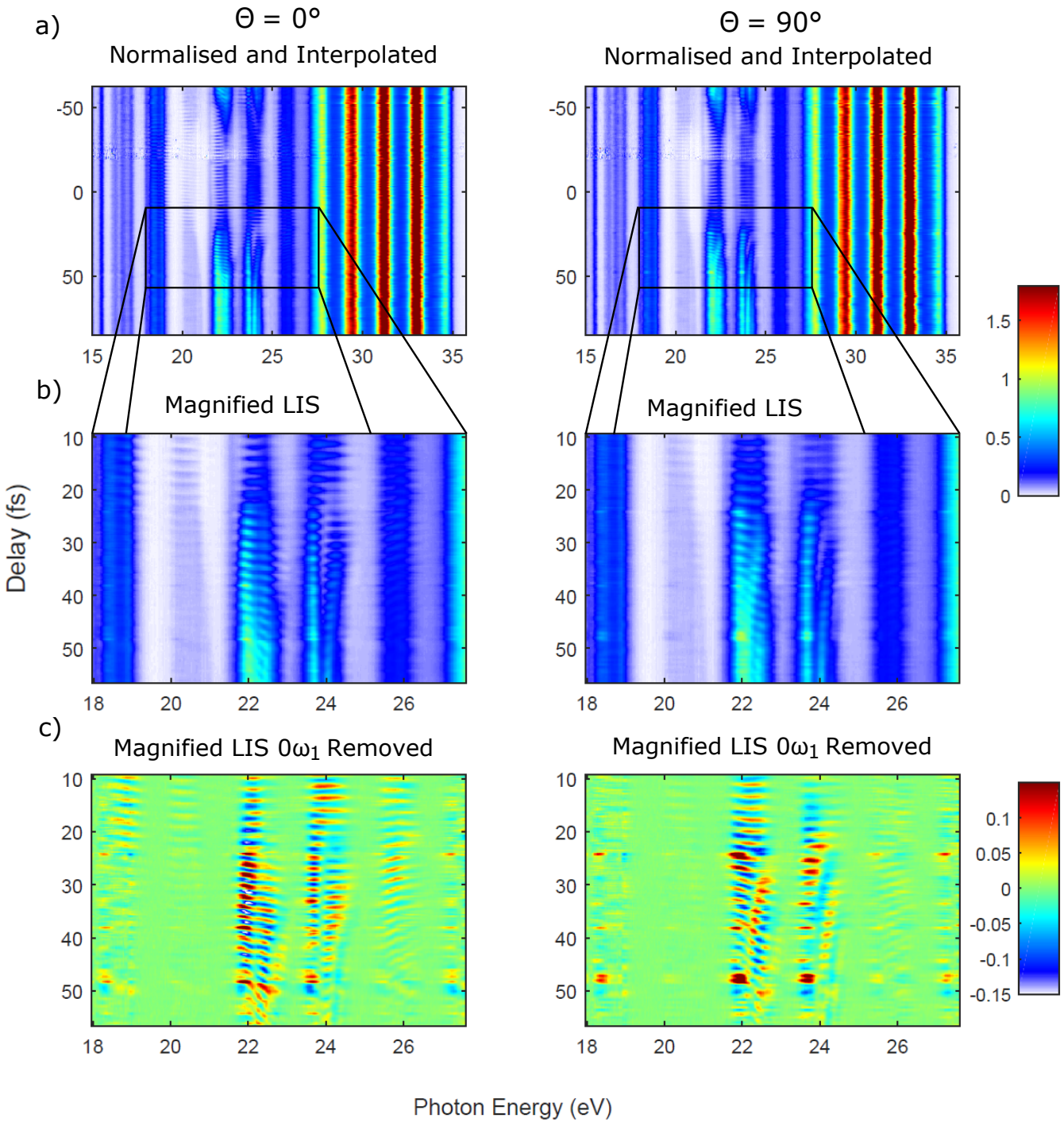


Figure 6.18: Normalised, a), and magnified, b), spectra investigating the light induced states in the harmonic orders around 22.1 eV and 23.9 eV with parallel, θ=0°, and perpendicular, θ=90°, aligned relative dressing field linear polarisation. c) Normalised, magnified spectrum with the zero order modulation removed, highlighting the differences in the harmonic modulations for the two compared dressing field polarisation states.

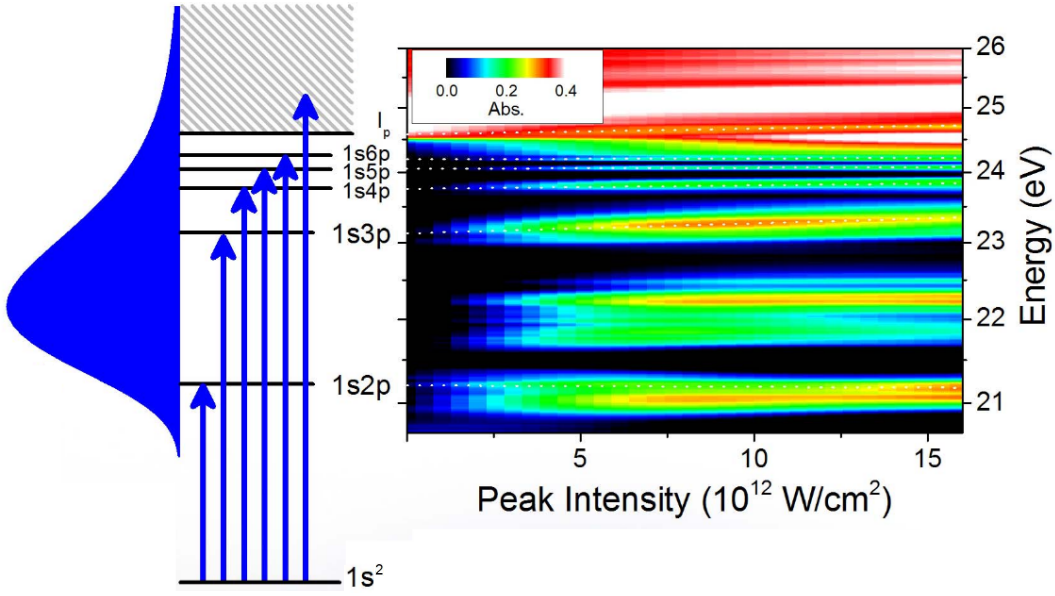


Figure 6.19: Experimentally determined absorbance spectrum for an isolated attosecond pulse generated and dressed using 730 nm. This Figure has been reproduced from reference [20]. CC BY-NC-ND 3.0.

harmonic 21 on the MCP for the second order light. Observing Figure 6.22 taken following the annular mirror exchange, harmonic 21 falls around 600 pixels on the energy axis. Second order components are much less visible in Figure 6.22 compared with Figure 6.14 supporting this.

6.2.2 Delay Dependence In He Target

To resolve the highest order modulation orders for the given experimental parameters, we acquired long, fine delay scans. As for the similar studies performed using laser dressed krypton, reducing the scan dimension from 2 parameters to 1 greatly reduced the scan duration, enabling faster, full interaction envelope scans to be recorded, minimising the effect of long term drifts in the system. An example of one such scan can be seen in Figure 6.20 a) and b), where a) depicts the raw spectrum recorded and b) shows the processed, normalised, phase corrected and interpolated data. The normalisation for harmonic flux was performed using the signal summed within the vertical black lines shown in Figure 6.20 a). Once again Fourier analysis was performed for photon energy ranges sampling different spectral regions within the observed modulating harmonic orders, indicated by the vertical black lines shown in Figure 6.20 b). The Fourier components within a sliding 15 fs FWHM super-Gaussian filter window can be seen in Figure 6.20 c) as a function of delay across the length of the scan duration. We observe clear $2\omega_1$ modulation for all but the highest sampled harmonic across

all, or part of the scan delay range indicating coupling between each of these harmonic orders through the dressing field. The highest harmonic indicates signs of $2\omega_1$ modulation, however the noise level is high compared with the signal. Strong $4\omega_1$ components are observed for all the below ionisation threshold harmonic orders, as well as indications of $4\omega_1$ in the two above threshold harmonics. A hint of $6\omega_1$ is visible in the harmonic order situated around 25.43 eV. Even though the amplitude is low, the lack of other noise makes this signal more convincing. Once again the results presented in Figure 6.20 c) are displayed on a log scale for clarity.

Extending once more the Fourier analysis to the whole spectral range, we can observe the Fourier components for different 15 fs FWHM, super-Gaussian temporal windows across the delay axis. This result is shown in Figure 6.21. Here we can clearly see the evolution of the $2\omega_1$ and $4\omega_1$ modulation components across the duration of the delay scan. The emergence of a $6\omega_1$ component in the directly above ionisation threshold harmonic centred around 25.43 eV can also be seen from 78.4 fs to 112.7 fs in delay. For modulations to occur at a frequency $6\omega_1$, this indicates a coupling of harmonic orders separated by two additional harmonics. We would therefore expect to also see a $6\omega_1$ component for the same delay range in the harmonic order situated around 20 eV. There are hints of possible $6\omega_1$ modulation at this photon energy from around the same delay position, however the magnitude of this signal is much weaker, possibly due to this harmonic falling within the damaged stripe on the MCP.

This scan has been performed over a set delay of 80 fs in increments of 0.2 fs steps, with a dressing field peak intensity of $4.0\times10^{13}\mathrm{W/cm^2}$. The central wavelength of the TOPAS signal was measured to be 1400 nm. Five images were recorded per delay point, with an exposure time of 1 s per image. Field free transmission (static absorption) references were recorded every four delay steps, and the mean of these interleaved references can be seen in Figure 6.22 a). The source harmonics were generated using xenon with a backing pressure of 4.6 mbar. The helium target backing pressure was measured to be 37 mbar. The evolution of both generation and target backing pressures throughout the delay scan can be seen in Figure 6.22 b). A narrow divergence selection was chosen to analyse this scan. The selected region is indicated by the full colour stripe shown in Figure 6.22 b). This was done to help isolate any high order components which may otherwise fall below the noise floor if regions of the harmonic with different phase response (i.e. short and long trajectory components) are averaged together in a larger divergence selection. Also, given the stability of this scan (recall the comparison between the raw and processed data shown in Figure 6.20 a) and b)), there was little change in the divergence spread of the source harmonics across the scan length. The Fourier axis was rescaled to ensure the extracted frequency components matched the $2n\omega_1$ values. The rescaling corresponded to a central input wavelength of 1370 nm.

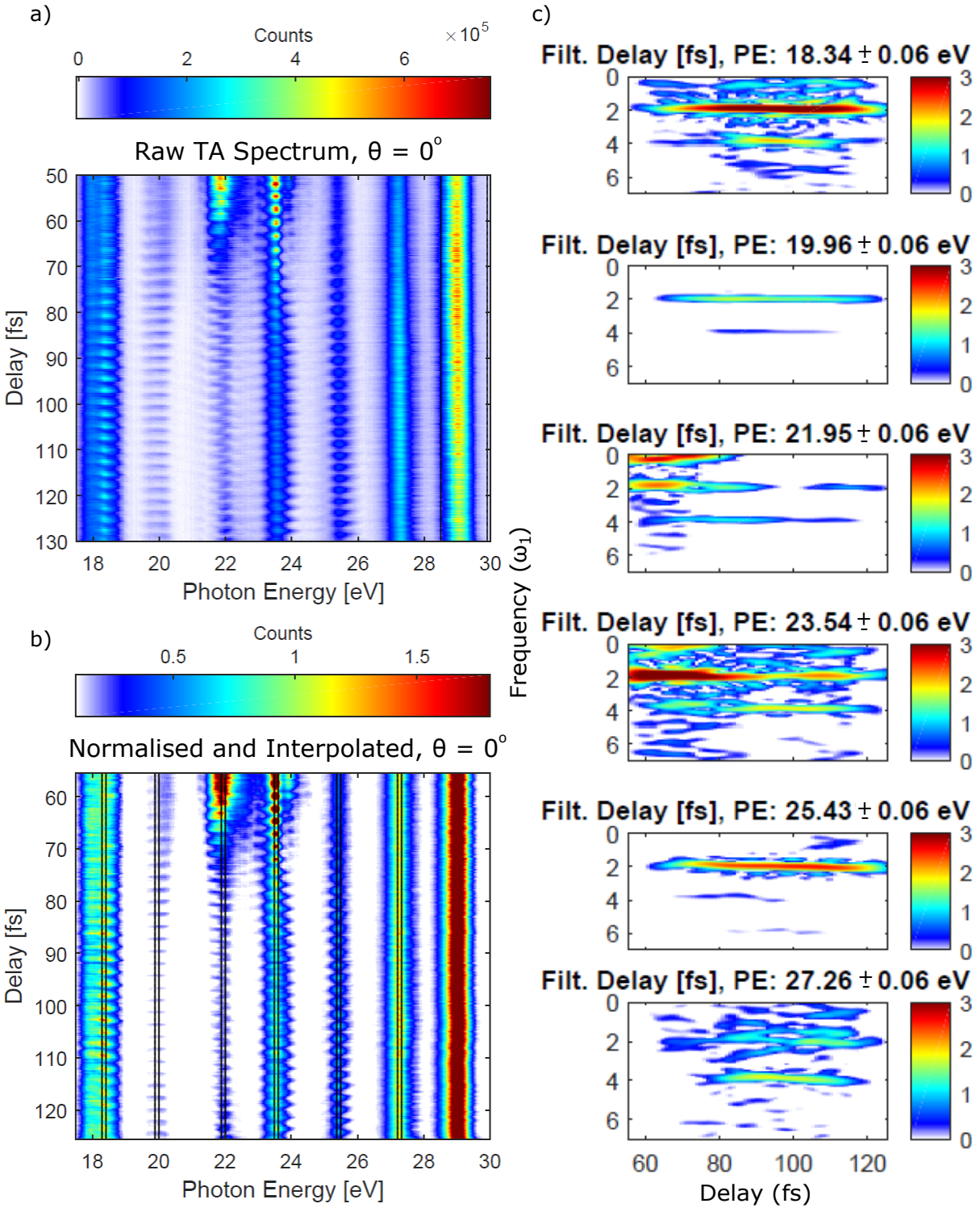


Figure 6.20: Raw, a), and processed, b), transient absorption delay measurement from laser dressed helium. The processed scan has been normalised, temporally corrected using the phase tagging reference and interpolated onto a linear delay axis. c) Log scale Fourier response at different delays throughout the scan duration obtained by sliding a 15 fs FWHM super-Gaussian temporal window filter across the scan delay axis and recording the resultant Fourier components. The dressing field peak intensity for the presented scan was calculated to be $4.0\times10^{13}\mathrm{W/cm^2}$.

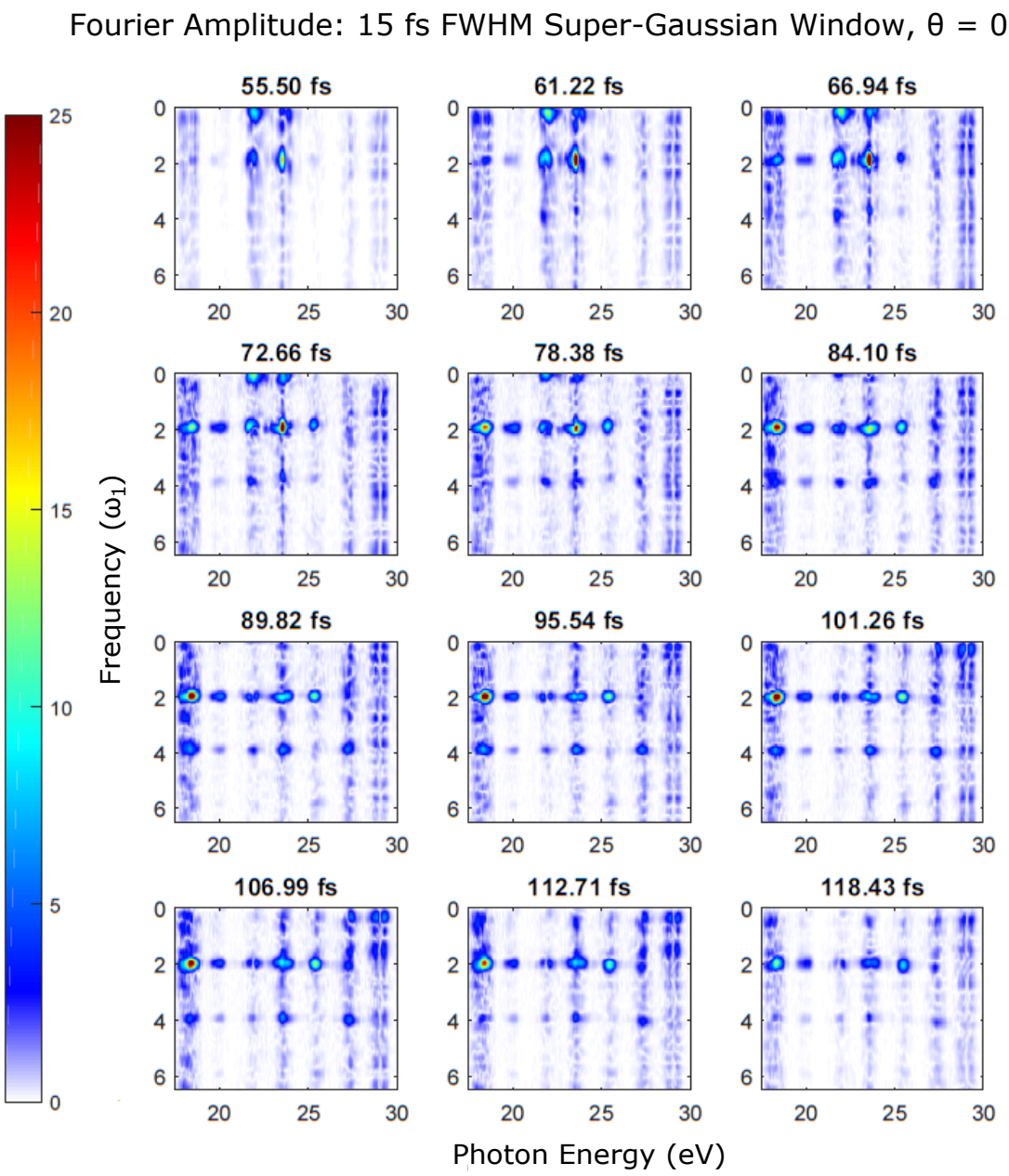


Figure 6.21: Fourier amplitude as a function of probing photon energy extracted from the one-dimensional laser dressed helium transient absorption delay scan, presented in Figure 6.20. Each panel corresponds to a different 15 fs FWHM, super-Gaussian temporal window within the scan duration. The central delay for each window is given in the title for each panel.

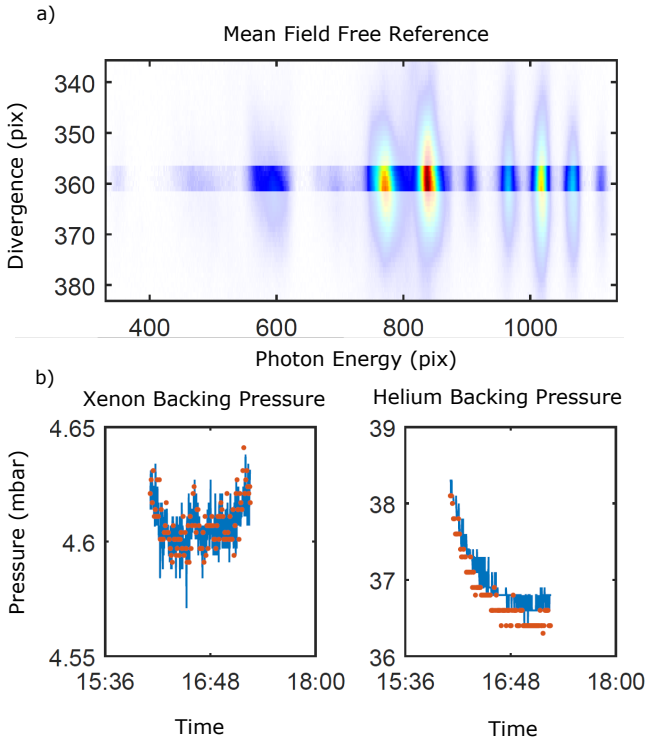


Figure 6.22: a) Mean harmonic spectrum recorded for the interleaved static absorption measurements recorded across the scan delay range shown in Figure 6.20. The selected divergence range is shown in full colour. b) The recorded generation and target backing pressures as a function of delay throughout the scan duration.

6.2.3 Discussion

We have probed the transient absorption of laser dressed helium using an attosecond pulse train and longer wavelength dressing field. Comparing the results obtained for the 1400 nm dressed helium with those obtained using the 800 nm dressing field presented in Chapter 5, we observe that when considering the effect on the delay dependent absorption modulation of changing the dressing field relative linear polarisation from parallel to perpendicular with respect to the probing XUV we see a similar, highly anisotropic response in the above ionisation threshold modulation. Again, the general behaviour of the below ionisation threshold modulation appears to be affected much less, as we also saw at the 800 nm wavelength.

For the 1400 nm data we observe hints of $6\omega_1$ modulation present in the signal. This is a higher frequency than was resolved using the 800 nm field. Reasons for this could be that by using the longer wavelength the $6\omega_1$ component is physically longer in duration. By sampling with similar absolute delay steps at 1400 nm as compared with a driving laser field of 800 nm, a much finer sampling will be obtained. For example: with 200 as sampling steps resolving $6\omega_1$ modulations at 800 nm driving laser wavelength, this will sample just over twice per full period, where a full $6\omega_1$ period corresponds to 440 as. This frequency is just resolvable according to the Nyquist theorem. Alternatively at 1400 nm driving wavelength, 200 as delay increments will sample nearly four times

per period, where a full period of $6\omega_1$ is equivalent to 770 as. With more samples per period for a given sampling step size, the $6\omega_1$ frequency will be more easily resolved. In addition, improvements to the laser system and beamline setup, increased referencing and data normalisation all act to reduce the effect of laser intensity fluctuation which we considered to be a significant factor in the 800 nm work.

The harmonic pulse train used to probe the dressed helium at 1400 nm was generated using xenon rather than krypton as for the 800 nm work presented in Chapter 5. The reason for this was to improve the source harmonic flux which, if we recall from Chapter 2, scales as λ^{-5} to $\lambda^{-6.5}$ [78,79]. By using xenon a higher flux was possible due to the lower ionisation threshold possessed by xenon, and favourable phase matching conditions that can be achieved.

Although we are still probing using an attosecond pulse train rather than an isolated attosecond pulse, the longer wavelength results in lower energy photons, so we now probe more finely around the helium edge due to the reduced harmonic separation. This allows more of the energy spectrum to be probed by the discrete harmonics.

Performing long scans we observe light induced states (LIS) in regions at the edge of the interaction envelope where the effective dressing field intensity is lower, and the multiphoton picture still applicable. The shifting of the LIS energy levels can be seen as the intensity gradient increases. As we increase the dressing field intensity we break down the conventional picture of the dressed atom. Long scans have inherent intensity gradient across them with the dressing field associated with the edges of the envelope at a much lower effective intensity than the peak overlap. Although possible assignments of LIS states have been suggested, given how close the different LIS values are, it is impossible to assign them with certainty. In addition, the calibration for the helium work was performed using the harmonic peaks rather than filter edges and so it is possible there is some small systematic offset in the energy calibration. There are several plausible reasons why we did not directly observe LIS using the 800 nm driving wavelength. For the work performed at 800 nm, the majority of the scans recorded were short duration ($\sim$6 fs), and centred around the peak of the interaction envelope. We noted that around the peak intensity of the 1400 nm studies we did not observe LIS which we understand to be due to the increased AC Stark effect with increasing dressing field intensity. As the dressing field intensity increases, the states increasingly shift, broaden and split, and individual states can no longer be well resolved. In addition, the harmonic energy spacing at the 800 nm driving wavelength was larger and so less of the energy spectrum was probed by the discrete harmonics, resulting in less opportunity to directly resolve LIS.

Chapter 7

Perspectives and Future Work

An ultrafast pump-probe beamline has been built and characterised, offering IR-pump-XUV-probe pulses with delay precision better than 150 as. Experiments performed using the setup have demonstrated its ability to make attosecond dynamics measurements [35], and to extend the current understanding of ultrafast electron dynamics in atoms. The beamline versatility ensures that future experiments can be performed not just using standard pump probe transient absorption in atoms, but also exploring ultrafast dynamics through pump probe methods using techniques such as molecular alignment [27, 28] or two colour fields [29, 30], in a range of different target media. The high temporal resolution and non-collinear setup allows a high degree of control over the pump-probe properties, which in turn can impart a high degree of control over the electrons. Future experiments could further explore the generation of XiHHG in the setup, as well as other quantum control experiments.

One key limiting factor for our experimental results was the short-term stability of the laser. The additional normalisation methods employed for the latter, 1400 nm work helped to isolate this effect from the recorded data, however improvement of the short-term laser stability would increase the signal to noise level, enabling weaker couplings to be detected more easily with the potential for higher order frequencies to be resolved. In addition, if fewer images were required to be averaged per delay point, this would reduce the scan duration times, resulting in more efficient data collection and less likelihood for long-term drifts to occur in the setup during the scan. Alternatively, if the repetition rate of the laser could be increased, this would also improve the statistics.

Throughout the work presented in this thesis, modifications were made to the Red Dragon laser system to improve short-term and long-term performance. By necessity, these improvements also affect the TOPAS output stability. Given the general direction of progression of the transient absorption work: probing core states from strong-field dressed atoms, and in the future, molecules, retaining the high energy probe cutoff provided by the TOPAS wavelength is vital. Two possible

ways to improve the effective short-term stability of the data could therefore be implemented as follows:

- Spatially filter the TOPAS signal, improving the beam spatial profile and minimising effects from spatially dividing the input using an annular mirror.
- Upgrade the entire beamline acquisition system to operate at 1kHz, recording images shot-to-shot, and binning the data outside certain thresholds, retaining only the best quality results.

Both of these options could be implemented with the current setup, and act to improve the overall result in different ways.

7.1 Spatial Filtering

The purpose of spatially filtering the beam would be to minimise changes between the pump and probe pulses due to any short- (and long-) term fluctuations in the spatial properties of the TOPAS beam profile. Filtering could be achieved using a standard diamond pinhole under vacuum, or alternatively using a hollow core fiber (HCF) setup. Implementing the latter would additionally enable pulse compression through SPM and subsequent chirp removal. For the heavy spatial filtering required to clean highly non-uniform input beams, the typical transmission through a spatial filter can be low. Using a HCF to simultaneously clean and compress the pulse would ensure some energy loss is compensated through the reduction in pulse duration. In addition, compressing the pulse duration down to a single cycle would allow for isolated attosecond pulse generation, enabling transient absorption spectroscopy to be performed with a continuum probe. This would fill the spectral gaps between the harmonics in the current recorded data, and increase the probing window beyond half a cycle of the driving laser. Improvement to the uniformity of the beam profile would also aid the repeatability of day to day alignment.

Feasibility experiments were performed using the HCF currently in situ in the laboratory with the TOPAS idler output (∼1800 nm) to generate harmonics in the generation chamber. It was found that with approximately 50% transmission through the HCF, the harmonic generation was only visible with the HCF in argon-filled, SPM mode rather than acting solely as a spatial filter. The process was not fully optimised, with no additional glass inserted into the input beam path for pulse compression other than the 3 mm UV-fused silica entrance window to the generation vacuum chamber. Using the HCF can significantly improve the quality of the beam profile, with an example shown in Figure 7.1. This Figure shows the improvement in the uniformity of the beam profile when the HCF is used as a spatial filter. Each image has been normalised. These images were recorded on a different day to the idler beamline tests, however they represent the level of beam quality improvement that can be obtained.

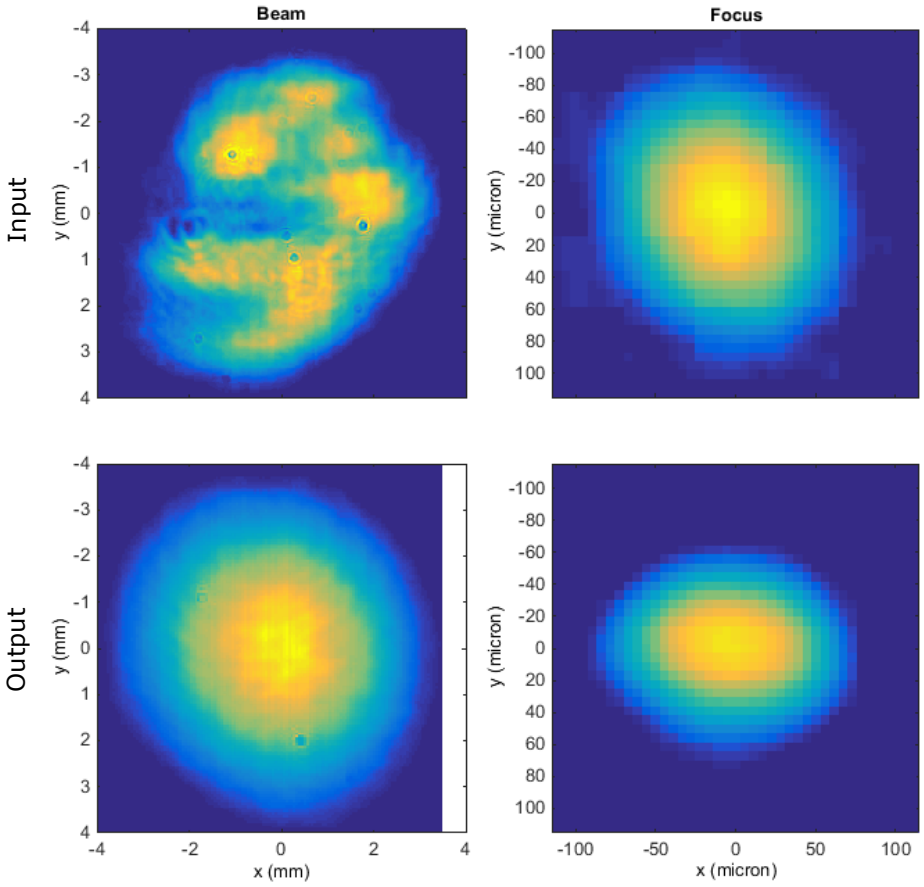


Figure 7.1: Image of the TOPAS idler beam profile and focus with and without spatial filtering through the hollow core fiber. Image provided courtesy of Dr Dane Austin.

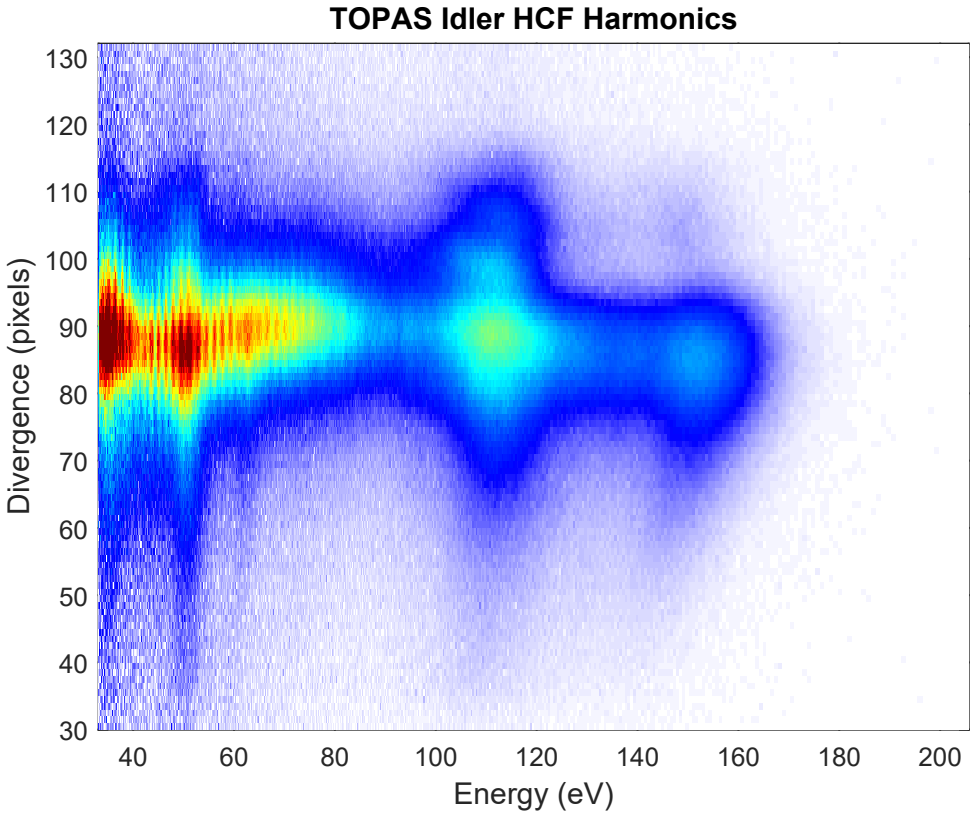


Figure 7.2: Image of the TOPAS idler harmonics generated using 314 mbar argon backing pressure in the generation target, and 350 mbar argon gradient fill in the hollow core fiber.

Even without full optimisation of the idler compression and subsequent high harmonic generation, there was some evidence of half-cycle cutoff behaviour in the recorded spectra indicating reasonable compression of the SPM broadened pulse. If we recall the single cycle behaviour discussion from Chapter 2, section 2.3, to reproduce the same harmonic spectrum with each laser shot for a single cycle pulse it is important to maintain a fixed carrier envelope phase (CEP) relationship for the generating field. If this is not the case, for an image generated by averaging together multiple laser shots, the position of the cutoff energy will vary shot to shot as the carrier wave changes under the envelope, blurring together the result. Since the TOPAS idler is passively CEP stable, we observed the cutoff energy of the harmonic spectrum shifting back and forth in energy on the timescale of seconds, indicating the pulse must be sufficiently short to be sensitive to the CEP. An image of the harmonic spectrum for an arbitrary CEP can be viewed in Figure 7.2. The harmonics shown were generated using 314 mbar backing pressure of argon with a single, 250 ms exposure image presented, corresponding to an average of 250 laser shots. The HCF was backed with 350 mbar argon in a gradient fill arrangement.

The TOPAS idler was tested rather than the signal for two key reasons:

1. The HCF was set up to receive the TOPAS idler, and it is non-trivial to adjust the HCF for different focusing and a different linear polarisation state. This is because the entrance and exit window to the fiber are aligned at Brewster angle to minimise reflection, and the signal and idler have orthogonal polarisation directions.

2. The idler wavelength can be compressed using simple fused silica, however around 1400 nm where the TOPAS signal is usually centred, specialist, expensive chirped mirrors would be required to compress the pulse following SPM broadening.

For both of these reasons, feasibility tests were performed using the idler.

7.2 Upgrading to 1kHz Beamline

Recording shot-to-shot information could allow the rejection of data outside given thresholds to improve the stability of the data through sorting. In addition to this, with shot-to-shot recording capability, referencing could be performed much more frequently, for example, a reference could be recorded for every image taken. This would effectively half the repetition rate of the laser, however with the current beamline referencing technique, time is currently taken to insert a block into the pump beam, record the reference, and remove the block again. With the beamline operating at 1kHz, referencing would need to be performed using a rotating chopper wheel synchronised to the pulse rate of the laser to achieve the chopping speeds required. With this method, time would not be wasted inserting and removing the block, compensating a little for the reduced repetition rate.

Assuming the short-term laser fluctuations are not dominated by shot-to-shot changes, the 1:1 referencing should also enable improved normalisation, and consequently improved results, again compensating for the reduced laser repetition rate through better quality data. It should be noted however that such extreme increase in referencing would not necessarily be beneficial if the shot-to-shot variation was very significant, since for a reference to be valid, it should be taken under the same conditions as the data. In this case, some averaging for the reference might actually be beneficial to ensure it is representative of the data to which is it compared. Another consideration would be to again combine separate intensity and static absorption referencing for the flux and spectral shape accordingly, as for the results presented in Chapter 6. Either way, it would be interesting to understand better the shot-to-shot result at 1kHz before pursuing either method. Ideally, each shot would be individually referenced concurrently with the data acquisition, however this would be very difficult to implement.

To upgrade the beamline to 1kHz, we would therefore like to have the following:

1. Ensure 1kHz acquisition capability through upgrading to a 1kHz camera imaging the MCP.

2. Synchronise a chopper wheel to block the dressing field at 500Hz i.e. record a static absorption reference for every data shot.

3. Record a measurement of the relative laser power for each shot, enabling binning of the data outside set thresholds.

Some progress has already been made towards achieving items 2 and 3, however at the time of writing this thesis it remains incomplete. This work has been primarily undertaken by Susan Parker and myself.

One consideration when upgrading to 1kHz would be if sufficient flux could be measured for each single shot of the laser above the inherent camera and MCP noise. This is something that would need to be explored further, however some increase to the signal could potentially be realised through increase in the MCP plate voltages and modifications to the generation target to improve phase matching.

7.3 Future Work

In addition to improving the short-term stability, another key area where improvement could be made is in the polarisation studies. Currently the set-up is limited to perform polarisation investigations just at parallel or perpendicular alignments of the laser dressing field relative to the harmonic probe field. Due to the polarisation dependent complex reflectivity of silver and gold mirrors, when non-axially aligned, linearly polarised laser light reflects from a non-normal incidence silver or gold plane mirror, the resultant reflected light will have a degree of ellipticity. Therefore simply rotating the half waveplate to control the dressing field linear polarisation with respect to the harmonic probe will not be valid for interim angles if subsequent non-normal reflections occur. This problem could be avoided by ensuring there are no reflections of the dressing beam following the control optics, impossible due to the recombining annular mirror and toroidal focusing mirror prior to the target chamber. Alternatively we would need to perform full polarisation characterisation of the dressing field beam directly before the target. This could be recorded using the insertable pickoff mirror inside the toroidal chamber, assuming that too was well characterised. Mapping out the changes required in the assembly of half and quarter waveplates to produce the desired results would allow intermediate angles to be studied.

Compensation for power changes from complex refractive indices would also need to be accounted for as we already did for the results presented in Chapter 6. For full characterisation, a high laser stability and repeatability would also be required to reduce the frequency at which it would need to be repeated. If the polarisation state of the dressing field at the target could be fully characterised, this could also enable studies into the ellipticity in addition to the full polarisation rotation.

Bibliography

[1] Françoise Provencher, Nicolas Bérubé, Anthony W. Parker, Gregory M. Greetham, Michael Towrie, Christoph Hellmann, Michel Côté, Natalie Stingelin, Carlos Silva, and Sophia C. Hayes. Direct observation of ultrafast long-range charge separation at polymer–fullerene heterojunctions. *Nature Communications*, 5:4288, July 2014.

[2] Richard Neutze, Remco Wouts, David van der Spoel, Edgar Weckert, and Janos Hajdu. Potential for biomolecular imaging with femtosecond X-ray pulses. *Nature*, 406(6797):752–757, August 2000.

[3] Ahmed H. Zewail. Femtochemistry: Atomic-Scale Dynamics of the Chemical Bond Using Ultrafast Lasers (Nobel Lecture) Copyright((c)) The Nobel Foundation 2000. We thank the Nobel Foundation, Stockholm, for permission to print this lecture. *Angewandte Chemie (International Ed. in English)*, 39(15):2586–2631, August 2000.

[4] Lukas Gallmann, Jens Herrmann, Reto Locher, Mazyar Sabbar, André Ludwig, Matteo Lucchini, and Ursula Keller. Resolving intra-atomic electron dynamics with attosecond transient absorption spectroscopy. *Molecular Physics*, 111(14-15):2243–2250, August 2013.

[5] P. B. Corkum and Ferenc Krausz. Attosecond science. *Nature Physics*, 3(6):381–387, June 2007.

[6] Ferenc Krausz. From femtochemistry to attophysics. *Physics World*, 14(9):41, 2001.

[7] Kun Zhao, Qi Zhang, Michael Chini, Yi Wu, Xiaowei Wang, and Zenghu Chang. Tailoring a 67 attosecond pulse through advantageous phase-mismatch. *Optics Letters*, 37(18):3891–3893, September 2012.

[8] T. H. Maiman. Stimulated Optical Radiation in Ruby. *Nature*, 187(4736):493–494, August 1960.

[9] P. A. Franken, A. E. Hill, C. W. Peters, and G. Weinreich. Generation of Optical Harmonics. *Physical Review Letters*, 7(4):118–119, August 1961.

[10] P. D. Maker, R. W. Terhune, M. Nisenoff, and C. M. Savage. Effects of Dispersion and Focusing on the Production of Optical Harmonics. *Physical Review Letters*, 8(1):21–22, January 1962.

[11] L. E. Hargrove, R. L. Fork, and M. A. Pollack. Locking of He–Ne laser modes induced by synchronous intracavity modulation. *Applied Physics Letters*, 5(1):4–5, July 1964.

[12] P. F. Moulton. Spectroscopic and laser characteristics of Ti:Al_2o_3. *Journal of the Optical Society of America B*, 3(1):125, January 1986.

[13] Donna Strickland and Gerard Mourou. Compression of amplified chirped optical pulses. *Optics Communications*, 55(6):447–449, October 1985.

[14] G. A. Mourou, C. L. Labaune, M. Dunne, N. Naumova, and V. T. Tikhonchuk. Relativistic laser-matter interaction: from attosecond pulse generation to fast ignition. *Plasma Physics and Controlled Fusion*, 49(12B):B667, 2007.

[15] Thomas Brabec and Ferenc Krausz. Intense few-cycle laser fields: Frontiers of nonlinear optics. *Reviews of Modern Physics*, 72(2):545–591, April 2000.

[16] P. M. Paul, E. S. Toma, P. Breger, G. Mullot, F. Augé, Ph Balcou, H. G. Muller, and P. Agostini. Observation of a Train of Attosecond Pulses from High Harmonic Generation. *Science*, 292(5522):1689–1692, January 2001.

[17] M. Hentschel, R. Kienberger, Ch Spielmann, G. A. Reider, N. Milosevic, T. Brabec, P. Corkum, U. Heinzmann, M. Drescher, and F. Krausz. Attosecond metrology. *Nature*, 414(6863):509–513, November 2001.

[18] Eleftherios Goulielmakis, Zhi-Heng Loh, Adrian Wirth, Robin Santra, Nina Rohringer, Vladislav S. Yakovlev, Sergey Zherebtsov, Thomas Pfeifer, Abdallah M. Azzeer, Matthias F. Kling, Stephen R. Leone, and Ferenc Krausz. Real-time observation of valence electron motion. *Nature*, 466(7307):739–743, August 2010.

[19] G. Gademann, F. Kelkensberg, W. K. Siu, P. Johnsson, M. B. Gaarde, K. J. Schafer, and M. J. J. Vrakking. Attosecond control of electron–ion recollision in high harmonic generation. *New Journal of Physics*, 13(3):033002, March 2011.

[20] Michael Chini, Xiaowei Wang, Yan Cheng, Yi Wu, Di Zhao, Dmitry A. Telnov, Shih-I Chu, and Zenghu Chang. Sub-cycle Oscillations in Virtual States Brought to Light. *Scientific Reports*, 3, January 2013.

[21] E. Goulielmakis, M. Schultze, M. Hofstetter, V. S. Yakovlev, J. Gagnon, M. Uiberacker, A. L. Aquila, E. M. Gullikson, D. T. Attwood, R. Kienberger, F. Krausz, and U. Kleineberg. Single-Cycle Nonlinear Optics. *Science*, 320(5883):1614–1617, June 2008.

[22] Mark J. Abel, Thomas Pfeifer, Phillip M. Nagel, Willem Boutu, M. Justine Bell, Colby P. Steiner, Daniel M. Neumark, and Stephen R. Leone. Isolated attosecond pulses from ionization gating of high-harmonic emission. *Chemical Physics*, 366(1–3):9–14, December 2009.

[23] P. B. Corkum, N. H. Burnett, and M. Y. Ivanov. Subfemtosecond pulses. *Optics Letters*, 19(22):1870–1872, November 1994.

[24] M. Nisoli, S. De Silvestri, and O. Svelto. Generation of high energy 10 fs pulses by a new pulse compression technique. *Applied Physics Letters*, 68(20):2793–2795, May 1996.

[25] Michael Chini, Kun Zhao, and Zenghu Chang. The generation, characterization and applications of broadband isolated attosecond pulses. *Nature Photonics*, 8(3):178–186, March 2014.

[26] J Levesque and P B Corkum. Attosecond science and technology. *Canadian Journal of Physics*, 84(1):1–18, January 2006.

[27] R. Velotta, N. Hay, M. B. Mason, M. Castillejo, and J. P. Marangos. High-Order Harmonic Generation in Aligned Molecules. *Physical Review Letters*, 87(18):183901, October 2001.

[28] Y. Mairesse, J. Levesque, N. Dudovich, P. B. Corkum, and D. M. Villeneuve. High harmonic generation from aligned molecules–amplitude and polarization. *Journal of Modern Optics*, 55(16):2591–2602, September 2008.

[29] N. Dudovich, O. Smirnova, J. Levesque, Y. Mairesse, M. Yu Ivanov, D. M. Villeneuve, and P. B. Corkum. Measuring and controlling the birth of attosecond XUV pulses. *Nature Physics*, 2(11):781–786, November 2006.

[30] I Jong Kim, Chul Min Kim, Hyung Taek Kim, Gae Hwang Lee, Yong Soo Lee, Ju Yun Park, David Jaeyun Cho, and Chang Hee Nam. Highly Efficient High-Harmonic Generation in an Orthogonally Polarized Two-Color Laser Field. *Physical Review Letters*, 94(24):243901, June 2005.

[31] S. Baker, J. S. Robinson, C. A. Haworth, H. Teng, R. A. Smith, C. C. Chirilă, M. Lein, J. W. G. Tisch, and J. P. Marangos. Probing Proton Dynamics in Molecules on an Attosecond Time Scale. *Science*, 312(5772):424–427, April 2006.

[32] Jon P. Marangos, Sarah Baker, Nathaniel Kajumba, Joseph S. Robinson, John W. G. Tisch, and Ricardo Torres. Dynamic imaging of molecules using high order harmonic generation. *Phys. Chem. Chem. Phys.*, 10(1):35–48, 2008.

[33] P. Johnsson, J. Mauritsson, T. Remetter, A. L'Huillier, and K. J. Schafer. Attosecond Control of Ionization by Wave-Packet Interference. *Physical review letters*, 99(23):233001, 2007.

[34] Ch Ellert, H. Stapelfeldt, E. Constant, H. Sakai, J. Wright, D. M. Rayner, and P. B. Corkum. Observing molecular dynamics with timed Coulomb explosion imaging. *Philosophical Transactions of the Royal Society of London A: Mathematical, Physical and Engineering Sciences*, 356(1736):329–344, February 1998.

[35] E. R. Simpson, A. Sanchez-Gonzalez, D. R. Austin, Z. Diveki, S. E. E. Hutchinson, T. Siegel, M. Ruberti, V. Averbukh, L Miseikis, C. S. Strüber, L. Chipperfield, and J. P. Marangos. Polarisation response of delay dependent absorption modulation in strong field dressed helium atoms probed near threshold. *New Journal of Physics*, 18(8):083032, 2016.

[36] Simon Hutchinson. *Apparatus design and experimental studies of XUV initiated HHG*. PhD thesis, Imperial College London, June 2014.

[37] Emma R. Simpson, Alvaro Sanchez-Gonzalez, Thomas Siegel, Zsolt Diveki, Simon E. E. Hutchinson, Lukas Miseikis, Christian Strüber, Dane R. Austin, and Jon P. Marangos. A beamline for attosecond pump-probe experiments: towards tracking ultrafast electron dynamics in atoms and molecules. In *Ultrafast Nonlinear Imaging and Spectroscopy III*, volume 9584, pages 958402–8. SPIE Optics and Photonics, San Diego, 2015.

[38] G. Mainfray and G. Manus. Multiphoton ionization of atoms. *Reports on Progress in Physics*, 54(10):1333, October 1991.

[39] M. Protopapas, C. H. Keitel, and P. L. Knight. Atomic physics with super-high intensity lasers. *Reports on Progress in Physics*, 60(4):389, April 1997.

[40] L.V. Keldysh. Ionization in the Field of a Strong Electromagnetic Wave. *Soviet Physics JETP*, 20(5):1307–1314, May 1965.

[41] G. K. Woodgate. *Elementary Atomic Structure*. Oxford University Press USA, 2nd edition, 1983.

[42] Hermann Haken and Hans Christoph Wolf. *The Physics of Atoms and Quanta*. Springer Berlin Heidelberg, Berlin, Heidelberg, 4th edition, 1994.

[43] Dr. Mike Tarbutt. Imperial College London, Atomic and Molecular Physics Notes. https://workspace.imperial.ac.uk/controlledquantumdynamics/Public/Lecture%20notes/Quantum%20Physics%20and%20Chemistry%20of%20Cold%20Matter/Atomic%20Physics%20Lecture%20Notes.pdf, 2012. [Accessed on 09/01/2017].

[44] Professor Andrei Tokmakoff. University of Chicago, Time-Dependent Quantum Mechanics and Spectroscopy Notes. http://tdqms.uchicago.edu/page/tdqms-notes, 2017. [Accessed on 09/01/2017].

[45] A. L'Huillier, L. A. Lompre, G. Mainfray, and C. Manus. Multiply Charged Ions Formed by Multiphoton Absorption Processes in the Continuum. *Physical Review Letters*, 48(26):1814–1817, June 1982.

[46] A. L'Huillier, L. A. Lompre, G. Mainfray, and C. Manus. Multiply charged ions induced by multiphoton absorption in rare gases at 0.53 μm. *Physical Review A*, 27(5):2503–2512, May 1983.

[47] A. B. Arons and M. B. Peppard. Einstein's Proposal of the Photon Concept—a Translation of the Annalen der Physik Paper of 1905. *American Journal of Physics*, 33(5):367–374, May 1965.

[48] G. S. Voronov and N. B. Delone. Ionization of the xenon atom by the electric field of ruby laser emission. *Soviet Journal of Experimental and Theoretical Physics Letters*, 1:66, April 1965.

[49] L. A. Lompre, G. Mainfray, C. Manus, and J. Thebault. Multiphoton ionization of rare gases by a tunable-wavelength 30-psec laser pulse at 1.06 μm. *Physical Review A*, 15(4):1604–1612, April 1977.

[50] Nikolai B. Delone and Vladimir Krainov. *Multiphoton Processes in Atoms*. Springer-Verlag Berlin Heidelberg, 1st edition, 1994 edition.

[51] M N R Ashfold and and J. D. Howe. Multiphoton Spectroscopy of Molecular Species. *Annual Review of Physical Chemistry*, 45(1):57–82, 1994.

[52] L. A. Lompre, A. L'Huillier, G. Mainfray, and J. Y. Fan. Electron energy measurements in multiphoton ionisation of xenon and neon. *Journal of Physics B: Atomic and Molecular Physics*, 17(23):L817, 1984.

[53] P. Agostini, F. Fabre, G. Mainfray, G. Petite, and N. K. Rahman. Free-Free Transitions Following Six-Photon Ionization of Xenon Atoms. *Physical Review Letters*, 42(17):1127–1130, April 1979.

[54] Y. Gontier, M. Poirier, and M. Trahin. Multiphoton absorptions above the ionisation threshold. *Journal of Physics B: Atomic and Molecular Physics*, 13(7):1381, 1980.

[55] P. Kruit, J. Kimman, H. G. Muller, and M. J. van der Wiel. Electron spectra from multiphoton ionization of xenon at 1064, 532, and 355 nm. *Physical Review A*, 28(1):248–255, July 1983.

[56] H. G. Muller, A. Tip, and M. J. van der Wiel. Ponderomotive force and AC Stark shift in multiphoton ionisation. *Journal of Physics B: Atomic and Molecular Physics*, 16(22):L679, 1983.

[57] A.M. Bonch-Bruevich, N.N. Kostin, V.A. Khodocoi, and V.V. Khromov. Changes in the Atomic Absorption Spectrum in the Field of a Light Wave. 1. *Soviet Physics JETP*, 29(1):82, 1969.

[58] P. H. Bucksbaum, R. R. Freeman, M. Bashkansky, and T. J. McIlrath. Role of the ponderomotive potential in above-threshold ionization. *JOSA B*, 4(5):760–764, May 1987.

[59] R. R. Freeman and P. H. Bucksbaum. Investigations of above-threshold ionization using subpicosecond laser pulses. *Journal of Physics B: Atomic, Molecular and Optical Physics*, 24(2):325, 1991.

[60] M. V. Ammosov, N. B. Delone, and V. P. Krainov. Tunnel ionization of complex atoms and of atomic ions in an alternating electromagnetic field. *Soviet Physics - JETP*, 64(6):1191, 1986.

[61] Zenghu Chang. *Fundamentals of Attosecond Optics*. Taylor & Francis, February 2011.

[62] S. Augst, D. D. Meyerhofer, D. Strickland, and S. L. Chin. Laser ionization of noble gases by Coulomb-barrier suppression. *Journal of the Optical Society of America B Optical Physics*, 8:858–867, April 1991.

[63] D.J. Griffiths. *Introduction to Electrodynamics*. Prentice-Hall, Inc., 3rd edition, 1999.

[64] Gennady L. Yudin and Misha Yu. Ivanov. Nonadiabatic tunnel ionization: Looking inside a laser cycle. *Physical Review A*, 64(1):013409, June 2001.

[65] Vladimir S. Popov. Tunnel and multiphoton ionization of atoms and ions in a strong laser field (Keldysh theory). *Physics-Uspekhi*, 47(9):855, 2004.

[66] Michael Fleischhauer, Atac Imamoglu, and Jonathan P. Marangos. Electromagnetically induced transparency: Optics in coherent media. *Reviews of Modern Physics*, 77(2):633–673, July 2005.

[67] Robert W. Boyd. *Nonlinear Optics, Third Edition*. Academic Press, 3rd edition, 2008.

[68] Geoffrey New. *Introduction to Nonlinear Optics*. Cambridge University Press, Cambridge, 2011.

[69] Jean-Claude Diels and Wolfgang Rudolph. 1 - Fundamentals. In *Ultrashort Laser Pulse Phenomena (Second Edition)*, pages 1–60. Academic Press, Burlington, 2006.

[70] G. Sansone, E. Benedetti, F. Calegari, C. Vozzi, L. Avaldi, R. Flammini, L. Poletto, P. Villoresi, C. Altucci, R. Velotta, S. Stagira, S. De Silvestri, and M. Nisoli. Isolated Single-Cycle Attosecond Pulses. *Science*, 314(5798):443–446, October 2006.

[71] A. Baltuška, Th Udem, M. Uiberacker, M. Hentschel, E. Goulielmakis, Ch Gohle, R. Holzwarth, V. S. Yakovlev, A. Scrinzi, T. W. Hänsch, and F. Krausz. Attosecond control of electronic processes by intense light fields. *Nature*, 421(6923):611–615, February 2003.

[72] E. Cumberbatch. Self-focusing in Non-linear Optics. *IMA Journal of Applied Mathematics*, 6(3):250–262, January 1970.

[73] Fujio Shimizu. Frequency Broadening in Liquids by a Short Light Pulse. *Physical Review Letters*, 19(19):1097–1100, November 1967.

[74] Richard G. Brewer. Frequency Shifts in Self-Focused Light. *Physical Review Letters*, 19(1):8–10, July 1967.

[75] A. C. Cheung, D. M. Rank, R. Y. Chiao, and C. H. Townes. Phase Modulation of Q-Switched Laser Beams in Small-Scale Filaments. *Physical Review Letters*, 20(15):786–789, April 1968.

[76] X. F. Li, A. L'Huillier, M. Ferray, L. A. Lompré, and G. Mainfray. Multiple-harmonic generation in rare gases at high laser intensity. *Physical Review A*, 39(11):5751–5761, June 1989.

[77] Ph. Balcou and Anne L'Huillier. Phase-matching effects in strong-field harmonic generation. *Physical Review A*, 47(2):1447–1459, February 1993.

[78] J. Tate, T. Auguste, H. G. Muller, P. Salières, P. Agostini, and L. F. DiMauro. Scaling of Wave-Packet Dynamics in an Intense Midinfrared Field. *Physical Review Letters*, 98(1):013901, January 2007.

[79] A. D. Shiner, C. Trallero-Herrero, N. Kajumba, H.-C. Bandulet, D. Comtois, F. Légaré, M. Giguère, J-C. Kieffer, P. B. Corkum, and D. M. Villeneuve. Wavelength Scaling of High Harmonic Generation Efficiency. *Physical Review Letters*, 103(7):073902, August 2009.

[80] A. McPherson, G. Gibson, H. Jara, U. Johann, T. S. Luk, I. A. McIntyre, K. Boyer, and C. K. Rhodes. Studies of multiphoton production of vacuum-ultraviolet radiation in the rare gases. *JOSA B*, 4(4):595–601, April 1987.

[81] Pascal Salières, Anne L'Huillier, and Maciej Lewenstein. Coherence Control of High-Order Harmonics. *Physical Review Letters*, 74(19):3776–3779, May 1995.

[82] Philippe Balcou, Pascal Salières, Anne L'Huillier, and Maciej Lewenstein. Generalized phase-matching conditions for high harmonics: The role of field-gradient forces. *Physical Review A*, 55(4):3204–3210, April 1997.

[83] N. H. Burnett, H. A. Baldis, M. C. Richardson, and G. D. Enright. Harmonic generation in CO2 laser target interaction. *Applied Physics Letters*, 31(3):172–174, August 1977.

[84] M. Ferray, A. L'Huillier, X. F. Li, L. A. Lompre, G. Mainfray, and C. Manus. Multiple-harmonic conversion of 1064 nm radiation in rare gases. *Journal of Physics B: Atomic, Molecular and Optical Physics*, 21(3):L31, 1988.

[85] P. B. Corkum. Plasma perspective on strong field multiphoton ionization. *Physical Review Letters*, 71(13):1994–1997, September 1993.

[86] Jeffrey L. Krause, Kenneth J. Schafer, and Kenneth C. Kulander. High-order harmonic generation from atoms and ions in the high intensity regime. *Physical Review Letters*, 68(24):3535–3538, June 1992.

[87] M. Lewenstein, Ph. Balcou, M. Yu. Ivanov, Anne L'Huillier, and P. B. Corkum. Theory of high-harmonic generation by low-frequency laser fields. *Physical Review A*, 49(3):2117–2132, March 1994.

[88] Anh-Thu Le, Hui Wei, Cheng Jin, and C. D. Lin. Strong-field approximation and its extension for high-order harmonic generation with mid-infrared lasers. *Journal of Physics B: Atomic, Molecular and Optical Physics*, 49(5):053001, 2016.

[89] D. Faccio, J. Dudley, and M. Clerici. *Frontiers in Modern Optics*. IOS Press, first edition, May 2016.

[90] Y. Mairesse, A. de Bohan, L. J. Frasinski, H. Merdji, L. C. Dinu, P. Monchicourt, P. Breger, M. Kovačev, R. Taïeb, B. Carré, H. G. Muller, P. Agostini, and P. Salières. Attosecond Synchronization of High-Harmonic Soft X-rays. *Science*, 302(5650):1540–1543, November 2003.

[91] Howard R. Reiss. Effect of an intense electromagnetic field on a weakly bound system. *Physical Review A*, 22(5):1786–1813, November 1980.

[92] F. H. M. Faisal. Multiple absorption of laser photons by atoms. *Journal of Physics B: Atomic and Molecular Physics*, 6(4):L89, 1973.

[93] Misha Yu Ivanov, Michael Spanner, and Olga Smirnova. Anatomy of strong field ionization. *Journal of Modern Optics*, 52(2-3):165–184, January 2005.

[94] L. E. Chipperfield, P. L. Knight, J. W. G. Tisch, and J. P. Marangos. Tracking individual electron trajectories in a high harmonic spectrum. *Optics Communications*, 264(2):494–501, August 2006.

[95] P. Rudawski, C. M. Heyl, F. Brizuela, J. Schwenke, A. Persson, E. Mansten, R. Rakowski, L. Rading, F. Campi, B. Kim, P. Johnsson, and A. L'Huillier. A high-flux high-order harmonic source. *Review of Scientific Instruments*, 84(7):073103, July 2013.

[96] Mette B. Gaarde, Jennifer L. Tate, and Kenneth J. Schafer. Macroscopic aspects of attosecond pulse generation. *Journal of Physics B: Atomic, Molecular and Optical Physics*, 41(13):132001, 2008.

[97] Anne L'Huillier, Philippe Balcou, Sebastien Candel, Kenneth J. Schafer, and Kenneth C. Kulander. Calculations of high-order harmonic-generation processes in xenon at 1064 nm. *Physical Review A*, 46(5):2778–2790, September 1992.

[98] Andy Rundquist, Charles G. Durfee, Zenghu Chang, Catherine Herne, Sterling Backus, Margaret M. Murnane, and Henry C. Kapteyn. Phase-Matched Generation of Coherent Soft X-rays. *Science*, 280(5368):1412–1415, May 1998.

[99] Mette B. Gaarde, Christian Buth, Jennifer L. Tate, and Kenneth J. Schafer. Transient absorption and reshaping of ultrafast XUV light by laser-dressed helium. *Physical Review A*, 83(1):013419, January 2011.

[100] C. G. Wahlström, J. Larsson, A. Persson, T. Starczewski, S. Svanberg, P. Salières, Ph. Balcou, and Anne L'Huillier. High-order harmonic generation in rare gases with an intense short-pulse laser. *Physical Review A*, 48(6):4709–4720, December 1993.

[101] Mengxi Wu, Shaohao Chen, Mette B. Gaarde, and Kenneth J. Schafer. Time-domain perspective on Autler-Townes splitting in attosecond transient absorption of laser-dressed helium atoms. *Physical Review A*, 88(4):043416, October 2013.

[102] S. H. Autler and C. H. Townes. Stark Effect in Rapidly Varying Fields. *Physical Review*, 100(2):703–722, October 1955.

[103] K. J. Boller, A. Imamoğlu, and S. E. Harris. Observation of electromagnetically induced transparency. *Physical Review Letters*, 66(20):2593–2596, May 1991.

[104] Shaohao Chen, Kenneth J. Schafer, and Mette B. Gaarde. Transient absorption of attosecond pulse trains by laser-dressed helium. *Optics Letters*, 37(12):2211, June 2012.

[105] U. Fano and J. W. Cooper. Spectral Distribution of Atomic Oscillator Strengths. *Reviews of Modern Physics*, 40(3):441–507, July 1968.

[106] He Wang, Michael Chini, Shouyuan Chen, Chang-Hua Zhang, Feng He, Yan Cheng, Yi Wu, Uwe Thumm, and Zenghu Chang. Attosecond Time-Resolved Autoionization of Argon. *Physical Review Letters*, 105(14):143002, October 2010.

[107] Robin Santra, Vladislav S. Yakovlev, Thomas Pfeifer, and Zhi-Heng Loh. Theory of attosecond transient absorption spectroscopy of strong-field-generated ions. *Physical Review A*, 83(3):033405, March 2011.

[108] Martin Schultze, Elisabeth M. Bothschafter, Annkatrin Sommer, Simon Holzner, Wolfgang Schweinberger, Markus Fiess, Michael Hofstetter, Reinhard Kienberger, Vadym Apalkov, Vladislav S. Yakovlev, Mark I. Stockman, and Ferenc Krausz. Controlling dielectrics with the electric field of light. *Nature*, 493(7430):75–78, January 2013.

[109] J. Mauritsson, T. Remetter, M. Swoboda, K. Klünder, A. L'Huillier, K. J. Schafer, O. Ghafur, F. Kelkensberg, W. Siu, P. Johnsson, M. J. J. Vrakking, I. Znakovskaya, T. Uphues, S. Zherebtsov, M. F. Kling, F. Lépine, E. Benedetti, F. Ferrari, G. Sansone, and M. Nisoli. Attosecond Electron Spectroscopy Using a Novel Interferometric Pump-Probe Technique. *Physical Review Letters*, 105(5):053001, July 2010.

[110] Niranjan Shivaram, Henry Timmers, Xiao-Min Tong, and Arvinder Sandhu. Attosecond-Resolved Evolution of a Laser-Dressed Helium Atom: Interfering Excitation Paths and Quantum Phases. *Physical Review Letters*, 108(19):193002, May 2012.

[111] Shaohao Chen, M. Justine Bell, Annelise R. Beck, Hiroki Mashiko, Mengxi Wu, Adrian N. Pfeiffer, Mette B. Gaarde, Daniel M. Neumark, Stephen R. Leone, and Kenneth J. Schafer. Light-induced states in attosecond transient absorption spectra of laser-dressed helium. *Physical Review A*, 86(6):063408, December 2012.

[112] M. Justine Bell, Annelise R. Beck, Hiroki Mashiko, Daniel M. Neumark, and Stephen R. Leone. Intensity dependence of light-induced states in transient absorption of laser-dressed helium measured with isolated attosecond pulses. *Journal of Modern Optics*, 60(17):1506–1516, October 2013.

[113] J. Herrmann, M. Lucchini, S. Chen, M. Wu, A. Ludwig, L. Kasmi, K. J. Schafer, L. Gallmann, M. B. Gaarde, and U. Keller. Multiphoton transitions for delay-zero calibration in attosecond spectroscopy. *New Journal of Physics*, 17(1):013007, 2015.

[114] Maurizio Reduzzi, Johan Hummert, Antoine Dubrouil, Francesca Calegari, Mauro Nisoli, Fabio Frassetto, Luca Poletto, Shaohao Chen, Mengxi Wu, Mette B. Gaarde, Kenneth Schafer, and Giuseppe Sansone. Polarization control of absorption of virtual dressed states in helium. *Physical Review A*, 92(3):033408, September 2015.

[115] Matteo Lucchini, Jens Herrmann, André Ludwig, Reto Locher, Mazyar Sabbar, Lukas Gallmann, and Ursula Keller. Role of electron wavepacket interference in the optical response of helium atoms. *New Journal of Physics*, 15(10):103010, 2013.

[116] P. P. Sorokin, N. S. Shiren, J. R. Lankard, E. C. Hammond, and T. G. Kazyaka. Stimulated electronic Raman scattering. *Applied Physics Letters*, 10(2):44–46, January 1967.

[117] Shaohao Chen, Mengxi Wu, Mette B. Gaarde, and Kenneth J. Schafer. Quantum interference in attosecond transient absorption of laser-dressed helium atoms. *Physical Review A*, 87(3):033408, March 2013.

[118] Xiaowei Wang, Michael Chini, Yan Cheng, Yi Wu, Xiao-Min Tong, and Zenghu Chang. Subcycle laser control and quantum interferences in attosecond photoabsorption of neon. *Physical Review A*, 87(6):063413, June 2013.

[119] J. Stuart Foster. Some leading features of the stark effect. *Journal of the Franklin Institute*, 209(5):585–624, May 1930.

[120] Benjamin J. Sussman. Five ways to the nonresonant dynamic Stark effect. *American Journal of Physics*, 79(5):477–484, May 2011.

[121] Philipp V. Demekhin and Lorenz S. Cederbaum. ac Stark effect in the electronic continuum and its impact on the photoionization of atoms by coherent intense short high-frequency laser pulses. *Physical Review A*, 88(4):043414, October 2013.

[122] Michael Chini, Baozhen Zhao, He Wang, Yan Cheng, S. X. Hu, and Zenghu Chang. Subcycle ac Stark Shift of Helium Excited States Probed with Isolated Attosecond Pulses. *Physical Review Letters*, 109(7):073601, August 2012.

[123] N. B. Delone and Vladimir P. Krainov. AC Stark shift of atomic energy levels. *Physics-Uspekhi*, 42(7):669, 1999.

[124] C. J. Joachain, N. J. Kylstra, and R. M. Potvliege. *Atoms in Intense Laser Fields*. Cambridge University Press, 2012.

[125] P. Mulser, S. Uryupin, R. Sauerbrey, and B. Wellegehausen. Ponderomotive potential and dynamical Stark shift in multiphoton ionization. *Physical Review A*, 48(6):4547–4550, December 1993.

[126] Kenneth J. Schafer, Mette B. Gaarde, Arne Heinrich, Jens Biegert, and Ursula Keller. Strong Field Quantum Path Control Using Attosecond Pulse Trains. *Physical Review Letters*, 92(2):023003, January 2004.

[127] J. Biegert, A. Heinrich, C. P. Hauri, W. Kornelis, P. Schlup, M. P. Anscombe, M. B. Gaarde, K. J. Schafer, and U. Keller. Control of high-order harmonic emission using attosecond pulse trains. *Journal of Modern Optics*, 53(1-2):87–96, January 2006.

[128] Jonathan Leeuwenburgh, Bridgette Cooper, Vitali Averbukh, Jonathan P. Marangos, and Misha Ivanov. Reconstruction of correlation-driven electron-hole dynamics by high-harmonic-generation spectroscopy. *Physical Review A*, 90(3):033426, September 2014.

[129] P. Emma, R. Akre, J. Arthur, R. Bionta, C. Bostedt, J. Bozek, A. Brachmann, P. Bucksbaum, R. Coffee, F.-J. Decker, Y. Ding, D. Dowell, S. Edstrom, A. Fisher, J. Frisch, S. Gilevich, J. Hastings, G. Hays, Ph Hering, Z. Huang, R. Iverson, H. Loos, M. Messerschmidt, A. Miahnahri, S. Moeller, H.-D. Nuhn, G. Pile, D. Ratner, J. Rzepiela, D. Schultz, T. Smith, P. Stefan, H. Tompkins, J. Turner, J. Welch, W. White, J. Wu, G. Yocky, and J. Galayda. First lasing and operation of an ångstrom-wavelength free-electron laser. *Nature Photonics*, 4(9):641–647, September 2010.

[130] J. P. Marangos. Introduction to the new science with X-ray free electron lasers. *Contemporary Physics*, 52(6):551–569, November 2011.

[131] W. Helml, A. R. Maier, W. Schweinberger, I. Grguraš, P. Radcliffe, G. Doumy, C. Roedig, J. Gagnon, M. Messerschmidt, S. Schorb, C. Bostedt, F. Grüner, L. F. DiMauro, D. Cubaynes, J. D. Bozek, Th Tschentscher, J. T. Costello, M. Meyer, R. Coffee, S. Düsterer, A. L. Cavalieri, and R. Kienberger. Measuring the temporal structure of few-femtosecond free-electron laser X-ray pulses directly in the time domain. *Nature Photonics*, 8(12):950–957, December 2014.

[132] Y. Ding, C. Behrens, R. Coffee, F.-J. Decker, P. Emma, C. Field, W. Helml, Z. Huang, P. Krejcik, J. Krzywinski, H. Loos, A. Lutman, A. Marinelli, T. J. Maxwell, and J. Turner. Generating femtosecond X-ray pulses using an emittance-spoiling foil in free-electron lasers. *Applied Physics Letters*, 107(19):191104, November 2015.

[133] J. C. Castagna, B. Murphy, J. Bozek, and N. Berrah. X-ray split and delay system for soft x-rays at LCLS. *Journal of Physics: Conference Series*, 425(15):152021, 2013.

[134] A. A. Lutman, R. Coffee, Y. Ding, Z. Huang, J. Krzywinski, T. Maxwell, M. Messerschmidt, and H.-D. Nuhn. Experimental Demonstration of Femtosecond Two-Color X-Ray Free-Electron Lasers. *Physical Review Letters*, 110(13):134801, March 2013.

[135] C. Behrens, F.-J. Decker, Y. Ding, V. A. Dolgashev, J. Frisch, Z. Huang, P. Krejcik, H. Loos, A. Lutman, T. J. Maxwell, J. Turner, J. Wang, M.-H. Wang, J. Welch, and J. Wu. Few-femtosecond time-resolved measurements of X-ray free-electron lasers. *Nature Communications*, 5:3762, April 2014.

[136] Chelsea E. Liekhus-Schmaltz, Ian Tenney, Timur Osipov, Alvaro Sanchez-Gonzalez, Nora Berrah, Rebecca Boll, Cedric Bomme, Christoph Bostedt, John D. Bozek, Sebastian Carron, Ryan Coffee, Julien Devin, Benjamin Erk, Ken R. Ferguson, Robert W. Field, Lutz Foucar, Leszek J. Frasinski, James M. Glownia, Markus Gühr, Andrei Kamalov, Jacek Krzywinski, Heng Li, Jonathan P. Marangos, Todd J. Martinez, Brian K. McFarland, Shungo Miyabe, Brendan Murphy, Adi Natan, Daniel Rolles, Artem Rudenko, Marco Siano, Emma R. Simpson, Limor Spector, Michele Swiggers, Daniel Walke, Song Wang, Thorsten Weber, Philip H.

Bucksbaum, and Vladimir S. Petrovic. Ultrafast isomerization initiated by X-ray core ionization. *Nature Communications*, 6:8199, September 2015.

[137] A Sanchez-Gonzalez, T R Barillot, R J Squibb, P Kolorenč, M Agaker, V Averbukh, M J Bearpark, C Bostedt, J D Bozek, S Bruce, S Carron Montero, R N Coffee, B Cooper, J P Cryan, M Dong, J H D Eland, L Fang, H Fukuzawa, M Guehr, M Ilchen, A S Johnsson, C Liekhus-S, A Marinelli, T Maxwell, K Motomura, M Mucke, A Natan, T Osipov, C Östlin, M Pernpointner, V S Petrovic, M A Robb, C Sathe, E R Simpson, J G Underwood, M Vacher, D J Walke, T J A Wolf, V Zhaunerchyk, J-E Rubensson, N Berrah, P H Bucksbaum, K Ueda, R Feifel, L J Frasinski, and and J P Marangos. Auger electron and photoabsorption spectra of glycine in the vicinity of the oxygen K-edge measured with an X-FEL. *Journal of Physics B: Atomic, Molecular and Optical Physics*, 48(23):234004, December 2015.

[138] A. Javan, W. R. Bennett, and D. R. Herriott. Population Inversion and Continuous Optical Maser Oscillation in a Gas Discharge Containing a He-Ne Mixture. *Physical Review Letters*, 6(3):106–110, February 1961.

[139] C. K. N. Patel. Continuous-Wave Laser Action on Vibrational-Rotational Transitions of CO2. *Physical Review*, 136(5A):1187–1193, November 1964.

[140] B. H. Soffer and B. B. McFarland. Continuously tunable, narrow-band organic dye lasers. *Applied Physics Letters*, 10(10):266–267, May 1967.

[141] J. E. Geusic, H. M. Marcos, and L. G. Van Uitert. Laser oscillations in Nd-doped yttrium aluminum, yttrium gallium and gadolinium garnets. *Applied Physics Letters*, 4(10):182–184, May 1964.

[142] T. Pollak, W. Wing, R. Grasso, E. Chicklis, and H. Jenssen. CW laser operation of Nd:YLF. *IEEE Journal of Quantum Electronics*, 18(2):159–163, February 1982.

[143] Peter Moulton. Ti-doped sapphire: tunable solid-state laser. *Optics News*, 8(6):9–9, November 1982.

[144] Kevin F. Wall and Antonio Sanchez. Titanium sapphire lasers. *Lincoln Laboratory Journal*, 3:447–462, 1990.

[145] Willis E. Lamb. Theory of an Optical Maser. *Physical Review*, 134(6A):A1429–A1450, June 1964.

[146] C. Iaconis and I.A. Walmsley. Spectral phase interferometry for direct electric-field reconstruction of ultrashort optical pulses. *Optics Letters*, 23(10):792, May 1998.

[147] J. Itatani, F. Quéré, G. L. Yudin, M. Yu. Ivanov, F. Krausz, and P. B. Corkum. Attosecond Streak Camera. *Physical Review Letters*, 88(17):173903, April 2002.

[148] D. J. Kane and R. Trebino. Characterization of arbitrary femtosecond pulses using frequency-resolved optical gating. *IEEE Journal of Quantum Electronics*, 29(2):571–579, February 1993.

[149] A.P.E Angewandte Physik & Elektronik GmbH. Spiders | A·P·E. https://www.ape-berlin.de/en/products/spiders, 2016. [Accessed on 21/10/2016].

[150] Thorlabs. Thorlabs Protected Silver Mirrors. https://www.thorlabs.com/newgrouppage9.cfm?objectgroup_id=903, October 2016. [Accessed on 21/10/2016].

[151] B. L. Henke, E. M. Gullikson, and J. C. Davis. X-Ray Interactions: Photoabsorption, Scattering, Transmission, and Reflection at E = 50-30,000 eV, Z = 1-92. *Atomic Data and Nuclear Data Tables*, 54(2):181–342, July 1993.

[152] D. J. Baker, D. E. Bedo, and D. H. Tomboulian. Continuous Photoelectric Absorption Cross Section of Helium. *Physical Review*, 124(5):1471–1476, December 1961.

[153] M. Ruberti, V. Averbukh, and P. Decleva. B-spline algebraic diagrammatic construction: Application to photoionization cross-sections and high-order harmonic generation. *The Journal of Chemical Physics*, 141(16):164126, October 2014.

[154] Christian Ott, Andreas Kaldun, Luca Argenti, Philipp Raith, Kristina Meyer, Martin Laux, Yizhu Zhang, Alexander Blättermann, Steffen Hagstotz, Thomas Ding, Robert Heck, Javier Madroñero, Fernando Martín, and Thomas Pfeifer. Reconstruction and control of a time-dependent two-electron wave packet. *Nature*, 516(7531):374–378, December 2014.

[155] S. Augst, D. Strickland, D. D. Meyerhofer, S. L. Chin, and J. H. Eberly. Tunneling ionization of noble gases in a high-intensity laser field. *Physical Review Letters*, 63(20):2212–2215, November 1989.

[156] B. Walker, B. Sheehy, L. F. DiMauro, P. Agostini, K. J. Schafer, and K. C. Kulander. Precision Measurement of Strong Field Double Ionization of Helium. *Physical Review Letters*, 73(9):1227–1230, August 1994.

[157] Jonathan Leeuwenburgh, Bridgette Cooper, Vitali Averbukh, Jonathan P. Marangos, and Misha Ivanov. High-Order Harmonic Generation Spectroscopy of Correlation-Driven Electron Hole Dynamics. *Physical Review Letters*, 111(12):123002, September 2013.

[158] W. C. Martin. Ongoing compilation of data for He I (NIST). http://physics.nist.gov/PhysRefData/Handbook/Tables/heliumtable5_a.htm, 2002. [Accessed on 21/10/2016].

[159] Michael Chini, Xiaowei Wang, Yan Cheng, and Zenghu Chang. Resonance effects and quantum beats in attosecond transient absorption of helium. *Journal of Physics B: Atomic, Molecular and Optical Physics*, 47(12):124009, 2014.

[160] M. Holler, F. Schapper, L. Gallmann, and U. Keller. Attosecond Electron Wave-Packet Interference Observed by Transient Absorption. *Physical Review Letters*, 106(12):123601, March 2011.

[161] Jonathan Mooney and Patanjali Kambhampati. Get the Basics Right: Jacobian Conversion of Wavelength and Energy Scales for Quantitative Analysis of Emission Spectra. *The Journal of Physical Chemistry Letters*, 4(19):3316–3318, October 2013.

[162] Jack Sugar and Arlene Musgrove. Energy Levels of Krypton, Kr I through Kr XXXVI. *Journal of Physical and Chemical Reference Data*, 20(5):859–915, September 1991.

[163] X-Ray Data from the X-Ray Data Booklet Online. http://www.osti.gov/dataexplorer/biblio/1077291-ray-data-from-ray-data-booklet-online. [Accessed on 14/02/2017].

[164] M. Drescher, M. Hentschel, R. Kienberger, M. Uiberacker, V. Yakovlev, A. Scrinzi, Th Westerwalbesloh, U. Kleineberg, U. Heinzmann, and F. Krausz. Time-resolved atomic inner-shell spectroscopy. *Nature*, 419(6909):803–807, October 2002.

[165] N. A. Hart, J. Strohaber, G. Kaya, N. Kaya, A. A. Kolomenskii, and H. A. Schuessler. Intensity-resolved above-threshold ionization of xenon with short laser pulses. *Physical Review A*, 89(5):053414, May 2014.

Appendix A

Copyright Permissions

The table below states the third-party copyright permissions sought for use in this thesis. Where email permission has been granted, these are presented in the following Figures.

Item	Page	Type of Work	Reference	Copyright Holder and Year	Licence	Permission
1	24	Fig.	[5]	Nature Publishing Group	3944180459358	✓
			[26]	© 2008 Canadian Science Publishing.	3944190244811	✓
2	25	Mod. Fig.	[14]	© IOP Publishing.	Email	✓
3	55	Partial Fig.	[90]	AAAS	3944191150941	✓
4	71	Fig.	[144]	The Lincoln Laboratory Journals	Email	✓
5	89	Mod. Fig.	[37]	SPIE	Shared Copyright	N/A
6	127	Fig.	[35]	© IOP Publishing.	CC BY 3.0	N/A
7	133	Mod. Fig.	[35]	© IOP Publishing.	CC BY 3.0	N/A
8	137	Fig.	[35]	© IOP Publishing.	CC BY 3.0	N/A
9	139	Fig.	[35]	© IOP Publishing.	CC BY 3.0	N/A
10	183	Fig.	[20]	Nature Publishing Group	CC BY-NC-ND 3.0	N/A

Kathryn Shaw <Kathryn.Shaw@iop.org> on behalf of Permissions <permissions@iop.org>
Fri 09/09, 16:19

Dear Emma Simpson,

Please accept my apologies for the mistake and confusion. Please see below for the correct permissions!

Thank you for your request to reproduce IOP Publishing material in your thesis.

Regarding:

Figure 2 (G A Mourou et al 2007 Plasma Phys. Control. Fusion 49 B667)

We are happy to grant permission for the use you request on the terms set out below.

Conditions

Non-exclusive, non-transferrable, revocable, worldwide, permission to use the material in print and electronic form will be granted **subject to the following conditions:**

- Permission will be cancelled without notice if you fail to fulfil any of the conditions of this letter.
- You will make reasonable efforts to contact the author(s) to seek consent for your intended use. Contacting one author acting expressly as authorised agent for their co-authors is acceptable.
- You will reproduce the following prominently alongside the material:
  - the source of the material, including author, article title, title of journal, volume number, issue number (if relevant), page range (or first page if this is the only information available) and date of first publication. This information can be contained in a footnote or reference note; or
  - a link back to the article (via DOI); and
  - if practical and IN ALL CASES for works published under any of the Creative Commons licences the words "© IOP Publishing. Reproduced with permission. All rights reserved"
- The material will not, without the express permission of the author(s), be used in any way which, in the opinion of IOP Publishing, could distort or alter the author(s)' original intention(s) and meaning, be prejudicial to the honour or reputation of the author(s) and/or imply endorsement by the author(s) and/or IOP Publishing.
- Payment of £0 is received in full by IOP Publishing prior to use.

This permission does not apply to any material/figure which is credited to another source in our publication or has been obtained from a third party. Express permission for such materials/figures must be obtained from the copyright owner.

If you have any questions, please feel free to contact our Permissions team at permissions@iop.org.

I should be grateful if you would acknowledge receipt of this email.

Kind regards,

Kathryn Shaw

Copyright & Permissions Team

Gemma Alaway – Rights & Permissions Adviser

Kathryn Shaw - Editorial Assistant

Contact Details

E-mail: permissions@iop.org

For further information: http://iopscience.iop.org/page/copyright

Please see our Author Rights Policy http://ioppublishing.org/author-rights/

Please note: We do not provide signed permission forms as a separate attachment. Please print this email and provide it to your institution as proof of permission.

Please note: Any statements made by IOP Publishing to the effect that authors do not need to get permission to use any content are not intended to constitute any sort of legal advice. Authors must make their own decisions as to the suitability of the content they are using and whether they require permission for it to be published within their article.

Figure A.1: Permissions email from Journal for Figure 1.2, modified from reference [14].

Permissions request for PhD Thesis - Modified Figure 2 - Relativistic laser-matter interaction: from attosecond pulse generation to fast ignition

Reply all

VT

Vladimir Tikhonchuk <tikhonchuk@u-bordeaux.fr>

Mon 26/09/2016 14:03

To: Simpson, Emma

Cc: christine labaune <christine.labaune@polytechnique.fr>; mike dunne <mike.dunne@stfc.ac.uk>; Natalia Naumova <natalia.naumova@ensta-paristech.fr>; gerard mourou <gerard.mourou@ensta.fr>

Dear Emma Simpson,
surely you can take this figure for your PhD thesis (with appropriate reference)
I believe all my colleagues share this permission
sincerely

--
Vladimir Tikhonchuk
Centre Lasers Intenses et Applications
University of Bordeaux
351, Cours de la Liberation
33405 Talence cedex
France
tel. : +33 5 40 00 37 64
fax : +33 5 40 00 25 80
email: tikhonchuk@u-bordeaux.fr
http://www.celia.u-bordeaux1.fr/

Figure A.2: Permissions email from Author for Figure 1.2, modified from reference [14].

MASSACHUSETTS INSTITUTE OF TECHNOLOGY
LINCOLN LABORATORY

244 WOOD STREET
LEXINGTON, MASSACHUSETTS 02420-9108

Area Code 781
981-4204

13 September 2016

Emma Simpson
PhD Candidate
Imperial College London

SUBJECT: Permission to use figure 4 in the Lincoln Laboratory Journal article 'Titanium Sapphire Lasers 'by K.F.Wall and A.Sanchez, Vol. 3, No. 3, 1990.

Dear Ms. Simpson,

The Massachusetts Institute of Technology and its Lincoln Laboratory, collectively MIT, is providing you with limited permission to use the subject copyrighted figure in your thesis.

Please include the following wording as an acknowledgement of this reprint.

> "Reprinted with permission courtesy of MIT Lincoln Laboratory, Lexington, Massachusetts"

Any other use of the content will require additional permissions.

Very truly yours,

David R. Granchelli
Manager
Communications and Community Outreach Office

DRG/aal

Figure A.3: Permissions email for Figure 3.2, reproduced from reference [144].

Permission request to use a modified figure in a PhD thesis

Reply all

Nicole Harris <nicoleh@spie.org>
Thu 08/09, 16:32
Simpson, Emma

Action Items

Dear Ms. Simpson,

Thank you for seeking permission from SPIE to reprint material from our publications. As author, SPIE shares the copyright with you, so you retain the right to reproduce your paper in part or in whole.

Publisher's permission is hereby granted under the following conditions:

(1) the material to be used has appeared in our publication without credit or acknowledgment to another source; and

(2) you credit the original SPIE publication. Include the authors' names, title of paper, volume title, SPIE volume number, and year of publication in your credit statement.

Sincerely,

Nicole Harris
Administrative Editor, SPIE Publications
1000 20th St.
Bellingham, WA 98225
+1 360 685 5586 (office)
nicoleh@spie.org

SPIE is the international society for optics and photonics. http://SPIE.org

SPIE.

Figure A.4: Permissions email for Figure 4.1, modified from reference [37].

Kathryn Shaw <Kathryn.Shaw@iop.org> on behalf of Permissions <permissions@iop.org>

Fri 09/09/2016 14:05

To: Simpson, Emma

Reply all

Action Items

Dear Emma Simpson,

Thank you for your email and for taking the time to seek this permission.

When you transferred the copyright in your article to IOP, we granted back to you certain rights, including the right to include the Final Published Version of the article within any thesis or dissertation (or individual components from it). Please note you may need to obtain separate permission for any third party content you included within your article.

Please include citation details, "© IOP Publishing. Reproduced with permission. All rights reserved" and for online use, a link to the Version of Record.

The only restriction is that if, at a later date, your thesis were to be published commercially, further permission would be required.

Please let me know if you have any further questions.

In the meantime, I wish you the best of luck with the completion of your dissertation.

Kind regards,

Kathryn Shaw

Copyright & Permissions Team

Gemma Alaway – Rights & Permissions Adviser

Kathryn Shaw - Editorial Assistant

Contact Details

E-mail: permissions@iop.org

For further information: http://iopscience.iop.org/page/copyright

Please see our Author Rights Policy http://iopublishing.org/author-rights/

Please note: We do not provide signed permission forms as a separate attachment. Please print this email and provide it to your institution as proof of permission.

Please note: Any statements made by IOP Publishing to the effect that authors do not need to get permission to use any content are not intended to constitute any sort of legal advice. Authors must make their own decisions as to the suitability of the content they are using and whether they require permission for it to be published within their article.

Figure A.5: Permissions email for Figures 5.2,5.4,5.6 and 5.7, reproduced and modified from reference [35].

Figure A.6: Permissions email for Figure 6.19, reproduced from reference [20].